University of
Strathclyde
Science

Enzyme responsive nanomaterials for cancer applications

A thesis presented to the Department of Pure and Applied Chemistry, University of Strathclyde in fulfilment of the requirements for the degree of Doctor of Philosophy.

2014

Daniela Kalafatovic

Declaration

This thesis is the result of the author's original research. It has been composed by the author and has not been previously submitted for examination which has led to the award of a degree.

Copyright

Signed:

Date:

Acknowledgements

I would like to thank my supervisor Prof. Rein Ulijn for the opportunity to work at his side in a very diverse and stimulating environment and for guiding me throughout the PhD and believing in my ideas. I am grateful to "our" group secretary Isabel Scott that made all the bureaucratic and other "impossible" issues possible, for her warm welcome at the very beginning, her presence, her young spirit and always positive attitude in all sorts of situations.

I would also like to thank Prof. Brian Saunders and his group (at the University of Manchester) for introducing me to the "polymer world", Prof. Nathan Gianneschi and the group (at UCSD; especially Anthony, Andrea and Joe) for their hospitality, friendship and introducing me to the Californian "way of Academic life" and Prof. Peter Cormack and his polymer group (at University of Strathclyde) for support with all kind of polymer issues. I am glad that I could meet such a great group of scientists and thankful to all for the advices, time and knowledge shared with me.

I would like to thank Patricia Keating (University of Strathclyde) for help with LCMS, MS and MALDI, for never giving up in finding new solutions and for useful result and technique discussions. I am thankful to Margaret Mullin (University of Glasgow) for help with EM techniques and patience with my numerous "just one last sample" requests in the late afternoon hours.

I am grateful to Prof. Kurt Anderson and Max Nobis (Beatson Institute for Cancer Research) for listening to my ideas and as a result setting up a great collaboration, for the hospitality in the Beatson institute and for numerous discussions of biology vs. chemistry worlds.

I am grateful to the Ulijn group for the support during these 3,5 years and for all "coffee" sessions in which we shared our chemistry and life problems, joys, dreams and passions. Especially I would like to thank Dr. Mischa Zelzer and Prof. Sangita Roy for their huge support, introduction to science from all points of view, for reviewing my writings, for being there at any time of day and night encouraging me to never give up, for teaching me life and patience and for continuously inspiring me.

A big thanks goes to all my friends here in Glasgow that made my stay so special: Stefania, Max, Fabio, Nuno, Elena, Iacopo, Luca, Lucio, Roberto,... I enjoyed so much our “Italian” gatherings and international dinners and chats, ceilidh and salsa dancing, road trips around Scotland, whiskey tastings and many other new experiences. To mention are also the great advices sent over skype by Tommy, Ozren, Giovanni, Manuela, David, Raffa, Manu.

A special thanks goes to Davide, for his support and love in these last part of the PhD. His patience, company and especially his midnight delicious “pasta” dishes during our late night working hours were invaluable.

Most of all, I would like to thank my parents, Sonia and Miso for the constant support and all their love; my grandmothers nonna Norma and nana Marijana and my grandfather Giorgio for their continuous encouragements, for their big interest in the topic and pride when thinking about me and “explaining” my work to their friends. In addition, I would like to thank my aunt Sara, for inspirational talks, for great optimism, huge knowledge and above all, her belief in my capabilities since the very first day of this “long” journey.

Grazie di cuore- without you, all this would have been impossible.

Daniela

Abstract

Expression levels of enzymes dictate the difference between health and disease in many cases, including cancer. This leads scientists to explore strategies to incorporate enzyme sensitivity in materials where the goal is to achieve dynamic and targeted changes in material properties to influence cancer cells.

Peptide amphiphiles were designed (PhAc-FFAGLDD (**1a**) and GFFLGLDD (**2a**) and their expected products of enzyme cleavage PhAc-FFAG (**1b**) and GFFLG (**2b**)) such that, upon cleavage by a disease-associated enzyme, reconfigure from micellar aggregates to fibres. After the designed peptides (**1a**, **1b**, **2a**, **2b)** were shown to be suitable for controlling the morphology of the supramolecular aggregates based on peptide length, hydrophobicity and charge, the enzyme triggered micelle to fibre transition was explored. Following this it was investigated whether the micelles were capable to perform as mobile vehicles for encapsulation and release of hydrophobic drugs. It was observed that the assembled fibres provide a scaffold for prolonged drug delivery due to the partial entrapment (localised depots) of the drug and the intrinsic biodegradable nature of peptide carriers themselves.

The capacity of retention of doxorubicin in the hydrophobic core of the micelles followed by its entrapment in the fibres was exploited in the development of a method for visualisation of fibre formation around cancer cells. *In vitro* studies were performed on human cancer cell lines using different types of microscopy. MMP-9 activity was quantified in the mentioned cancer cell lines. In addition, preliminary toxicity studies of the designed peptides to cancer cells were performed. Being purely peptidic (compared to conventional aromatic or aliphatic peptide amphiphiles), these systems have the advantage of being non toxic to cells and can be used as carriers for doxorubicin *in vivo*. They are currently tested on animal models where the cancer growth is slowed down by administration of doxorubicin loaded peptides compared to doxorubicin only.

Another, complementary system was investigated based on crosslinked polymer particles- microgels as a possible way to obtain enzyme responsive materials. Amine rich microgels, poly(VAM-co-BEVAME) were synthesised and functionalised post-polymerisation with peptides. Due to aggregation issues these systems were not further explored for biomedical applications.

Contents

Index of figures and tables

Chapter 1

Chapter 2

Chapter 3

Chapter 4

Chapter 5

1 Introduction to thesis

1.1 Motivation

Today cancer is a big problem faced by society as it is still one of the main causes of death in the world. The conventional cancer therapy based on chemotherapy, radiation and surgery is still not able to eradicate cancer completely. The current therapy approaches have limitations in that they are not sufficiently specific, effective or localized. Advances are being made in cancer treatment as nanotechnology is developing new directions informed by new understanding of cancer mechanisms and biochemistry- such as enzyme over-expression.[1]

Nanotechnology today offers a variety of inventive nanoscale systems having organic, inorganic and biological origins.[2] Very recently some examples of ERMs (enzyme responsive materials) based on self-assembly of aromatic peptide amphiphiles have been considered for cancer imaging and therapy.[3]

In this thesis, the importance and the emerging trends in the field of enzyme triggered self-assembly of peptide based materials for targeted delivery of anticancer therapeutics using a minimalistic approach will be highlighted. Simple, cost effective, safe and most importantly efficient carriers for selective cancer targeting are required to facilitate standard cancer treatments. For this purpose biocompatible, peptide based nanomaterials that undergo a morphology change in response to a cancer associated enzyme are developed in this thesis. The mechanism of their action would have the advantage of going from free flowing to localized drug delivery systems only in cancer tissues. Such systems could provide new ways of addressing imaging, diagnostics and ultimately treatment.

(1) Peer, D.; Karp, J. M.; Hong, S.; Farokhzad, O. C.; Margalit, R.; Langer, R. *Nat Nanotechnol* **2007**, *2*, 751.

(2) Schroeder, A.; Heller, D. A.; Winslow, M. M.; Dahlman, J. E.; Pratt, G. W.; Langer, R.; Jacks, T.; Anderson, D. G. *Nat Rev Cancer* **2012**, *12*, 39.

(3) (a) Gao, Y.; Shi, J. F.; Yuan, D.; Xu, B. *Nat. Commun.* **2012**, *3*(b) Gao, Y.; Berciu, C.; Kuang, Y.; Shi, J.; Nicastro, D.; Xu, B. *ACS nano* **2013**, *7*, 9055(c) Kuang, Y.; Shi, J.; Li, J.; Yuan, D.; Alberti, K. A.; Xu, Q.; Xu, B. *Angew Chem Int Edit* **2014**.

1.2 Objectives

In this thesis, two different strategies to incorporate enzyme sensitivity in materials were explored with the goal to achieve dynamic and targeted changes in material properties. The main approach is based on self-assembly of aromatic peptide amphiphiles. It was the objective to exploit peptide-self assembly and its versatility to form fibrillar structures in a controlled (enzyme-triggered) manner. The second approach involves the development of enzyme responsive microgel particles where enzyme induced swelling is of interest for drug delivery applications.

Firstly, we set out to develop peptide based enzyme responsive systems able to undergo a morphological change from micellar aggregates to fibres in response to cleavage by MMP-9. This required a design study based on literature examples where MEROPS database was used as a starting point to determine the substrates for MMP-9. The micelle to fibre morphological transition was then exploited for localised formation of a depot for slow release of hydrophobic, anti-cancer therapeutics (e.g. doxorubicin) only in the presence of the target enzyme. *In vitro* and *in vivo* investigations are expected to show the ability of the designed systems to influence/slow tumour growth.

In addition, post-polymerisation modification of microgel particles with peptide sequences was assessed with the goal to achieve enzyme triggered swelling of microgels. This approach could have potential in biomedical application if a drug is loaded into the polymeric particle. After swelling only in the presence of the enzyme the payload could be released on demand.

By working in parallel on these two different approaches, MMP-9 sensitive peptide amphiphiles were found to be more promising as carriers in terms of cost (easily synthesized and scalable) and toxicity. Some additional advantages are their inherent biocompatibility (made of natural amino acids) and ability to mimic more complex protein assemblies present in the body. This was later confirmed by cell viability studies conducted on cancer cells. Therefore our main focus was put on developing MMP-9 responsive peptide amphiphiles for slow release of doxorubicin with future applications *in vitro* and *in vivo*.

1.3 Layout of the thesis

The thesis is split into several Chapters. The first Chapter is composed of a literature review focused on the state of the art of the use of nanotechnology for application in cancer therapy (Fig 1.1). In particular, self-assembly based nanomaterials are discussed with the emphasis on enzyme responsive peptide amphiphiles and the progress made in the field.

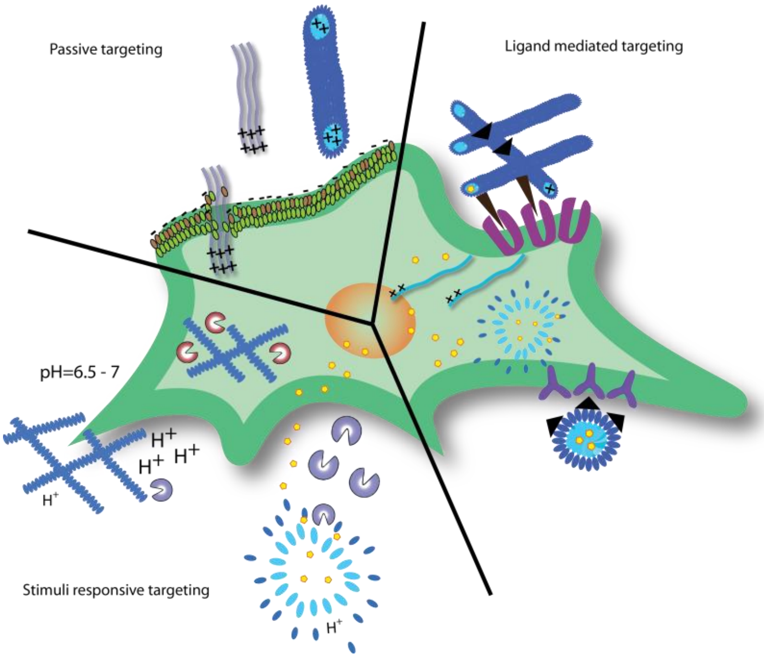

Figure 1.1. Schematic representations of possible mechanisms for targeting cancer with peptide-based materials.

The literature review is followed by a series of experimental Chapters. Each experimental Chapter has its own introduction, experimental section and a results and discussion section.

The first experimental Chapter (Chapter 3) investigates peptide amphiphiles (PhAc-FFAGLDD and GFFLGLDD) that undergo MMP-9 triggered micelle-to-fibre transitions (Fig. 1.2). The enzyme induced morphological transition was exploited for *in situ* formation of nanostructured depot for slow release of doxorubicin.

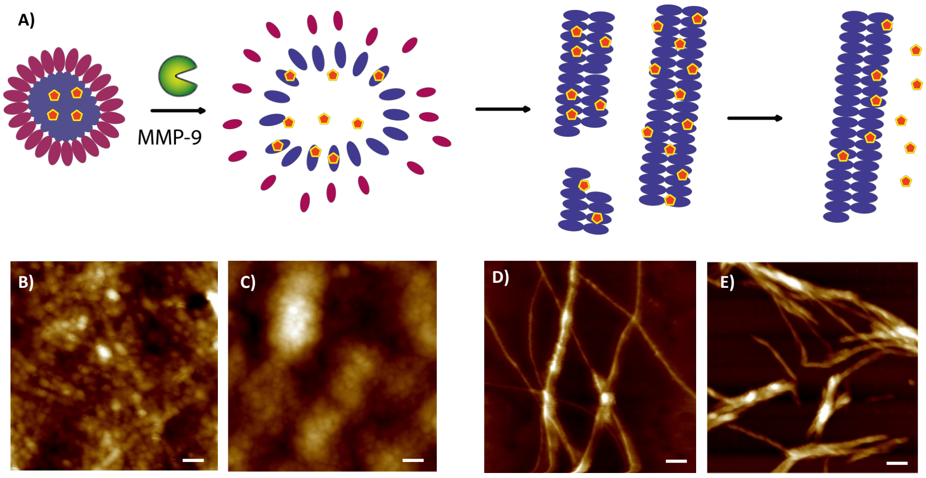

Figure 1.2. A) Schematic representation of micelle to fibre transition induced by MMP-9 cleavage showing disassembly of micelles and the re-assembly into fibres after the removal of the hydrophilic group enabling prolonged drug release. B), C), D) and E) AFM images of micelle to fibre transition induced by MMP-9: PhAc-FFAGLDD (B) to PhAc-FFAGL (D) and GFFLGLDD (C) and GFFLGL (E). Scale bars are 200 nm.

This concept was further explored in terms of visualisation of fibre formation around cancer cells (Fig. 1.3) in Chapter 4. This Chapter is a collaboration project with the Beatson Cancer Research Institute, Glasgow, UK. Human cancer cell lines (cervical and breast cancer) were provided and handled by Max Nobis at the Beatson Cancer Research Institute. MMP-9 activity of these cancer cell lines was quantified and different microscopy techniques were used (confocal microscopy, TEM and SEM) to study the fibre formation in presence and absence of cancer cells/enzymes. In addition, *in vivo* studies are ongoing to assess the ability of new peptide carriers to affect tumour growth in mice (briefly discussed in Appendix I).

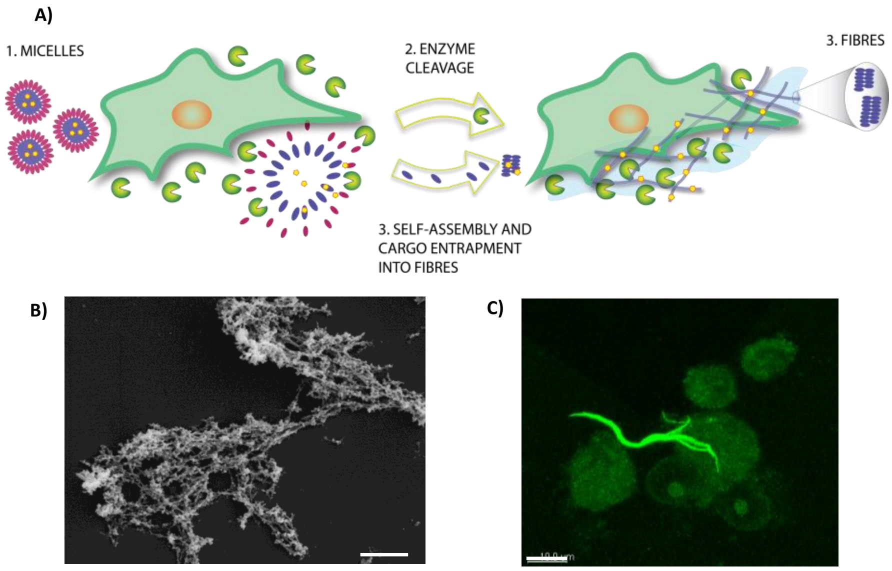

Figure 1.3. A) Schematic representation of enzyme triggered formation of local depots for slow release of doxorubicin in proximity of cancer cells. B) SEM image of fibres formed after MMP-9 treatment of GFFLGLDD. C) MBA-MD-231- cells treated with GFFLGLDD loaded with riboflavin.

In Chapter 5 amine rich enzyme responsive microgels are described. This is a collaboration project with the School of Materials, University of Manchester, UK. Microgels were designed and optimised by the Saunders group at the University of Manchester. These microgels were considered for further studies at University of Strathclyde. In this Chapter a method development for post-polymerisation modification (with peptides) of amine rich microgels is presented in order to introduce enzyme responsiveness into the system (Fig. 1.4).

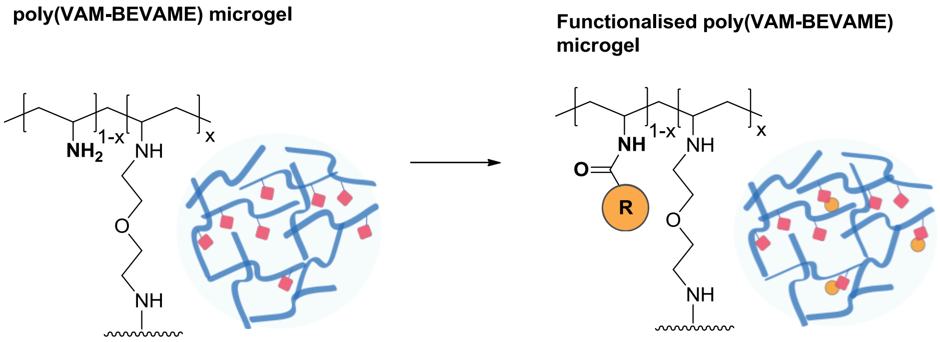

Figure 1.4. Schematic representation of post –polymerisation modification of microgels.

This is followed by an overall conclusion and future work section that sums up the achievement of the work and the next steps that will be performed.

2 Literature review

2.1 Nanotechnology for biomedical applications i.e. cancer therapy

One major area of interest in biomedicine is cancer, being one of the main causes of death in the world,[4] and the second most common cause of death in the United States according to the American Society of Clinical Oncology (ASCO).[4] This agency publishes an “Annual Report on Progress Against Cancer” summarizing the recent advances in cancer research including information about the annual progress that nanotechnology makes in reaching the clinic.[4] Even though advances are made in cancer treatment, the conventional cancer therapy, which is still not able to eradicate cancer completely, to date, is mainly based on chemotherapy, radiation and surgery. This limits its efficiency in treating/addressing specifically cancer cells causing many undesired effects to normal tissues.[5] In order to improve the quality of life of cancer patients one focus has been put on nanotechnology and its tremendous progress in the last decades.

Cancer nanotechnology emerges as a multidisciplinary field that designs and develops materials at the nanoscale to research potential new routes to cancer and metastatic cancer treatment.[2] Many nanosystems have been developed in laboratories across the globe but the translation from laboratory to clinic is a slow and tedious process and many systems i.e. designed nanocarriers fail clinical trials because of limited delivery efficiency and selectivity *in vivo*.[2] However, designing new materials focusing on better understanding of the tumour microenvironment and targeting specific targets holds great promise for new systems to reach the clinic. Nevertheless, some examples of anti-cancer nanotechnology systems have reached the clinic with FDA approved treatments of cancer/metastatic cancer such as: doxorubicin loaded PEGylated liposome based formulations (Doxil) for the treatment of ovarian cancer and Karposi’s sarcoma[2,6] and paclitaxel protein (albumin)-bound nanoparticles (Abraxane)[4,7] approved for the treatment of metastatic breast cancer, to name just a few. Among more than 40 nanotherapeutics that have reached the clinic for treatment and imaging of various diseases only 25% are related to cancer applications.[2,8] However, a new generation of nanomedicines in the stage of transition from laboratories to preclinical and clinical studies are being developed primarily for cancer applications.[8]

Nanotechnology today offers a variety of inventive nanoscale systems having organic, inorganic and biological origins. These are mainly based on building blocks of different structural and functional properties including biologic materials (DNA, proteins, peptides, lipids, polysacharides), polymers, metals (gold, iron), and carbon based materials. A variety of new materials with potential application in drug delivery are liposomes[9], micelles (lipid, peptide or polymer based)[10], silica particles[11], gold nanomaterials[12], magnetic nanoparticles (iron-oxide)[13], quantum dots[14], polymer-peptide conjugates[15], polymer-drug conjugates[16], various polymeric systems (hydrogels, micelles, dendrimers, core-shell nanoparticles)[17], functionalized carbon nanotubes[18], nanodiamonds[19], DNA origami cages[20] and many others.[8]

Nanotechnology tools designed and/or used to fight cancer are mainly based on nanoparticulate systems including polymeric (polymer-drug conjugates) and lipid-based systems (liposomes). The first liposomal nanoparticulate system for the treatment of Kaposi's sarcoma was approved by FDA in 1995, and later on extended also to treatment of ovarian cancer. The most widely utilised polymer for drug-delivery applications is polyethylene glycol (PEG) which is able to decrease the immunogenicity of administrated systems (e.g. proteins). An example of its commercialisation is PEG–l-asparaginase (Oncospar; Enzon) FDA approved in 1994 for the treatment of leukaemia.[21] These examples show how liposomes and polymer–drug conjugates have been important in setting the foundations for the field of nanotechnology based, advanced drug delivery systems.[21-22] A review summarizing the examples of polymeric and liposomal nanoparticles in clinical development for cancer treatment was recently published.[5] Challenges of metastatic cancer targeting and examples of therapeutic nanocarriers used for their diagnosis and treatment were shown underlining the progress that has been made in the field (Fig. 2.1).[2]

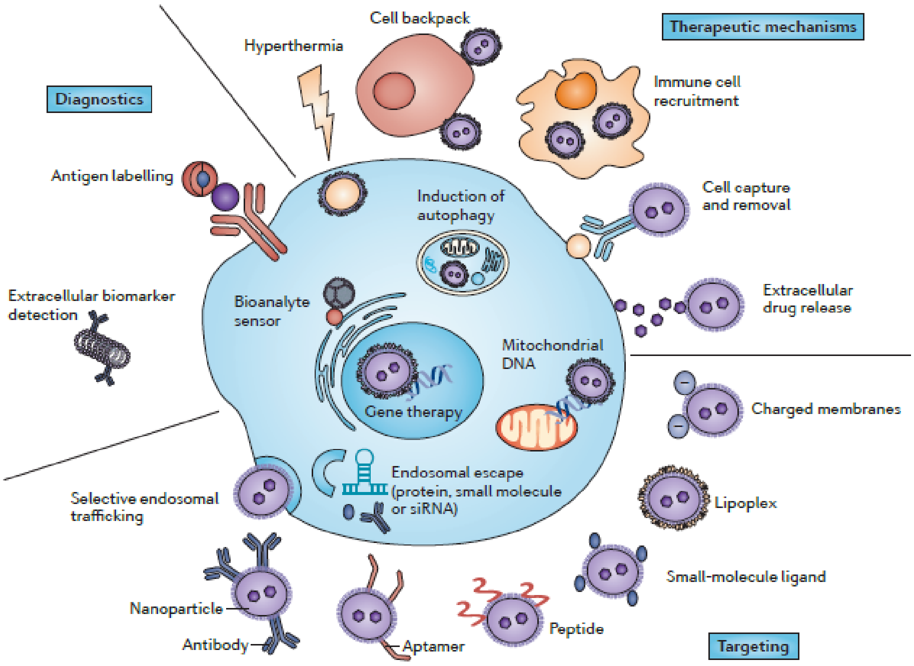

Figure 2.1. State of the art showing nanomaterials strategies used to selectively target cancer cells for therapeutic and diagnostic applications (taken form reference 2).[2]

The design of the previously mentioned nanomaterials relies on cancer targeting mechanisms and their efficiency is related to the capacity to selectively reach the tumour site. As the main challenges in the development of anti-cancer therapeutic agents are the improvement of targeting selectivity and a better delivery efficiency an accurate knowledge of the tumour mechanisms is essential.[5] The targeting of delivery vehicles to tumour tissues can be achieved by either active or passive targeting or a combination of the two. In recent years, stimuli sensitive nanosystems emerged as a new targeting strategy where the transformation of the nanocarriers is triggered by the tumoural extracellular environment.[23] It is well known that the tumour microenvironment is characterised by specific physiological and physico-chemical conditions such as low pH, hyper-proliferation, accelerated metabolism and/or specific enzyme and receptor over-expression. All of these factors individually, and nowadays more frequently combinations of them are exploited for the design of novel nanosystems able to target cancer selectively. This concept will be discussed in more detail in section 2.3.

Different strategies are used in the design of nanomaterials, some of them copying processes used by nature (biology) to build mimics of proteins and extracellular matrices. One example of this is exploiting self-assembly[24] (at the molecular level) to create more complex/ordered structures (at nanometre scale) giving rise to nanomaterials with various architectures widely used by the research community in the recent years.[25] Self-assembly occurs spontaneously in nature and is ubiquitous in processes essential to life such as protein folding and formation of complementary chains of DNA. Simple building blocks such as peptides, oligonucleotides and lipids are observed to spontaneously form highly ordered structures such as proteins, DNA assemblies and membranes, respectively. This principle can be exploited to form desired self-assembled structures by designing building blocks that will spontaneously assemble in a controlled manner. This is a powerful approach, because the control over self-assembly process gives opportunities for designing new materials in a controlled fashion where different functionalities are decorating the supramolecular structure with high localised density (e.g. cell targeting motifs (RGD – fibronectin derived cell adhesion ligand)[25a] or epitopes promoting cell differentiation (IKVAV)[26]) for applications in drug delivery, regenerative medicine and tissue engineering. Design of synthetic extracellular matrices for applications in regenerative medicine and 3D cell cultures constitutes an example.[25c] Many of the nanotechnology tools used to fight cancer mentioned above are indeed based on self-assembly (liposomes, DNA delivery systems, peptides and polymers). Therefore, selective cancer targeting can be achieved by supramolecular materials and particular attention will be paid in this review on peptide based self-assembly as an approach to design materials that contain within their structure the information necessary for selective targeting. Different aspects of cancer cells can be targeted as peptides are versatile systems having inherent biocompatibility and biodegradability, the ability to undergo self-assembly and to form different architectures as a result of their structure and the hydrophobicity/philicity balance. They are substrates of proteases that can target intracellular or extracellular enzymes, can mimic cell-binging motifs, show pH responsive behaviour, and present many other advantages. Mimicking natural phenomena to design new materials brings us to work at the interface between nanomaterials and biology. This will be discussed more in detail in the next section (section 2.2).

Being a wide field of research that is in continuous expansion, it is difficult to address and cover the huge progress and recent advances made in cancer nanotechnology. Self-assembly based materials based on liposomes, DNA, DNA-gold nanoparticles conjugates, polymers, polymer-peptide conjugates and peptide assemblies are being developed for detection and treatment of cancer. Therefore, the focus will be put on recent advances of the self-assembly (peptide and polymer-peptide conjugates) approach to develop targeted, peptide based, enzyme triggered delivery systems for cancer therapy. Emphasis will be on examples covering different stages of research, from their design to *in vitro* evaluations and *in vivo* applications. A wide range of peptide materials that follow different design strategies have been developed. However, no supramolecular, solely peptide based nanocarrier has reached the clinic yet and it is plausible to assume that peptide self-assembly is underdeveloped compared to other systems such as liposomes already actively used in cancer therapy.

2.2 Peptide self-assembly for biomedical applications (cancer therapy)

The early 1990's saw a birth of a new area of molecular self-assembly based on synthetic peptides with pioneering work presented by Ghadiri[27] and Zhang[28]. This field has seen a rapid growth and today peptide self-assembly is increasingly investigated for a wide range of applications in biomedicine including drug-delivery, diagnostics, tissue engineering and regenerative medicine.[25a-c,26,29] Peptide self-assembly is of interest for biomedical applications because of the inherent biocompatibility and biodegradability of peptides, but also because enzyme responsiveness can be easily achieved. Kaplan in 2000,[30] followed by Xu in 2004,[31] introduced the concept of enzyme controlled self-assembly. Both authors exploit phosphatase catalysed dephosphorylation, in the former case to control solubility[30] and in the latter to induce hydrogleation[31] setting ground to a new era of enzyme responsive supramolecular materials. This is attractive as enzymatic control over self-assembly can be exploited but also enzymes over-expressed in various disease states can be targeted. Thus, enzyme catalysis presents an attractive means to control self-assembly on demand and under physiological conditions. This aspect will be covered in more detail in sections 2.4 and 2.6.2.

The 20 gene-encoded amino acids, together with a variety of non-natural ones, constitute a versatile toolbox. A rich chemical and structural diversity can be achieved by designing building blocks composed of sequences of amino acids (peptides) that can spontaneously assemble into nanostructures of different architectures. Supramolecular assembly of the molecular building blocks composed of specific peptide chains is based on the same principle found in nature during protein folding. Since the elucidation, in the early 1950's, of secondary structures in proteins, such as β-sheets[32] and β-hairpins, α-helices and coiled coils[33], great advances have been made in the understanding of protein folding as the different natures of amino acid side chains determine the behaviour and the folding characteristics. Today we know that synthetic peptides can self-assemble into a variety of nanoscale morphologies directed by the amino acid sequence[34] and the mode of assembly.[35] Molecular self-assembly process is based on weak, non-covalent, interactions such as hydrogen bonds, electrostatic interactions that involve charged groups, van der Waals interactions, hydrophobic interactions and aromatic π-stacking. The nanostructures form as a result of interactions between complementary peptide chains that mimic the basic conformational units found in proteins.

Fibrillar structures reported in literature are obtained using a variety of peptide designs. Self-assembled fibrous peptide or protein based materials were classified by Woolfson[25b] in 3 main classes being: i) α-helical, ii) amyloid like (β-sheet like) and iii) peptide-synthetic hybrid amphiphiles known as aliphatic peptide amphiphiles (PA), shown in figure 2.2 a-c.[25b] In addition, another important class to mention is aromatic peptide amphiphiles (figure 2.2 d). These classes are exploited for the design of fibrillar nanostructures that can further entangle to form 3D networks resulting in hydrogels. Of these classes, the β-structured systems have been the most extensively studied so far.

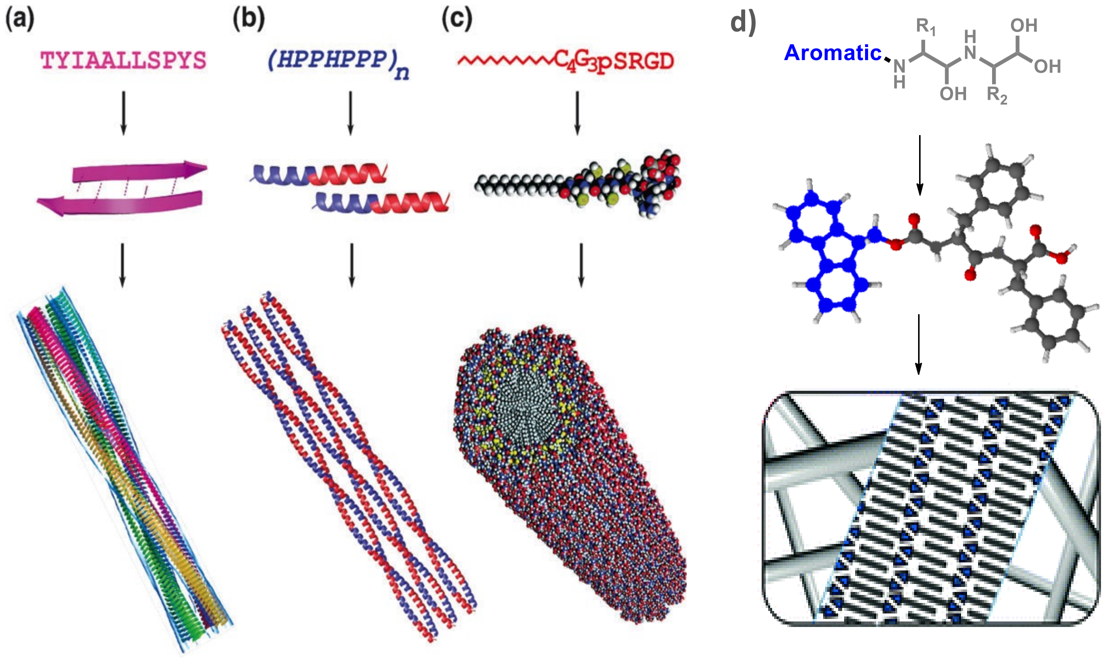

Figure 2.2. Schematic representation of different types of fibrillar assemblies, that depict different mechanisms of assembly peptide based nanomaterials can undergo (taken form reference 25b): a) β-sheet like assemblies,[25b] b) α-helical assemblies, [25b] c) aliphatic peptide amphiphiles;[25b] and d) aromatic peptide amphiphiles (in part taken from reference 36)[36].

α-helical assemblies

α-helical secondary structures form when the peptide backbone of a single amino acid chain coils due to repeating backbone dihedral angles. In this conformation each amino acid residue hydrogen bonds with the amino acid residue, which is four positions further along the chain. Assemblies based on α-helical conformation are characterized by an α-helical coiled coil motif with the repeating heptad unit (*abcdefg*)$_n$, where each letter indicates a precise position and accommodates a specific amino acid type, as shown in figure 2.3.[25b,c] For example in *a* and *d*, which stand for positions one and four respectively, only hydrophobic amino acids can be accommodated, creating a required spacing between hydrophobic units. The fifth and seventh position (*e* and *g*) closely located on neighboring helices usually contain oppositely charged amino acid residues. This electrostatic attraction can contribute to the stabilization of the helices. The other three positions (*b*, *c* and *f*) are the solvent exposed residues and have less restrictions, thus different residues can be explored for them. This type of self-assembly gives a precise control over oligomerisation, as the direct contributions of amino acids forming the structure are understood and interactions between backbones controlled (occur to lower extent compared to β-sheet like structures).

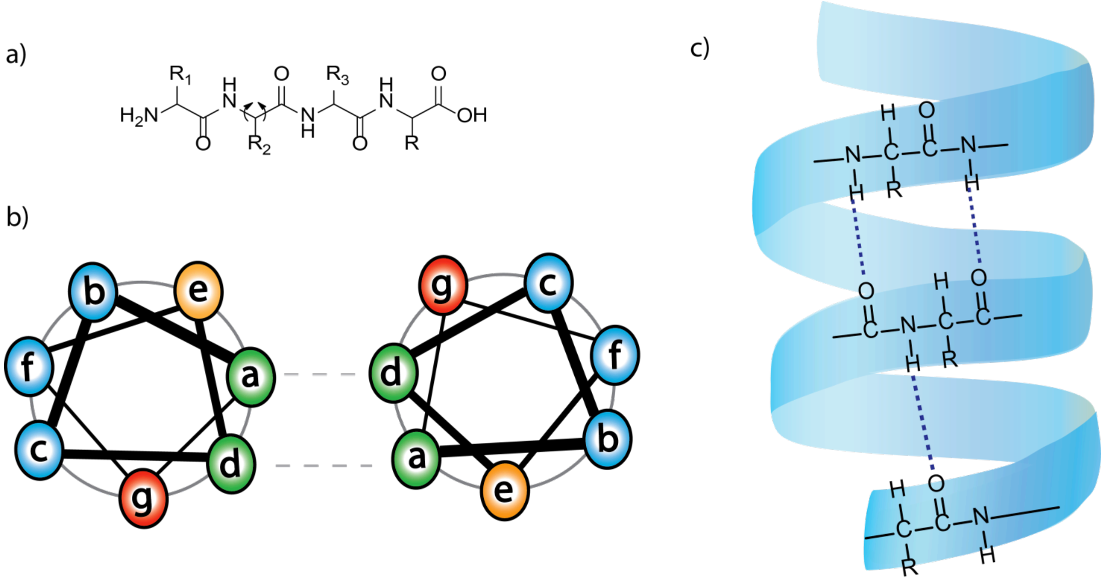

Figure 2.3. Schematic representation of a) peptide chain with dihedral angles, b) heptad units: (*abcdefg*)$_n$ where the *a* and *d* (green) are hydrophobic amino acids, *e* and *g* (orange and red) are oppositely charged amino acid residues and *b*, *c* and *f* (blue) represent the solvent exposed amino acids and c) α-helix structure indicating hydrogen bonding.

First examples of rationally designed self-assembling hydrogels based on peptides that assemble into α-helical structures were presented by Woolfson and co-workers for potential applications such as scaffolds for cell culture and tissue engineering as they supported growth and differentiation.[37] Examples of α-helical peptide assemblies investigated for anti-cancer applications are based on antimicrobial cationic peptides. These peptides tend to assume a bioactive helical conformation when in contact with cancer cell surfaces.[38] However, they are not administered as nanostructures, but as soluble inactive forms that were found to assemble due to the contact with negatively charged membranes to give cytotoxicity. α-helical fibrous materials were reported using long peptide sequences (> 25 amino acid residues) of *de novo* design to obtain control over fibre formation.[39]

β-sheet like assemblies

Fibrillar assemblies of proteins based on β-sheets were found in some degenerative disease states such as Alzheimer, where self-assembly of mis-folded proteins results in amyloid fibrillar aggregates. β-sheet like fibrils are dominated by intermolecular hydrogen bonding between adjacent chains and can be formed by proteins, peptides of *de novo* design, β-hairpins, aromatic peptide amphiphiles and aliphatic peptide amphiphiles. The hydrogen bonds extensively form between carbonyl and secondary amino groups on the peptide backbone when they are closely aligned. The formation of β-sheets can occur in two ways: parallel, where the direction of every N (N-terminus) to C (C-terminus) peptide backbone is in the same direction and anti-parallel, where the peptide backbones are parallel but the direction of the peptide chains is alternating, going from N to C and from C to N as shown in figure 2.4. In β-sheet like structures the β-strands that hydrogen bond to form sheets run perpendicularly to the fibre axis. β-sheet formation in engineered nanostructures is obtained by alternating hydrophobic with hydrophilic residues, by introducing aromatic moieties (aromatic peptide amphiphiles) or by basing the design on known β-sheet forming moieties (aliphatic peptide amphiphiles). β-sheet forming peptides based on EAK and RADA (peptide sequences), where hydrophobic amino acids residues are alternated with hydrophilic, charged amino acids have been studied primarily for regenerative medicine applications.[40]

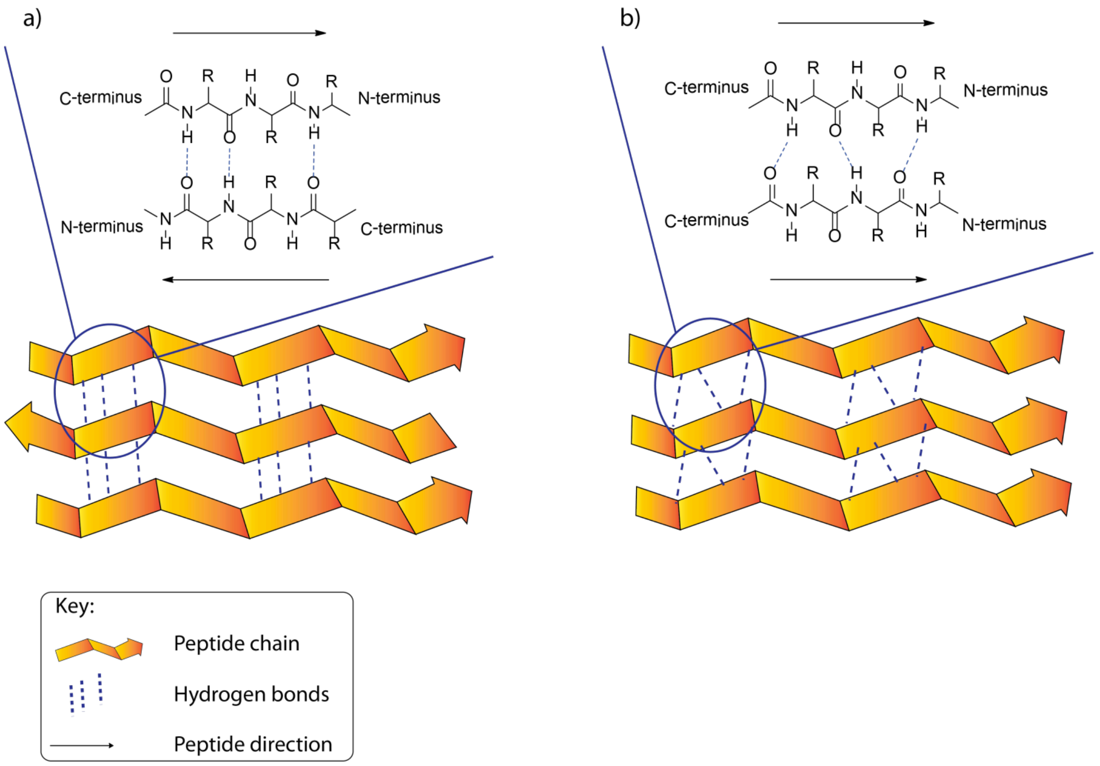

Figure 2.4. Schematic representation of a) anti-parallel and b) parallel β-sheets found in proteins and synthetic peptides.

Aliphatic peptide amphiphiles (PAs)

PAs pioneered by Hartgerink and Stupp consist of a peptidic part (usually β-sheet forming) and a hydrophobic alky chain (from naturally occurring fatty acids) that favor the assembly into nanostructures having a hydrophobic core and a peptide decorated shell.[41] Even if the peptide part is often based on β-sheet like assembly (based on hydrogen bonding) these are treated separately as the hydrophobcity is introduced in the form of alkyl chain to favor hydrophobic collapse while the peptidic part has mainly a function of introducing the desired functionality. However, the overall assembly into fibrillar nanostructures results from a balance between hydrophobic collapse of the alkyl chains and hydrogen bonding in the β-sheet-forming region. These systems have the advantage to assemble into fibers, with the self-assembling and functional units being incorporated into the same molecule. This is valuable in the design of nanomaterials with high local concentrations of specific peptides at the outer surface, that are of interest for cell targeting (RGD, IKVAV) or for inducing cell toxicity (KLAK)[42]. An example is given by fibres decorated with cationic, cytotoxic KLAK peptides, known to disrupt mitochondrial and/or plasma membranes. KLAK peptide nanostructures were found to be readily internalised by cancer cells causing cell death. This concept can be used towards the development of potential drug-free, biodegradable therapeutics.[42] Some PAs recently reported by Stupp and co-workers are designed and explored as nanotechnology platforms for cancer therapy.[42-43] So far, they constitute the main class of self-assembling peptides explored for cancer applications (drug delivery), among the other types of peptide based nanostructures mentioned. An interesting approach is the encapsulation of an anticancer agent, such as camptothecin, by hydrophobic collapse.[43b] Encapsulation of camptothecin into nanofibres was performed using a solvent evaporation method, where both the peptide amphiphile and the hydrophobic drug were dissolved in a mutual solvent. After solvent removal water was added and water–induced hydrophobic collapse obtained, resulting in nanostructures containing high concentrations of the anticancer agent. Gradual release of the drug from the nanofibres was observed over the period of 1 week. This system was then investigated *in vitro* and *in vivo* for potential cancer treatment and showed that the camptothecin had enhanced antitumour potential when encapsulated in the peptide amphiphiles due to the peptide induced cytotoxicity. However, the *in vivo* studies did not show a significant difference in tumour growth compared to the camptothecin only. If further developed, great therapeutic potential could be achieved using these systems by encapsulating the drug in pro-apoptotic or cytotoxic peptides and/or peptides sequences that can target tumours.

Aromatic peptide amphiphiles

Of particular interest are aromatic peptide amphiphiles based on low molecular weight hydrogelators. Short peptides, that are as short as 2 amino acid residues, have been reported to self-assemble into fibers that can further interact and entangle to form hydrogels.[29b,44] The use of very short peptides was pioneered by Gazit[45] who showed diphenylalanine (FF) nanotube formation as a result of a combination of hydrogen bonding and π-stacking of hydrophobic peptidic residues. Since then the field of short peptide gelators (<5 amino acids) has grown considerably. They are often modified at the N-terminus with aromatic groups such as phenyl, naphthyl, fluorenyl and others, which contributes to hydrophobic interactions and π-π stacking between aromatic moieties.[46] Hydrogels based on small aromatic peptide gelators have been explored for various biomedical applications, ranging from tissue engineering to drug delivery. An example of hydrogels used as drug delivery platforms for cancer therapy is given by a tetrapeptidic hydrogel used for the entrapment and slow release of an anticancer drug, doxorubicin.[29a] It was investigated whether the hydrogelation can occur in the presence of doxorubicin and if the physically entrapped drug can be released at physiological and a slightly acidic pH. Hydrogelation was confirmed and the release was observed in both conditions suggesting that the reported tetrapeptides are promising drug delivery vehicles for future applications.

In summary, even though the fibrillar nanostructures and the resulting hydrogels are extensively studied for a variety of applications and their mechanisms of assembly are being elucidated, still little is known about their applications in cancer therapy.[44] Especially, small molecular peptide based gelators together with enzyme induced fibre and hydrogel formation have recently been discovered as a potential new route for anti-cancer therapy development exemplified by some pioneering work by Xu and coworkers.[3c,47] This aspect will be explored in more detail in section 2.6.2 dealing with supramolecular ERMs (enzyme responsive materials) for cancer applications.

2.3 Targeting of tumour tissues

The concept of targeted drug delivery has its origins with Paul Ehrlich, founder of chemotherapy, and is best described by the metaphor of the “magic bullet” intended to fight human diseases.[48] The concept derives from the capacity to treat bacteria selectively without harming the host. Based on this idea, Ehrlich discovered the first effective syphilis treatment, for which he was awarded the Nobel Prize. When this concept is applied to cancer therapy it describes what would be the ideal treatment, selective for cancer cells, giving little or no side effects and having the drug accumulating at the desired site. The magic bullet theory became the inspiration for many scientists for more than a 100 years trying to develop efficient and innovative cancer targeting methodologies and vehicles. Since then, tremendous progress has been made in the understanding of processes targeting cancer cells, together with the diagnostic and therapeutic mechanisms. A summary of our actual knowledge underlying the mentioned processes from the point of view of the cell is shown in figure 2.5.

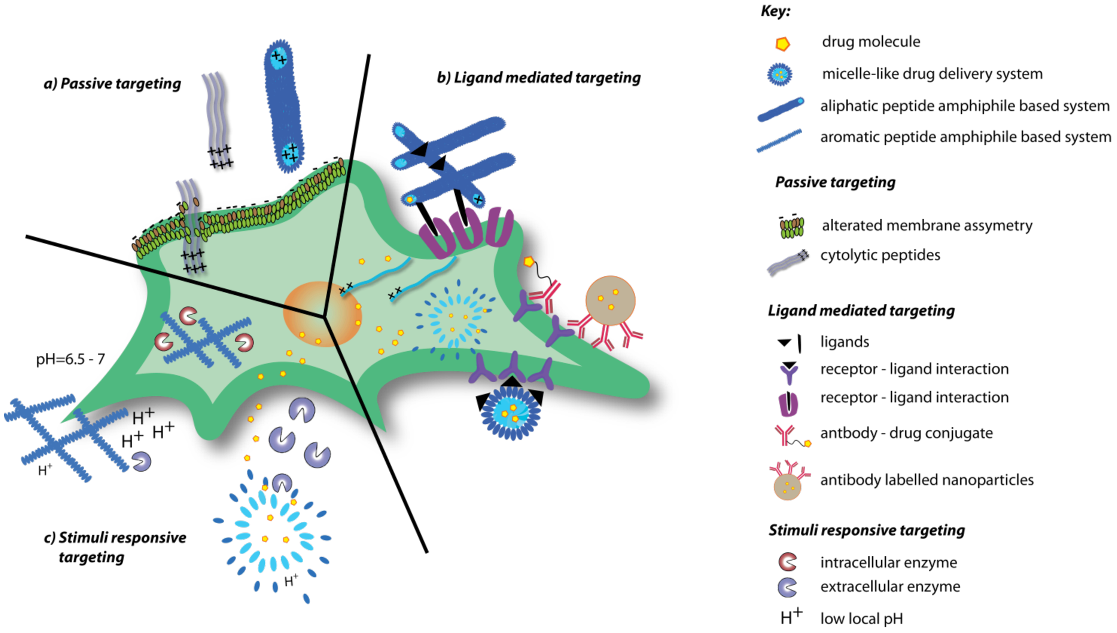

Figure 2.5. Possible mechanisms for targeting cancer: a) passive targeting is presented by loss of lipid asymmetry of the membrane, b) active targeting is presented by various ligand-receptor interactions; and c) stimuli responsive targeting is based on lower values of local pH and enzyme over-expression.

Today, targeting specific diseases with therapies that have better selectivity (for cancer, drug-resistant bacteria strains, etc.) with reduced side effects, is increasingly exploited in designing drug delivery systems. This is possible due to our increased knowledge and better understanding of mechanisms involved in several diseases including cancer, but also the biological processes that govern the nanomaterials retention in the tumour. In recent years, mechanisms have been elucidated involved in cancer genesis, growth and spreading to other tissues (metastasis). Several attempts to develop cancer specific carriers have been made, with some being highly successful in reaching clinical trials. The first generation of nanoparticles used for specific cancer treatments were liposomes and polymer-drug conjugate based systems.[21] Ideally, when administrating anti-cancer drugs/ nanocarriers loaded with drugs, they should first be able to target tumour cells selectively. Once in the tumour tissue, they should selectively kill the cancer cells by increasing the intracellular concentration of administrated drugs.

As mentioned already, targeting of cancer cells/tumour tissues can be active, passive or stimuli responsive. Active targeting is based on the specific interaction between receptors and ligands and/or antigen-antibody interactions. A full account of systems based on active targeting is beyond the scope of this thesis but is mentioned here briefly, as many peptide based anticancer systems rely on this type of targeting mechanism or make use of a combination of active targeting with passive and/or stimuli responsive.[49] Passive targeting exploits the characteristic cancer cell and tumour architecture, resulting in the enhanced permeability and retention effect (EPR) present in cancer tissues due to an irregular vasculature and undeveloped lymphatic drainage system. Stimuli responsive targeting takes advantage of the distinctive tumour microenvironment (low pH, enzyme overexpression), where nanocarriers are activated by the targeted stimuli that in turn trigger a material response. In addition, external stimuli such as temperature and external magnets can be exploited for stimuli responsive targeting. The possible ways to target cancer are shown in table 2.1 with emphasis on peptide based self-assembly examples, where data is available. Peptide based self-assembly systems were mainly developed for pH and enzyme responsive targeting. However, also examples of active (integrins) and passive (lipid asymmetry) targeting were reported.

Table 2.1. Possible ways to target cancer with nanotechnology with the emphasis on supramolecular peptide materials, where data is available. (Note that no supramolecular peptide based nanocarriers were reported to be part of preclinical and/or clinical studies).

Target	**Examples**	**Marker/Effect**	**Examples**	**Status**
Stimuli-sensitive targeting				
a) Endogenous stimuli				
Enzymes[50]	MMP-9 Phosphatase	Enzyme cleavable substrates	GPLG↓LAG[51,52] Nap-FFY**p**[3c,53] KRRAS**p**VAGK[54]	*In vivo* *In vivo* *In vitro*
Local pH	6.5.-7.00[55] 6.15-7.40[56]	pH sensitive systems	KFG vesicles[57]	*In vitro*
b) External stimuli				
Temperature	Hyperthermia (e.g. 42 °C in some carcinomas) Local heating of the tumour (e.g. with ultrasound) [23]	Temperature responsive systems	Poly(NIPAM) modified liposomes[58]	*In vitro*
External Magnets	Use of external magnets[23]	Magnetic targeting by guiding nanoparticles to a particular site	Iron oxide nanoparticles metallic iron-doxorubicin conjugate[59]	*In vivo*[60] Clinical trials[23,59]
Passive targeting				
Increased metabolic rate	Increased lactic acid production (Warburg effect)[61]	Increased internalisation	Nap-FF[46b]	*In vitro*
Loss of lipid asymmetry	Net negative charge on the cell surface	Positively charged peptides	SVS-1 [62] $(KLAKLAK)_2$[42] RRRRRRRR[49]	*In vitro* *In vitro* *In vitro*
EPR effect[63]	10-100 nm[21,64]	Accumulation of nanoparticles at tumour site	Peptide-polymer conjugates[52] Polymer-drug conjugates, liposomes, nanoparticles[23]	From *in vitro/ in vivo* to clincal[23]

Active (receptor mediated) targeting				
Receptors[65]	Integrins[66] Folate receptors[67]	Specific ligands	Integrin binding domains (RGD[49,68], IKVAV[26]) Folic acid	From *In vitro* to preclinical[23]
	Antigens / epitopes on receptors[23]	Antibodies and antibody fragments	Monoclonal antibodies (bevacizumab - anti-VEGF, Avastin®)[23]	Clinical[23]

2.3.1 Targeting of cancer cell membrane and tumour architecture

Enhanced permeability and retention (EPR) effect

As tumours are rapidly expanding, their uncontrolled growth results in the production of new and irregular vasculature. This neovasculature surrounding cancer cells presents gaps in the endothelium, favouring the crossing of the macromolecules from the circulation to the tumour tissues (extravasation) giving rise to the EPR effect (figure 2.6). The tumour vasculature is hyperpermeable because the rapidly growing tumour needs an easy way to access the necessary nutrients and oxygen. This in turn presents a weak point and many nanocarriers can exploit this weakness to passively accumulate in the tumour tissue. In addition, the lymphatic system in growing tumours is not well developed and this aids the retention of nanocarriers in the tumour tissue for longer times.

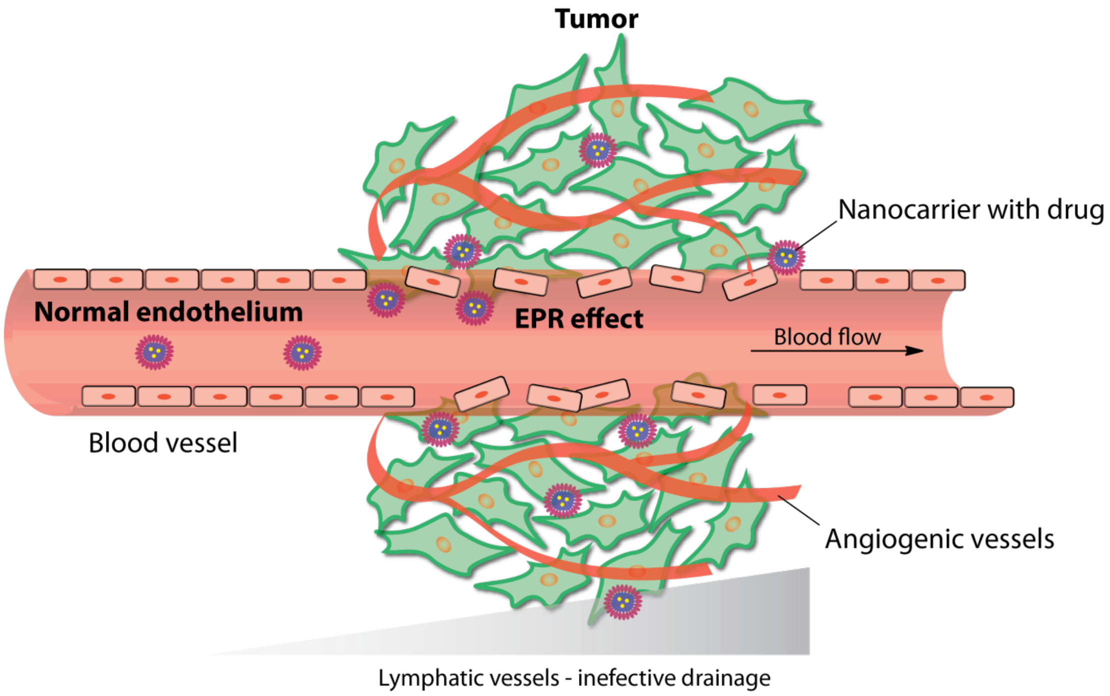

Figure 2.6. **Schematic representation of the EPR effect** showing the hyperpermeable vasculature surrounding cancer cells that presents gaps in the endothelium, favouring the crossing of the macromolecules from the circulation to the tumour tissues (extravasation). In addition, the lymphatic system in growing tumours is not well developed which aids the retention of nanocarriers in the tumour tissue for longer times.

The size, shape and surface characteristics of nanocarriers are key elements for the EPR effect to be successful.[69] The *in vivo* behaviour of nanoparticles greatly depends on their colloidal dimensions.[70] The preferred size range for drug delivery using nanoscale particles have been reported to be between 10 to 100 nm.[21] If the particles are too small (less 10 nm) they are rapidly removed by extravasation and renal clearance. Particles with a size ranging from *circa* 100 to 200 nm and larger are mostly sequestered by the spleen due to mechanical filtration and are eventually removed by the cells of phagocyte system. Non-spherical shapes can extend their circulation times *in vivo*.[21] Particle geometry has been shown to influence particles internalisation, but rules for exploiting particle shape are still not completely established. The nanocarrier surface characteristics are also important as they determine the fate of the particles *in vivo*, due to the possibility of immune system activation. Nanocarriers can also be designed to contain ligands for specific targets on their surface. Many examples of the EPR effect providing selectivity for tumour delivery of self-assembled materials were reported, but often this is not the only targeting strategy.[71] Sensitivity to other conditions (pH, enzymes, specific ligands) is used in combination with the EPR effect aiding the accumulation of nanosystems in cancer tissues.[52] In drug delivery applications, polymer-drug conjugates are mainly exploiting the EPR effect as the size of polymers can be precisely controlled and tuned on demand to fulfil specific requirements. However, significant challenges remain, because certain small tumours do not exhibit the EPR effect (present in tumours of more than 100 mm^3 in volume)[2], but also because the vascularisation is not homogeneous and the permeability of the vessels can vary within a single tumour.[1] Therefore, the EPR effect has limited efficiency when the aim is to target and treat small and unvascularized metastasis.

Loss of lipid asymmetry

Another target exploited in selectively killing tumour cells is based on the loss of phospholipid asymmetry of membranes in cancer cells (figure 2.7). While normal mammalian cells have an asymmetric distribution of phospholipids in both leaflets of the membrane resulting in an overall neutral charge, cancer cells tend to lose this asymmetry and present an overall negative charge at the membrane surface.[72] This is due to a translocation of the negatively charged phosphatidylserine to the outer side of the membrane.[73] In addition, aberrant glycoproteins (mucins) containing high levels of sialic acid are present on the membrane surface due to changes in glycosylation.[74]

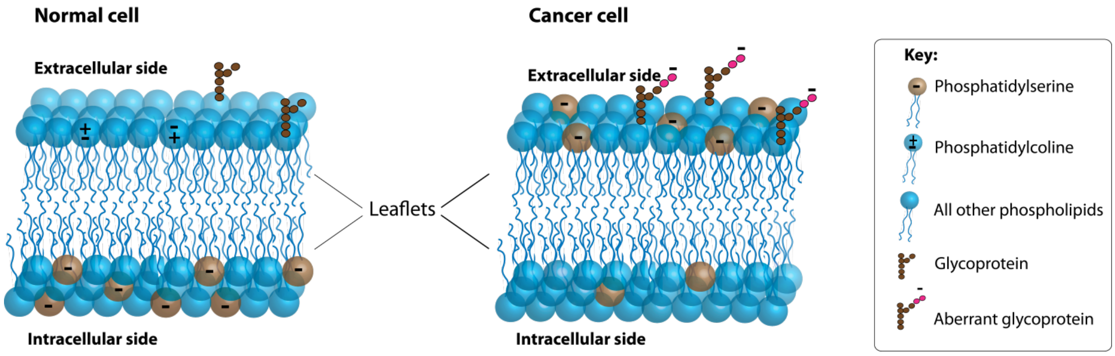

Figure 2.7. Schematic representation of normal vs. cancer cell membrane pointing out the overall negative charge at the outer leaflet of the cancer cell phosholipid bilayer.

For this reason peptides containing cationic domains were explored to selectively target cancer cells for self-delivery or cell lysis. Several cationic antimicrobial peptides have been shown to have anticancer activity and selectivity toward cancer cells because of the similar electronegative character of bacterial cell membranes for which they were originally designed.[38,75] These examples are based on the bioactive helical conformation that the peptides, normally unstructured in solution, adopt when in contact with cancer cell surfaces. A recent example of the use of an antimicrobial cationic 18-amino acid residue peptide (SVS-1) that disrupts cancer cell membranes exploiting their aberrant phospoholipid distribution was presented by Schneider and co-workers.[62] The SVS-1 peptide was observed to fold on the surface of cancer cells and adopting an amphiphilic β-hairpin structure capable of membrane disruption, while it remained unfolded in aqueous solution. This membrane-induced folding, driven by the electrostatic interaction between the positively charged peptide and the negatively charged membrane surface of cancer cells, is essential for its anticancer activity and constituted the first example of an anticancer β-hairpin peptide with this mechanism.

Stupp and co-workers developed this concept further and explored how supramolecular materials based on PAs having hydrophobic domains and cationic charge interact with cells, unlike their soluble, unassembled counterparts.[76] They found that supramolecular materials with nearly identical chemical composition can instruct cell death or survival depending on the β-sheet forming propensity. Fragments that show more propensity to form β-sheets tend to form more cohesive fibres, where the structures reinforced by hydrogen bonding support cell viability. On the other hand, nanostructures based on weaker interactions were able to promote disruption of lipid membranes, causing cell death. This was concluded after they systematically studied the effect of the hydrophobic collapse, charge and hydrogen bonding on the self-assembling morphology and cell viability. Hydrophobicity and cationic charge were found to be essential for cytotoxicity, as reducing the hydrophobic tail or the overall cationic charge resulted in lower toxicity of the peptide amphiphiles examined.

Importance of hydrophobicity for cytotoxicity

An example highlighting the importance of the hydrophobicity in inducing cytotoxicity was presented by Xu's group, where a simple self-assembly motif (Nap-FF that stands for naphthalene and two phenylalanine residues) able to form nanofibres in water, showed selective anticancer activity towards HeLa and glioblastoma cells, and little toxicity towards normal cells.[46b] In this study it was shown how supramolecular assemblies (fibres) were toxic to cancer cells compared to their monomeric, non-toxic counterparts and that hydrophobicity played a key role in this cytotoxicity. A mechanism of action of the small-molecule based assemblies is the disruption of microtubules dynamics. The reason why it selectively occurs in cancer cells is linked to the accelerated metabolism of cancer cells, described as the Warburg effect (see next section, 2.3.2) combined with the faster accumulation of fibrillar aggregates in cancer cells, most likely due to the EPR effect.

2.3.2 Targeting of cancer cell metabolism, pH and enzymes

Warburg effect

Another characteristic of tumour cells is an increased metabolic rate (increased glycolysis) resulting in the production of high levels of lactic acid described as the Warburg effect.[61] The aerobic glycolysis involves several enzymes that can be potential targets for future anti-cancer therapeutics. As a consequence the pH of the tumour microenvironment is lower (6.5-7) than that of the healthy cells (physiological pH – 7.4).[77] A few examples in literature show how this increased metabolic rate provides selectivity for cancer cells.[46b,78] Therapeutic targeting of cancer cell metabolism is still in development as many aspects are still poorly understood, but holds a great promise for the development of new classes of anti-cancer agents.[61,78-79]

pH of the extracellular environment

pH is one of the most common stimuli used to trigger drug release and to regulate self-assembly. The pH of the extracellular environment of cancer cells is slightly acidic, hence it is used to trigger conformational changes and/or selectively induce degradation of nanomaterials in the proximity of cancer cells. pH responsive self-assembled nanocarriers have been extensively studied.[10b,17c,80] The pH responsiveness often results in the degradation of the carrier followed by drug release. Recently, Bhattacharya and co-workers presented an example of pH targeted anticancer drug delivery based on a simple peptide self-assembly system.[57] A KFG tripeptide sequence of interest, because it is present on the tyrosine kinase nerve growth factor receptor, was reported to undergo concentration dependent self-assembly. Different architectures were observed: vesicles (at lower concentration) and nanotubes (at higher concentration) that correspond to a switch from random coil to β-sheet like structures at the molecular level, respectively. Furthermore, the potential of the reported vesicles to perform as pH sensitive doxorubicin delivery systems, selective for cancer cells was assessed. The studied vesicles were stable at physiological pH (7.4), but were shown to rupture in slightly acidic conditions (pH = 6), making them suitable for selective cancer targeting and pH triggered drug release. Indeed, doxorubicin loaded vesicles imparted higher toxicity than free doxorubicin, being more efficient in delivering the cargo inside cancer cells.

Targeting multiple stimuli is common in designing cancer targeting nanomaterials. An example is a pH responsive peptide based micellar system containing RGD (for the targeting over-expressed integrins).[68a] This peptide amphiphile (V_6KKGRGDS) self-assembles into micelles at physiological pH, however due to lysine protonation at pH=5 values, and consequent repulsion between peptide chains the micelles dissolve. This micelle disruption is followed by a rapid release of loaded doxorubicin selectively in cancer cells, due to the RGD tumour targeting motif.

Enzyme overexpression

Enzymes present much more specific and localised stimuli compared to pH. Their localised action, that allows spatio-temporal control over material changes, ability to induce signal amplification and their disregulation in cancer states makes them valuable targets in cancer nanotechnology. Examples of enzymes involved in cancer states are mainly related to a family of matrix metalloproteinases (MMPs) involved in the degradation of the extracellular matrix which is essential for cancer cell migration and metastasis. In addition, other enzymes such as phosphatases, kinases, etc. are found to be over-expressed in cancer. MMPs are considered to be principal mediators of alteration in cancer progression.[81] This can be exploited in site specific drug delivery, where the excess of enzymes can be used as a trigger for the release of drugs. The drug (prodrugs or physically entrapped drugs) in this case would be released in a controlled manner only if and where the enzyme of interest is present/over-expressed. Enzyme over-expression can be targeted extracellularly either when the proenzyme forms are secreted and subsequently activated (e.g. MMPs involved in ECM degradation or phosphatases involved in regulation of signal transduction) or by targeting membrane bound enzymes (e.g. transmembrane MMPs- TM-MMPs or surface bound phosphatases) as shown in figure 2.8. Intracellular proteases, esterases or kinases have also been found in high concentration in cancer associated states (figure 2.8).

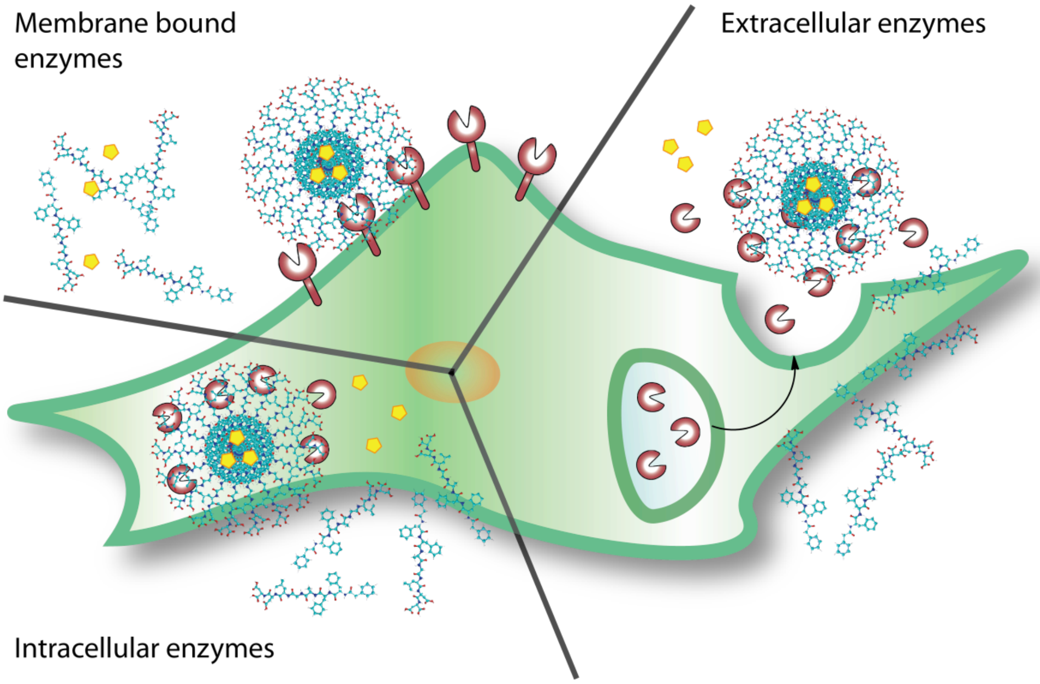

Figure 2.8. Schematic representation of different ways to target enzymes: extracellularly (surface bound enzymes or secreted enzymes) and intracellularly.

Bioengineered cells as vectors for targeted delivery

A number of additional approaches are being explored to enhance the delivery of therapeutics in a tumour selective manner. An example worth mentioning are the bioengineered cells used as targeted delivery carriers of a prodrug and its activating enzyme, reported by Troyer *et al.*[82] Monocyte-like cells known to infiltrate tumour sites were engineered to express an enzyme (in its inactive form) necessary to activate a prodrug that was subsequently incorporated in the cell cytoplasm. Once the engineered cells reached the tumour site, the enzyme activation was performed using an external agent (in this case doxycycline) administrated two days later.[82a] Compared with control experiments, this specific approach resulted in considerable tumour volume reduction. Other examples of cell vectors are being studied and their selective targeting of tumour cells assessed as a potential more homogeneous way to target cancer cells.

2.3.3 Further perspectives and considerations - ECM as a possible target

Copying nature to produce scaffolds to support cells – e.g. extracellular matrix mimics has been addressed widely for applications in regenerative medicine and tissue engineering (figure 2.9). The extracellular matrix (ECM) is made of multiple molecular constituents such as proteins, proteoglycans, growth factors, etc. These components form a physical network that is essential for supporting cell communities. Mimicking the ECM is useful for tissue regeneration and damage repair applications, but it could be also used to selectively develop synthetic mimics of the extracellular matrix, that could block cell growth and migration. Using nature’s machinery to instruct non-endogenous material formation such as synthetic ECM, would be an interesting topic to investigate. This could be realised exploiting natural metabolic pathways of specific cells (cancer, bacteria and other pathogen microbes) to create artificial environments that could selectively target cancer cells and/or bacteria cells for therapy purposes.

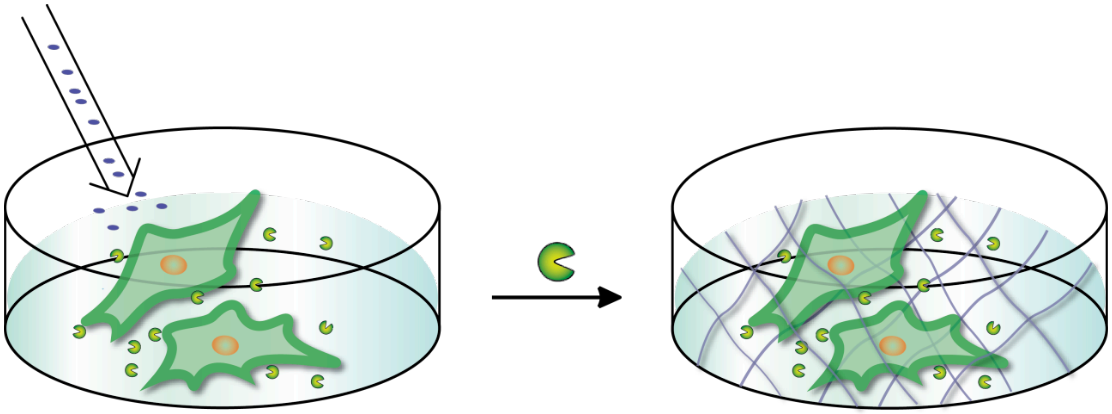

Figure 2.9. Schematic representation of exploiting extracellular enzyme overexpression to create synthetic mimics of ECMs.

While not directly relevant to cancer, targeting bacteria, and especially the drug-resistant strains, is important and challenging as is cancer targeting. An outstanding example of how bacteria can be selectively killed was recently presented by Alexander and co-workers.[83] Even if not closely related to our topic, a new approach where polymers are created *in situ* around bacteria cells, exploiting specific bacteria cell metabolic pathways (i.e. copper homeostasis – bacterial redox cascades) is worth being mentioned, as the concept may translate to cancer application. In this example, an inherent bacterial redox system is used to induce a copper mediated radical polymerisation of synthetic monomers at the cell surface, shown in figure 2.10.[83] As this process is specific to bacteria, it is designed to selectively inactivate them only where and when the polymerisation occurs. In addition, the authors observed a bacterial templating effect, as different bacteria were able to synthesize different polymers around them. Removal of copper and the toxicity associated with its presence in high concentrations are some of the issues that slow the transition of polymeric systems to the clinics. But in this case, an inherent copper source is used to mediate the *in vivo* polymerisation, having a tremendous advantage to produce polymers that can selectively inhibit microbial growth.

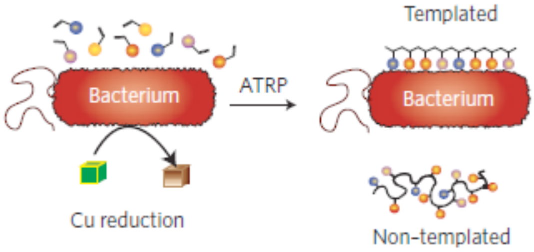

Figure 2.10. Schematic (taken form reference 83) of bacteria induced synthesis of polymeric/synthetic mimics of ECM exploiting the bacterial metabolism (copper reduction) to initiate the polymerisation process.[83]

If this approach could be selectively applied to cancer cells, it would open up new possibilities for cancer therapy. However, a better knowledge into the field of cancer specific metabolic routes/mechanism is required. In particular, processes typical for cancer cells, that when exploited as targets would not harm healthy cells and tissues, would need to be identified. Some studies are being conducted in this fashion, but for now only to block cancer cells migration and limit cellular mass exchange. An early example of peptide based hydrogels for cell entrapment was shown by Stupp and Hartgerink, where the reported peptide amphiphiles undergo metal ion mediated self-assembly forming 3D hydrogel networks around cells.[41b] In this case the application would be in regenerative medicine as peptide based supports favour cell growth, due to cell entrapment. Here, self-assembly can be triggered upon contact with living tissues or cell suspensions in culture media without the ability to distinguish between diseased and healthy cells. However, not all peptide sequences designed were appropriate for cell entrapment as they were found to be toxic, and their further investigation for cancer therapy was proposed.

Potential inhibition of cancer cell growth and prevention of cancer cell migration was recently presented by Xu and co-workers.[3c] The formation of hydrogels around cancer cells blocks the migration of secreted enzymes (phosphatases) that remain entrapped in the gel network formed. This suggests that nutrients and other important factors are unable to access tumour cells and are decisive of their fate (apoptosis). Being an example of enzyme triggered supramolecular material for anti-cancer application it will be discussed in more detail in section (2.6.2.1).

In summary, the examples of targeting cancer using peptide based nanomaterials mentioned so far, highlight the use of different approaches and targeting strategies. The designed materials were able to act directly on cancer cells by membrane disruption, by direct interference with the metabolism or by increased intracellular uptake of loaded drugs specifically released at the point of interest, due to stimuli triggered release. Also indirect disruption of the tumour microenvironment can be achieved by acting upon enzymes, whose activity is directly involved with the extracellular matrix degradation. However, an indirect way of blocking cancer cells would be interesting to consider, which would consist of designing artificial extracellular matrixes specifically around cancer cells.

In conclusion to this section, the use of a variety of targeting mechanisms shows how nanotechnology is making huge progress in the field of cancer therapy. Promising and innovative ways to treat cancer are being assessed, with some reaching clinical trials. Examples range from artificially creating barriers to cancer cell migration, to selectively delivering cytotoxic peptides or anti-cancer drugs using a wide range of materials and architectures.

2.4 Enzymes as triggers and targets for cancer therapy

Exploiting enzymes in drug delivery was initially based on developing their direct inhibitors through design of synthetic molecules able to directly bind or inhibit the desired enzyme. Some examples include kinase inhibitors (Dasatinib and Imatinib), which are in clinical use for treatment of certain kinds of cancer.[84] An alternative approach is to design prodrugs and make them enzyme responsive. First examples of enzyme responsive systems were based on the prodrug approach, where a drug was covalently conjugated to a polymeric support through an enzyme cleavable linker. The function of the polymer was to temporarily protect the drug and increase its circulation times, while enzyme responsiveness is exploited to release the drug in the presence of the desired, over-expressed enzyme. The field of enzyme responsive materials was further developed and a variety of new approaches are being explored for biomedical applications, including introduction of enzyme sensitive crosslinks in polymeric particles and triggering self-assembly using enzymes.

The main advantages of using enzymes as triggers to induce changes in chemical and physical properties of materials are signal amplification, activating cascades of reactions in live cells, involvement in numerous biochemical processes within the body, high selectivity and specificity for their substrates.[85,86] Other advantages of using enzymes as triggers are their inherent biocompatibility and localised responses. There is no need to introduce them as external stimuli, as they can be already found in the biological environment of interest. In addition, their over-expression in disease states makes them valuable targets for biomedical applications.

Different enzymes have been reported to be over-expressed in cancer states and have been exploited in the development of enzyme responsive materials (ERMs). Different types of enzyme catalysed reactions have been reported so far to develop ERMs: bond formation (condensation), bond cleavage (hydrolysis) or REDOX chemistry. A complete list of enzymes used for development of ERMs can be found in a review recently published.[50] The most common enzymes used for development of ERMs are: proteases, kinases, phosphatases and endonucleases.[50] However, as research on ERMs as well as on drug delivery increases, the number of targeted enzymes used to trigger drug delivery broadens and many other enzymes are being explored. Proteases and endonucleases are mainly employed to cleave peptides and oligonucleotides, respectively. On the other hand, kinases and phosphatases are involved in phosphorylation and dephosphorylation of their respective substrates (mainly peptide based), making them of interest for the development of reversible systems, due to their complementary action. A list of cancer related enzymes used for the development of enzymes responsive materials is shown in table 2.2. The enzyme names associated with the asterisk in the table are the ones used for the development of self-assembly based enzyme responsive materials. The most studied enzymes for anti-cancer therapy applications are phosphatasese/kinases and MMPs.

In this work, firstly the prodrug approach will be briefly discussed as an example of using enzymes for drug delivery applications, before ERMs were developed. Next, ERMs will be introduced and enzyme responsive microgels shortly considered. Subsequently, enzyme responsive supramolecular materials will be discussed. Emphasis will be put on the development of supramolecular peptide based ERMs for applications in cancer therapy.

Table 2.2. Enzymes used for cancer related ERMs.

Enzyme	Substrate/ Example	Catalysed reaction	ERM strategy	Enzyme malfunction/ Relevance
β-D-glucuronidase	β-D-glucuronic acid	Hydrolysis of complex carbohydrates	Prodrug approach[87]	High extracellular concentrations[87a]
Caspases	RGD↓ containing synthetic peptides[88]	Peptide bond hydrolysis after aspartic acid	Design of caspase activators[89]	Down-regulated[90]
Cathepsins	GF↓LG GF↓LGK	Peptide bond hydrolysis with broad specificity	Prodrug approach[91] Degradable peptide crosslinker in polymeric nanoparticles[92]	Over-expressed and present extracellularly
Dipeptidyl peptidase IV*	N-terminal A*XX*-P[93] (A*XX*P↓S(Ac))	Peptide bond hydrolysis of proline containing peptides (growth factors, chemokines, etc.)	Enzyme triggered self-assembly for prodrug design and biosensor technology[93]	Implicated in cancer[94]
Esterases*	Nap-FF ester derivative[47]	Hydrolysis of esters into an acid and an alcohol	Intracellular hydrogelation in cancer cells to induce cell death	High intracellular expression levels in HeLa cells[47]
Furin	Hydrolysis after RX(K/R)R↓	Peptide bond hydrolysis for activation of a number of proproteins[95]	Degradable peptide crosslinker in polymeric nanocapsules[96] for intracellular delivery of proteins	Implicated in cancer
Hyaluronidase*	Hyaluronic acid (HA)	Hydrolysis of hyaluronic acid	Release of the cytotoxic peptide amphiphiles by degradation of supramolecular membranes for cancer therapy [43a]	Accelerated degradation of HA in tumour environments[97]
Kinases*	Nap-FFGE**Y**[98] KRRA**S**VAGK[54] LRRA**S**LG[51]	Phosphorylation of hydroxyl groups in peptide sequences – involved in signal transduction	Disassembly of supramolecular nanostructures and gel-sol transitions in dynamic self-assemblies for cancer therapy[51,54,98]	Aberrant activation in cancer cells; extracellular biomarker for cancer

MMPs*	PVG↓LIG GPLG↓LAG GPLG↓IAGQ	Peptide bond hydrolysis of ECM proteins (e.g. collagen)	Targeted drug delivery systems for cancer therapy[99] Accumulation- tumour diagnostic tool[51] Prodrug approach[100]	Over-expressed in various cancers, extracellularly secreted or membrane bound
Methionine sulfoxide reductases*	Poly(methionine)	Reduction of methionine sulfoxide to methionine	Intracellular release of drugs due to morphology transition[101]	Upregulated in oxidative stress environments - cancer
Phosphatases*	Nap-FFGEY**p**[98] Fmoc-Y**p**[102] Nap-FFY**p**[3c,53] KRRAS**p**VAGK[54] LRRAS**p**LG[51]	Dephosphorylation of orthophosphoric monoesters in peptides-involved in signal transduction	Hydrogel formation *in vitro* and *in vivo* for visual enzyme assay, enzyme immobilisation, inhibition of cancer cell growth and migration	Over-expressed in cancer cells, intracellularly and extracellularly
Plasmin	VR↓N AFK↓	Peptide bond hydrolysis after arginine or lysine	Biodegradable PEG-peptide hydrogels[103] for development of cell responsive materials[104]	High concentration in cancer cells
Prostate-specific antigen (PSA)*	HSAKFY↓SG[105] SSF↓YSGGGC[106] HSSKLQ↓L[107]	Peptide bond hydrolysis preferentially after large hydrophobic amino acids; broad specificity[108]	Hydrogelation based enzyme visual assay[105] Gold nanoparticles detection assay[106] Prodrug approach[107]	Clinical marker for prostatic malignancy[109]
Thrombin*	VPR↓GS[110] LTPR↓gelator CGFPR↓GC	Peptide bond hydrolysis between R and G	Fibre formation for fabrication of 3D nanostructures[110] Hydrogelation based enzyme visual assay[111] Gold nanoparticles based visual protease assay[112]	Promotes malignancy in cancer
Tyrosinase*	Ac-YYYY-OMe[113]	Oxidation of phenols to quinones	Disassembly of supramolecular nanostructures and gel-sol transition for controlled drug release	Over-expressed[113]
Urokinase plasminogen activator*	SGR↓SANA SGR↓SAN	Degradation of extracellular matrix	Targeted drug delivery by hydrogel degradation[114] Quantum dot-based assay for detection of protease activity[115]	Implicated in cancer invasion and metastasis[116]

2.4.1 MMPs

A specific class of enzymes are matrix metalloproteinases (MMPs). The first member of the metalloproteinase family was discovered in 1962, in the tail of the metamorphosing tadpole by Gross and Lapiere.[117] MMPs are a family of zinc endopeptidases involved in the degradation of extracellular matrix (ECM). Based on their ability to degrade the ECM (collagen, gelatine, etc.) and on the similarities they have in terms of primary structures MMPs can be classified as: collagenases, gelatinases, stromelysins, membrane-type MMPs and others that do not belong to the mentioned subgroups.[118] In detail, collagenases (MMP-1, MMP-8, MMP-13, MMP-18) degrade triple-helical regions of collagen (type I, II and III). Gelatinases (MMP-2 and MMP-9) degrade heat-denatured collagens (gelatines), but cleave also type IV and V collagens. Stromelysins (MMP-3, MMP-10, MMP-11) degrade various non-collagenous ECM components such as aggrecan, fibronectin, etc.[118] MMPs are mainly extracellular enzymes, secreted by cells as proenzymes. However, membrane bound members of this family were also reported (membrane-type MMPs). All MMPs are multidomain enzymes containing a propeptide, a catalytic and a hemopexin domain (the utility of this domain is not yet clear). In addition, gelatinases (MMP-2 and MMP-9) have also three fibronectin type II-like repeats responsible for the enzyme binding to gelatine and other substrates. All MMPs except MMP-23 have a cysteine switch sequence motif (PRCG[V/N]PD) important to maintain the proenzyme inactive as it ligates the catalytic zinc atom of the active site. Another sequence that is conserved among MMPs is the zinc binding motif (HE*X*GH*XX*G*XX*H) characterised by the presence of three histidines that bind Zn^{2+}.[118]

The substrate specificities of these enzymes are complex and the peptide substrate specificities do not necessarily match with the specificities found for (fibrous) proteins. For example a specific site on triple-helical collagen (Gly775-Ile776) is efficiently cleaved giving an example of the cleavage site being G↓I. The cleavage of smaller peptides is much less specific, but for the design purposes amino acids found in naturally occurring substrates are used such as glycine for P1 position, while hydrophobic amino acids such as isoleucine or leucine are found in P1’ position.[104] In addition, there is no clear distinction between the specificities of various members of MMP family as their catalytic domains are superimposable, with the most prominent difference being the size of the S1' specificity pocket. Therefore, the P1' position on the peptide is critical for the substrate recognition. However, other subsites highly influence the substrate specificity. It was early shown that the length of the peptide substrate determines the catalytic efficiency of MMPs, as they have extended substrate binding sites.[118] Little or no activity was reported for residues shorter that 6 amino acids (P3-P3' according to Schechter and Berger's model[119]).[118] This was recently confirmed by a study showing how the specificity of MMP-9 depends on the length of the peptide sequence but also on the large group substitutions on the N-terminus.[120]

In summary, MMPs were found to be over-expressed in various disease states, including cancer, which makes them valuable targets for development of ERMs for biomedical applications from sensing, to drug delivery and tissue engineering. A list of examples of MMPs used for ERMs development and the substrates used are shown in table 2.3. In addition, possible applications for the designed systems are presented in this table, with emphasis on supramolecular materials that undergo specific responses upon enzyme treatment.

Table 2.3. Example of substrates and MMPs used for the development of supramolecular ERMs.

MMP type	**Entry**	**Substrate**	**Material type**	**Application**
			Polymer peptide conjugates	
MMP-2/9	1	GPLG↓LAG[51,52]	Nor-GPLGLAGGWGERDGS	Probe aggregation in tumour tissue – diagnostic tool
	2	GPQG↓IFGQ[121]	p(NIPAm)-SGPQGIFGQMG-p(OEGMA)	Micelles for drug delivery
	3	GPLG↓IAGQ[100]	HSA-GPLGIAGQ-doxorubicin	Prodrug approach for cancer therapy
MMP-2	4	PVG↓LIG[99]	PVGLIG-b-PTMC	Targeted drug delivery systems for cancer therapy
	5	GPVG↓LIGK[122]	PEO-PEG-PEO (Pluronic®)-GPVGLIGK	Thermogel degradation for cancer drug delivery
MMP-9	6	GPKG↓LKGA[105]	PEG_4RRSP-GPKGLKGA-PABA	Hydrogelation based enzyme visual assay
			Aliphatic peptide amphiphiles	
MMP-2	7	GTAG↓LIGQ[123]	Palmitoyl- GTAGLIGQERGDS	ECM mimics for tissue regeneration
MMP-7	8	GGGHGPLGLARK[124]	Palmitoyl- GGGHGPLGLARK	Micelle to fibre transition for enzyme visual assay
			β-sheet forming peptides	
MMP-2	9	PVG↓LIG[125]	Pure peptide based platform $(RADA)_3$- PVG↓LIG-$(RADA)_3$	Biofunctional scaffolds for tissue engineering
MMP-13	10	PPTG↓FKVK[126] PPTG↓LKVK PPTG↓IKVK PPTG↓AKVK	IKVKIKVKVPPTG**X**KVKIKV Where X=F/L/I/A	Potential to mimic extracellular matrixes for facilitating repair of damaged tissues
			Aromatic peptide amphiphiles	
MMP-9	11	CG↓LDD[127]	Purely peptidic - FFFFCGLDD	Hydrogel formation

2.5 Prodrug approach

Prodrugs are defined as compounds that qualitatively maintain the pharmacologic effects, but have different physic-chemical properties from the parent drug.[128] The term pro-drug was first introduced by Albert in 1958[129], to indicate compounds that undergo biotransformation before exhibiting their pharmacological effects.[130] Problems such as lack of solubility, poor bioavailability or lack of chemical stability could be overcome by using the prodrug approach, which consists of the introduction of chemical modifications on the parent drug.[130]

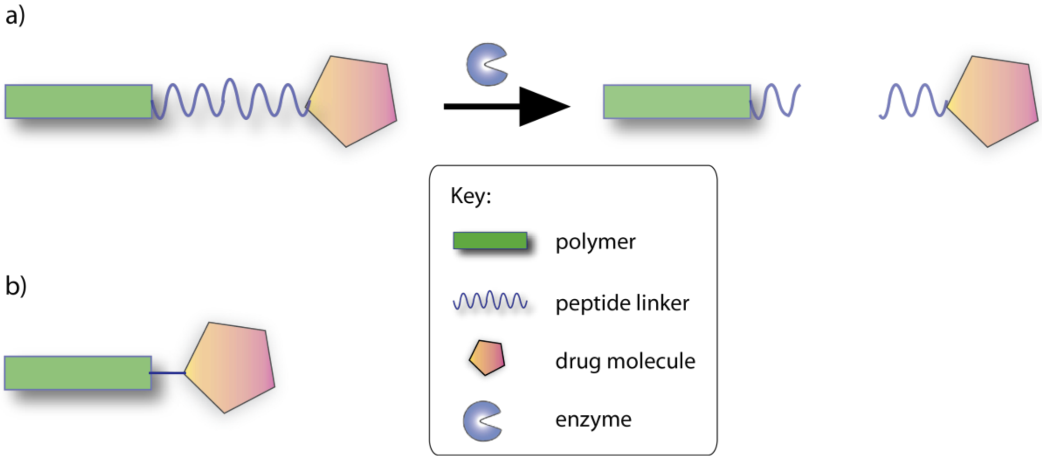

Figure 2.11. Schematic representation of the prodrug: a) attached to the polymer through an enzyme cleavable linker and b) attached directly to the polymeric support.

There are examples of prodrugs, where the drug is covalently attached to a polymer either directly or through an enzyme cleavable linker as shown in figure 2.11, which requires the modification of the drug. In the latter case, the drug is released after cleavage of a linker by an enzyme. An example of a drug directly attached to the polymer is doxorubicin covalently attached to N-(2-hydroxypropyl) methacrylamide (HPMA) copolymer that was evaluated in phase II clinical trials for some types of cancer and has shown less overall toxicity and lower side effects than the equivalent dose of free doxorubicin.[131] Prodrug systems will not be considered in detail here, because they go beyond the scope of this project. Some examples of enzyme activation of prodrugs will be mentioned in this section. An example is given by systems, where cancer drugs are covalently attached to polymers using enzyme cleavable linkers, obtaining selective drug release at tumour sites, that have high levels of proteases. A dextran – peptide – methotrexate conjugate was designed, where dextran is used as a polymer carrier, because it is biocompatible and biodegradable, while methrotrexate constitutes an anticancer drug.[132] They are linked together with enzyme cleavable peptide sequences sensitive to MMPs. Exploiting the increased levels of MMPs in the vicinity of the tumour, the peptide sequence can be cleaved and the drug released. In this case, the release of the active compound is regulated by enzyme kinetics and one molecule is released for each peptide bond cleaved. Another example of the prodrug approach where doxorubicin is linked to human serum albumin (HSA), through a peptide linker sensitive to MMP-2 and MMP-9 was reported.[100] The enzyme activity is exploited to release the anticancer agent (doxorubicin) from its macromolecular carrier. After enzyme cleavage, the liberated doxorubicin-tetrapeptide was found to be less active than free doxorubicin, as it showed decreased cytotoxic activity due to its covalent bond with the peptide (chemical modification in the 3-amino position of doxorubicin are known to be problematic and often lead to loss of cytotoxicity).

Recently, an interesting example of the supramolecular prodrug approach was reported by Zhang and co-workers.[49] A multifunctional amphiphilic peptidic prodrug based on an aliphatic PA conjugated to the anticancer drug, doxorubicin was described. The PA containing GRGDS and an octaarginine (R_8) as a hydrophilic head and an alkyl chain conjugated to doxorubicin as a hydrophobic tail self-assembled into spherical multifunctional nanoparticles. The RGD sequence was incorporated for tumour targeting, while the octaarginine had a function of increasing the solubility of doxorubicin and to confer membrane-penetrating properties. The self-assembled structures presented a hydrophobic core containing doxorubicin and a hydrophilic shell decorated with peptides (having cell targeting and membrane penetrating activities) and were designed to undergo intracellular protease mediated degradation and release of doxorubicin. Cathepsin B, a protease with broad specificity was used as a model enzyme to assess doxorubicin release. However, *in vitro* and *in vivo* doxorubicin release was mediated by a variety of intracellular proteases[49], showing little specificity for the cancer-associated enzyme of interest. An increased selectivity of doxorubicin conjugated to the peptide amphiphile was proven for HeLa cells compared to a normal cell line, but again the doxorubicin cytotoxicity was lowered by the covalent conjugation to the peptidic carrier.

A limitation of the prodrug approach is the need to chemically modify the drug, that is often inactivated by covalent modifications. Subsequently, different approaches have been explored that are based on polymeric particles, capable of physically entrapping drug molecules, which would allow higher loading capacity, increased circulation times and possibly target the desired site in the body.

2.6 Enzyme responsive materials (ERMs)

Expression levels of enzymes dictate the difference between health and disease in many cases, including cancer. This observation suggests incorporating enzyme sensitivity in materials could be of use in management of disease states, where the goal is to achieve dynamic and targeted changes in material properties. ERMs are a class of smart materials that undergo morphological changes in the presence of the target enzyme. A variety of inorganic (metals, silicates) and organic (naturally occurring and artificial polymers and peptides) materials have been used. Recent advances in this field were extensively reviewed by Zelzer *et al.*, showing how this area of research has increased in the last decade.[50] Enzyme responsive materials were classified into 5 classes schematically represented in figure 2.12 being: i) polymer hydrogels, ii) supramolecular materials, (iii) self-immolative materials, iv) surfaces and v) particles. Each of these classes includes many examples, with the enzymatically controlled supramolecular materials being the most common.[50]

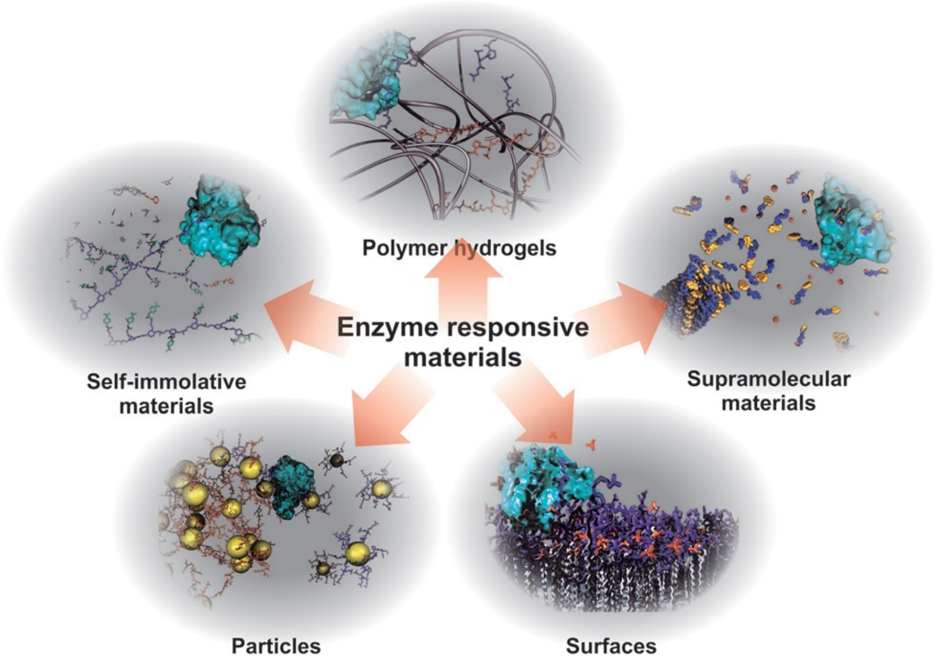

Figure 2.12. Different classes of enzyme responsive materials (taken from reference 48).[50]

2.6.1 Polymeric particles – microgels / chemically crosslinked hydrogels

Microgels are crosslinked polymer particles with colloidal dimensions (10-1000 nm). They can undergo morphological transitions, when they sense a change in the environment such as pH, temperature, ionic strength, light.[133] Enzymes have been reported to trigger polymer particle dissolution, but have not yet been used on microgels to trigger swelling. Chemically crosslinked microgels are of interest, because of their unique property of reversible swelling-deswelling upon application of the mentioned stimuli. They can behave as reservoirs that can protect drug molecules from the surrounding environment, without requiring covalent modification of the drug. Physically entrapped drug molecules can then be released, as required if the stimulus is present.

The earliest report of microgel synthesis was by Staudinger and Husemann in 1935 that polymerized divinylbenzene into a branched network.[134] The term microgel was introduced later, in 1949 by Baker, to describe crosslinked polybutadiene latex particles.[135] Originally, the word “micro” was referred to the size of gel particles, while “gel” was related to the ability of these particles to swell in the suitable solvent. Today, this term is still widely used in polymer science to indicate colloidal dispersions of gel particles. In literature, in addition to the term "microgel", various terms can be found to define chemically crosslinked polymer particles: hydrogels (related to water as swelling solvent)[136], nanogels (referred to the size of particles in nm), latex particles, submicron gel beads, etc.[137] In addition, "microgels" are often used to indicate polymeric particles having micron-range size, creating confusion, because they are not in the colloidal range. According to the IUPAC definition (IUPAC Recommendations 2007), a microgel stands for a "particle of gel of any shape with an equivalent diameter of approximately 0.1 to 100 μm" to distinguish it from the nanogel, which is defined as "particle of gel of any shape with an equivalent diameter of approximately 1 to 100 nm".[138] Throughout this review we will refer to microgels as crosslinked polymer particles having colloidal dimensions (10-1000 nm).

A variety of colloidal microgels have been designed and synthesised so far, and mainly the stimuli used to control their behaviour are pH (e.g. acrylic acid based)[139,140,141,142] and temperature (e.g. poly(*N*-isopropylacrylamide) based)[143,142]. The presence of the ionisable groups in the structure of polymers makes them pH responsive. Microgels can be classified as cationic, neutral or anionic depending on the monomers used to prepare them. The majority of the research conducted on pH responsive microgels is based on anionic, carboxylic acid functionalised ones. The first example of pH responsive microgels with high concentration of primary amines, was reported by Saunders and co-workers.[144] Amine rich, enzyme responsive microgels of colloidal size have not yet been reported and would constitute interesting platforms for development of vehicles for anticancer agents. Their size and enzyme responsiveness would be advantageous for targeted cancer therapy. However, being based on new polymers (not FDA approved) they are rarely biocompatible, which would constitute an issue in their biomedical applications.

Polymeric particles containing enzyme cleavable crosslinks

One approach to develop enzyme responsive microgels is the introduction of enzyme cleavable peptide linkers as crosslinks within the polymer particles (figure 2.13), where drug molecules could be physically entrapped. Enzymes degrade these linkers upon cleavage, which could result in the dissolution of the structure and release of payload at the desired site. As an example, a protease responsive macrogel (600 µm when swelled) where the crosslinker used is a tetrapeptide sensitive to chymotrypsin was reported.[145] The hydrogels were prepared by introducing peptide sequences containing cysteine on methacrylamide monomers giving rise to polymerizable peptides. The hydrogels were made by photopolymerisation of pre-polymer solution containing the peptide crosslinker. Upon the introduction of chymotrypsin the structure was dissolved due to the dissolution of peptide crosslinks.

A similar system using PEG-based monomers was reported by Lutolf *et al.*, where a peptide crosslinker sensitive to MMPs was used and its network degradation assessed by treatment with MMPs.[146] The system was developed as a cell-sensitive system by introducing a peptide crosslinker made of RGD based sequences flanking the MMP cleavable sequence. Modified RGD based sequences were introduced as pendant functions to confer adhesiveness to a non-adhesive PEG network, while MMP sensitive sequences were introduced to obtain enzyme responsiveness. After cleavage of the crosslinks by MMPs initial hydrogel swelling was observed, followed by microgel degradation due to the digestion of the crosslinks.[146]

The same concept based on a different polymeric system (using thermoresponsive and pH responsive building blocks) was reported by Kim *et al.*[147] N-isopropylacrylamide-co-acrylic acid (NIPAAm-co-AAc) based hydrogels containing peptide crosslinks sensible to MMPs were developed. Hydrogels were obtained by radical addition polymerisation using NIPAAm and AAc monomers and peptides modified with reactive acrylate groups. The peptide crosslinker with bifunctional acryl groups was synthesised first, by modifying the amine groups of lysine and glutamine present on the peptide sequence with acryloyl chloride. In this way the acrylic group was added to the peptide sequence that was ready to be polymerised with the other monomers. Hydrogels with different amounts of crosslinker were synthesised and the degradation with MMPs assessed, which depended on the enzyme concentration and crosslink density of the hydrogel.[147a] In addition, hydrogels containing a cell-adhesive signal (RGD) and MMP degradable domains were further developed by the same group.[147b]

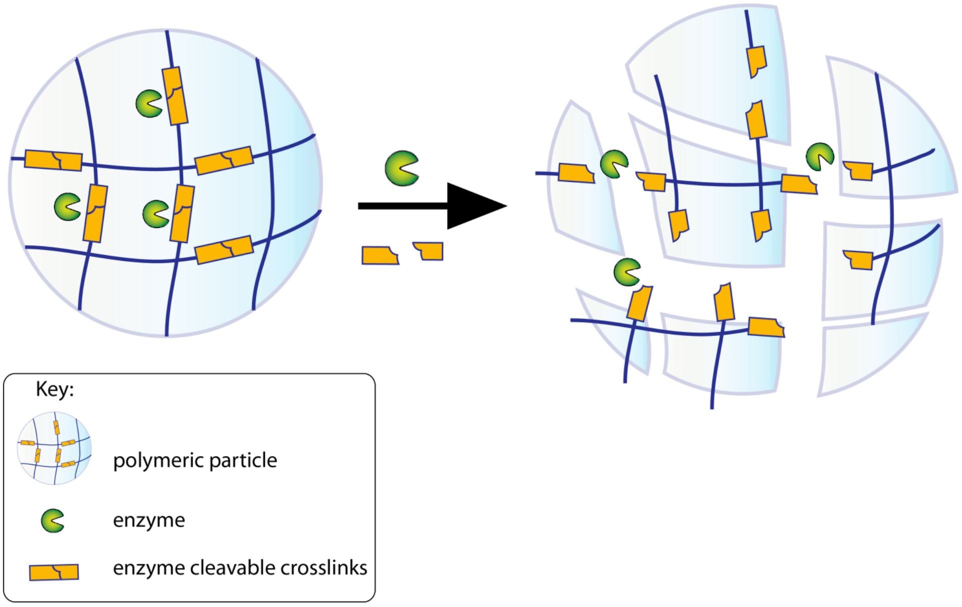

Figure 2.13. Schematic representation of enzyme induced microgel dissolution.

In summary, all these examples describe enzyme responsive systems where the final physical structure of the polymer changes upon enzyme cleavage. The peptide sequences are degraded and the dissolution of the gel takes place.

Microgels with pendant peptide sequences

A different approach in developing enzyme responsive microgels can be followed where the peptide sequences are not introduced as crosslinks but as pendant sequences as shown in figure 2.14. After enzymatic cleavage, these structures would not dissolve and release products generated during the degradation of polymers in the body in case of drug delivery. Pioneering work in this area by Thornton *et al.* shows micrometer sized (250 μm) polymeric beads functionalized with a zwitterionic peptide sequence, which acted as enzyme substrates.[148] These PEGA beads presented enzyme triggered swelling caused by an increase in internal particle charge (an overall positive charge), due to the enzyme hydrolysis of the peptide sequence present on the particles. They demonstrated that this selective enzyme triggered particle swelling can be used to release payload molecules, dextran[148a] and protein payloads (avidin and albumin).[148b] In the latter case, a specific design to control the release was exploited, consisting in the charge matching of peptide linkers to the charge of the protein payload.[148b] Avidin (anionic) and albumin (cationic) were chosen as protein payloads, because of their opposite charges at physiological pH. PEG-based hydrogel particles with overall cationic charge were used for controlled release of the cationic albumin, while the particles with an overall negative charge were used for controlled release of the anionic avidin. In case of oppositely charged, polymeric particles and protein payload (e.g. cationic particles and anionic avidin, and *vice versa*) the release was poor due to electrostatic attraction between the payload and the peptide, suggesting their poor performance as drug delivery systems. This system has been improved by McDonald *et al.*[85], by incorporating branched peptides to increase bead swelling, in smaller (20 µm) sized beads. In these examples, physically (rather than chemically) entrapped payloads are released due to enzyme cleavage of peptide cleavable linkers with rationally positioned charged groups.[85] A limitation of these systems is their large size, which results in slow response times and limited potential for application in drug delivery.

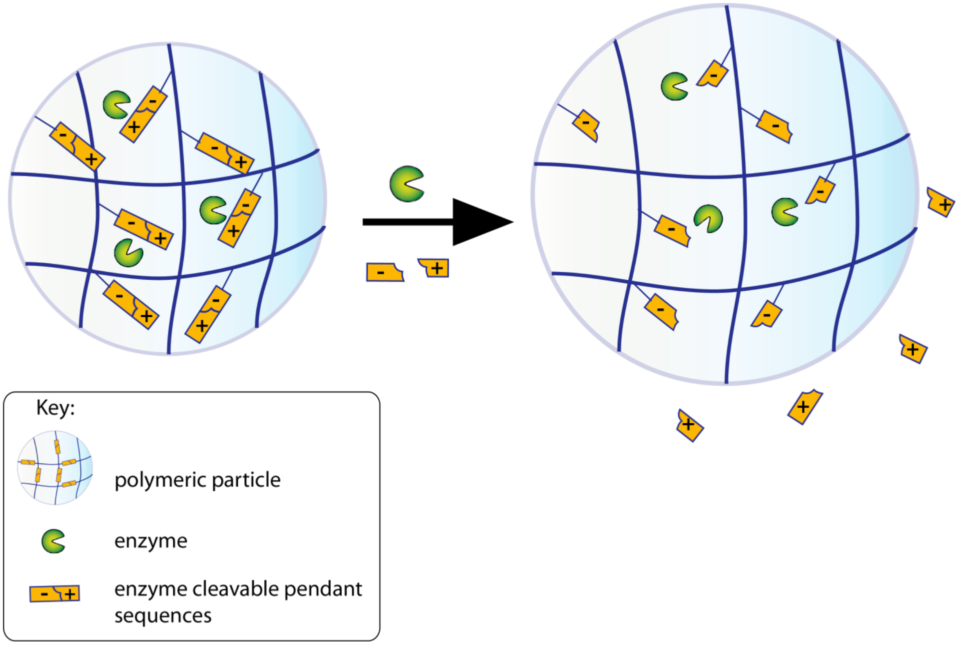

Figure 2.14. Schematic representation of enzyme induced microgel swelling.

2.6.2 Supramolecular peptide based ERMs for cancer applications

Three main classes of peptide based supramolecular materials are studied in the context of ERMs: (i) aromatic peptide amphiphiles, (ii) aliphatic peptide amphiphiles (PAs) and (iii) polymer-peptide conjugates. Enzymes are used to trigger different responses of these materials including enzyme induced: (i) formation, (ii) degradation or (iii) reconfiguration of nanostructures, as shown in figure 2.15. The development of dynamic and reversible systems able to control the assembly and disassembly is still a challenge in the field of ERMs, even if some dual responsive systems were developed.

Even though anti-cancer applications of peptide based ERMs are in their infancy, examples based on supramolecular peptide and polymer-peptide amphiphiles able to degrade selectively in tumour sites have been shown to be effective in delivering drugs *in vitro* and *in vivo*. Enzyme triggered reconfiguration of materials is a new direction in supramolecular peptide material development for cancer applications. So far, no purely peptidic supramolecular system has reached clinical trials for cancer applications. They were explored in terms of biocompatibility and possible therapeutic applications such as inhibition of tumour growth and prevention of cancer cell migration.

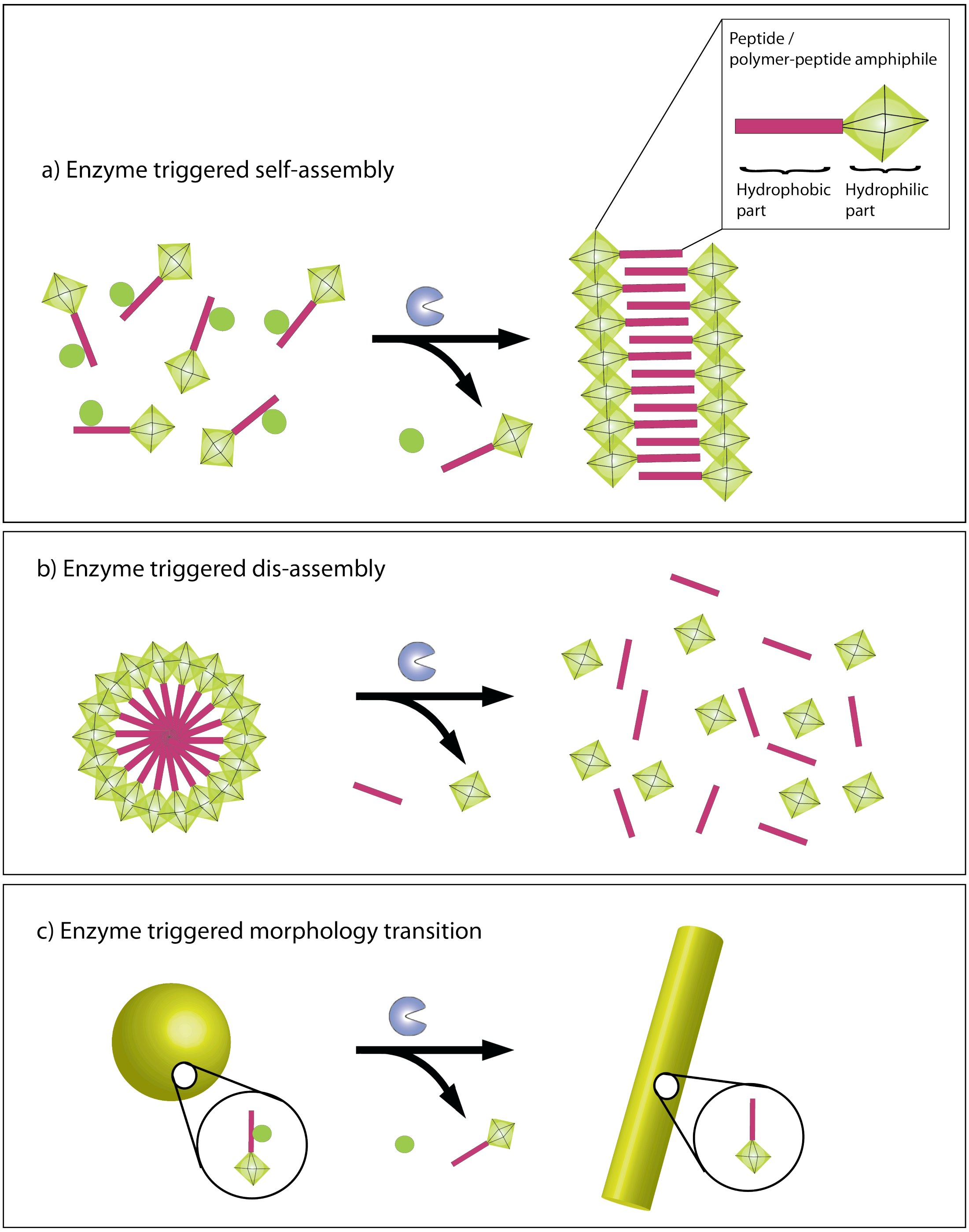

Figure 2.15. Schematic representation of enzyme induced responses of supramolecular peptide based ERMs.

2.6.2.1 Enzyme induced formation of nanostructures

Enzymatic catalysis presents an attractive way to control molecular self-assembly.[149] The advantages include specificity, selectivity and localized action of enzymes, that result in a better spatio-temporal control of self-assembly. Using enzymes is possible to control/induce the assembly, by introducing structural modifications on demand. Most examples in this section are based on bond cleavage strategies and involve the removal of the hydrophilic phosphate group from a precursor that results in a more hydrophobic and less soluble compound, that self-assembles into a hydrogel. In systems where pairs of enzymes were used, phosphatases triggers gelation, while a second enzyme (kinase, tyrosinanse) induces gel-sol transitions.

The most common supramolecular ERMs are based on the enzymatic triggered formation of nanostructures *via* self-assembly (Fig 2.15a). Different enzymes have been used to induce formation of hydrogelators. Of biological relevance are phosphatases[150] involved in the dephosphorylation of phosphorylated tyrosine containing peptides. In addition, matrix metalloproteinases (MMPs)[127] have been exploited in cleaving peptide bonds, by selective removal of solubilizing peptide or polymer domains. Other relevant examples of enzyme induced hydrogelation are subtilisin cleavage of esters and thermolysin amide bond formation *via* condensation (the direct reversal of hydrolysis).[151]

2.6.2.1.1 Peptide ERMs for cancer applications

The most studied enzymatically controlled supramolecular self-assembly systems are those based on aromatic peptide amphiphiles, that consist of short peptide sequences (typically up to five amino acids) modified with aromatic groups (fluorenyl, naphtyl or pyrenyl), that tend to self-assemble giving rise to β-sheet-like fibrillar structures.[152] Multiple fibrils can further assemble to form fibres, that can further interact and entangle to form hydrogel networks.

Since the first example of enzyme triggered hydrogelation reported by Xu and co-workers, based on the dephosphorylation of an Fmoc protected amino acid derivative (Fmoc-Yp), many other aromatic peptide amphiphiles based hydrogelators were designed, exploiting the same enzymatic reaction.[31] Examples include Nap-FFGEYp[98], Nap-FFYp[53], Ac-YYYpY-OMe[113] and Fmoc-FYp[36]. MMP-9 triggered hydrogelation based on a purely peptidic substrate, FFFFCG↓LDD is an interesting example, as it is the first example of use of MMP-9 to trigger hydrogelation.[127] In addition, aliphatic peptide amphiphiles and peptide-polymer conjugates were enzymatically triggered to form nanostructures and/or hydrogels. A list of examples of enzyme triggered formation of nanostructures with possible biomedical applications is shown in table 2.4.

Table 2.4. Examples of enzyme triggered formation of nanostructures with possible biomedical applications.

Precursor	**Enzyme**	**Gelator**	**Transition**	**Application**	**Current studies**	**Ref.**
Aromatic peptide amphiphiles						
Nap-FFGEYp[98]	Phosphatase	Nap-FFGEY	Hydrogelation	Hydrogel formation	*In vivo*	98
Fmoc-FYp[36]	Phosphatase	Fmoc-FY	Micelle to fibre transition	Fundamental	/	36
PABA-F_5Phe-Phe-GPKG↓LKGA/ HSAKFY↓SG / LTPR↓	MMP, PSA,[105] Thrombin[111]	PABA-F_5Phe-Phe-	Hydrogelation	Visual assay for diagnosis	*In vitro*	105, 111
Fmoc-Yp[102]	Phosphatase	Fmoc-Y	Hydrogelation	Detection of inhibitors of enzymes	/	102
Nap-FF-ester[47]	Esterases	Nap-FF	Hydrogelation	Cancer cell death induction	*In vitro*	47
FFFFCG↓LDD[127]	MMP-9	FFFFCG	Hydrogelation	Fundamental	/	127
Nap-FFYp[3c]	Phosphatase	Nap-FFY	Fibre network formation/ hydrogelation	Inhibition of cancer cell migration	*In vivo*	3c
Ac-YYYpY-OMe[113]	Phosphatase/ Tyrosinanse	Ac-YYYY-OMe	Hydrogel dissolution	Controlled release (model drug)	*In vitro*	113
Aliphatic peptide amphiphiles						
KRRASVAGK[C_{12}]	Phosphatase/ kinase pair		Sol-to-gel / Gel-to-sol	Doxorubicin release[54]	*In vitro*	54

Cancer Diagnosis

Hydrogel formation due to dephosphorylation of Fmoc-Yp was used to develop a visual assay for detecting inhibitors of enzymes. In the presence of the inhibitors of the acid phosphatase no hydrogelation would be observed, due to the inhibition of the enzyme, while in the absence of inhibitors hydrogelation would occur. Even if this presents an easy and rapid protocol, it has accuracy limitations (in determining the IC_{50} of the enzyme). Another limitation would be that hydrogelation (self-assembly) should not be disturbed by the presence of inhibitors themselves, but should be based only on their ability to inhibit the enzyme.[102] Later, this concept was extended to detection of enzyme activity *via* gelation for different proteases (thrombin[111] and MMP-9[105]). In both cases the enzyme detection system was designed to contain a gelator, a recognition sequence for the target enzyme and a solubility factor. p-aminobenzamide-F_5Phe-Phe gelator was linked to a PEG solubility factor through the enzyme cleavable sequence (LTPR↓ for thrombin or GPKG↓LKGA for MMP-9). After the cleavage of the sensor by a target enzyme, another enzyme is used (aminopeptidase that cleaves off the N-terminus of a peptide) to remove the residual amino acids from the gelator scaffold. Gelation was observed only when the targeted enzyme efficiently cleaved the sensor, giving the possibility to develop a general method easily extendable to other proteases. The MMP-9 triggered hydrogelation assay constitutes an example of diagnostic application *in vitro* with a detection limit of 50 nM, which is within the levels of circulating MMP-9 in cancer patients (71±60 nM for non-small cell lung cancer).[105] If a lower detection limit is required this could be achieved by using a gelator with lower critical gelation concentration or by designing a different recognition sequence with higher specificity toward the enzyme of interest.

Mutter's group introduced a class of "switch peptides", where the conformational transition is induced by enzyme triggered acyl migration.[153] Conformational transition and self-assembly of various peptides was achieved by using N-protecting groups that were sensitive to different enzymes (trypsin, esterase, pyroglutamate aminopeptidase and cancer relevant dipeptidyl peptidase IV[93]). The N-terminal enzyme triggered deprotection induced acyl migration, that resulted in self-assembly with possible application in prodrug design and biosensor technology.

Cancer treatment by intra/extracellular hydrogelation

Overexpression of enzymes in the intracellular environment enables the development of systems able to form hydrogels inside cells. Intracellular hydrogelation inside mammalian cells and bacteria was reported by Xu and co-workers.[47] In this example, intracellular esterases triggered the hydrogelation of a Nap-FF ester derivative inside HeLa cells, which resulted in a change in viscosity of the cytoplasm and caused cell death. The hydrogel formation was selective for HeLa cells, as the expression levels of esterases were higher than those found in normal cells.

In addition, extracellular enzymes can be targeted to trigger extracellular hydrogelation. Systems were developed where a phopshatase/kinase pair is used to control the assembly and disassembly of simple molecules. Nap-FFGEYp was designed to form hydrogels, due to removal of the phosphate group present on the precursor by a phosphatase. The reverse action of gel-to-sol transition was achieved by using a kinase in the presence of ATP to control the phosphorylation, i.e. the attachment of the phosphate group on the tyrosine residue of the designed peptide. This phosphorylation resulted in the increase of the solubility and dissolution of the previously formed hydrogel. The hydrogel could then be restored by using a phosphatase. This is the first example of using a pair of enzymes to control hydrogelation.[98] In addition, this system was shown to be able to form hydrogels *in vivo* when injected into mice.

Enzymatically controlled nanostructure formation and degradation using pairs of enzymes was also reported for aliphatic peptide amphiphiles. Stupp and co-workers designed an aliphatic PA KRRASVAGK[C_{12}], where phosphorylation/ dephosphorylation switch is used to control fibre disassembly and assembly, respectively.[54] The protein kinase A (PKA) is used to selectively disassemble the nanofibres, which can be restored by treatment with alkaline phosphatase. PKA induced disaggregation of nanostructures could be exploited in cancer therapy. To test the feasibility of the designed system to function as an enzyme sensitive drug encapsulation tool, doxorubicin was encapsulated within the peptide amphiphile nanostructures and its release monitored in presence and absence of PKA. Enzyme triggered doxorubicin release was confirmed to be faster and more efficient. Cell cytotoxicity studies showed selectivity of the doxorubicin loaded nanostructures towards cancer cells, known to overexpress PKA, over non-cancer cell lines suggesting specifically targeted release in the presence of cancer cells.

Another example using two enzymes to control the assembly and disassembly was given by the Ac-YYYpY-OMe peptide amphiphile designed as a substrate for phosphatase and tyrosinase, an oxidative enzyme over-expressed in malignant melanoma.[113] Phosphatase action was used to induce hydrogelation by the removal of the phosphate group, while tyrosinase was explored for the gel-to-sol transition because in the presence of oxygen was able to transform tyrosine to quinone disrupting π- π interactions between phenol rings. Controlled release of a model drug molecule (Congo red) was demonstrated upon addition of tyrosinase indicating the potential use of these hydrogels in drug delivery applications.

The first example of the use of MMP-9 to form a peptide based supramolecular hydrogel was reported by Xu and co-workers.[127] A peptidic system, FFFFCG↓LDD was designed, where the hydrophilic blocking group is removed from the hydrogelator unit upon treatment with MMP-9. Even if not yet shown, triggering hydrogelation exploiting MMP-9 over-expression opens up new possibilities for creating biomaterials able to block metastasis or could be exploited for developing enzyme assays for sensing MMPs.

A way for potential inhibition of cancer cell growth and prevention of cancer cell migration by extracellular hydrogel formation was presented by Xu and co-workers.[3c] In this study, a naphthalene-capped D-tripeptide (Nap-FFY), which is resistant to proteolysis in cellular environment due to the presence of D-amino acids, was found to form fibres selectively on HeLa cells, due to enzyme-instructed self-assembly of soluble monomers. Fibre network formation was induced by over-expressed surface and secretory phosphatases. *In vitro* studies on multidrug resistant uterine sarcoma cells (MES-SA/Dx5) confirm the inhibition of their growth, due to selective formation of networks of fibres able to block nutrients exchange and therefore induce apoptosis, when compared to epithelial cells that remain viable when treated with the peptide.

2.6.2.1.2 Polymer-peptide ERMs for cancer applications

Cancer Diagnosis

Peptide-polymer conjugates able to undergo enzyme triggered self-assembly have also been studied. A poly(ethylene glycol)-functionalised amphiphilic oligopeptide able to undergo enzymatically triggered self-assembly was reported by Koga *et al.*[110] In this study, a β-sheet forming peptide ($L_4K_8L_4$) was conjugated to a hydrophilic PEG segment through a thrombin cleavable linker (VPRGS). The overall conformation of the conjugate was α-helical, due to the fact that the hydrophilic PEG-tail increases its solubility in water. Upon enzyme action, the PEG unit was removed, which allowed the peptidic part to assemble into β-sheets and form nanofibres. An anticancer application was not yet shown for this system, however, as thrombin was reported to promote malignancy in cancer, a metastatic diagnostic tool could be developed in future.

Cancer Treatment

Acid phosphatase responsive PEO-peptide conjugates, that self-assemble into aggregates with peptide core and PEO shell due to phosphate group removal, were reported by Kühnle and Börner.[154] The peptide segment was based on five repeats of alternating threonine and valine diads ($(TV)_5$), that has high propensity of forming β-sheet type assemblies. By introducing three phospho-threonines in the $(TV)_5$ peptide structure the β-sheet formation is suppressed as the phosphate groups prevent the self-assembly of the bioconjugate. The addition of the phosphatase serves as a switch for the activation of the self-assembly process and suggests a peptide guided organization of the bioconjugate. This strategy, that utilises enzymes to specifically manipulate peptide segments in peptide-polymer conjugates, allows the regulation of the bioconjugate characteristics and could be further developed for drug delivery applications.

Enzyme triggered self-assembly of non-peptidic materials is rare, but nevertheless some examples were reported in literature. Enzymatically triggered self-assembly of block copolymers into spherical colloidal nanostructures, under physiological conditions was presented by Amir *et al.*[155] Vinyl monomers containing enzymatic substrates (phosphate moieties) were polymerised with PEG macroinitiator to yield water soluble double-hydrophilic block copolymers. Upon enzymatic cleavage by phosphatase the solubilising phosphate groups were removed, giving rise to an amphiphilic block copolymer that undergoes self-assembly. Spherical nanostructures with PEG based hydrophilic shell and hydroxystyrene hydrophobic core were obtained, that could be useful in future as carriers for hydrophobic drugs.

2.6.2.2 Enzyme induced degradation of supramolecular structures

Enzyme induced degradation of supramolecular structures (Fig. 2.15 b) is based either on enzymatically induced changes in solubility (e.g. introducing phosphate groups by kinase) or on direct degradation of the substrates by proteolysis (e.g. fragmentation into smaller, non-assembling molecules by MMPs). The enzyme induced increase in the solubility of building blocks results in disassembly of the structure. The main application associated with enzyme triggered degradation of supramolecular nanostructures is tissue engineering and drug delivery.

2.6.2.2.1 Degradation of peptide ERMs for cancer applications

Cancer diagnosis

A triple helical optical probe based on collagen type V mimic for the detection of MMP-2 and MMP-9 activity *in vivo* was developed, based on a peptide conjugated to a near-infrared fluorescent dye.[156] The natural collagen sequence (residues 437−447 of type V collagen) was adapted to contain a pair of lysine residues flanking the hydrolysis site, easily modified at the side chains with fluorescent dyes and repeating Gly-Pro-4-hydroxy-L-proline sequences at N- and C-termini, that drive the self-assembly of three single-stranded peptides into triple-helical conformation. When self-assembled into triple helical structures, these probes show no signal due to self-quenching of dyes when in close proximity, however, in the presence of MMP-2/9, the substrate (GPPG↓VVGEK) is hydrolysed, which results in the release of dyes and an amplified fluorescence signal is detected. This was confirmed *in vivo*, where an enzyme induced fluorescence signal was detected in mice bearing a human fibrosarcoma tumour cells, while the signal was quenched in the presence of MMP inhibitors.

Another study shows how enzymatic activation influences the distribution of peptides and peptide fragments in cancer cells. An MMP-2 cleavable peptide (IPVS↓LRSK) containing a FITC molecule of the N-terminus was modified with coumarin-343 at the C-terminus. Its distribution was studied *in vivo* in the presence and absence of MMP-2. While no accumulation was observed for normal cells, when administered to cancer cell lines cleavage of the probe occurs. As a consequence, the FITC containing fragment remains distributed extracellularly, while the coumarin-343 containing fragment is internalised by the cells. This example shows how enzyme activity can influence the distribution of peptide fragments in solid tumour by regulating their cellular uptake.[157] It should be noted that, unlike the other examples (based on supramolecular structures) discussed in this section, this example is not based on a degradation of a supramolecular structure, but on different distribution of peptide fragments in presence of cancer cells (cancer related enzymes).

Cancer treatment

A system sensitive to urokinase plasminogen activator (uPA) was developed, where two β-sheet forming peptides based on the KLD-12 self-assembly motif are flanking the SGR↓SANA substrate peptide.[114] The KLDLKL-SGR↓SANA-DLKLDLKL peptides, where the FITC tag was covalently attached to the N-terminus of the building blocks, were formulated into self-assembly matrices. uPA triggered degradation of the matrix was monitored by the release of the fluorescent reporter attached. These systems were further modified with a membrane penetrating arginine rich sequence, to enhance cell delivery and loaded with mitochondrial disruption peptide, KLAKLAKKLAKLAK that was released in the presence of uPA, giving high cytotoxicity to cells.

Recently, MMP induced hydrolysis of supramolecular peptide filaments for drug delivery application in cancer therapy was reported by Cui and co-workers.[158]

In this work, β-sheet rich supramolecular filaments were obtained by pH induced self-assembly of peptide sequences linking a hydrophobic oligoproline segment to an amyloid-derived peptide sequence (GNNQQNY). A short alkyl chain (C_8) was included in the structure to enhance the assembly potential. Subsequently, the obtained filamentous structure was stabilised using a crosslinking strategy to covalently lock the structure, where the crosslinks were displayed at the surface of the nanofibres. This consisted of the introduction of MMP-2 sensitive peptide crosslinks (GPQG↓IAGQ and IPVS↓LRSG) to confer fibre stability at physiological pH and introduce enzyme sensitivity in the material. Upon treatment with MMP-2, the supramolecular fibrillar filaments undergo dissociation into individual building units. This new platform could be extended to other types of enzymes and offers potential uses in drug (protein) delivery.

An example for the on-demand release of chemotherapeutics in the presence of MMPs was developed and then tested *in vitro*. Physically crosslinked nanosized hydrogels obtained by mixing a negatively charged natural polypeptide, gelatine (type B from bovine skin, commercially available) with cationic surfactants such as the commercially available CTAB or peptide amphiphiles containing multiple arginines attached to alkyl chains, were reported.[159] Prior to mixing, gelatine was modified with succinic anhydride to obtain negative charges. When the surfactant micelles were then mixed with gelatine, stabile core-shell like nanogels formed that are sensitive to MMP-9 (able to degrade gelatine) and show high encapsulation stability. This was confirmed also in the *in vitro* environment. Such systems were used for doxorubicin encapsulation and MMP-9 triggered release in a SCC-7 cell line, which is known to have MMPs over-expressed. In the presence of MMP-9, the doxorubicin was successfully released and showed toxicity to the cells treated, while in the presence of MMP-9 inhibitors this toxicity was not observed.

MMP-9 responsive collagen mimetic lipopeptides able to self-assemble into vesicles were reported, to which a PEG moiety was introduced through a disulfide bridge sensitive to reductive environment.[160] The PEG was added to increase the circulation times, but also to protect the vesicles from enzymatic degradation. It was hypothesised, that in the extracellular environment where glutathione is found, these nanovesicles will undergo reduction, which would result in the PEG removal and would make the resulting structures MMP-9 responsive (GPQG↓IAGQ). The vesicles were encapsulated with an anticancer drug, gemcitabine and effective enzyme triggered drug release was observed in three dimensional spheroid cell cultures. The *in vivo* performance of the vesicles, following intravenous administration in mice models with human pancreatic cancer, showed the capacity of the designed system to reduce tumour growth more efficiently compared to the control nanovesicles (without the MMP-9 enzyme substrate).

The concept of supramolecular membranes for cancer therapy was introduced by Stupp and co-workers, where $(KLAKLAK)_2$ based cytotoxic aliphatic PA (C_{16}-VVVAAAGG$(KLAKLAK)_2$) self-assemble into membranes when in contact with hyaluronic acid.[43a] Initially, the co-assembly is due to charge complexation, which is followed by a diffusion barrier creation and perpendicular growth of fibres. The membrane composition influences its (membrane) morphology and thus its degradation in response to the enzyme, and in particular the rate of release of the cytotoxic peptide. The *in vitro* behaviour of MDA-MB-231 and SKBR-3 breast cancer cells was investigated when in contact with the membranes. These membranes can act either as reservoirs of cytotoxic peptides, when the hyaluronidase induced fragmentation releases cytotoxic (KLAK) fragments, or as constructs with highly surface-localised toxicity to be used for eliminating the residual cancer cells after surgery. In the first case, the cancer cell lines having higher hyaluronidase activity compared to the epithelial ones, become more susceptible to the cytotoxic metabolic products. In the case of cell seeded on the membranes, MB-MDA-231 breast cancer cells were observed to adhere to the membranes, but were found dead after a few hours indicating the potential use as materials with high surface toxicity in cancer therapy.

2.6.2.2.2 Degradation of polymer - peptide ERMs for cancer applications

Cancer diagnosis

Recently, radiolabeled self-assembled glycol chitosan nanoparticles for multimodal imaging were reported.[161] A combination of near-infrared fluorescence optical probe and PET (Positron emission tomography) imaging was used for whole body (mice) imaging based detection of metabolic and/or molecular aberrations such as protease over-expression. Self-assembled chitosan nanoparticles were prepared, that were modified post-assembly *via* copper-free click chemistry with ^{64}Cu, and MMP-9 sensitive peptide sequences (GPLG↓VRGKGG) containing near-IR fluorescent dyes. Their potential to act as probes for tumour detection was tested in tumour bearing mice. The *in vivo* multimodal imaging confirmed the accumulation of the probe in tumour tissues and the increased MMP-9 activity, showing that the developed probe is useful for an accurate diagnosis of cancer states.[161]

Cancer treatment

The idea that disassembly of a supramolecular structure could result in release of anticancer drugs in the desired site was explored for peptide-polymer conjugates, too. A peptide-polymer conjugate responsive to gelatinases was reported by de Graff *et al.* where a peptide, substrate of MMP-2 and MMP-9 (SGPQG↓IFGQMG), was decorated at the N- and C- termini with two growing polymer chains. The peptide was positioned between a hydrophilic and a thermosensitive polymer blocks forming peptide-hybrid ABC block copolymers.[121] These amphiphilic block copolymers self-assembled into MMP sensitive micelles, that could be loaded with drug molecules and potentially used as drug delivery systems in cancer states, due to collagenase induced removal of the hydrophilic corona of the micelles.

Lecommandoux and co-workers reported enzyme sensitive PVG↓LIG-PTMC (poly(trimethylene carbonate)) amphiphilic hybrids composed of an MMP-2 sensitive, hydrophilic peptide and a hydrophobic, biodegradable polymer suitable to target the tumour microenvironment.[99] Different lengths of the polymeric blocks having increasing hydrophobicities directed the self-assembly into various submicrometer-sized spherical morphologies being vesicles, micelles and core-shell nanoparticles. All the nanostructures undergo MMP-2 triggered disassembly, with the vesicles being more resistant, probably due to the fact that the interior surface of the vesicles is not easily accessible to the enzyme.

2.6.2.3 Enzyme triggered reconfigurations

As described so far, enzymes can be used to induce the formation or degradation of nanostructures. The development of dynamic systems, where the disassembly and assembly of nanostructures can be controlled by enzymes, is attractive from the point of view of mimicking the dynamic remodelling observed in the natural ECM and physiological processes using synthetic materials. The approach for developing enzyme responsive dynamic self-assembly systems, is based on morphology transitions from one type of supramolecular assembly to another (Fig. 2.15 c). Many examples of enzyme triggered structural transitions reported in literature are based on polymeric micelles.[162]

2.6.2.3.1 Reconfiguration of peptide ERMs for cancer applications

Examples of micelle to fibre transitions were reported for both aromatic and aliphatic peptide amphiphiles, both characterised by macroscopically observable morphology changes from solutions to hydrogels. First, a micelle to fibre transition of Fmoc-FYp dipeptide in response to alkaline phosphatase was reported by Sadownik *et al.*[36] This aromatic peptide amphiphile undergoes a transition from a free flowing micellar solution to a gel-forming nanofibre network, due to the enzyme mediated phosphate group removal. A similar transition was reported by Koda *et al.* for an aliphatic peptide amphiphile responsive to a protease.[124] Palmitoyl-GGGHGPLGLARK composed of an MMP-7 responsive peptide sequence attached to an alkyl chain self-assembled into micelles. Upon enzyme cleavage, palmitoyl-GGGHG fibre forming unit formed hydrogels. This hydrogelating system could find applications as a visual assay for detection of MMP-7.

2.6.2.3.2 Reconfiguration of polymer - peptide ERMs for cancer applications

Cancer Diagnosis

Peptide-polymer, block copolymer amphiphiles containing substrates for four different cancer associated enzymes: protein kinase A, protein phosphatase-1, and matrix metalloproteinases 2 and 9 were reported.[51] Reversible switching of morphology using a phosphorylation/dephosphorylation cycle was shown together with the study of peptide sequence directed changes of morphology induced by proteolysis. The designed peptide-polymer conjugates, containing a hydrophobic block (phenyl groups) and a hydrophilic block (peptides), self-assembled into micelles displaying peptide side chains (enzyme substrates) in the hydrophilic shell. These materials could reversibly change the structure form micelles to larger aggregates, using the kinase/phosphatase pair as 3 cycles of phosphorylation/ dephosphorylation were successfully performed. They were also shown to undergo an irreversible transformation from micelles to amorphous networks in response to MMPs. In this case the position of the cleavage site in the amphiphile was critical for the morphology change. When the cleavage site for MMPs was positioned in the proximity of the backbone, a more pronounced morphological change was observed.[51] The MMP-2 and MMP-9 (GPLG↓LAG) ability to trigger the transition from micelles to micrometer scale aggregates was later exploited by the same group for enzyme-directed accumulation of nanoparticles selectively in tumour tissues *in vivo*.[52] Enzyme responsive particles able to generate a FRET (Förster resonance energy transfer) signal in tumour tissue were obtained, by introducing donor or acceptor dyes in the previously described MMP responsive polymer-peptide conjugates. In response to the cancer-associated enzyme, these systems produced a fluorescence signal in the tumour site.[52] Although not yet shown, these systems could be exploited for prolonged drug release in tumours. This concept was further extended to attachment of near-infrared dyes (Alexa Fluor 647 dyes) on polymer-peptide conjugates exploiting the advantage of long wavelengths for deep in tissue imaging.[163]

Cancer Treatment

An interesting example, where the morphology transition is based on enzyme catalysed reduction was presented by Deming and co-workers.[101] In this example, enzyme responsive co-polypeptide vesicles were designed based on poly(methionine)-b-poly(leucine-phenylalanine) hydrophobic precursor, that was oxidized in mild conditions to methionine sulfoxide containing peptide amphiphiles, able to assemble into vesicles. The possibility to interchange methionine residues between hydrophobic (reduced) and hydrophilic (oxidized) using mild oxidation conditions and the incorporation of enzyme responsiveness was exploited. Intracellular reductases, i.e. methionine sulfoxide reductases (MSR) known to catalyse the reduction of metionine sulfoxide to methionine, were chosen as a target enzyme. Enzyme triggered change in self-assembled morphology from vesicles to sheet-like assemblies was observed upon MSR addition, able to regenerate hydrophobic methionine segments. The release of a model drug molecule (Texas Red labelled dextran) was studied in the presence of the enzyme confirming that MSR induced disruption of vesicles resulted in cargo release. As MSR enzymes are found up-regulated in oxidative stress environments, such as cancer and injury states, targeting of these enzymes provides a new opportunity to intracellularly release drugs in oxidatively stressed tissues. This example differs from conventional ERMs typically developed to be responsive to enzymes that catalyse coupling or cleavage reactions.

2.7 Conclusions and future perspectives

In summary, various ways of cancer targeting by taking advantage of enzyme over-expression have been explored. Targeting dis-regulated levels of enzymes seems to be a valid approach as enzymes show a number of unique advantages compared to other stimuli. Exploiting their spatio-temporal control enables triggering of structural changes in the desired tissue or organ. The emphasis is on self-assembling peptides and peptide-polymer conjugates as nanomaterials for biomedical applications such as diagnosis and drug delivery. Recently, effort has been put on developing supramolecular, enzyme responsive, peptide nanomaterials for cancer diagnosis and treatment, able to efficiently target the tumour tissue, while reducing the side effects in other tissues and organs.

Substantial effort has been put on the elucidation of peptide self-assembly mechanisms that can lead to the design of more sophisticated systems. However, it is important to move towards real life applications of the enzyme responsive materials, that are able to undergo dynamic changes in material properties only when needed. Many materials described in this text are based on synthetic polymers combined with peptides and some require toxic methodologies for their preparation. Removal of the by-products, catalysts and often solvents used during the preparation step can be difficult to achieve.

Many known enzymes and enzymatic reactions remain unexplored in the development of ERMs and may require investigation to lead to the discovery of new dynamic systems for drug delivery applications. By learning from biology new aspects could be added to the existing materials exploiting more complex mechanisms.

Selectively targeting cancer cells leading to *in vivo* applications still remains a challenge for supramolecular ERMs based on peptides. Recently, animal models have been tested with the objective to identify possible candidates for further studies and maybe in a not so far future, FDA approval. New therapies with no side effects are still an imperative, but the attempts made by nanotechnology will possibly lead to the development of an efficient and successful cancer therapy.

3 MMP-9 triggered micelle-to-fibre transitions for slow release of doxorubicin[ǂ]

[ǂ] The work in this Chapter has been published, in part, as communication in Biomaterials Science. DOI: 10.1039/C4BM00297K

Declaration of contribution to accepted article:

Any reproduced work from the submitted article I was solely responsible for, including the written article itself, unless otherwise stated. FTIR data were provided by Dr. Pim Frederix.

3.1 Introduction

Peptide self-assembly is increasingly investigated for a plethora of applications in biomedicine including drug release, tissue engineering, diagnostic studies and regenerative medicine.[25a-c,26,29a,b,43a] These nanostructures are of interest as they may contain bioactive peptide ligands, as well as structural components which enable access to a variety of nanoscale morphologies dictated by the amino acid sequence[34] but also by the route of assembly[35]. Enzymatic catalysis presents an attractive way to control molecular self-assembly.[50,150,164] In this approach, non-assembling precursors that are "blocked" with enzyme cleavable groups are converted to self-assembling building blocks (including hydrogelators), enabling self-assembly on-demand under physiological conditions. The most frequently studied biocatalytic self-assembly systems are those based on aromatic peptide amphiphiles. These consist of short peptide sequences modified with aromatic groups such as phenyl, naphthyl, fluorenyl and others.[152] Different enzymes such as phosphatases[150,3b,36,165] and proteases (including matrix metalloproteinases (MMPs))[120,127] have been used to trigger molecular self-assembly *in vitro* and *in vivo*[3b,52].

Expression levels of enzymes dictate the difference between health and disease in many cases, including cancer. MMPs are a family of zinc dependent endopeptidases that are involved in the digestion and remodelling of the extracellular matrix.[166] Some members of this family, such as MMP-9 have been reported to be over-expressed in breast, cervical, colon and other types of cancer.[167] This makes them valuable triggers for responsive biomaterials and targeted self-assembly. Typically, MMP responsive peptide-based systems act *via* hydrolysis and dissociation of structures i.e. using enzymatic cleavage to trigger dissociation of hydrogels (containing MMP sensitive crosslinks)[122,168], supramolecular peptide filaments[158] and polymer-peptide hybrids[99]. The first example of the use of MMP-9 to form (rather than degrade) a peptide based, supramolecular hydrogel was presented by the Xu group.[127] A morphology change induced by MMP-7 was previously shown for an aliphatic, palmitylated peptide amphiphile system.[169] A very recent study shows the development of a selective assay for MMP-9 *via* gelation.[105]

3.2 Objectives

Based on this knowledge, the development of a peptide based enzyme responsive system, that is able to undergo a morphological change from micellar aggregates to fibres in response to cleavage by MMP-9 (Fig. 3.1 A) was set out, and its design for localised formation of a depot for slow release of hydrophobic drugs (e.g. doxorubicin) at the cancer site was assessed.

There are three requirements for such a system: (i) a biocompatible fibre forming self-assembly unit (Phenylacetyl-FFAG/GFFLG) that also provides the hydrophobic binding region for drug candidates, (ii) the MMP-9 cleavable sequence and (iii) a hydrophilic unit (LDD) that modifies the amphiphilic balance of the precursor to favour micelle formation (Fig. 3.1 B). Thus, upon MMP-9 cleavage, the peptide micelles reconfigure into fibres, due to a change in hydrophobic/philic balance of the sequence. In turn, this aspect may be used for hydrophobic drug entrapment into fibres, presenting a unique advantage for the development of drug delivery systems for prolonged release times after initial exposure.

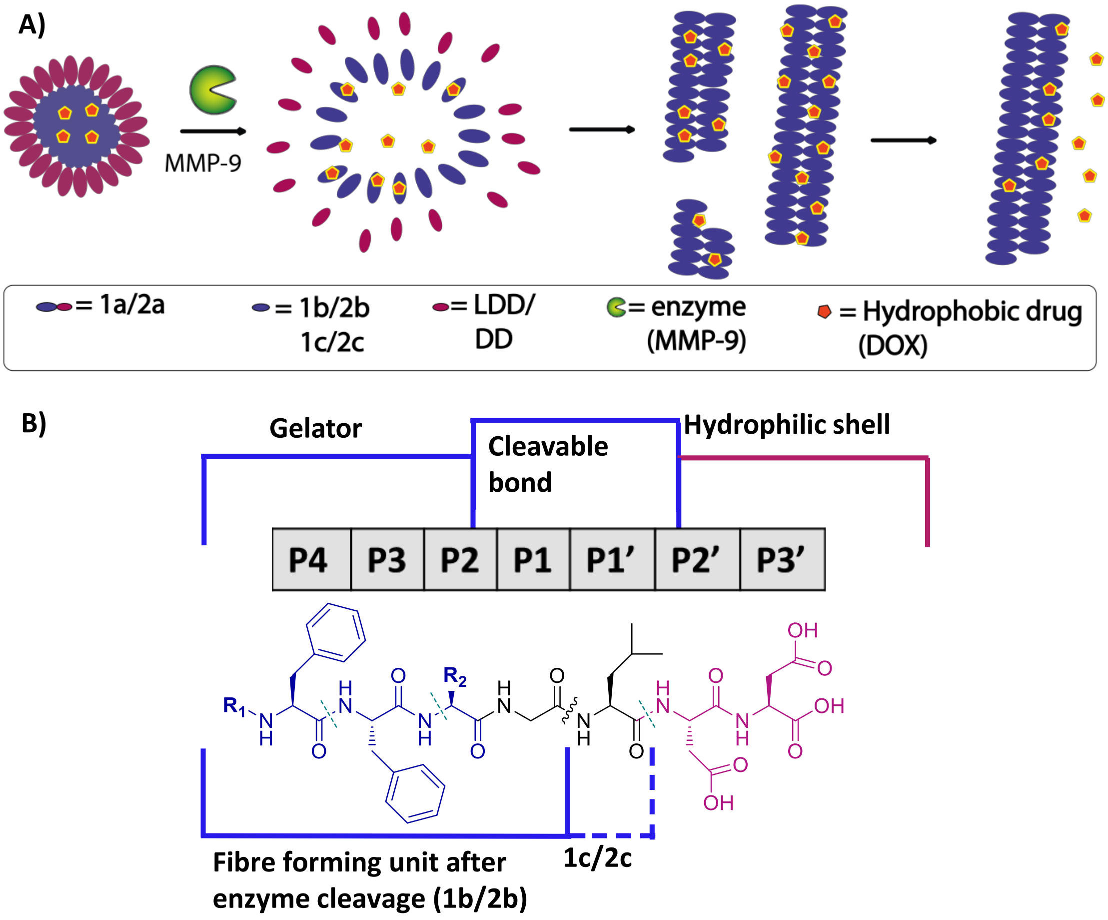

C)

Peptide	R_1	R_2	Sequence
1 a / 1b / 1c	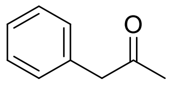	$-CH_3$	**PhAc**-FF**A**GL**DD** / **PhAc**-FF**A**G / **PhAc**-FF**A**GL
2 a / 2b / 2c	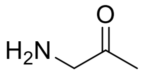	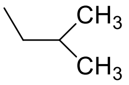	**G**FF**L**GL**DD** / **G**FF**L**G/ **G**FF**L**GL

Figure 3.1. A) Schematic representation of micelle to fibre transition induced by MMP-9 cleavage showing an enzyme induced disassembly of micelles and the re-assembly into fibres, after the removal of the hydrophilic group. The fibre formation due to the new hydrophobicity/philicity balance is in turn advantageous for prolonged drug release. B) Structure of the biocatalytic gelation system components where the P4-P3'[119] positions on the designed peptides are shown and also the expected (G↓L) and observed (L↓D, F↓L and F↓F) MMP-9 cleavage sites, in accordance with previous studies that also showed a shift in specificity of this enzyme when short i.e. heptapeptide substrates are used.[120,127]

3.3 Design of MMP-9 substrates

In order to design the enzyme cleavage site, the MEROPS[170] database was used, which provides cleavage patterns for peptidases based on a collection of experimental data from literature. This can be used for the design of substrates that simultaneously meet the three criteria mentioned. MMP-9's specificity preference for P4 – P3' (Fig. 3.2) subsites (based on 367 cleavages reported in literature) is based on the GPX$_1$G↓LX$_2$G sequence with G↓L (P1-P1') being the cleavable bond, X$_1$ (P2) being preferentially alanine or leucine, and X$_2$ (P2') glycine as a first choice.[170] MMP-9 requires longer substrates, of for example 7 residues (i.e. P4-P3'), in order to be able to recognise and efficiently cleave the G↓L bond[171], with GPLG↓LAG being an example.[172] The length of the substrate and large substitutions (i.e. pyrene, naphthalene, etc.) at the N-terminus can lead to a shift in specificity of MMP-9.[120] To fulfil the requirement of the gelator (fibre forming) unit in the P3 and P4 positions phenylalanine-phenylalanine [45] was used (proline and glycine preferred, but phenylalanine known to be tolerated in P3 and P4). In P2 we chose alanine (**1a**)/leucine (**1b**), while in P2' and P3' (referred to as amino acids flanking the scissile bond towards the C-terminus) aspartic acid-aspartic acid, was used, as it is known to be tolerated in both positions, and will provide a negatively charged surface of the micellar aggregates.

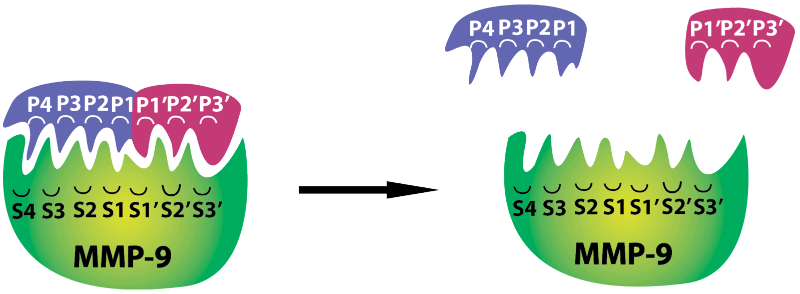

Figure 3.2. Schematic representation of the Schechter and Berger model for MMP-9 and the designed substrate where P4-P3' positions are shown to interact with S4-S3' subsites in the active site of the enzyme.

3.4 Results and discussion

3.4.1 Peptide synthesis and characterisation

First the PhAc-FFAGLDD (**1a**), GFFLGLDD (**2a**) and their expected products of enzyme cleavage PhAc-FFAG (**1b**) and GFFLG (**2b**) were synthesized and characterized by HPLC and LCMS. Self-assembly was assessed by atomic force microscopy (AFM), Fourier transform infrared spectroscopy (FTIR), dynamic light scattering (DLS), rheology and fluorescence.

Solid phase peptide synthesis (SPPS) and characterisation

The four peptides (**1a**, **1b**, **2a** and **2b**) produced by SPPS were analysed by HPLC and LCMS to confirm the identity and purity of the obtained products. When needed, the preparative HPLC was used to purify the compounds.

1a peptide sequence (Fig. 3.3 A) was analyzed by HPLC using two different gradients (Fig. 3.3 B and C): HPLC (20-80% Solvent B (0.1% TFA in acetonitrile), retention time = 22.2 min) and HPLC (30-50% Solvent B, retention time = 32.3 min). LCMS results are as follows: LC (5-100% Solvent D (5 mM ammonium acetate in acetonitrile), retention time = 10.7 min), MS (mass calculated: $[M-H]^-$= 900.4, mass observed: $[M-H]^-$= 900.3) shown in figure 3.3 D.

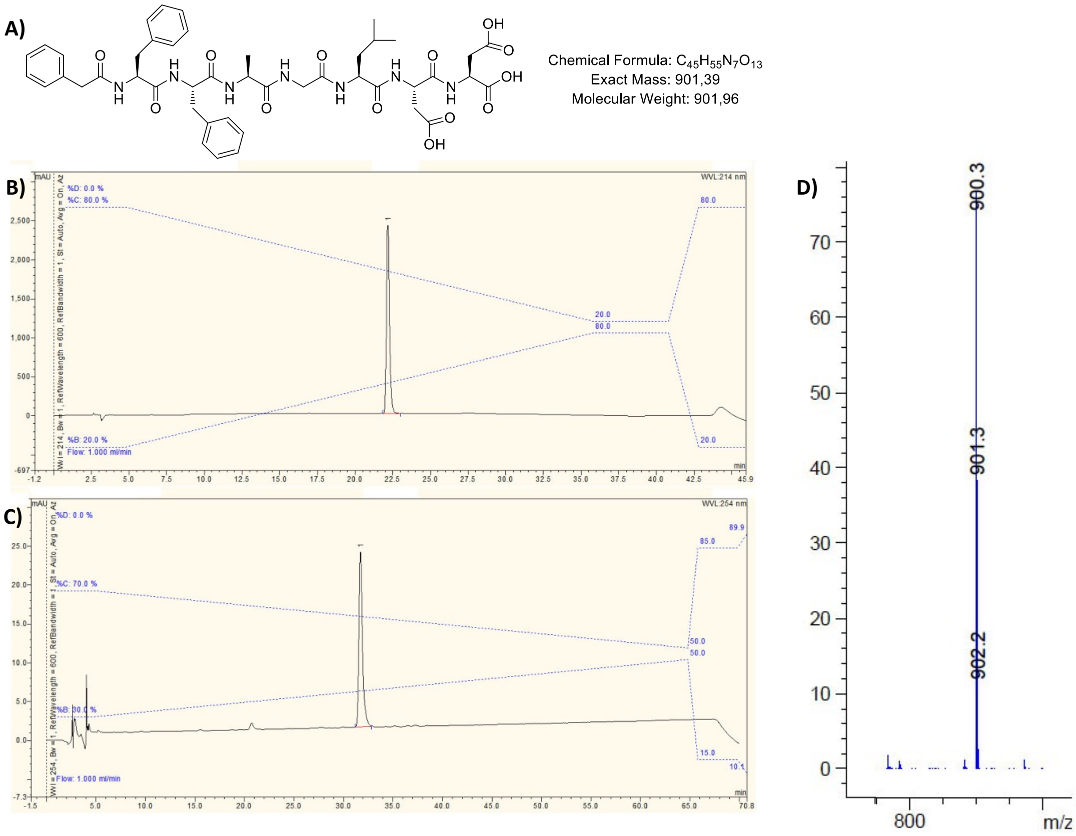

Figure 3.3. A) Chemical structure of PhAc-FFAGLDD (**1a**); B) HPLC chromatogram for **1a** (20-80% solvent B gradient, detection wavelength = 214 nm); C) HPLC chromatogram for **1a** (30-50% solvent B gradient, detection wavelength = 254 nm); D) Fragment of MS spectra showing the negative ion of **1a** detected.

1b peptide sequence (Fig. 3.4 A) was analyzed by HPLC using two different gradients (Fig. 3.4 B and C): HPLC (20-80% Solvent B, retention time = 22.2 min) and HPLC (30-50% Solvent B, retention time = 27.7 min). LCMS results are as follows: LC (5-100% Solvent D, retention time = 11.2 min) and MS (mass calculated: $[M+H]^+ = 559.3$, mass observed: $[M+H]^+ = 559.2$), shown in figure 3.4 D.

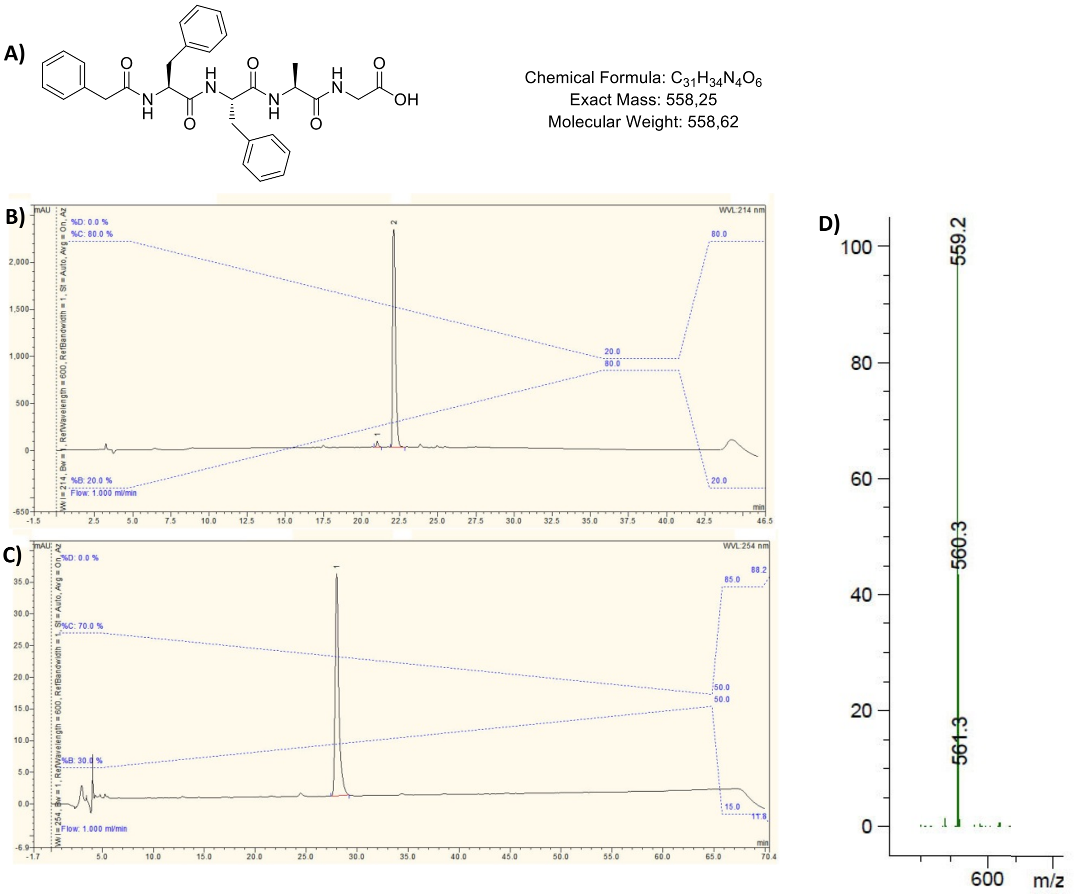

Figure 3.4. A) Chemical structure of PhAc-FFAG (**1b**); B) HPLC chromatogram for **1b** (20-80% solvent B gradient, detection wavelength = 214 nm); C) HPLC chromatogram for **1b** (30-50% solvent B gradient, detection wavelength = 254 nm); D) Fragment of MS spectra showing the positive ion of **1b** detected.

The reason why two different gradients were used for HPLC analysis in case of **1a** and **1b** is that both, the long sequence (**1a**) and the expected cleavage product (**1b**) have the same retention time (22.2 min) when analyzed using 20-80% acetonitrile gradient. Therefore, to separate the two peaks and provide optimal conditions for enzyme studies the new 30-50% acetonitrile gradient was used showing retention times of 32.3 min for **1a** and 27.7 min for **1b**.

2a peptide sequence (Fig. 3.5 A) was analyzed by HPLC (20-80% Solvent B) and shows a retention time of 16.8 min (Fig. 3.5 B). LCMS results are as follows: LC (5-100% Solvent D, retention time =10.1 min) and MS (mass calculated: $[M-H]^-$ = 881.4, mass observed: $[M-H]^-$ = 881.3), shown in figure 3.5 C.

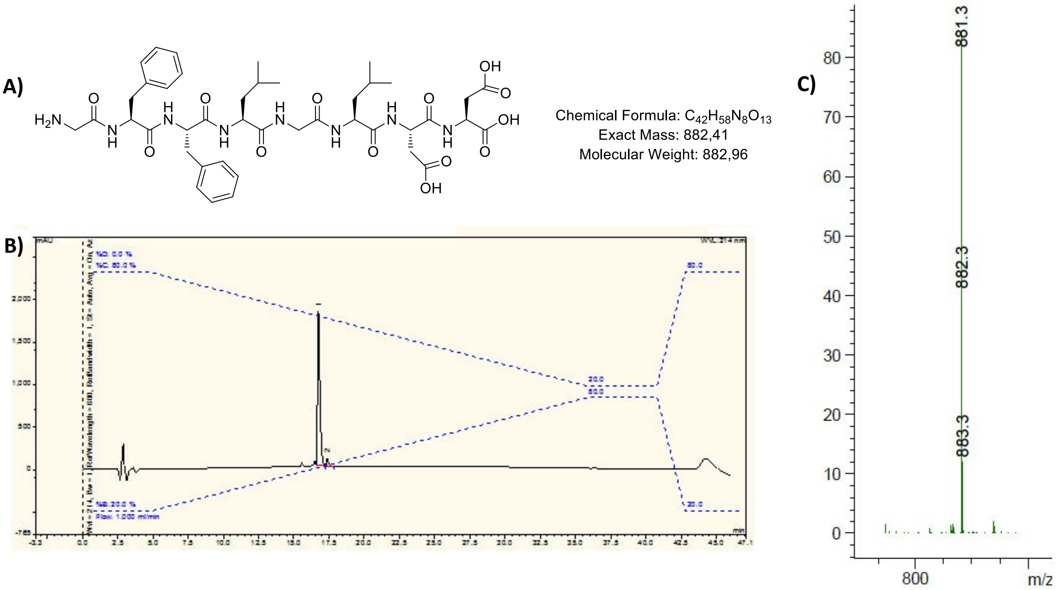

Figure 3.5. A) Chemical structure of GFFLGLDD (**2a**); B) HPLC chromatogram for **2a** (20-80% solvent B gradient, detection wavelength = 214 nm); C) Fragment of MS spectra showing the negative ion of **2a** detected.

2b peptide sequence (Fig. 3.6 A) was analyzed by HPLC (20-80% Solvent B) and shows a retention time of 15.6 min (Fig. 3.6 B). LCMS results are as follows: LC (5-100% Solvent D, retention time = 10.1 min) and MS (mass calculated: $[M+H]^+$= 540.3, mass observed: $[M+H]^+$ = 540.3), shown in figure 3.6 C.

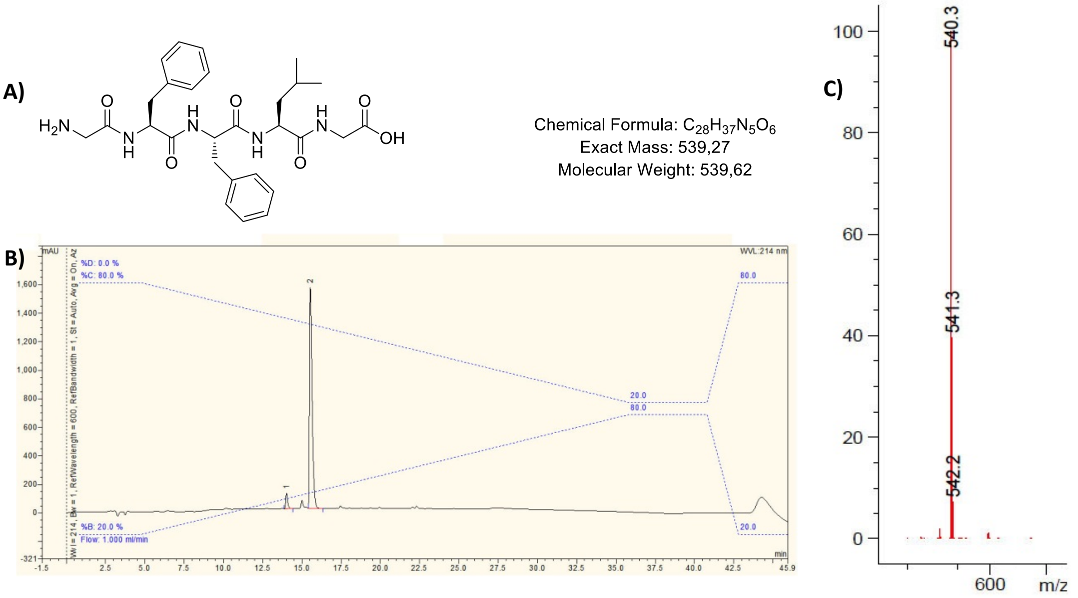

Figure 3.6. A) Chemical structure of GFFLG (**2b**); B) HPLC chromatogram for **2b** (20-80%

solvent B gradient, detection wavelength = 214 nm); C) Fragment of MS spectra showing the positive ion of **2b** detected.

Characterisation of self-assembling behaviour of peptide amphiphiles

The micelle forming peptides (**1a** and **2a**) were directly dissolved in deionized water, the pH adjusted to 7.4 and their self-assembly behaviour investigated after a cycle of alternating sonication and vortexing. For the expected enzyme cleavage peptide fragment i.e. **1b**/**2b** the peptide was dissolved in DI water and the pH was increased (NaOH 0.5 M) to solubilise **1b**/**2b**, followed by a slow decrease of pH achieved by addition of HCl 0.5 M, to a final pH of 6.5 – 7 to trigger gelation. This slightly acidic pH corresponds to that of the tumour microenvironment.[55] Gelation was observed for the expected MMP-9 cleavage products **1b** and **2b**. **1b** forms a transparent gel (Fig. 3.7 A) while an opaque gel is observed for **2b** (Fig. 3.8 A).

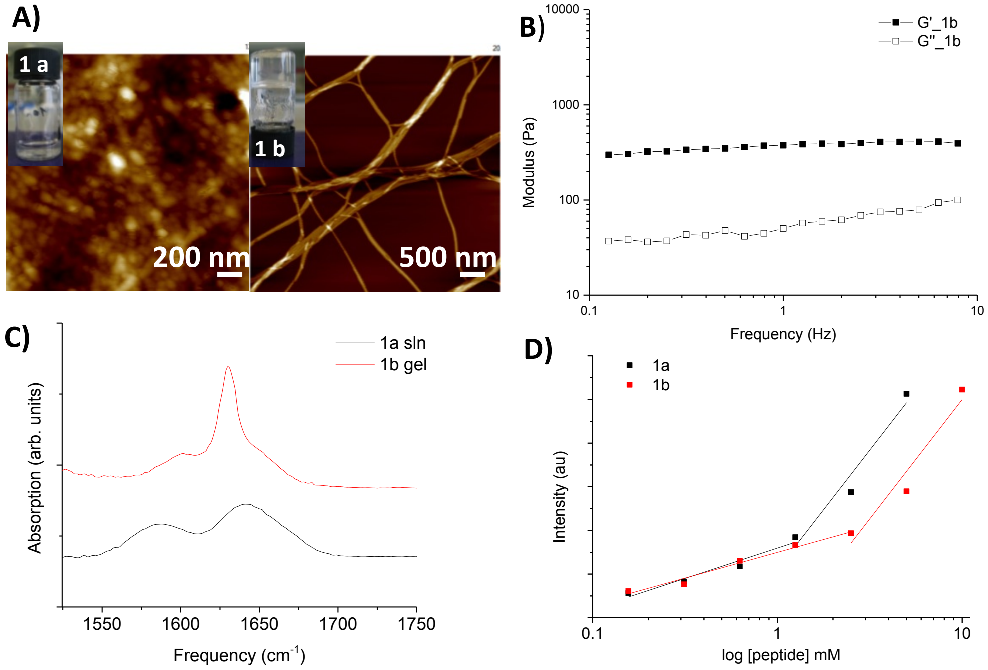

Figure 3.7. A) Atomic force microscopy (AFM) showing the micellar aggregates (solution) for **1a** and fibres (hydrogels – 20 mM) for **1b**. B) Rheology data for **1b** gel showing the plot of G' (elastic modulus) and G'' (viscous modulus) against frequency. C) FTIR absorption spectrum in the amide I region (in D_2O at pH 7): **1a** (solution) and **1b** (gel). D) Critical aggregation concentration (CAC) of 1.3 mM (**1a)** and 2.9 mM (**1b)**.

The AFM characterisation of the peptides revealed spherical aggregates for **1a** (44 ± 6 nm) and **2a** (42 ± 4 nm) while fibres were found for **1b** and **2b** having micron scale length and 20-50 nm range width which corresponds to the size of peptide based fibres reported in literature.[34c] Alternative supramolecular organisation was further supported by infrared (IR) spectroscopy data (Fig. 3.7 C and 3.8 C) suggesting the presence of ordered structures for the examined peptides due to aggregation *via* intramolecular hydrogen bonding.[173] Peptides **1a** and **2a** show a red shift and a broad peak at 1643 cm^{-1} compared to 1650-1655 cm^{-1} absorption values typical for free peptides in solution. The 1570-1580 cm^{-1} absorption band is attributed to the aspartic acid side chain carboxylate group present in **1a** and **2a**. Extended structures are observed for **1b** characterised by a pronounced narrowing of the peak typical for short peptide β-sheets at 1630 cm^{-1} and for **2b** showing a more complex pattern indicating extended nanostructures, while the 1595 cm^{-1} characteristic of the C-terminus carboxylate group has a low intensity.[174] Rheology measurements of the **1b** hydrogel show the elastic modulus (G') of 360 Pa, an order of magnitude higher than its viscous component (G"= 32 Pa) which is characteristic of entangled networks (Fig. 3.7 B). The same behaviour is observed for the hydrogel **2b** having the elastic modulus of $G'=10.9 \times 10^3$ Pa and the viscous modulus of G"= 662 Pa (Fig. 3.8 B), being a stiffer gel compared to **1b**.

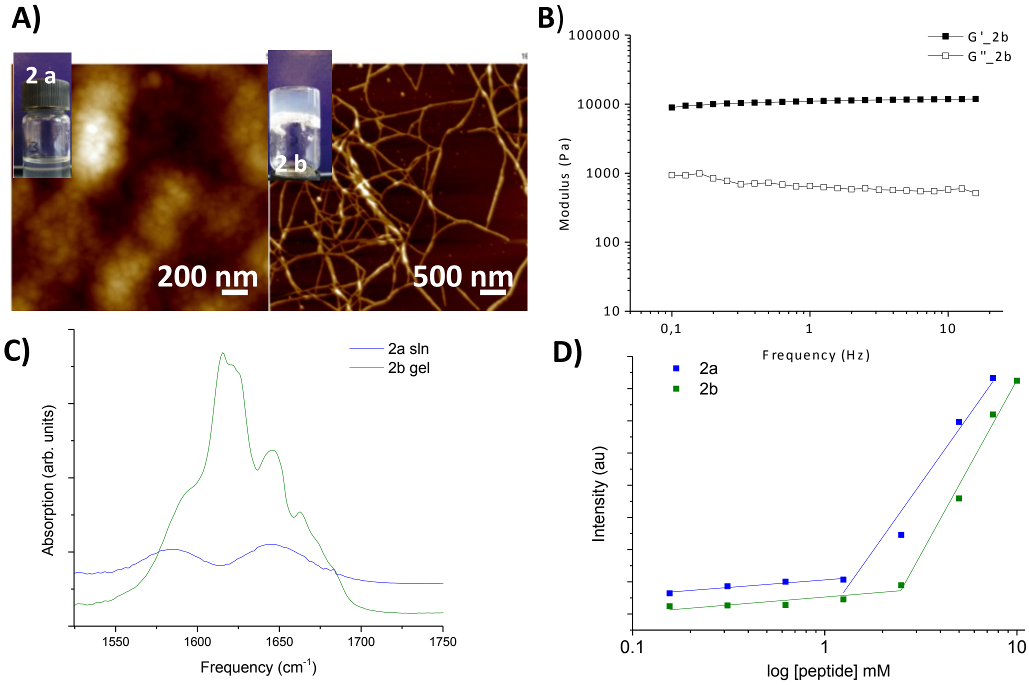

Figure 3.8. A) Atomic force microscopy (AFM) showing the micellar aggregates (solution) for **2a** and fibres (hydrogels – 20 mM) for **2b**. B) Rheology data for **2b** gel showing the plot of G' (elastic modulus) and G'' (viscous modulus) against frequency. C) FTIR absorption spectrum in the amide I region (in D_2O at pH 7): **2a** (solution) and **2b** (gel). D) Critical aggregation concentration (CAC) of 1.4 mM (**2a)** and 2.5 mM (**2b)**.

Furthermore, DLS experiments (autocorrelation functions in figure 3.9; size distributions in figure 3.10; sizes (R_H) in nm in table 3.1) were performed for peptide solution samples **1a, 1b, 2a** and **2b** at various concentrations ranging from 0.625 mM to 5 mM to find the best concentration range for data analysis. From the autocorrelation functions in figure 3.9, observing the different decay rates, can be seen that peptide solutions **1a** and **1b** show stable size in the concentration range of 0.625-2.5 mM while the size of the aggregates further increases at concentrations of ≥ 5 mM. Peptide **2a** shows stable sizes over the range of concentrations examined while peptide **2b** shows big aggregates (slower decay rate) with variable size at concentrations higher than 0.625 mM. Therefore, diffusion coefficients for all peptide solutions are presented for samples at 0.625 mM and the corresponding R_H values were calculated. Although the R_H approximation is referred to spherical particles and not applicable to fibres, these data are shown for comparison, in order to see the difference between micellar aggregates and fibres (Table 3.1).

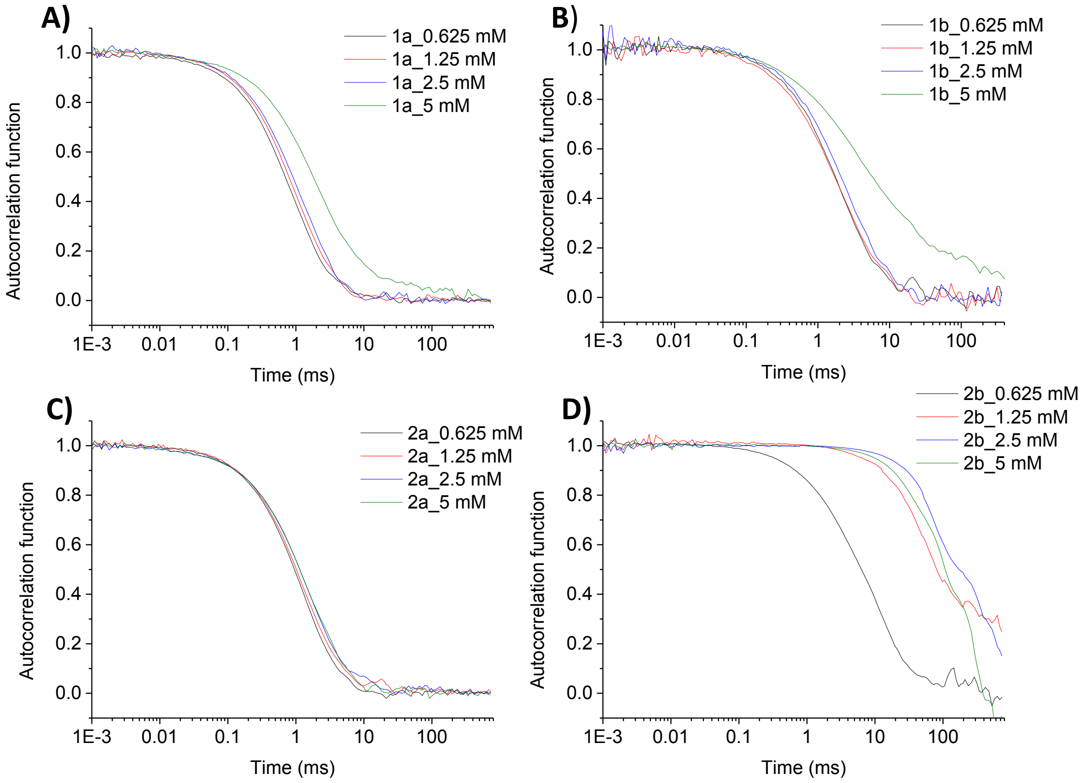

Figure 3.9. Autocorrelation functions of peptide solutions at different concentrations: A) **1a**, B) **1b**, C) **2a** and D) **2b** showing the behaviour of each peptide at varying concentrations.

Table 3.1. R_H values for peptide solutions of **1a**, **1b**, **2a** and **2b** at various concentrations.

Peptide	**1a**		**1b**		**2a**		**2b**	
Concentration (mM)	R_H (nm)	sd	R_H (nm)	sd	R_H (nm)	sd	R_H (nm)	sd
5	328	26	639	48	239	4	38.4x10^3	4.1x10^3
2.5	205	18	392	52	234	13	38.6x10^3	32.8x10^3
1.25	167	5	307	28	233	12	13.2x10^3	2.8x10^3
0.625	165	3	358	17	241	24	968	41

The diffusion coefficients (D) of samples **1a** (micellar aggregates) and **1b** (fibres) at 0.625 mM are 1.5x10^{-12} m^{2}s^{-1} and 6.8x10^{-13} m^{2}s^{-1} corresponding to R_H values of 165 nm and 358 nm, respectively (Fig. 3.10 A and C). The diffusion coefficients (D) of samples **2a** (micellar aggregates) and **2b** (fibres) at 0.625 mM are 1.13×10^{-12} and 2.5×10^{-13} m^2s^{-1} corresponding to R_H values of 241 nm and 968 nm, respectively (Fig. 3.10 B and C). Both peptides (**1a** and **2a**) show faster decay rates, thus smaller size for micellar aggregates compared to fibres (**1b** and **2b**). The higher values of R_H compared to AFM (dry samples) indicate that in the solution state the aggregates are bigger than the collapsed, dried ones.

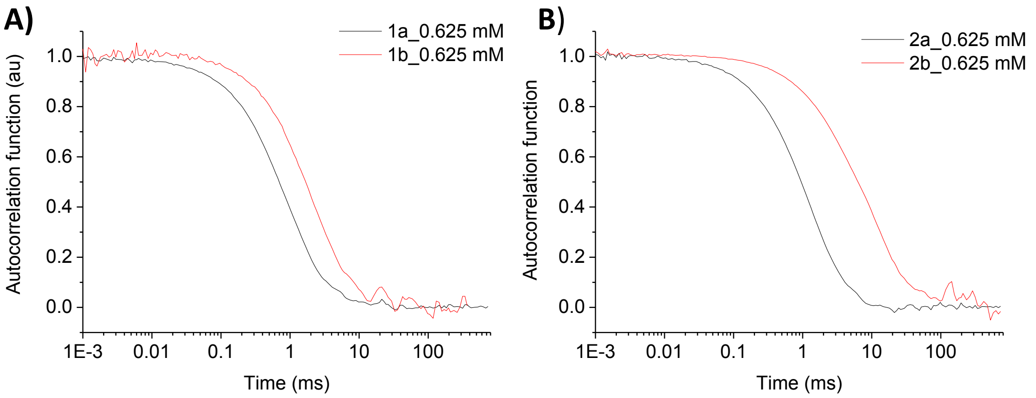

C)

Peptide	**1a**	**1b**	**2a**	**2b**
D (m^2s^{-1})	1.5×10^{-12}	6.8×10^{-13}	1.13×10^{-12}	2.5×10^{-13}
R_h (nm)	165	358	241	968

Figure 3.10. A) Autocorrelation functions of peptides **1a** and **1b** and B) **2a** and **2b** at the concentration of 0.625 mM indicating a difference in decay rates for micellar aggregates and fibres.

In order to further investigate the self-assembly behaviour of peptide amphiphiles the critical aggregation concentration (CAC) in water was determined by using the fluorescence intensity of the 8-anilino-1-naphthalenesulphonic acid (ANS probe) as a function of the peptide concentration (Fig. 3.7 D and 3.8 D). Varying concentrations (5 mM, 2.5 mM, 1.25 mM, 0.625 mM, 0.312 mM, 0.156 mM and 0.078 mM) of each peptide were used after a series of dilutions was made from a 10 mM peptide stock solution. 1 µL of the ANS stock solution (0.01 M in methanol) was added to 1 mL aqueous solution of peptides to reach the final probe concentration of 1×10^{-5} M and the fluorescence emission measured immediately after mixing. The ANS fluorescence was monitored at room temperature using an excitation wavelength of 360 nm and fluorescence emission recorded over a range of

370 nm to 700 nm. The CAC calculation method was adapted from literature.[175] CAC was calculated by plotting the intensity of ANS at the emission maximum against the log of peptide concentration. The two trendline equations from each graph were set as equal and from there the value of *x* at the turning point, corresponding to the log concentration, was calculated. By solving 10^x the CAC in mM was obtained.

The determined CAC values were 1.3 mM for PhAc-FFAGLDD, 2.9 mM for PhAc-FFAG, 1.4 mM for GFFLGLDD and 2.5 mM for GFFLG. The fluorescence emission spectra for the four peptides containing ANS are presented in the figure 3.11. In order to determine CAC the emission maximum (450 nm for **1a** and **1b,** and 470 nm for **2a** and **2b)** was plotted over varying peptide concentrations. The two distinct peaks in the fluorescent emission spectra indicate the distribution of the probe in two different environments: hydrophobic core of micelles (450-470 nm) and hydrophilic solvent- water (525-550 nm). It can be noted that the CAC values for the peptides show different values, and in particular longer peptides (**1a** and **1a**) show lower CAC values than their shorter counterparts (**2a** and **2b**). As these molecules have different peptide lengths as well as different compositions and aggregation modes it is not straightforward to directly compare them in terms of CAC as different non-covalent interactions are involved (hydrophobic, H-bonding, electrostatic and Van der Waals). The cumulative effect of these interactions influences the aggregation.

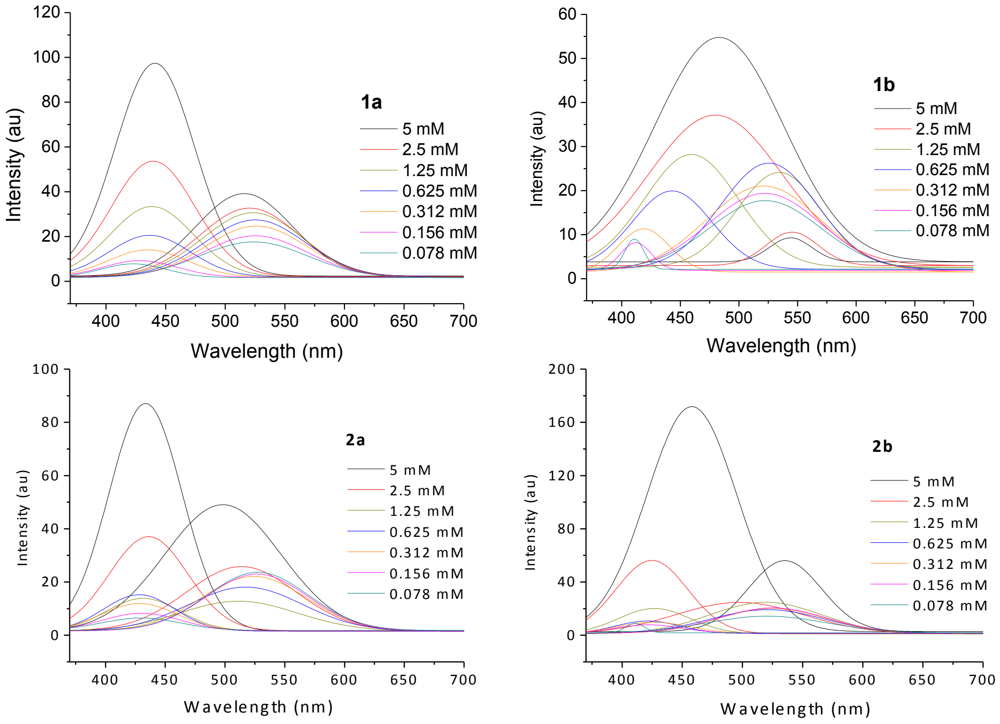

Figure 3.11. A) Fluorescence intensities of the ANS probe for different concentrations of each peptide: **1a**, **1b, 2a** and **2b** (λ_{ex} = 360 nm).

Furthermore, the critical micelle concentration (CMC) for **1a** and **2a** was determined by using pyrene as fluorescent probe. Varying concentrations (5 mM, 2.5 mM, 1.25 mM, 0.625 mM, 0.312 mM, 0.156 mM and 0.078 mM) of each peptide were used. A diluted pyrene solution was added to each of the seven different concentrations of peptide solutions to reach the final probe concentration of 6.25 x 10^{-6} M. These samples were then excited at 338 nm and fluorescence emission was monitored over a range of 360 nm to 410 nm. The ratio of the fluorescence intensity of the first (λ_{em}=372 nm) and the third peak (λ_{em}=384 nm) was plotted as a function of the peptide concentration (Fig. 3.12). The value calculated to be 1.25 mM for both peptides is in the same range of the CAC values for **1a** and **2a**.

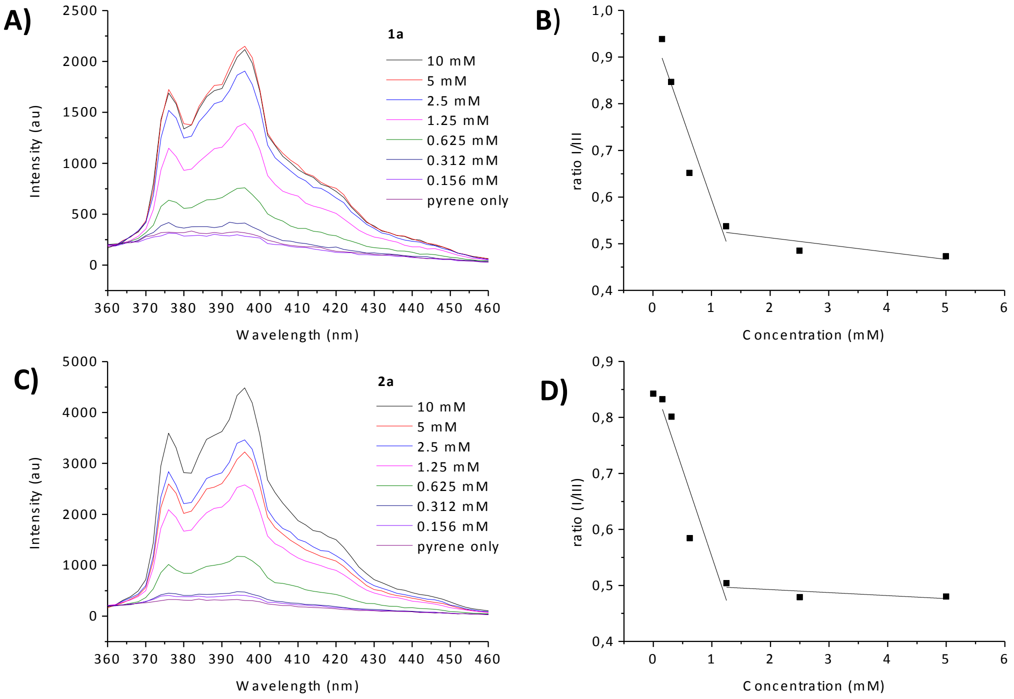

Figure 3.12. A) and C) Fluorescence intensities of pyrene for different concentrations of **1a** and **2a** (λ_{ex} = 295 nm) respectively. B) and D) The ratio of the first (λ_{em}=372 nm) and the third peak (λ_{em}=384 nm) in the emission spectra of pyrene plotted against peptide concentration for peptide surfactants **1a** and **2a** respectively.

3.4.2 Enzymatic hydrolysis to trigger micelle to fibre transition

After the designed peptides **1a**, **1b**, **2a** and **2b** showed to be successful in controlling the morphology of the supramolecular aggregates based on the peptide length i.e. hydrophobicity, the enzyme triggered micelle to fibre transition for **1a** and **2a** peptide amphiphiles was explored (Fig. 3.13). **1a** and **2a** were treated with 50 ng/mL MMP-9 for 96 h. The enzyme concentration was chosen based on examples found in literature.[172] In addition, the selected concentration is in range of the MMP-9 concentration secreted by cancer cells.[176]

The conversion and product identification was assessed by HPLC and LCMS while the morphological change was monitored by AFM, where fibre formation was observed (Fig. 3.18 B and 3.19 B).

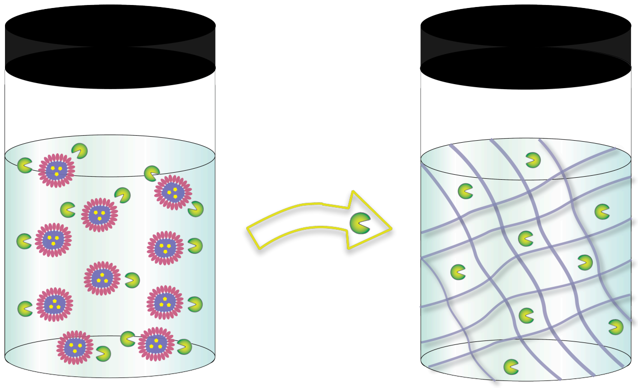

Figure 3.13. Schematic representation of enzyme triggered micelle to fibre transition.

Peptide **1a** (Fig. 3.14 A) showed complete conversion after 96 h to PheAc-FFAGL (**1c**) and DD fragments indicating the shift of the MMP-9 specificity for this heptapeptide to GL↓D instead of the expected G↓L. This is in accordance with reported observations that cleavage sites of heptapeptides catalysed by MMP-9 differ from those of longer peptide sequences or proteins.[120] According to MEROPS leucine and aspartic acid are tolerated in P1 and P1' positions respectively, but they do not seem to be preferentially recognised and reported as a cleavage site for MMP-9. The DD fragment is not shown in the HPLC chromatograms as it washed out from the column quickly, most likely with the solvent peak, due to its high hydrophilicity but also lacks a good chromophore.

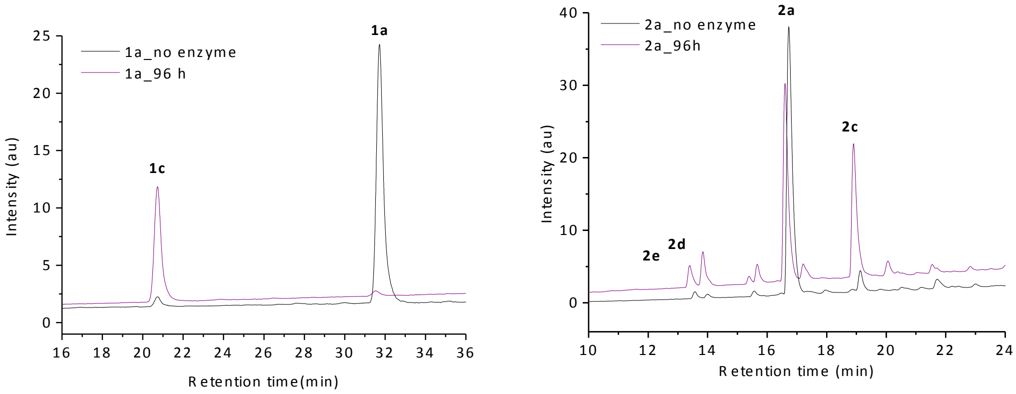

Figure 3.14. A) HPLC chromatogram showing complete conversion of **1a** (PhAc-FFAGLDD) to **1c** (PhAc-FFAGL) after 96 h MMP-9 treatment. B) HPLC chromatogram showing that the digestion of **2a** leads to a formation of different fragments being: **2c** (GFFLGL), **2d** (GFF) and **2e** (FLGLDD). A more detailed HPLC monitoring showing all time points examined is below in the following text (Figures 3.17 and 3.18). The wavelength for all the chromatograms was 254 nm.

More in detail, PhAc-FFAGLDD was converted to PhAc-FFAGL after 96 h (Fig. 3.15): HPLC (30-50% Solvent B, retention time of product = 21.6 min). MALDI (mass calculated: $[M+H]^+ = 671.39$, mass observed: $[M+Na]^+ = 694.38$).

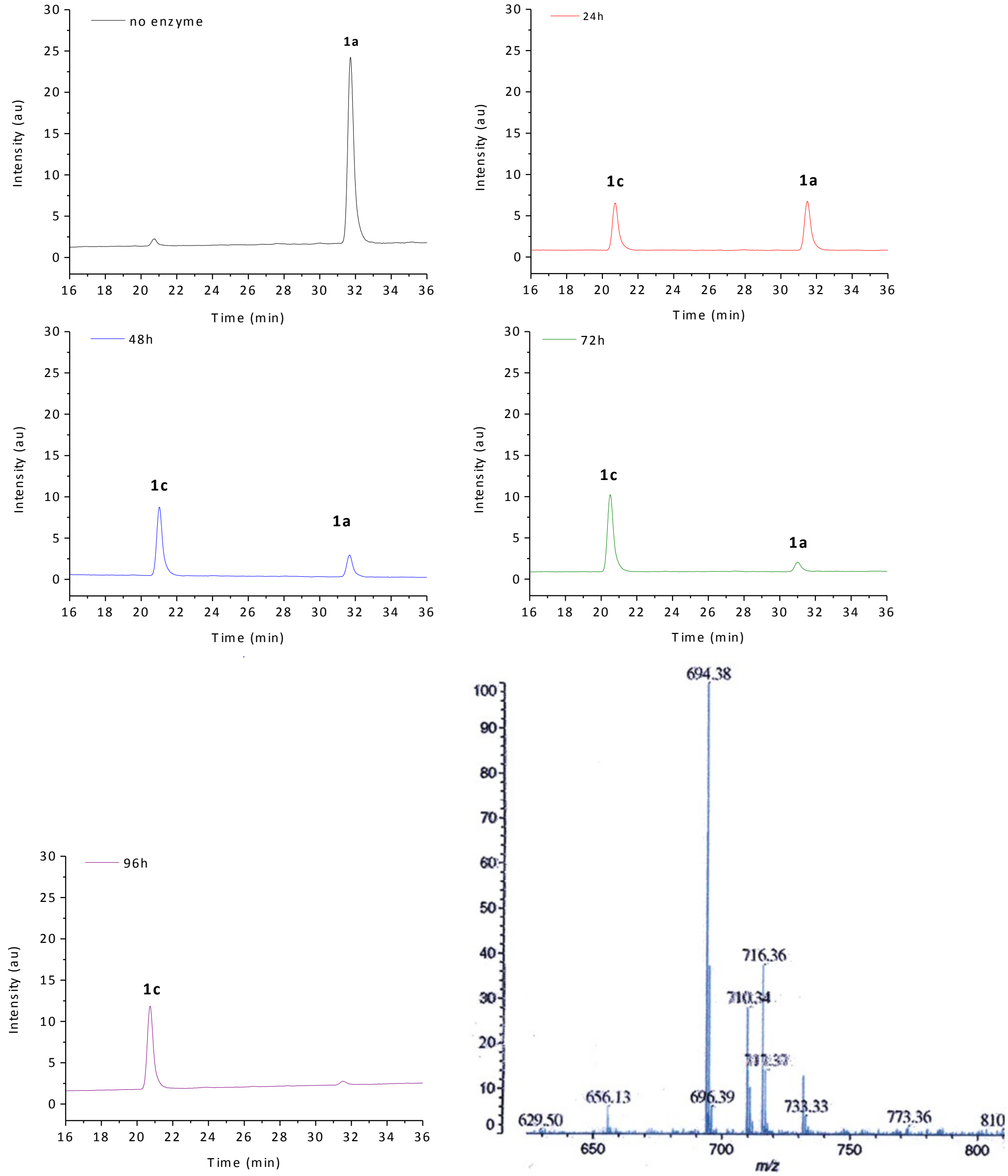

Figure 3.15. HPLC chromatograms showing the MMP-9 induced digestion of **1a** monitored over 96 h. Product formation at different time points is showed: time 0 (no enzyme), 24 h, 48 h, 72 h and 96 h. The chromatograms show slow conversion to PhAc-FFLGL (**1c**) being the only product (the DD fragment is too hydrophilic to be detected with the gradient and column used). At the end is added the MALDI spectra recorded after enzyme treatment, showing the sodium adduct of **1c** detected.

Peptide **2a** shows conversion to different products, the main one being GFFLGL (**2c**), corresponding to the fragment that is one residue longer than the expected product, as observed with **1a**, indicating a shift in MMP-9 specificity (Fig. 3.14 B). Other products formed, but in lower quantities are: the GFF (**2d**) + LGLDD (not detected at 254 nm due to lack of chromophore) fragments and GF + FLGLDD (**2e**). As the conversion was not complete after 96 h, the hydrolysis of this peptide was studied for 120 h showing further breakage of the substrate but possibly also of the products i.e. GFFLGL is digested to GF + FLGL (**2f**). This shows some residual cleavage by MMP-9 at the F↓L and F↓F bonds. A similar behaviour was previously reported where F↓C bond was cleaved.[127]

More in detail, GFFLGLDD is converted to 3 main products after 96 h (Fig. 3.16 and 3.17):

a) GFFLGL (**2c**): HPLC (20-80% Solvent B, retention time = 18.9 min). LCMS: LC (5-100% Solvent D, retention time = 10.3 min), MS (mass calculated: $[M-H]^-$= 651.36, mass observed: $[M-H]^-$ = 651.3)
b) GFF (**2d**): HPLC (20-80% Solvent B, retention time = 14.1 min). LCMS: LC (5-100% Solvent D, retention time = 8.6 min), MS (mass calculated: $[M-H]^-$= 368.17, mass observed: $[M-H]^-$ = 368.1)
c) FLGLDD (**2e**): HPLC (20-80% Solvent B, retention time = 13.7 min). LCMS: LC (5-100% Solvent D, retention time = 8.5 min), MS (mass calculated: $[M+H]^+$= 679.32, mass observed: $[M+H]^+$ = 679.3)

After 120 h further fragmentation of the substrate is observed, but also the digestion of the GFFLGL product (**2c**) into GF and

d) FLGL (**2f**): HPLC (20-80% Solvent B, retention time = 17.2 min). LCMS: LC (5-100% Solvent D, retention time = 9.3 min), MS (mass calculated: $[M-H]^-$ = 447.27, mass observed: $[M-H]^-$ = 447.1)

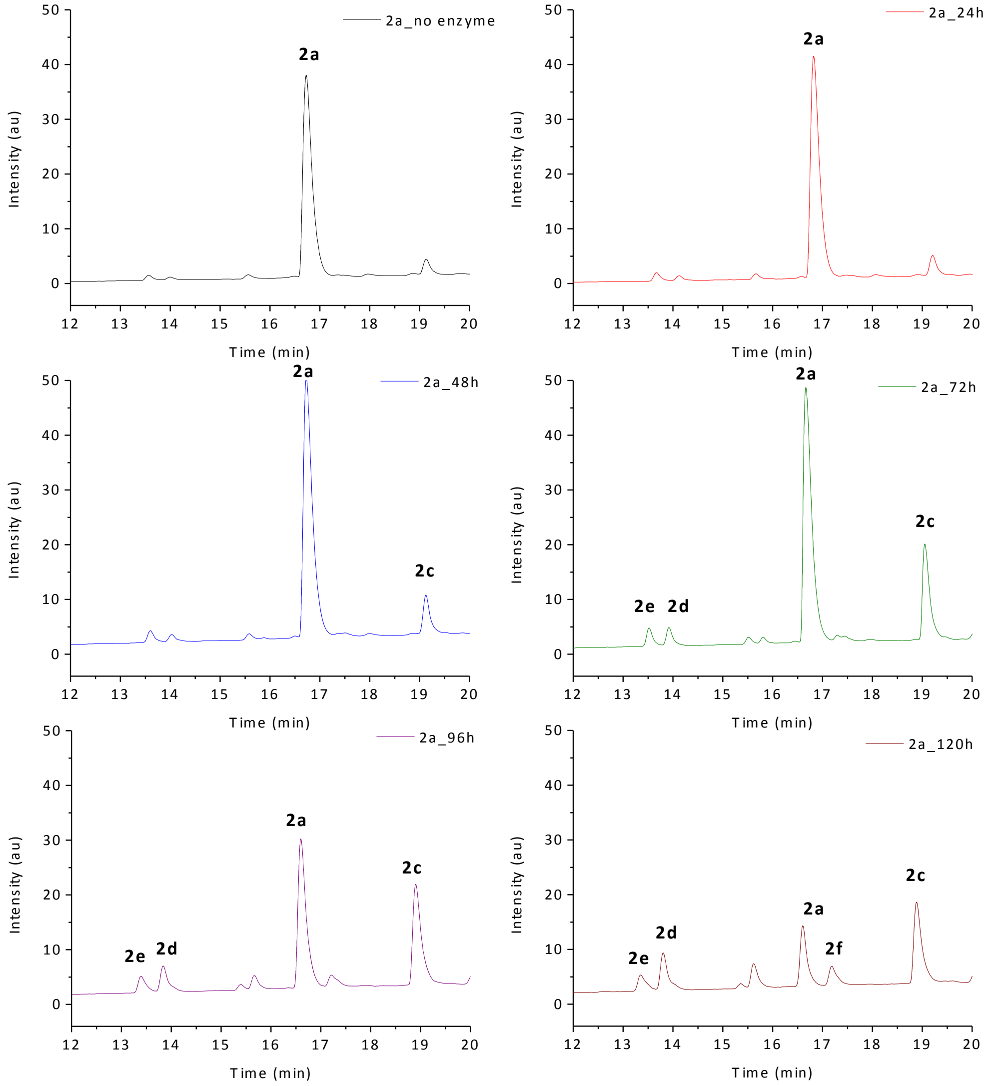

Figure 3.16. HPLC chromatograms showing the MMP-9 induced digestion of **2a** monitored over 120 h. Product formation at different time points is showed: time 0 (no enzyme), 24 h, 48 h, 72 h, 96 h and 120 h.

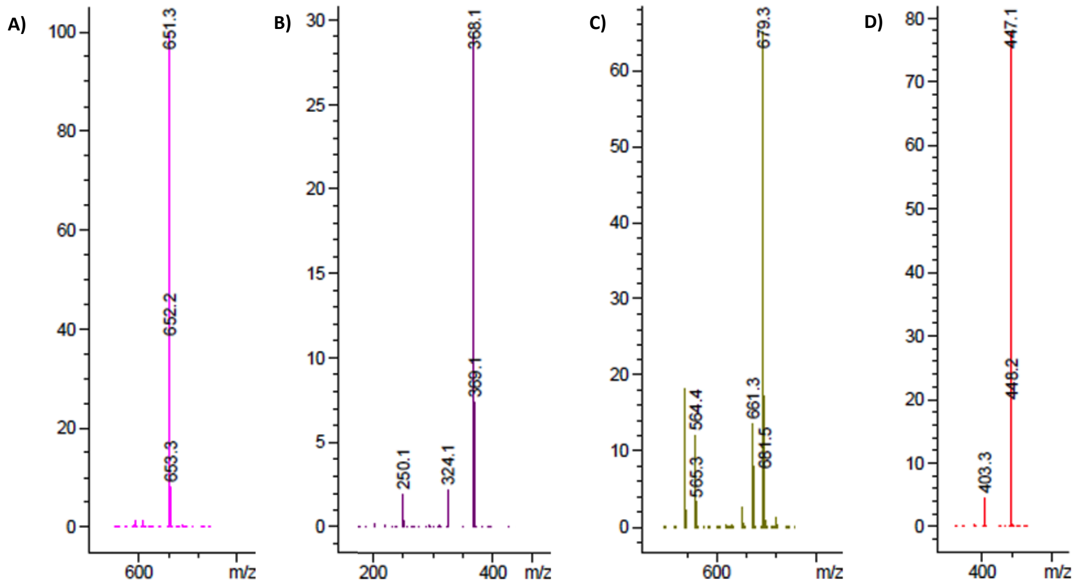

Figure 3.17. Fragments of MS spectra showing the detected: A) the negative ion of **2c**; B) the negative ion of **2d**; C) the positive ion of **2e**; and D) the negative ion of **2f**.

As formation of fibres was observed by AFM and TEM for both **1c** and **2c** (*vide infra*), it is clear that the pentapeptidic and hexapeptidic residues, respectively are able to self-assemble into fibres due to the removal of the DD unit (Fig. 3.18 B+C and 3.19 B+C). According to MEROPS, phenylalanine is well tolerated in both P1 and P1' positions, while leucine is preferred in P1', in agreement with the observed additional cleavage between F↓L and F↓F residues.

3.4.3 Enzyme triggered doxorubicin release/entrapment studies

Following this it was investigated whether the micelles were capable of performing as mobile vehicles for drug encapsulation to immobilised fibre networks for release of hydrophobic drugs. For this purpose, the release of an anticancer drug, doxorubicin, was studied. Doxorubicin was solubilized in DMSO by sonication and a 1 mM stock solution was made and subsequently diluted into the suspension of peptide micelles (final concentration of doxorubicin: 5 μM). The samples were then sonicated to allow doxorubicin diffusion into the hydrophobic core of the micelles. After doxorubicin was loaded into the micelles, its release by passive diffusion was monitored over time by fluorescence microscopy. Fluorescence intensity of doxorubicin at 596 nm which corresponds to the maximum intensity (λ_{ex}=480 nm) was monitored over 96 h when incorporated into the **1a/2a** peptide systems. A control experiment with free doxorubicin (doxorubicin in water, no peptide present) shows a decrease in fluorescence intensity over time, probably due to aggregation. Due to poor solubility in water doxorubicin on its own is not reproducible but when incorporated into peptides, becomes more stable. The interaction of doxorubicin with the hydrophobic environment of **1c/2c** results in higher values of fluorescence intensity compared to free doxorubicin in water (doxorubicin emission in solvents of different polarity is shown in Fig. 3.30 (*vide infra*). For **1a** and **2a** doxorubicin fluorescence intensity drops slightly over 48 h suggesting that the doxorubicin is incorporated into micelles over that time period, followed by significant decrease after 72 h suggesting its release. When treated with MMP-9, there is a release of doxorubicin from micelles (significant drop in fluorescent intensity upon exposure to water) followed by entrapment into fibres (resulting in an increase in fluorescent intensity) (Fig. 3.18 A and 3.19 A). A similar discontinuous behaviour with a formation of a temporary environment was reported for a phosphatase responsive system.[177] Even if the release profile after 48 h is similar for the MMP-9 treated and untreated **1a/2a** the advantage of the presence of the enzyme is that a localised effect is obtained as the fibres are significantly less mobile that the micelles.

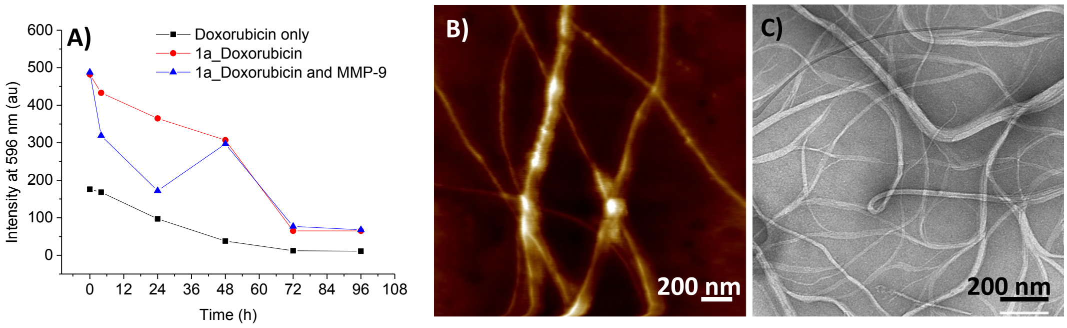

Figure 3.18. A) Fluorescence intensities of doxorubicin monitored over time for doxorubicin only, doxorubicin loaded into precursor peptide (**1a**) micelles and MMP-9 treated precursor peptide (**1a**) micelles loaded with doxorubicin. B) AFM images of MMP-9 induced fibre formation (PhAc-FFAGL) (**1c**) after 96 h C) TEM images of doxorubicin loaded samples treated with MMP-9 for 72 h showing that fibre formation was not disrupted by the presence of the drug. All experiments were carried out in PBS at pH 7.4

After fibre formation, the increase of fluorescence intensity suggests that the doxorubicin is entrapped in the fibres, which is further confirmed by the release studies performed on gels (Fig. 3.21) where a sustained release over time is observed (264 h). Furthermore, TEM images were obtained on enzyme treated doxorubicin loaded peptides that confirm fibre formation and show that the presence of doxorubicin did not disrupt fibre formation (Fig. 3.18 C and 3.19 C).

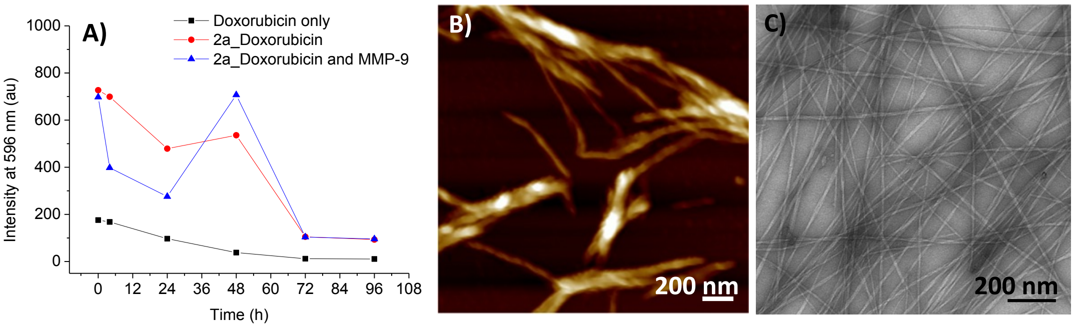

Figure 3.19. A) Fluorescence intensities of doxorubicin monitored over time for doxorubicin only, doxorubicin loaded into precursor peptide (**2a**) micelles and MMP-9 treated precursor peptide (**2a**) micelles loaded with doxorubicin. B) AFM images of MMP-9 induced fibre formation (GFFAGL) (**2c**) after 96 h C) TEM images of doxorubicin loaded samples treated with MMP-9 for 72 h showing that fibre formation was not disrupted by the presence of the drug. All experiments were carried out in PBS at pH 7.4

The changed hydrophobicity/philicity balance results in entrapment of the hydrophobic drug instead of release. In addition, the release studies conducted on gels show a constant release of doxorubicin over long time periods (264 h) confirming the possibility of the system to temporarily retain the payload followed by its prolonged release times after initial exposure (Fig. 3.21). For this purpose gels (**1b** and **2b**) were prepared by dissolving the peptide in water containing doxorubicin. After gelation, 1 mL of PBS was added on top of the gels to study the release of doxorubicin from the fibres (gel) into the added PBS by passive diffusion. 100 μL aliquots were taken at different time points: time zero (immediately upon addition), 30 min, 1h, 2h, 3h, 4h and subsequently every 24 h. After all 10 aliquots (100 μL each) of PBS containing doxorubicin have been taken, a new 1 mL of PBS wad added on top of the gels and aliquots taken every 24 h (Fig 3.20). Each aliquot was then diluted in 900 µL of DI water prior the fluorescence measurement was taken.

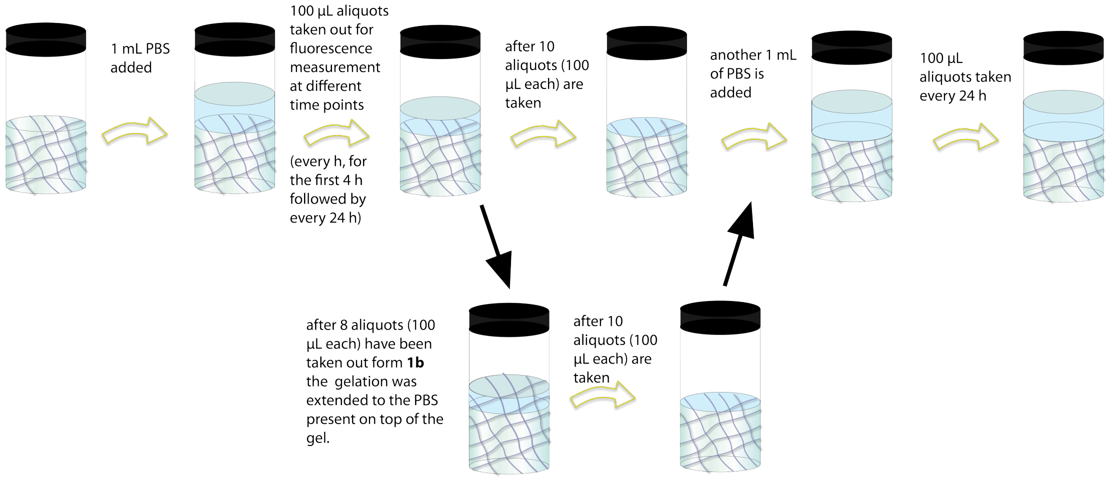

Figure 3.20. Schematic representation of the release experiment performed on **1b** and **2b** gels.

The results indicate that doxorubicin is entrapped in the fibres and slowly released over time from the gels. However, a rapid increase of fluorescence intensity is observed for **1b** gel system after 48 h due to the fact that the gelation was extended to the added PBS. What was measured for 72 h and 96 h time points was doxorubicin containing gel diluted in DI water, which explains the high fluorescence intensities.

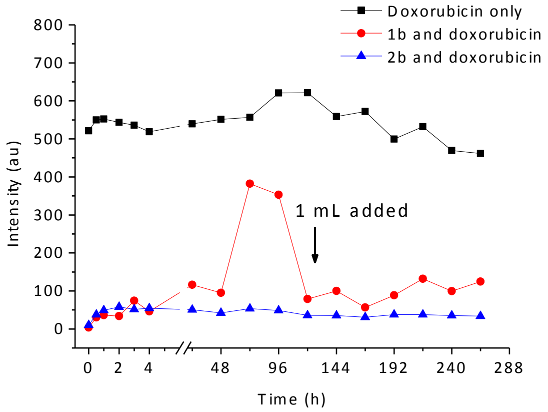

Figure 3.21. Doxorubicin release after addition of 1 mL of PBS monitored over 96 h, followed by the addition (after 96 h) of another 1 mL of PBS on top of the gel and monitored for 264 h in total.

The results obtained from the release experiments confirm that fibre formation (gelation) results in the formation of local depots of doxorubicin from where doxorubicin can be released constantly over longer time periods (e.g. 264 h). However, this is only an indicative study because when fibre formation is triggered by enzymes, gelation is not expected as the peptide concentrations used are below the critical gelation concentration. Nevertheless, with this experiment is confirmed the expected behaviour of doxorubicin prolonged release from peptide gels.

3.4.4 Further investigations of doxorubicin physical entrapment

Confocal microscopy studies were conducted in wet (PBS) environment with the purpose to observe morphological changes of peptide carriers during the MMP-9 treatment. This was done to develop a method for doxorubicin loaded fibre visualisation around cancer cells (See Chapter 4). A systemic study was performed monitoring the effect of peptide concentration of 2.5 mM, 1.25 mM, 0.625 mM and 0.312 mM on structural changes of peptide assemblies loaded with doxorubicin during confocal imaging. In addition, fluorescence spectroscopy was used to monitor the effect of peptide concentration on doxorubicin entrapment for these four different concentrations.

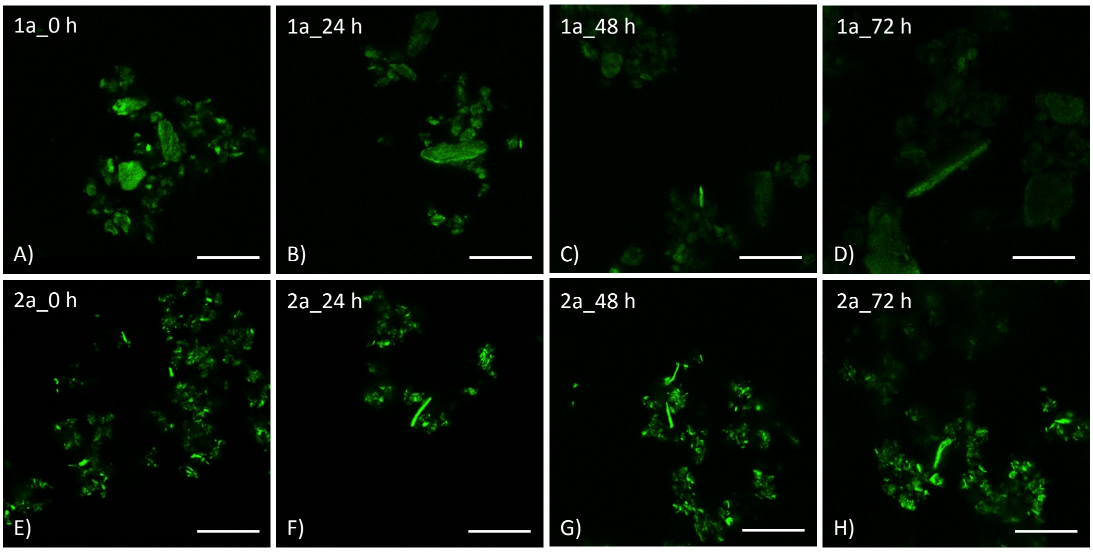

Figure 3.22. Confocal images (scale bars: 50 μm): showing doxorubicin loaded into micellar aggregates (**1a**/**2a** - starting material at the concentration of 2.5 mM) followed by 24 h, 48 h and 72 h images of the **1a** and **2a** treated by MMP-9.

Both peptides **1a** and **2a** (over the mentioned range of concentrations) were treated with MMP-9 for 72 h and the results are shown for 2.5 mM (Fig. 3.22), 1.25 mM (Fig. 3.23), 0.625 mM (Fig. 3.24) and 0.312 mM (Fig. 3.25). Samples were prepared as described in section 3.4.3. Briefly, peptide solutions of various concentrations were prepared. Micelles are expected to form when the peptide concentration is above the CMC. Doxorubicin (1 mM stock solution in DMSO) was then diluted in the suspension of peptide micelles to a final concentration of 5 µM. Subsequently the samples were sonicated to allow the diffusion of doxorubicin into the hydrophobic core of the micelles. After sonication, 100 µL aliquots of each peptide concentration (micelles loaded with doxorubicin) mentioned above (for **1a** and **2a**) were transferred to a glass bottom 96-well plate. MMP-9 (final concentration: 50 ng/mL) was added to peptide solutions of various concentrations and the 96-well plate was incubated at 37°C. Every 24 h confocal images were taken by imaging single wells of the well plate.

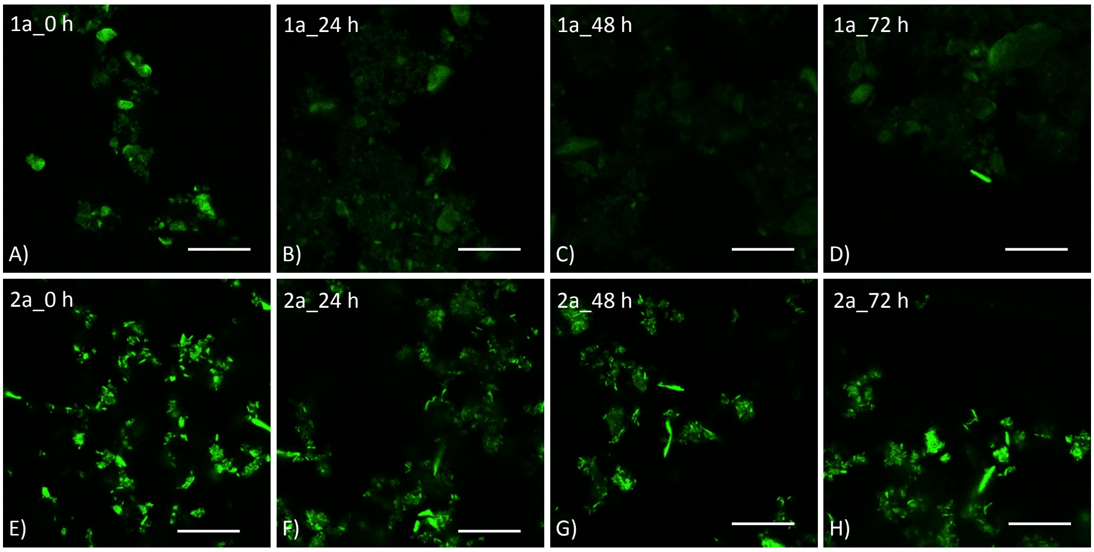

Figure 3.23. Confocal microscopy images of **1a** and **2a** at the concentration of 1.25 mM treated with MMP-9 captured at A) and E) time zero (no enzyme); B) and F) 24 h; C) and G) 48 h; D) and H) 72 h. Scale bars: 50 µm.

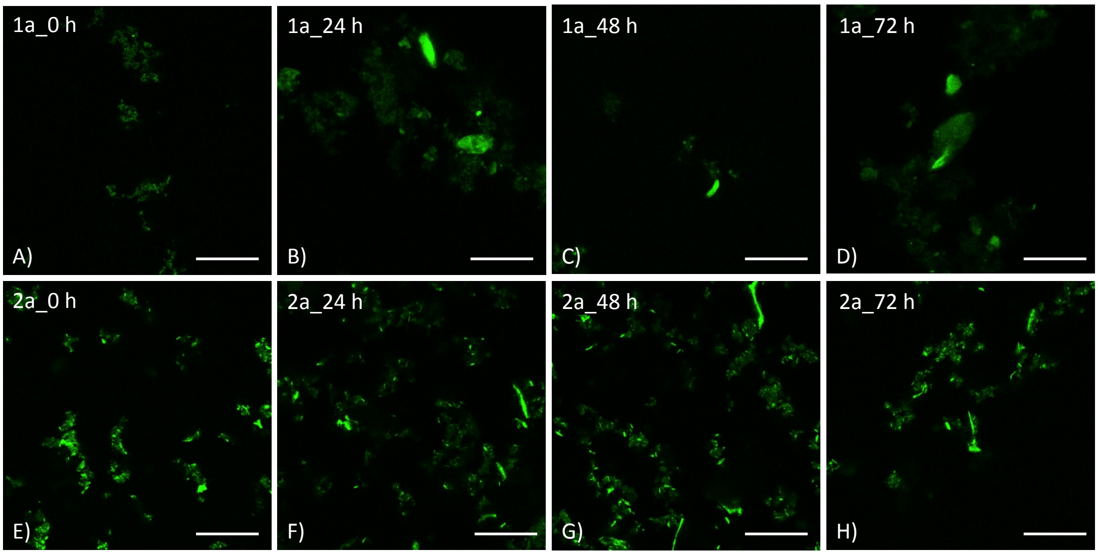

Figure 3.24. Confocal microscopy images of **1a** and **2a** at the concentration of 0.625 mM treated with MMP-9 captured at A) and E) time zero (no enzyme); B) and F) 24 h; C) and G) 48 h; D) and H) 72 h. Scale bars: 50 μm.

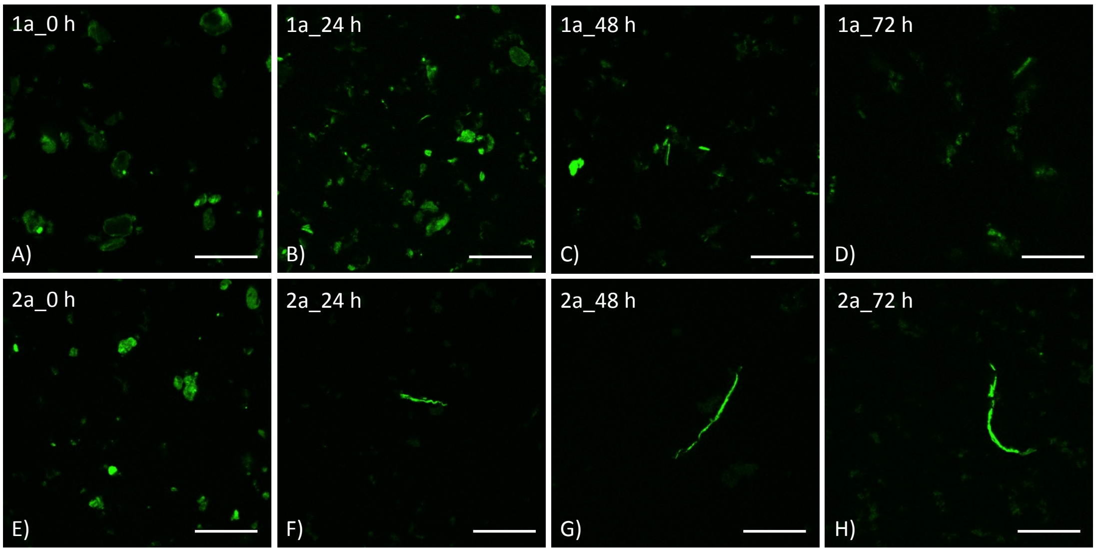

Figure 3.25. Confocal microscopy images of **1a** and **2a** at the concentration of 0.312 mM treated with MMP-9 captured at A) and E) time zero (no enzyme); B) and F) 24 h, C) and G) 48 h; D) and H) 72 h. Scale bars: 50 μm.

This technique did not prove to be successful for monitoring micelle to fibre morphology transition because the size of the fibres is in the nanometer range therefore is difficult to observe single fibres due to resolution limits. Loading the peptides with doxorubicin allows the visualisation of bigger aggregates and it confirms that structures form and that the doxorubicin is retained inside them. Even though is not possible to observe a clear morphological change over 72 h using confocal microscopy, it is still possible to observe doxorubicin fluorescence signal, meaning that the drug is retained within the structures formed. Compared to the control experiments with doxorubicin in water, without peptide carriers and in the presence of MMP-9 where no doxorubicin signal (fluorescence intensity) is observed during the time period of 72 h (Fig. 3.26), confocal images show that the loaded peptides have the ability to retain the payload. It should be noted that during confocal imaging different regions of the sample were imaged. Therefore, the observed features may have different fluorescence intensities. In addition, release of doxorubicin is expected from both micelles and fibres suggesting lower fluorescence intensity after 48 h. In particular, this is observed for **1a**, suggesting that **2a** is able to retain the payload for longer time periods. Therefore, **2a** might be a more promising candidate for the future experiments *in vivo*.

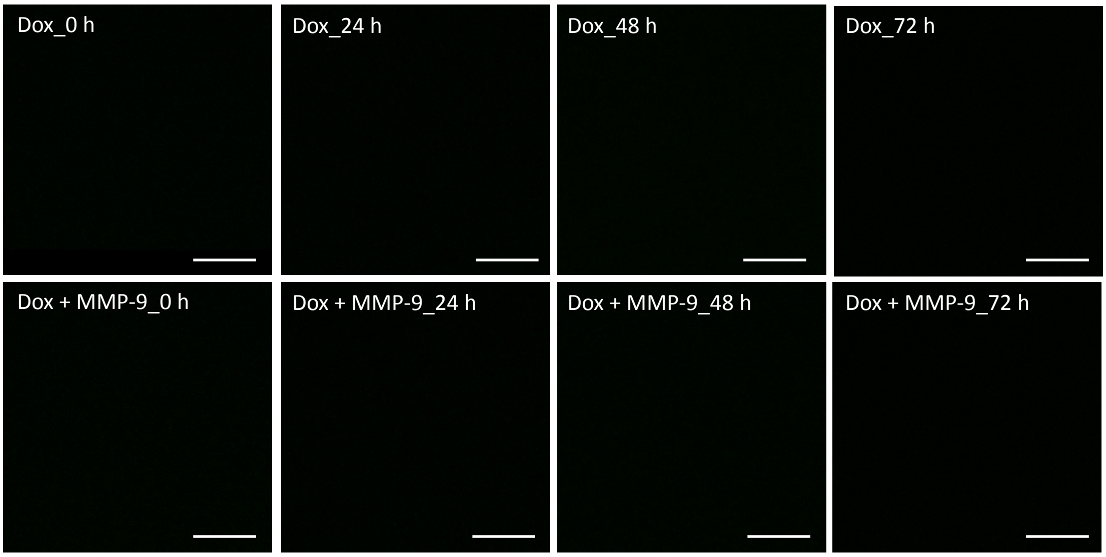

Figure 3.26. Confocal microscopy images of doxorubicin and doxorubicin in the presence of MMP-9 at different time points: time zero, 24 h, 48 h and 72 h. Scale bars: 50 μm.

When confocal imaging was performed on dry samples (Fig. 3.27) fibrillar networks were observed for both peptides (**1a** and **2a**) after enzyme treatment. For this purpose, samples were left to dry out and confocal imaging was performed on two representative samples, with the best two images presented here.

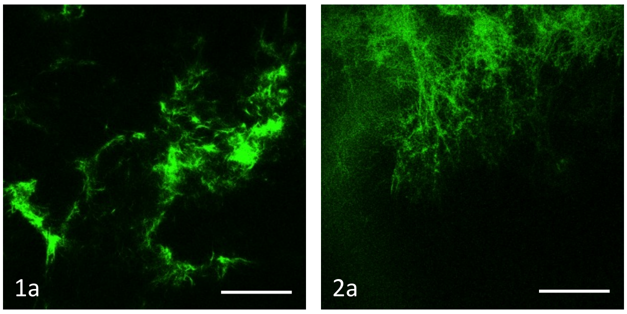

Figure 3.27. Confocal images of dried samples **1a** and **2a** treated with MMP-9 for 96 h and 24 h respectively. Scale bars: 50 μm.

Fluorescence spectroscopy was used in addition to confocal imaging to study the behaviour of doxorubicin in the presence of peptides. Fluorescence intensities for peptides at different concentrations were recorded for untreated and MMP-9 treated doxorubicin loaded micellar aggregates (Fig. 3.28 and 3.29). In addition, the study of doxorubicin in solvents with different polarities is shown to confirm that doxorubicin is loaded into peptides. A decrease in solvent polarity resulted in an increase in fluorescence intensity (Fig. 3.30). This result is in agreement with the fluorescence results obtained for doxorubicin loaded into peptides. When doxorubicin is loaded into the micelles thus in more hydrophobic environment compared to water (free doxorubicin) the fluorescence intensity increases.

Plots showing the comparison in behaviour of MMP-9 treated micellar aggregates of **1a** and the untreated ones, for each concentration point are presented (Fig. 3.28).

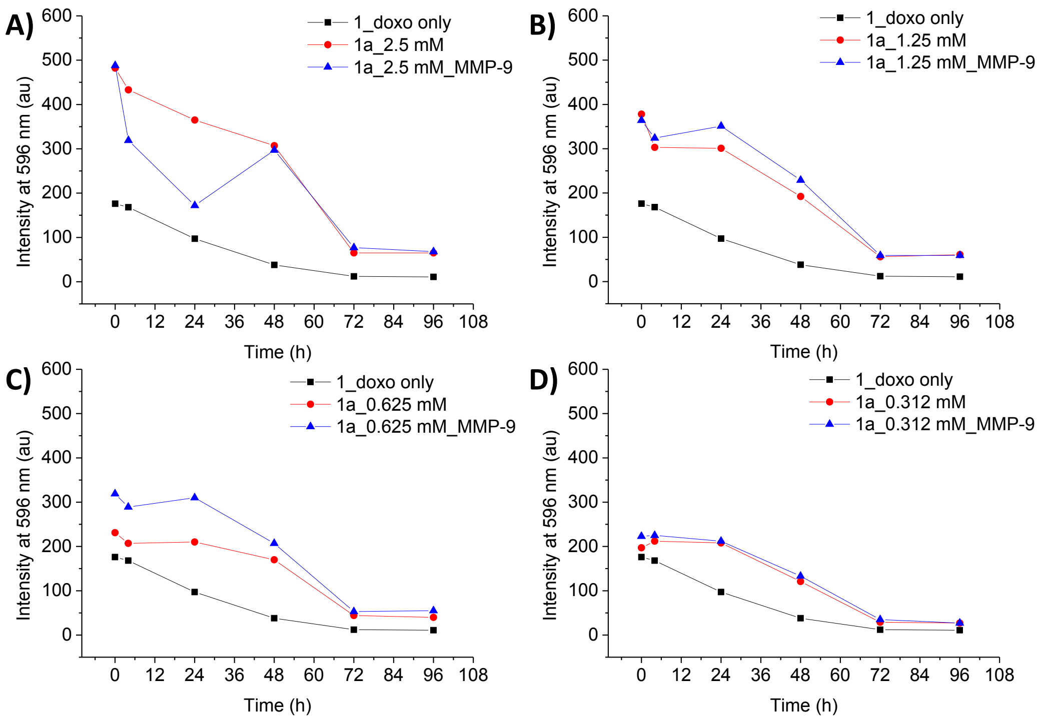

Figure 3.28. Fluorescent intensities of **1a** loaded with doxorubicin and MMP-9 treated **1a** loaded with doxorubicin compared to doxorubicin in water, for different concentrations of **1a** A) 2.5 mM, B) 1.25 mM, C) 0.625 mM and D) 0.312 mM.

Before enzyme treatment, fluorescent intensities of doxorubicin show a concentration dependent behaviour in the presence of **1a**. This can be seen for the point zero of each peptide concentration in figure 3.28 (fluorescent intensities of doxorubicin recorded are: 480 au in presence of **1a** at the concentration of 2.5 mM, 380 au for 1.25 mM, 230 au for 0.625 mM and 200 au for 0.312 mM of **1a**). Increasing concentration of peptide corresponds to an increased fluorescence intensity of doxorubicin. However, there is no linear correlation between peptide concentration and doxorubicin intensity. After addition of MMP-9 a discontinuous behaviour was recorded for **1a** at the concentration of 2.5 mM (above the CMC), as discussed in section 3.4.2 (for figures 3.18 and 3.19). This discontinuous behaviour was not observed for 1.25 mM, 0.625 mM and 0.312 mM of **1a** after MMP-9 treatment. According to expectations 1.25 mM sample was expected to show similar behaviour to **1a** at 2.5 mM, being this concentration the critical concentration for micelle formation. The 0.625 mM and 0.312 mM concentrations were used as a control as the micelle to fibre transition was not expected to occur. However, the

CMC is a bulk property of materials and some localized points of aggregation are still expected to be found in solution, as confirmed by confocal microscopy. Therefore, the confocal images show aggregation points even below the expected aggregation concentration (Figures 3.24 and 3.25). From the fluorescence results shown in figure 3.28 it can be concluded that the best concentration to further study the micelle to fibre transition is at 2.5 mM.

Also, plots showing the comparison in behaviour of MMP-9 treated micellar aggregates of **2a** and the untreated ones, for each concentration point are presented (Fig 3.29). A similar behaviour described above for doxorubicin in the presence of **1a** is also observed for **2a**. Doxorubicin intensity is higher when the peptide concentration is higher (the recorder intensities for time zero are: 730 au for 2.5 mM, 770 au for 1.25 mM, 245 au for 0.625 mM and 220 au for 0.312 mM). The discontinuous behaviour upon addition of MMP-9 was observed only for 2.5 mM peptide (**2a**) concentration confirming that this is the optimal peptide concentration for further studies. Also in this case, points of localised aggregation can be visualised with confocal microscopy for concentrations below the CMC (Figures 3.24 and 3.25).

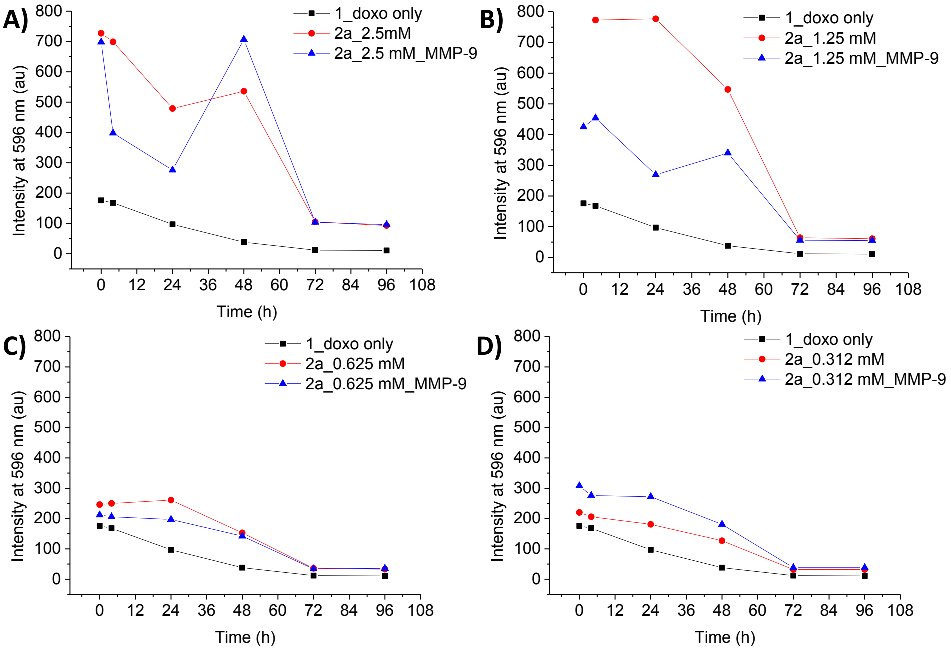

Figure 3.29. Fluorescent intensities of **2a** loaded with doxorubicin and MMP-9 treated **2a** loaded with doxorubicin compared to doxorubicin in water, for different concentrations of **2a**: A) 2.5 mM, B) 1.25 mM, C) 0.625 mM and D) 0.312 mM.

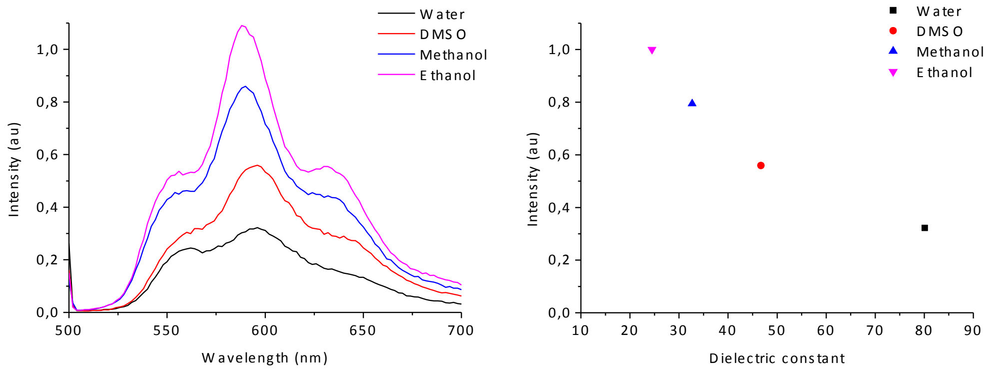

Figure 3.30. A) Fluorescent emission spectroscopy (normalized) of doxorubicin in solvents with different polarities (i.e. dielectric constant): ethanol, methanol, DMSO and water. B) Maximum doxorubicin emission intensity (596 nm) plotted against the dielectric constant of the examined solvents.

These results serve as a starting point towards method development for fibre visualisation around cancer cells where the MMP-9 is secreted by the cells and localized fibre formation expected. However, the examined peptides do not present any chromophores/fluorophores covalently incorporated in the structure, but only physically entrapped doxorubicin which makes it challenging to observe the morphology changes. A more specific tag, Thioflavin T that selectively binds to β-sheet regions and shows fluorescence signal only in the presence of fibres would need to be considered as part of future experiments. Attempts of fibre visualisation around cancer cells will be described in the next Chapter (Chapter 4).

A possible way to enhance resolution in future studies could be based on Stochastic Optical Reconstruction Microscopy (STORM). In a recent publication by Meijer and co-workers, this technique has been shown to be efficient in the visualisation of one-dimensional (1D) aggregates based on self-assembly.[178] However, in their example the fluorophores were covalently attached to the self-assembling monomer allowing better control over the visualisation process. Future work on our systems will consider STORM on physically entrapped doxorubicin in peptide nanofibres as a possible visualisation method that could guarantee a better resolution compared to the methods used so far (See Chapter 4).

3.5 Conclusions

In conclusion, new MMP-9 responsive peptide amphiphiles are shown here that self-assemble into spherical aggregates. Enzyme triggered micelle to fibre transition suggests that they are substrates of MMP-9 and are capable of encapsulation and controlled release of doxorubicin. These observations suggest their use as mobile carriers for the anticancer drug that in turn is expected to be selectively delivered to tumour tissues, where the peptides would assemble to form a localised fibre based depot by exploiting local MMP-9 overexpression and increased activity. Furthermore, the assembled fibres provide a new scaffold for prolonged drug delivery due to the partial entrapment of the drug and the intrinsic biodegradable nature of peptide carriers themselves.

These are very challenging systems to develop in terms of MMP-9 specificity where the substrate has to contain the right structural information to behave as a smart system able to undergo a morphological transition. Being based on simple and short peptide sequences MMP-9 is challenged to cleave efficiently the substrate at the expected cleavage site G↓L being well known for longer substrates and/or proteins. However, the ability to reorganize from a micellar to a fibrillar supramolecular structure and its application is drug delivery is a new concept not addressed before. Mainly, drug vehicles based on supramolecular assemblies are prodrug based or designed to disassemble and degrade in the presence of the enzyme in order to release the loaded drug. Creating localised depots of anticancer drugs around cancer cells can be beneficial for the development of anticancer therapy. In order to prove the feasibility of the system to treat cancer states and its ability to function *in vitro* and *in vivo* further examination and mechanism clarification is needed. Thus, we set out to apply what we learned here to cells and finally to animal models. When used *in vivo* these systems may also respond to other MMPs and specifically to MMP-2 due to some overlapping in specificity profiles.

3.6 Materials and methods

3.6.1 Materials

All reagents were purchased from Sigma Aldrich and used without further purification unless differently stated. Peptide grade N,N-Dimethylformamide (DMF) was obtained by Rathburn chemicals. The preloaded Wang resins were purchased from Merck (Novabiochem). Monomeric MMP-9 proenzyme from human neutrophils (as a solution in 50mM TRIS, containing 200mM sodium chloride, 5mM calcium chloride, 1 μM zinc chloride, 0.05% Brij-35 and 0.05% sodium azide) and MMP-9 catalytic domain (as a solution in 50mM TRIS, containing 5mM calcium chloride, 300mM sodium chloride, 20μM zinc chloride, 0.5% Brij-35 and 30% glycerol, at pH 7.5) were acquired from Enzo Life Sciences.

3.6.2 High-performance liquid chromatography (HPLC)

HPLC analyses of peptides were performed using Dionex P680 HPLC system equipped with a Macherey-Nagel C18 column of 250 mm length, 4.6 mm internal diameter and 5 μm particle size equipped with UV-Vis detector. The gradient: (Solvent A: 0.1% TFA in water; Solvent B: 0.1% TFA in acetonitrile) 20-80% B was utilised, with each run lasting a total of 46 minutes using a flow rate of 1 mL min^{-1} and detection wavelengths set at 214 nm and 254 nm using the UV-Vis detector. For separation of peptides **1a** and **1b** a 30-50% B gradient was utilised with each run lasting a total of 70 minutes using a flow rate of 1 mL min^{-1} and detection wavelengths set at 214 nm and 254 nm using the UV-Vis detector.

3.6.3 Liquid chromatography-mass spectrometry (LC-MS)

LC-MS obtained at the University of Strathclyde Mass Spectrometry facility was used to confirm peptide molecular weights. All analyses were carried out on a reverse-phase 15 cm Kinetex C18, 150 x 4.6 mm, 5 micron column. The LC-MS instrument was an Agilent 1200 Series HPLC, coupled to an Agilent 6130 Dual source MS detector. The gradient: (Solvent C: 5 mM ammonium acetate in water;

Solvent D: 5 mM ammonium acetate in acetonitrile) 0-3 min 5% D, 3-17 min 5-100% D, 17-27 min 100% D, 27-33 min 100-5% D, and 33-36 min 5% D was used in all analyses; the flow rate was set at 1 mL min^{-1} and detection wavelengths at 214 nm. Mass detection was set to analyse in Scan mode with electrospray ionisation (MM-ES+APCI). For all peptides examined both positive and negative ions were detected but only one (positive or negative ion) is shown for peptide characterisation to avoid redundancy.

3.6.4 Atomic force microscopy (AFM)

AFM was performed using a Veeco diINNOVA Scanning Probe Microscope (VEECO/BRUKER). The samples were placed on a trimmed and freshly cleaved mica sheet (G250-2 Mica sheets 1" x 1" x 0.006"; Agar Scientific Ltd, Essex, UK) attached to an AFM support stub and left to air-dry overnight in a dust-free environment, prior to imaging. All the images were obtained in tapping mode. The resolution of the scans is 512 x 512 pixels. Typical scanning parameters are the following: tapping frequency 308 kHz, integral and proportional gains 0.3 and 0.5, respectively, set point 0.5–0.8 V and scanning speed 1.0 Hz. The images were analysed using NanoScope Analysis software Version 1.40.

Sample preparation

Micellar suspensions were prepared by dissolving the peptide amphiphiles in PBS and adjusting the pH at 7.4 followed by sonication (10 min). If too concentrated a 1:10 dilutions were performed in PBS before placing 10µL mica covered AFM supports.

Gels were prepared as described in section 3.6.12, at 20 mM peptide concentration and diluted 1:10 (if needed, 1:100) before imaging.

3.6.5 Transmission electron microscopy (TEM)

TEM imaging was performed at the University of Glasgow Electron Microscopy facility, using a LEO 912 energy filtering transmission electron microscope operating at 120kV fitted with 14 bit/2 K Proscan CCD camera. Carbon-coated copper grids (200 mesh) were glow discharged in air for 30 s. The support film was touched onto the gel surface for 3 s and blotted down using filter paper. Negative stain (20 ml, 1% aqueous methylamine vanadate obtained from Nanovan; Nanoprobes) was applied and the mixture blotted again using filter paper to remove excess. The dried specimens were then imaged.

3.6.6 Fluorescence studies

Fluorescence emission spectra for determination of critical aggregation concentration were measured on a Jasco FP-6500 spectrofluorometer. The CAC experimental setup is described more in detail in section 3.6.13. The ANS probe was excited at 360 nm and the data collected in the range between 370 and 700 nm. The excitation and emission bandwidths were both set to 5 nm. Fluorescence emission spectra for determination of critical micelle concentration were measured on an X Fluor Safire 2 fluorescence plate reader (version: V 4.62n) at the Beatson Cancer Research Institute (Glasgow). The CMC experimental setup is described more in detail in section 3.6.13. The pyrene probe was excited at 338 nm and the emission data were collected in the range between 360 to 410 nm. The emission wavelength step size was set to 2 nm and the excitation and emission bandwidths to 5 nm each. Fluorescence emission spectra for determination of doxorubicin release from micellar aggregates and after enzyme treatment was measured on an X Fluor Safire 2 fluorescence plate reader (version: V 4.62n) at the Beatson Cancer Research Institute (Glasgow). Doxorubicin was excited at 480 nm and the emission intensity at 596 nm was monitored over time. The doxorubicin release form **1b** and **2b** gels was monitored using Jasco FP-6500 spectrofluorometer using the same parameters mentioned above.

3.6.7 Confocal Microscopy

Samples were imaged in a liquid state using a Nikon A1 (Tokyo, Japan) or an Olympus FV1000 (Leica, Milton Keynes, UK) at the Beatson Cancer Research Institute (Glasgow). Identical exposure times and processing were used in all experiments. For doxorubicin visualization images were acquired using a 488 nm laser, 8 % laser power over a field of view of 200 by 200 μm.

3.6.8 Fourier Transform Infrared Spectroscopy (FTIR)

FTIR measurements were performed at the Department of Physics, University of Strathclyde. Spectra were recorded on a Bruker Vertex 70 spectrometer, averaging 25 scans per sample at a resolution of 1 cm^{-1}. Samples were sandwiched between two 2 mm CaF_2 windows separated with a 50 μm polytetrafluoroethylene (PTFE) spacer.

3.6.9 Dynamic Light Scattering (DLS)

DLS was performed at the Department of Chemical Engineering, University of Strathclyde. DLS measurements were carried out by using a ALV (ALV, GMBH, Germany) spectrophotometers using vertically polarized He-Ne laser light (25 mW with wavelength of 632.8 nm) with an avalanche photodiode detector. The DLS measurements were carried out at angle of 90° at 25 °C. Intensity autocorrelation functions were recorded and analysed by means of the cumulant method in order to determine the intensity weighted diffusion coefficients D and the average hydrodynamic radius R_H by using the Stokes-Einstein equation, $R_H = kBT/6\pi \eta D$, where kB is the Boltzmann constant, T is the absolute temperature and η is the solvent viscosity at the given temperature.

Autocorrelation functions were recorded for peptide solutions of **1a**, **1b, 2a** and **2b** at various concentrations (5 mM, 2.5 mM, 1.25 mM, 0.625 mM). Diffusion coefficients and the corresponding R_H values were calculated for peptide solutions at 0.625 mM. Furthermore cumulative method was used to plot size distributions and determine R_H for micellar aggregates and fibres. Although the R_H approximation is referred to spherical particles and not applicable to fibres, for comparison of size and in order to see the difference between the two systems the size distributions were plotted.

Sample preparation

Micellar suspensions (5 mM) were prepared by dissolving the peptide amphiphiles in PBS and adjusting the pH at 7.4 followed by sonication (10 min). A series of dilutions, in PBS, were made prior to DLS measurement.

Gels were prepared as described in section 3.6.12, at 20 mM peptide concentration and subsequently diluted, in PBS, to form 5 mM, 2.5 mM, 1.25mM, 0.625 mM peptide solutions.

3.6.10 Rheology

To assess the mechanical properties of the **1b** and **2b** hydrogels, dynamic frequency sweep experiments were carried out on a strain-controlled rheometer (Bohlin C-CVO) using a parallel-plate geometry (20 mm) with a 0.25 cm gap. The temperature of the sample stage was maintained at 25°C using an integrated temperature controller. To minimize solvent evaporation and to keep the sample hydrated a solvent trap was used and the atmosphere within was kept saturated. To ensure the measurements were made in the linear viscoelastic regime, an amplitude sweep was performed and the results showed no variation in elastic modulus (G') and viscous modulus (G'') up to a strain of 1%. The dynamic modulus of gels was measured as a frequency function, where the frequency sweeps were carried out between 0.1 and 10 Hz.

3.6.11 Solid phase peptide synthesis (SPPS) procedure

All peptide sequences where prepared using the standard Fmoc SPPS on Wang resin pre-loaded with the first amino acid. The chain growth was performed with a three-fold excess of amino acid over the resin in DMF, using N,N,N′,N′-Tetramethyl-O-(1H-benzotriazol-1-yl) uronium hexafluorophosphate (HBTU) and N,N-Diisopropylethylamine (DIPEA) as activating and coupling reagents in 1:2 ratio respectively relative to the amino acid. Fmoc removal was carried out with 20% piperidine in DMF. The cleavage of the peptides from the resin was achieved using a cleavage cocktail: 95% TFA, 2.5 % triisopropylsilane (TIS), and 2.5 % water. The crude peptide was precipitated and washed in cold diethyl ether and subsequently dissolved in water to allow further purification by preparative HPLC. For the dissolution of hydrophobic sequences minimal amount of acetonitrile was used to ease the dissolution of any non-dissolved material (in water). The samples were then characterised by reverse phase high-performance liquid chromatography (HPLC) and liquid chromatography-mass spectrometry (LCMS) to determine the purity and M_w

of the product. The peptides were purified by Almac Sciences (Elvingston Science Centre, Gladsmuir, East Lothian, Edinburgh, EH33 1EH, Scotland).

3.6.12 Gel preparation

Samples were prepared by suspending the peptide powder (PhAc-FFAG of GFFLG) to a total peptide concentration of 10, 20 and 30 mM in DI water. NaOH solution (0.5 M) was added drop wise to reach complete dissolution of the peptide (pH 9-10), followed by vortexing and sonication until full dissolution. HCl (0.5 M) was then drop wise added to neutralize solution's basicity (pH 6.8.-7.4) followed by vortexing and sonication to trigger gelation. Immediately after that, the solution was allowed to gel on the bench. All characterizations were performed after 24 hours unless otherwise mentioned.

3.6.13 Determination of Critical Aggregation Concentration (CAC) and Critical Micelle Concentration (CMC)

Critical aggregation concentration measurement was carried out for PhAc-FFAGLDD, PhAc-FFAG, GFFLGLDD and GFFLG using 8-Anilino-1-naphthalenesulphonic acid (ANS) as a fluorescence probe.[179] Varying concentrations (5 mM, 2.5 mM, 1.25 mM, 0.625 mM, 0.312 mM, 0.156 mM and 0.078 mM) of each peptide were used. A 0.01 M ANS stock solution was made in methanol. 1 μL of the ANS stock solution was added to 1 mL aqueous solution of peptides (to reach the final probe concentration of $1x\ 10^{-5}$ M) and the fluorescence emission measured immediately after mixing. The ANS fluorescence was monitored at room temperature using an excitation wavelength of 360 nm. Fluorescence emission was monitored over a range of 370 nm to 700 nm. The CAC calculation method was adapted from literature.[175] CAC was calculated by plotting the absorption of ANS at 470 nm (at the emission maximum) against the log of peptide concentration. The two trendline equations from each graph were set as equal and from there the value of x at the turning point, corresponding to the log concentration, was calculated. By solving 10^x the CAC in mM is obtained.

Critical micelle concentration measurement was carried out for PhAc-FFAGLDD and GFFLGLDD using pyrene as a fluorescent probe following a previously reported method.[36] Varying concentrations (5 mM, 2.5 mM, 1.25 mM, 0.625 mM, 0.312 mM, 0.156 mM and 0.078 mM) of each peptide were used. A stock solution of 2.5 mM was made in methanol, which was then diluted 20 times. 5 µL of the diluted solution of pyrene was added to each of the seven different concentrations of peptide solutions (to reach the final probe concentration of 6.25×10^{-6} M). These samples were then excited at 338 nm and fluorescence emission was monitored over a range of 360 nm to 410 nm. CMC was obtained by plotting the ratio the first peak (λ_{max}=372 nm) and the third peak (λ_{max}=384 nm) against concentration.

3.6.14 MMP-9 activation

The proenzyme was activated by incubation with 2 mM p-aminophenyl mercuric acetate (APMA). A 10 mM stock solution of APMA was made in 0.1M NaOH. This stock was diluted 5x to give a final APMA concentration of 2 mM. 1:1 volume ratio (MMP-9:APMA) were used for activation that was performed at 37°C for 2 h. When the catalytic domain was used no activation was required.

3.6.15 Digestion of substrates by MMP-9

The digestion of the peptides was carried out at 37°C in PBS for 96 h at a volume of 1 mL for peptides only and in a well plate at a final volume of 100 µL for peptides loaded with doxorubicin.

A 10 mM stock solution of each peptide was made by dissolving the peptide in PBS buffer (pH=7.4). The peptide solution was diluted to a final concentration of 5 mM and MMP-9 was added to give a final enzyme concentration of 50 ng/mL. The reaction was then incubated at 37°C for the desired time (96 - 120 h). After enzyme addition the morphology change was monitored by confocal microscopy over time. The final products were analysed also by TEM and AFM.

For the drug release studies and confocal imaging doxorubicin (final concentration: 5 µM) was added to the peptide solution and sonicated for 15 min before the addition of the enzyme.

The products of enzyme cleavage were analysed by HPLC and MALDI/LCMS.

3.6.16 Release studies of doxorubicin from 1b and 2 b gels

1b and **2b** gels were prepared as described above. Doxorubicin was diluted in the DI water used to make the gel to give a final concentration of 5 µM. 1 mL of PBS was added on top of the gel and 100 µL aliquots were taken, diluted into 900 µL of DI water and doxorubicin fluorescence emission was monitored over time (time zero, 30 min, 1 h, 2 h, 4h, 24 h, 48 h, 72 h and 96 h). After 96 h another 1 mL of PBS was added at the top of the gel and the emission of doxorubicin recorded in the same way as before (120 h, 144 h, 168 h, 192 h, 216 h, 240 h and 264 h).

3.6.17 Physical entrapment of doxorubicin

Doxorubicin was solubilized in DMSO by sonication and a 1 mM stock solution was made and subsequently diluted into the suspension of peptide micelles (final concentration of doxorubicin: 5 µM). The samples were then sonicated to allow doxorubicin diffusion into the hydrophobic core of the micelles. Confocal images were taken for the loaded micelles (starting material) and for the micelles treated with MMP-9. Confocal imaging was used to monitor the MMP-9 triggered morphology change accompanied by doxorubicin release/entrapment.

3.6.18 Doxorubicin release from micelles (1a and 2a)/ entrapment into fibres (1c and 2c) at different peptide concentrations

A systemic study was performed to assess how peptide (substrate) concentration affects micelle to fibre transition and the process was monitored using fluorescence. Four different concentrations of peptide were chosen: 2.5 mM, 1.25 mM, 0.625 mM, 0.312 mM. Doxorubicin fluorescence was recorded for each peptide concentration for untreated and MMP-9 treated doxorubicin loaded micellar aggregates.

3.6.19 The behaviour of doxorubicin monitored in different solvents

A 1 mM stock of doxorubicin in DMSO was diluted in solvents with different polarities: ethanol, methanol, DMSO and water[180] to a final concentration of 5 μM. The doxorubicin fluorescent emission was recorded (λ_{ex} = 480 nm).

4 Method development for fibre visualisation in the proximity of cancer cells*

*The research described in this Chapter was carried out in collaboration with the Beatson Cancer Research Institute. All cell work (seeding of cells and their handling for all the visualisation processes and for the MMP-9 activity assay) was performed by Max Nobis.

4.1 Introduction

A next step towards the application of the micelle to fibre transition of peptide amphiphiles introduced in the previous Chapter is their visualisation *in vitro*. In order to prove the mechanism of cancer inhibition due to the mentioned transition and fibre formation in the locality of cancer cells different microscopy techniques (confocal and EM) were assessed. Visualisation of fibres formed by enzymatic conversion of aromatic peptide amphiphiles inside and/or outside cells is a new direction of research with only a few examples appearing in the literature in recent years. These examples will be considered in detail in section 4.3 in order to describe the state of the art in this area. Certain key figures from other publications focused on the visualisation of supramolecular fibres will be presented to provide context for the obtained results.

In contrast to supramolecular enzyme responsive small-molecule systems, the visualisation methods are better developed for more conventional polymeric structures i.e. polymer-peptide conjugates showing different modifications (near IR fluorescent dyes, FRET systems and heavy metal complexes) introduced on polymeric backbones (Chapter 2, Section 2.6.2).[52,161,163,181] These systems are more robust given the stability of polymeric structures (due to high Mw, compared to supramolecular fibres composed of low molecular mass gelators studied here) and possibility to easily incorporate fluorescent dyes without disrupting the self-assembly.

4.2 Objectives

In the present study we set out to determine whether the visualisation of enzyme triggered fibre formation around cancer cells was possible using three techniques that have previously been described: confocal microscopy, TEM and SEM. Our goal was to confirm fibre formation around cancer cells in the presence of MMP-9 using aromatic peptide amphiphiles PhAc-FFAGLDD (**1a**) and GFFLGLDD (**2a**) as substrates for the enzyme (Fig. 4.1). For this purpose we first experimentally determined the MMP-9 concentration in different cancer cell lines:

cervical cancer cell line (HeLa) and breast cancer cell lines (MDA-MB-231 and MDA-MB-231-luc-D3H2LN). As cancer cells secrete MMPs in the extracellular space, localised fibre formation in the presence of these enzymes is expected.

We are particularly interested in developing methods for efficient fibre visualisation in the presence of cancer cells without covalently modifying the peptides with fluorescent probes or heavy metals. The main reason behind this approach is to avoid toxicity issues and/or disruption of the self-assembly of the peptidic systems (described in detail in Chapter 3). Instead, a fluorescent model drug, riboflavin was physically entrapped in the fibres for imaging purposes. Exploiting the fact that after MMP-9 treatment of **1a** and **2a** doxorubicin re-enters a hydrophobic environment by becoming entrapped in the fibres (described in Chapter 3), here we used riboflavin as physically entrapped fluorophore for confocal imaging. The anticancer drug (doxorubicin) was not used in this stage, as it would potentially even at low concentration be toxic to cells, hampering visualization of intact cells *in vitro*.

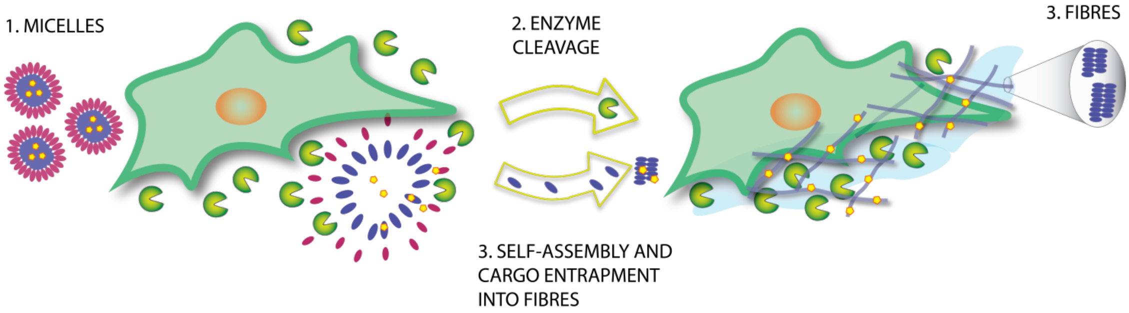

Figure 4.1. Schematic representation of enzyme triggered micelle to fibre transition in proximity of cancer cells that results in the formation of local depots for slow and localised release of doxorubicin.

4.3 Background to method development

The first examples of imaging of enzyme triggered gel/fibre formation in live cells and around cancer cells, using aromatic peptide amphiphiles, were developed by Xu and co-workers.[3] In a first study, focusing on intracellular imaging of biocatalytic self-assembly, a peptide backbone (Phe-Phe-Lys) was modified with an aromatic moiety (naphthalene) at the N-terminus that favours aggregation through aromatic interactions. The peptide also contained a phosphorylated tyrosine residue at the C-terminus that provides charges to disrupt assembly and incorporates enzyme (phosphatase) responsiveness as described in Chapter 2 (Section 2.6.2.1). In addition, a fluorophore is introduced at the side chain of the lysine, to obtain a precursor of the fluorescent hydrogelator. NBD (4-nitro-2,1,3-benzoxadiazole), which is known to provide a more intense fluorescence signal in hydrophobic environment compared to water, was used as a fluorophore. Both *in vitro* and *in cellulo* studies were conducted. In the presence of phosphatase the hydrogels form due to dephosphorylation and result in the enhancement of the fluorescent signal of NBD. *In cellulo* studies show fibre formation inside live cells. In addition, localisation of self-assembly was determined to be in the proximity of the endoplasmic reticulum (ER). This example emphasized how the choice of the fluorophore (NBD) was essential for successful imaging inside live cells due to its effects on gelation ability. For example, substituting NBD with rhodamine fails to provide the contrast necessary for imaging, because the rhodamine containing peptide is not a gelator (i.e. forms disordered aggregates, but not fibres). The authors explain the difference in contrast between the soluble precursors and the nanofibre forming hydrogelators by localized high concentration points of the fluorophore in the presence of fibres. The homogeneous distribution of the fluorophores, when in solution, results in a low contrast because they fluoresce identically within each pixel. In contrast, when the nanofibres form the fluorophores are localized inside them. Therefore, the fibres contain more fluorophores within each pixel compared to the rest of the solution and consequently fluoresce more brightly. Accordingly, when NBD is embedded in the hydrogels (5.92 mM) the fluorescence intensity is high and provides a good contrast for fluorescent imaging. However, fibre formation can occur without the formation of bulk hydrogels. At the concentration used for this experiment (500 μM), the confocal microscopy image (figure 4.2 A) shows fluorescent micro-sized regions. According to authors, these present low mobility and are composed of fibre networks, shown by TEM (figure 4.2 B). No bulk hydrogel was observed as the concentration used (500 μM) for imaging was below the critical gelation concentration (2 mM), but high enough to observe fibre formation.

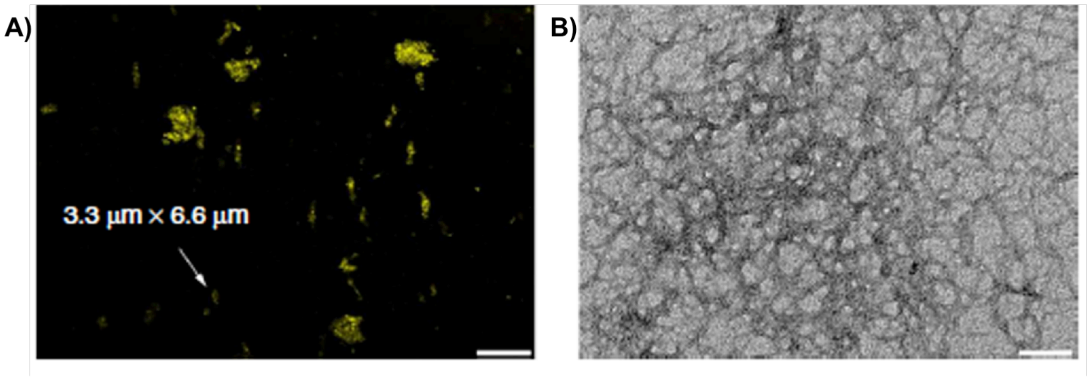

Figure 4.2 A) Confocal microscopy showing that the fluorescent spot indicated by an arrow consists of a network of fibres confirmed by TEM image in B), taken from reference 165b.[165b] (Scale bars: for confocal image, 25 µm; for TEM, 100 nm).

This concept was further developed by Xu and co-workers, where the spatial distribution of small molecules in cellular environment was studied.[182] The distribution was based on naphtyl-peptide derivatives (Nap-FFKYp) conjugated to different fluorophores: NBD (4-nitro-2,1,3-benzoxadiazole), dansyl, DBD (4-(*N,N*-dimethylsulfamoyl)-2,1,3-benzoxadiazole) and rhodamine shown in figure 4.3.

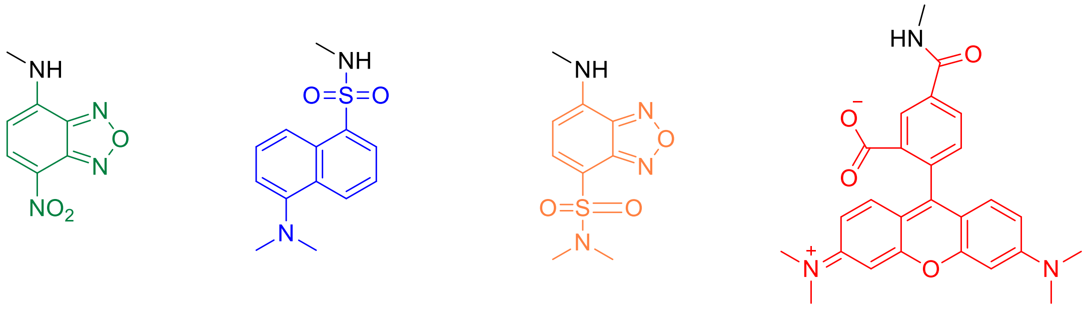

NBD Dansyl DBD Rhodamine

Figure 4.3. Chemical structures of NBD (4-nitro-2,1,3-benzoxadiazole), dansyl, DBD (4-(*N,N*-dimethylsulfamoyl)-2,1,3-benzoxadiazole) and rhodamine with the -NH- (black) indicating the point of covalent attachment to the peptide- lysine side chain).

Depending on the fluorophore used these molecules present different states of assembly, even before treatment with phosphatase. Depending on their state of assembly (no assembly- soluble molecules; thin nanofibres; thick fibres; disordered aggregates) each kind of fluorescent molecule/aggregate diffuses in cells with different rates and can be found at different locations. The soluble NBD containing molecules diffuse into the cytoplasm where in proximity of the RE they form fibres, due to the activity of alkaline phosphatase. The dansyl containing peptide derivatives, before enzyme treatment, show small amounts of thin nanofibres that accumulate in the membranes of cells. This is due to the hydrophobicity of the dansyl-lysine motif that exhibits higher solubility in the phospholipid membranes compared to water. After dephosphorylation, nanofibres surrounded by non-fibrillar aggregates are observed. In live cells this results in the self-assembly on cell membranes, where the nanostructures formed show cytotoxicity. The DBD peptide derivative self-assembles into fibres that, after enzyme cleavage, further assemble giving rise to bundles of strongly inter-connected fibres. These fibrillar aggregates were found to remain outside the cells as live HeLa cells are unable to uptake them, where they show toxicity at the concentration between 200 and 500 μM. For the rhodamine tagged peptide amphiphile in its phosphorylated and dephosphorylated form, disordered aggregates are observed and none of the two is a hydrogelator. *In vitro* these molecules show random distribution, being found inside and outside of cells, showing both cells with high fluorescence and background fluorescence. The rhodamine containing peptide amphiphiles that enter the cells are dephosphorylated and form aggregates that are cytotoxic when used at high (200-500 μM) concentrations. These observations show how the presence of fluorophores conjugated to peptidic gelators has toxic effects and is undesirable for *in vivo* real life applications. However, it constitutes a useful example of methodology for imaging of the self-assembly of small molecules inside cells.

To overcome the problem of incorporation of high concentrations of toxic dyes in the aromatic peptide amphiphile structures, which can easily disrupt the desired fibre formation, an example of self-assembly of non-fluorescent small molecules (Nap-FFKYp) was assessed inside live mammalian cells where low concentrations of fluorophore containing molecules (Nap-FFK(dansyl)Yp) were co-assembled.[3b] In this work, confocal imaging of the self-assembly into fibres was based on the use of low concentrations of fluorescence labeled peptide precursors, low enough not to result in cytotoxic effects and high enough to give a fluorescent signal. This was achieved by incubating HeLa cells with a mixture of low concentration (200 nM) of fluorescent precursor with high concentration (500 μM) of the non-fluorescent analogue. Once internalised by cells, these molecules would co-assemble into fibres due to dephosphorylation by intracellular phosphatases. Ultrastructural changes were observed between treated and untreated cells. High accumulation of vesicles that show fluorescence signal in cytoplasmic region was recorded for peptide treated cells. As both hydrogelators share the same self-assembly motif, their co-assembly into fibrillar structures was confirmed and the confocal imaging shows their distribution inside live cells. In addition, a useful technique was used in this study, namely correlative light and electron microscopy (CLEM), where on the same sample fluorescence imaging can be performed just before preparing the sample for electron microscopy imaging.[3b] In this way, the correlation between the two microscopy techniques is more straightforward and provides a better comparison of the results obtained. Still, the resolution of TEM is not sufficient to distinguish the filamentous assemblies of the cytoskeleton (actin filaments) and the exogenous peptide based self-assembled nanofibres. In figure 4.4 CLEM results taken form Xu's publication are shown where fluorescence microscopy and TEM were performed on the same cell.[3b] From the TEM images is not possible to clearly see the fibres. However, as the authors associate hydrogelation with high fluorescence intensity, TEM imaging was performed on the same region that showed fluorescent signal (fluorescence microscopy). High magnification TEM images of that region showed low electron dense pools (indicated by arrowheads in figure 4.4 G and H). The authors conclude that these low electron-dense regions contain hydrogelator even though there is no direct proof of the formed fibres.

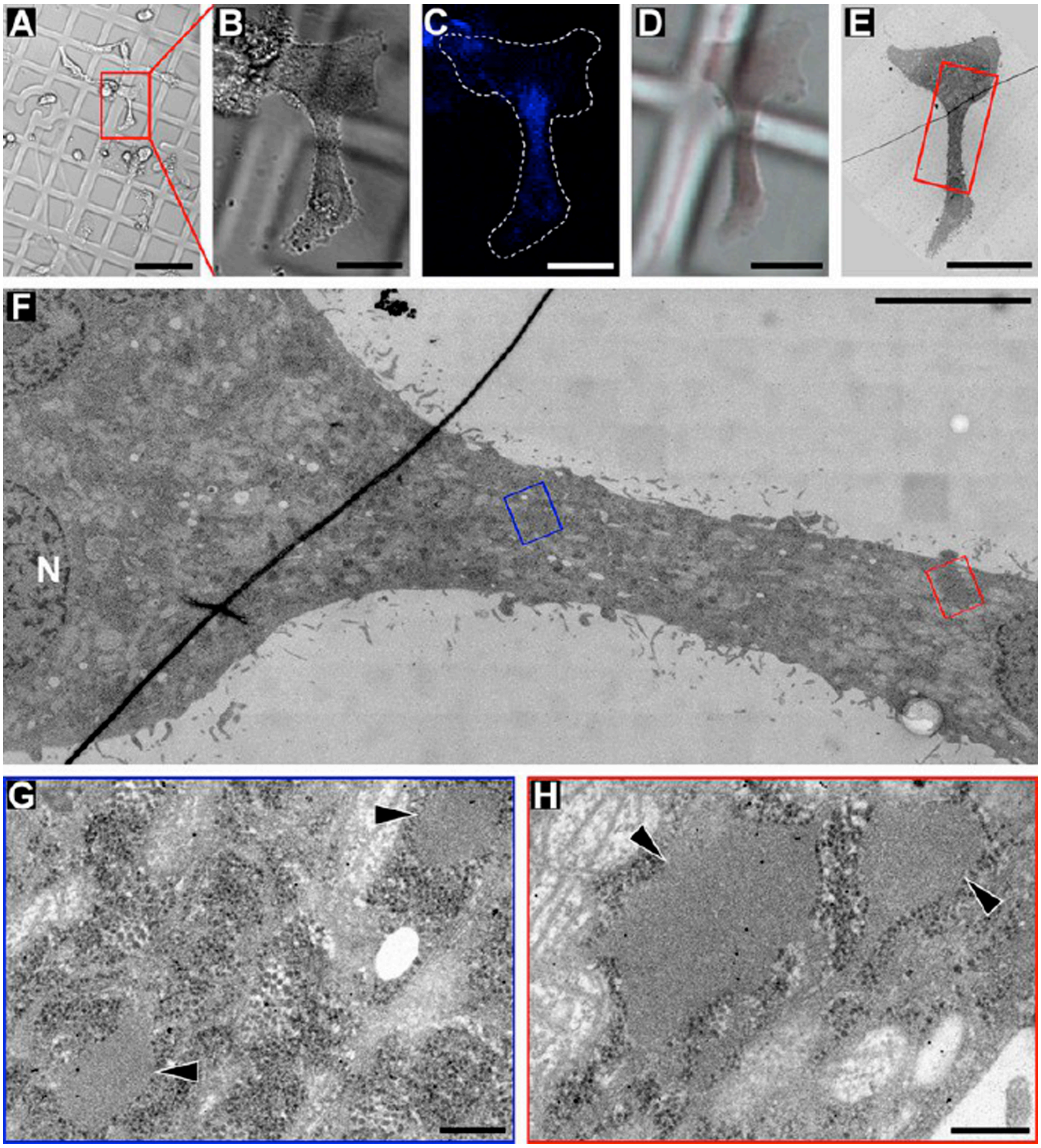

Figure 4.4. CLEM of HeLa cells treated with peptide (200 nM of fluorescent precursor + 500 μM of non-fluorescent analogue), taken from reference 3b.[3b] This figure shows: A) – C) differential interference contrast (DIC) and fluorescence microscopy images recorded just before freeze-drying of the sample (the sample was marked for tracking the cell of interest with CLEM). According to the authors, in C) the highest intensity of fluorescence signal in the narrow part of the cell indicates a high concentration of hydrogelators in that region of the cell. D) DIC of the same cell after freeze-drying; E) Low magnification TEM of the same cell; F), G) and H) higher magnification TEM of regions of interest- arrowheads indicate low electron-dense pools, that presumably contain hydrogelator.

The concept of enzyme triggered fibre formation around cancer cells, i.e. nanoscale network visualisation in extracellular space was reported for the first time by Xu and co-workers (Chapter 2).[3c] The ability of a phosphatase responsive aromatic peptide amphiphile (Nap-FFYp) that forms fibres when incubated with HeLa cells (in presence of secretory and surface phosphatases) was assessed by confocal microscopy and SEM. The visualisation of fibres in the presence of cells was achieved using SEM. These SEM images revealed different cell surface morphology for treated (porous structures) and untreated (smooth surface) HeLa cells (*vide infra*, figure 4.6). In addition, a β-sheet specific stain, Congo red was used to confirm the presence of fibres around single cells. The red fluorescence signal that outlined the cell shape in the presence of the peptide was observed using confocal microscopy. Lower signal was detected in the absence of the self-assembling peptide. Again, because of resolution limitations of confocal microscopy, the network morphology of the regions showing fluorescence signal around cancer cells was not directly visualised.

The examples described so far are based on the use of a combination of confocal or fluorescence with electron microscopy in order to confirm the nanostructures formed. Often, a described behaviour (i.e. fibre formation) in absence of cells is assumed to occur also in their presence without necessarily the need of its direct visualisation. However, it would be interesting to observe directly the mechanism of fibre formation in presence of cells.

Although not yet used in the context of biocatalytic self-assembly, super-resolution techniques, such as stochastic optical reconstruction microscopy (STORM) are emerging. An example of using STORM for imaging of supramolecular polymers to obtain quantitative information about the structure and the dynamics of the aggregates (single fibres) was reported by Meijer and co-workers.[178] In detail, the single-colour, 1-D self-assembled structures based on co-assembly of dye labeled and unlabeled monomers were assessed. The degree of labeling of the fibres was controlled by the ratio of dye-labeled and unlabeled monomers. After mixing single-coloured fibres (labeled with two different cyanine fluorescent dyes: Cy3 and Cy5, each having different excitation wavelenghts) the mechanism of monomer exchange was monitored by observing the migration of Cy3 labeled monomers to a Cy5 labeled fibre and *vice versa*. At the beginning of the experiment the fibres are either green (Cy3) or red (Cy5), but after 24 h all the fibres contain both the monomers. The mechanism of the monomer exchange was elucidated with precision. However, in order to extract quantitative data from STORM images, the development of a specific analytical methodology was required. This study constitutes an example of the use of STORM technique providing a resolution down to 50 nm, which could be applied for the study of other supramolecular fibres. Figure 4.5 shows the STORM images of fluorescently labeled supramolecular polymers indicating the possibility to visualise single fibres.

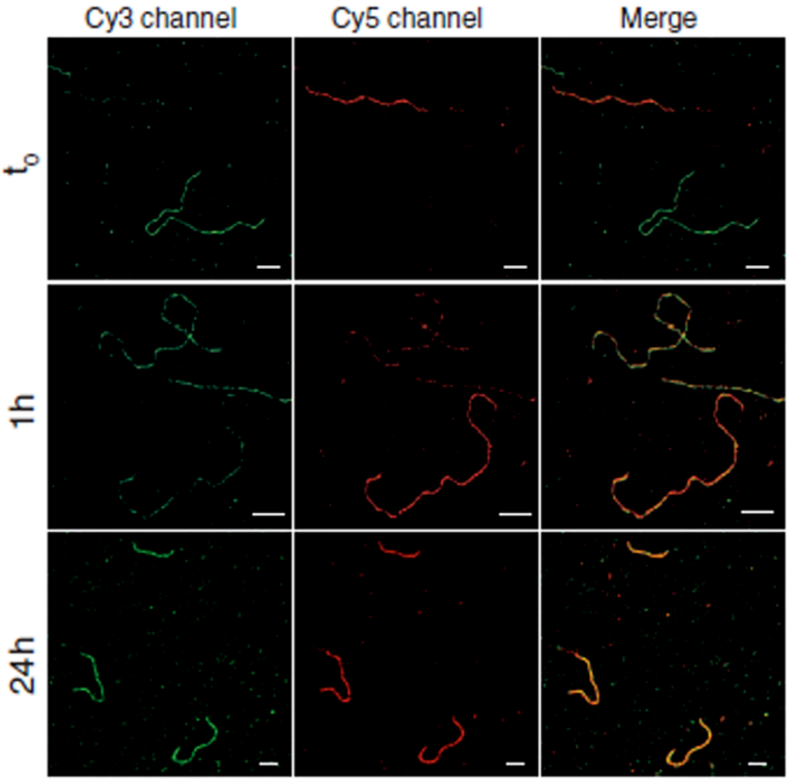

Figure 4.5. STORM imaging of Cy5- and Cy3-labeled polymers (5% labeling) at different mixing time points taken from reference 178.[178]

EM is a convenient method for visualisation of cell and/or single organelles morphology. TEM and SEM visualisation conventionally require sample fixation for better imaging results. For TEM, the first fixation step (pre-fixation) required uses glutaraldehyde to fix the cells to glass slides. The second fixation step (post-fixation) is performed with osmium tetroxide, followed by various washing steps with ethanol and embedding into resin for analysis of cell sections. SEM usually requires pre-fixation that is followed by freeze-drying/critical point drying and applying of a metal coating (e.g. gold). While the mentioned fixation steps are necessary for cleaner (e.g. avoiding of crystals) images of cells, they can interfere with the visualisation of exogenous fibres formed by self-assembly of aromatic peptide amphiphiles. Xu and co-workers reported such a problem stating that repeated washes with ethanol or acetone (used for sample dehydration in TEM) are responsible for fibre destruction.[3c]

SEM was shown to be a useful technique for imaging of cancer cells and in particular for visualisation of fibres formed on the surface of cancer cells.[3c] Some examples of using SEM will be shown here in order to give an idea of the appearance of cancer cells and later (see Results and Discussion) as a reference point for our own studies. As already mentioned, the first demonstration of aromatic peptide amphiphile based hydrogel formation around cancer cells using SEM was presented by Xu and co-workers (Fig 4.6).[3c] In the presence of the hydrogelator, HeLa cells change morphology showing porous structures over the surface of cells compared to the smooth surface of untreated cells (Fig. 4.6). Cell fixation processes usually used for SEM and TEM sample preparation were avoided in order to be able to preserve the nanofibres that formed on the cell surface. Instead, the cells grown on glass slides were freeze-dried and analysed directly by SEM.

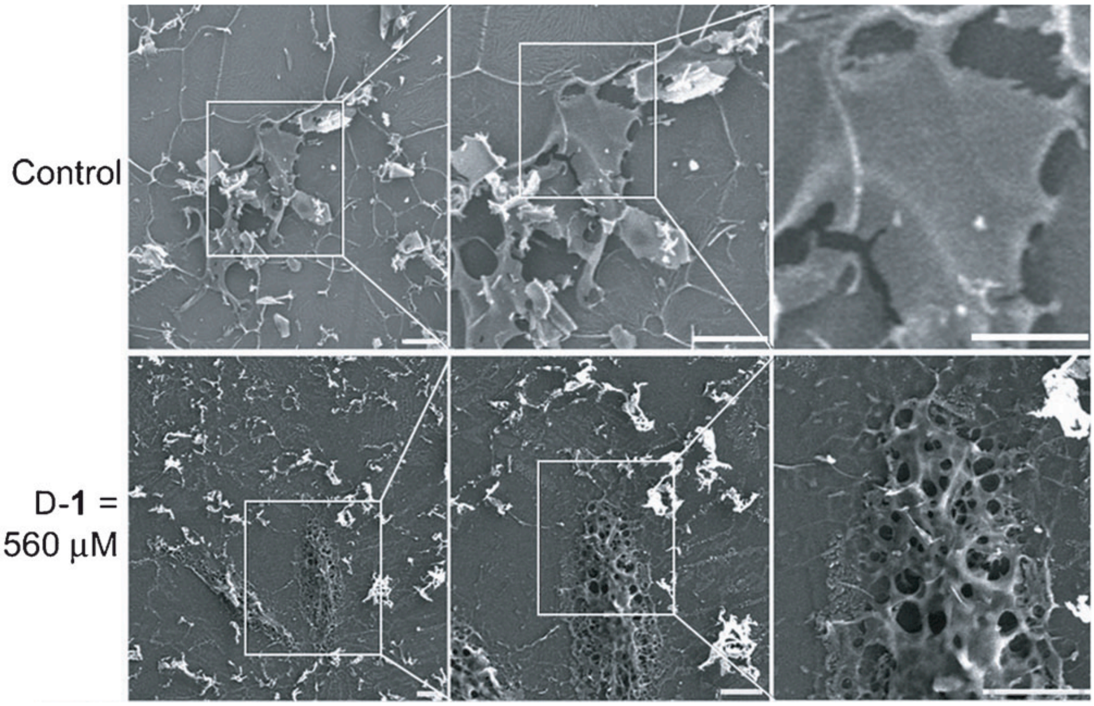

Figure 4.6. SEM images of freeze-dried HeLa cells treated with D-1, for untreated control or treated at 560 μM taken from Xu's publication.[3c] (Scale bar=10 μm).

Another example of using SEM to study the effect of a peptide that adopts a β-hairpin structure when in contact with cancer cells (an 18-residues anticancer peptide - SVS-1) and its interaction with cell membranes was reported by Schneider and co-workers.[62] This peptide was shown to be capable of cancer cell membrane disruption (Chapter 2, Section 2.3.1). Schneider and Pochan have extensively studied the self-assembly of β-hairpin type peptides able to form hydrogels.[126,183] MAX1 sequence (a 20-amino-acid peptide comprised of two β-strands with alternating valine and lysine residues) and its variants were reported to form fibrils and hydrogels.[184] More recently, Schneider and co-workers presented a β-hairpin SVS-1 peptide for cancer applications (Chapter 2, Section 2.3.1).[62] In this example, focus has been put on membrane integrity of cells in presence of SVS-1 rather than on its fibril forming capability. To directly visualize cell membrane integrity as a function of the added peptide SEM and TEM were performed. SEM images (Fig. 4.7) of untreated A549 lung cancer cell line show intact cell membrane and regular cell morphology compared to the SVS-1 peptide treated ones that present sponge-like morphology and pore formation. At higher peptide concentration (80 μM) disruption of cell membranes is also observed for noncancerous cells (HUVEC) confirming that the membrane disruption by SVS-1 is independent of the cell type at that concentration. In this example cells were fixed with glutaraldehyde prior to SEM imaging and after being treated with peptide. No fibrillar structures were observed with SEM. In addition, TEM imaging was performed to check whether the peptide fibrils that could form after interaction with the membrane are responsible for its disruption. With TEM no fibrillar structures were observed either and the authors concluded that a fibrillogenesis-based mechanism of membrane disruption was unlikely. However, from the experimental section it can be seen that TEM samples underwent complex processing (pre- and post-fixation) prior to imaging. This could have destroyed the fibres formed and interfered with their visualisation as suggested by Xu and co-workers.[3c]

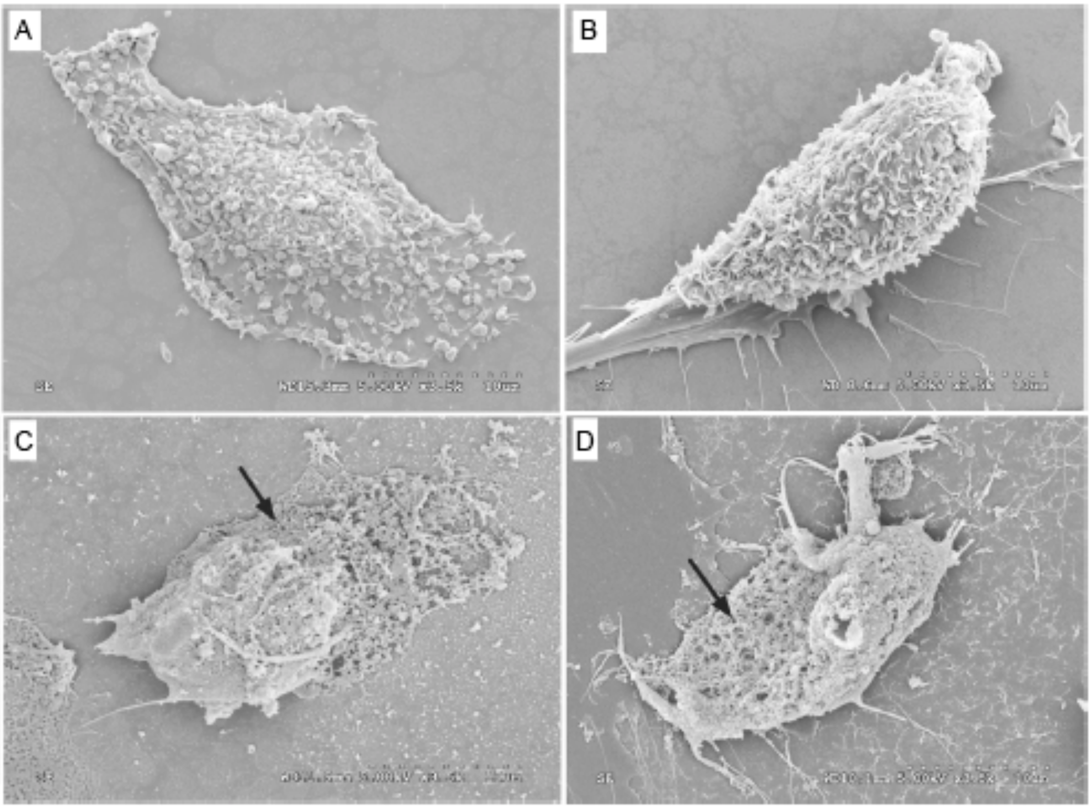

Figure 4.7. SEM images taken form reference 62 (Schneider and co-workers)[62] showing membranes of untreated A549 (lung carcinoma) cancer cells (A) and noncancerous HUVEC cells (B) appearing intact. A549 cells (C) incubated with a β-hairpin peptide (8 μM of SVS-1) in serum-free media. HUVEC cells (D) incubated with the SVS-1 peptide (80 μM- large excess). Cells display pore formation (arrow). (Scale bar: 10 μm).

Although not focusing on fibril forming peptides, Austin *et al.* demonstrate the effects of the interaction of Neopetrosiamide A (a 28 amino acid residue tricyclic peptide) known to inhibit tumour cell invasion with cancer cells.[185] This study is relevant as it shows representative SEM images of MDA-MB-231 (Fig. 4.8) cells along with the TEM images (Fig. 4.9) indicating typical cancer cell morphology for these two EM techniques. MDA-MB-231 cells were imaged using SEM in the presence and absence of the peptide (Fig. 4.9). It was found that the peptide stimulates the formation of membrane-bound protrusions on the surface of treated cells and the release of membrane-bound vesicles.

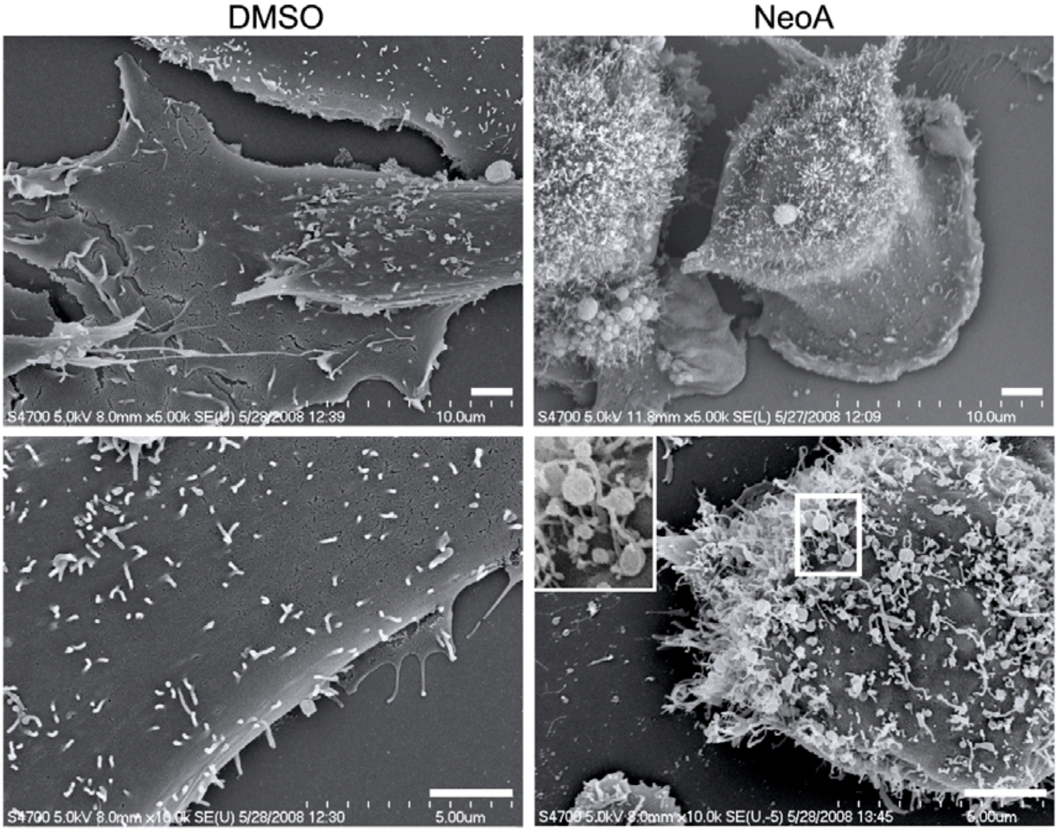

Figure 4.8. SEM images of MDA-MB-231 cells taken from reference 185, showing the cell surface with increasing number of membrane projections upon treatment with NeoA (right panels). MDA-MB-231 cells treated with DMSO (left panels) are used as control. (Scale bars: 2 μm).[185]

SEM is clearly showing the cell surface with the increasing number of membrane protrusions compared to the control sample, while TEM indicates high number of vesicles and further confirms protrusion formation in the presence of NeoA. All the features observed with EM here are indeed integral parts of the cancer cells, which in turn might make it difficult to visualize of any exogenous fibrillar structures, if expected to be present/formed.

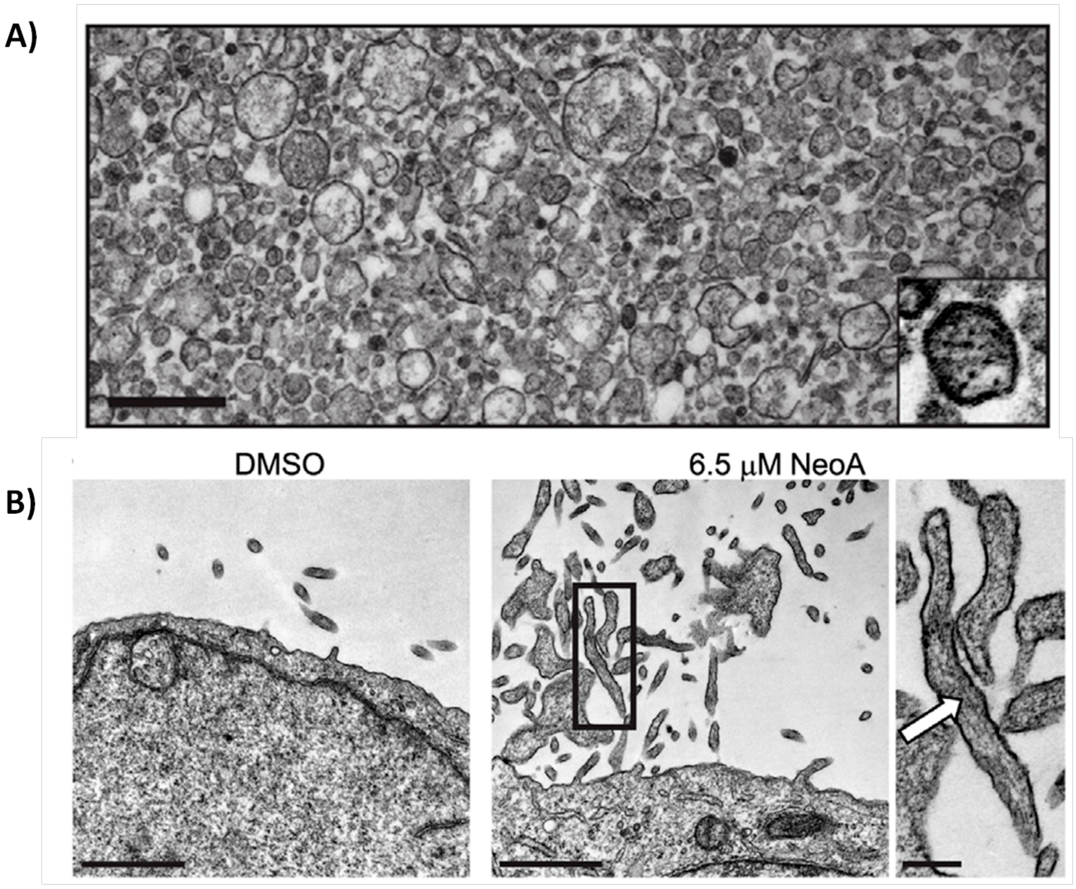

Figure 4.9. TEM images taken form reference 185: A) of TEM of vesicles from the medium of NeoA treated cells (scale bar: 0.5 μm); and B) of membrane protrusions at the cell surface. Actin filaments are indicated by the arrow (end right panel). (Scale bars: left and middle panels, 1 μm; right panel, 0.2 μm).[185]

Another example of the morphology of MDA-MB-231 cells using SEM was shown by Kniss and co-workers.[186] In this study it was demonstrated that myoferlin is abundantly expressed in invasive breast tumour cells. Following myoferlin depletion cancer cells undergo morphology change from elongated shape to a more flat and circular morphology and reduction of cell invasiveness. SEM images show lamellipodia and filopodia as filaments present in the proximity of cancer cells (Fig.4.10).

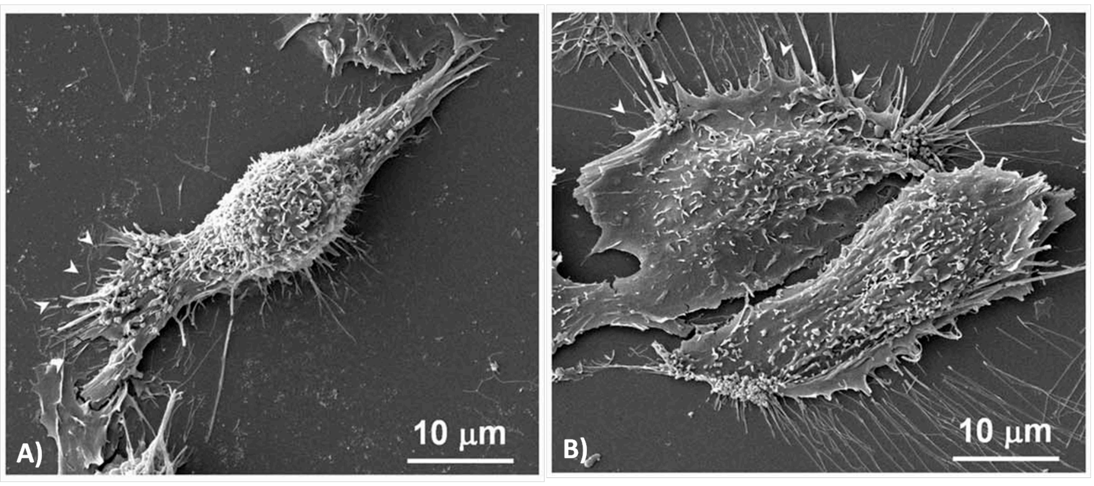

Figure 4.10. SEM images taken form reference 186 showing the A) elongated shape of lentiviral control (LTV-ctrl) cells and B) the more flat and circular morphology of myoferlin depleted (MYOF-KD) cells. Cytoplasmic protrusions, lamellipodia and filopodia are observable.[186]

The selected four examples of SEM images show the morphology expected for cancer cells and the morphology alterations that these cancer cells can undergo in the presence of different (bioactive) peptides- some of them with fibril forming capability, others that are not known to assemble into fibrous structures. In addition, these images show how the surface of cancer cells is not entirely smooth and can contain protrusions and inherently present fibrillar structures. Complementing SEM, TEM imaging was successful in imaging cells and confirming the presence of organelles and membrane protrusions.

With SEM imaging both, Xu[3c] and Schneider[62] show a similar porous morphology of the cell surface when studying peptide nanostructure formation and interaction with cells. Xu and co-workers confirm the fibre network formation on cell surface, while Schenider and co-workers show membrane disruption. The SEM sample preparation for these two examples differs in that in the former case cells were freeze-dried immediately after treatment with peptide, while in the latter case cell fixation with glutaraldehyde was performed. In both examples TEM imaging was, however, not successful in visualising fibres after fixation processing.

Further examples focused on biological investigations using EM such as vesicle secretion and membrane protrusion formation and/or presence. They are based on the same sample preparation and processing (primary fixation with glutaraldehyde, post-fixation with osmium tetroxide for TEM and gold coating application for SEM) in both cases. These conventional sample preparation steps for cell visualisation might be simplified and/or omitted if peptide nanostructure formation in proximity of cells is the objective of the study, as shown by Xu's group.[3c] It is worth mentioning that cryogenic electron microscopy methods may prove useful in that they do not require staining and pre-treatment (fixation) steps.

4.4 Results and discussion

Aromatic peptide amphiphiles, **1a** and **2a** (described in detail in Chapter 3) were assessed in the presence of cells with confocal microscopy, SEM and TEM in order to determine structure/fibre formation around cancer cells.

In literature, the precise concentrations of MMPs associated with cancer are rarely reported. MMP-9 is known to be over-expressed in various types of cancer, including ovarian, breast and prostate tumours.[167c] However, a clear quantification and direct comparison is difficult as different cell lines can show different patterns of over-expression. For this purpose, we experimentally determined MMP-9 concentration in different cancer cell lines: cervical cancer cell line (HeLa) and breast cancer cell lines (MDA-MB-231 and MDA-MB-231-luc-D3H2LN). Cells of these three cell lines were stimulated with PMA (phorbol 12-myristate 13-acetate) to induce enzyme secretion, as described previously.[176] The reason for this is that cells would not produce MMPs at any rate, as they were grown on glass bottom/plastic dishes rather than in a 3D environment containing ECM (extracellular matrix) components that would elicit their expression (i.e. that is what is happening when cells are grown on orgnaotypic culture- collagen plugs).

4.4.1 MMP-9 quantification in human cancer cells lines

The concentration of MMP-9 secreted by different human cancer cell lines (human cervical adenocarcinoma cells- HeLa and human breast adenocarcinoma cells- MDA-MB-231 and MDA-MB-231-luc-D3H2LN) was determined by an

ELISA based assay (Fig. 4.11). The MMP-9 activity assay (SensoLyte® Plus 520) was performed on the supernatant collected. The cells were either grown in medium containing 10% serum or serum starved overnight and then stimulated with PMA (phorbol 12-myristate 13-acetate). The reason for this is that MMP-9 overexpression *in vivo* is regulated by cytokines and signal transduction pathways, including the PMA activated pathways.[167c] Cells were stimulated with PMA following a literature method.[167c] PMA stimulation was performed for 24 h. In addition, cells were grown on organotypic (collagen-like) matrices to assess if the MMP-9 secretion increases. With this method the invasiveness of the cells can be also measured. HeLa (cells grown on plastic: 18 ± 3 ng/mL) and MDA-MB-231 (cells grown on plastic: 14 ± 2 ng/mL) cancer cell lines show similar MMP-9 concentration independently of the presence of an organotypic matrix (cells grown on collagen: 20 ± 1 ng/mL). On the other hand, the MDA-MB-231-luc-D3H2LN cell line shows higher concentration of MMP-9 (32 ± 7 ng/mL) compared to that in absence of organotypic matrices (19 ± 4) confirming that this cell line has increased invasive nature. In serum, with no PMA stimulation (cells grown on plastic) no MMP-9 activity was detected (table 4.1).

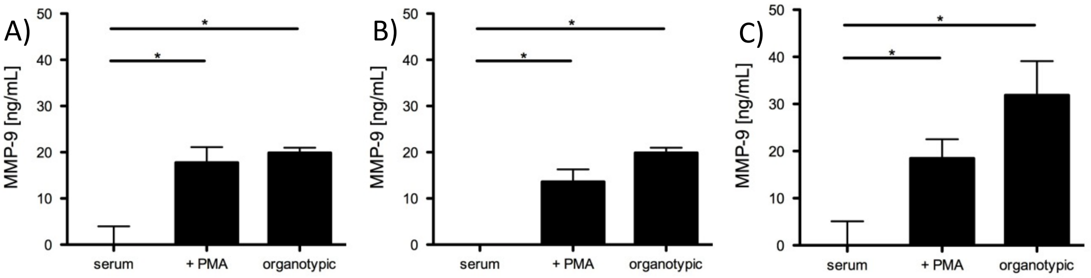

Figure 4.11. MMP-9 activity was quantified before and after treating cells with PMA (100 nM) and when cells are seeded on an organotypic matrix for A) HeLa B) MDA-MB-231 and C) MDA-MB-231-luc-D3H2LN by fluorimetric ELISA.

Table 4.1. MMP-9 concentrations detected in different human cancer cell lines.

	Cell line		
Condition	**HeLa: MMP-9 (ng/mL)**	**MDA-MB-231: MMP-9 (ng/mL)**	**MDA-MB-231-luc-D2H3LN: MMP-9 (ng/mL)**
Serum	-2 ± 6	-17 ± 11	-0.3 ± 5
PMA induced	18 ± 3	14 ± 2	19 ± 4
Organotypic	20 ± 1	20 ± 1	32 ±7

4.4.2 Confocal microscopy

Having established MMP secretion, the next step was to visualise nanostructures surrounding cancer cells. In order to visualise fibre formation around cells, riboflavin was loaded into micelles and the micelle to fibre transition was monitored over time using confocal microscopy. Riboflavin (vitamin B2) was used as a model drug (as it is hydrophobic but less toxic to cells than doxorubicin) in order to observe the effect of fibre formation without killing the cells. Doxorubicin (as used in the previous Chapter) is an anticancer agent that shows high toxicity,[187] while riboflavin is a vitamin used in food industry and naturally occurrs in aliments. Initially, the micelle to fibre transition of **1a** and **2a** containing riboflavin in absence of the cells was assessed. After 24 h of treatment fibrillar structures were observed with confocal microscopy. For **2a** treated with MMP-9 also a ramification can be seen after 24 h (Figure 4.12 I and J). However, the fibrillar structures observed are not single fibres but most likely they are made of boundless of fibres if we take into account the large scale bars of confocal images compared to TEM and AFM (see TEM and AFM images of peptide fibres in Chapter 3, figures 3.20 B+C and 3.21 B+C).

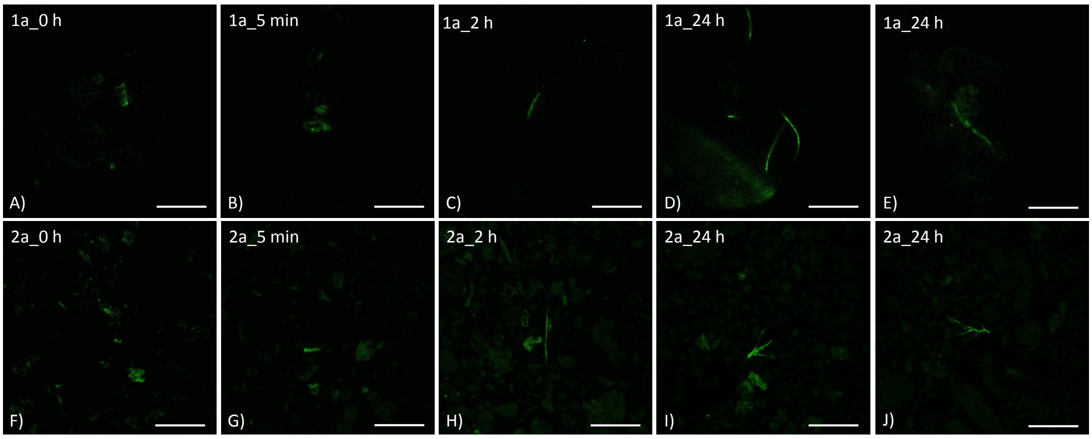

Figure 4.12. Confocal microscopy images of **1a** and **2a** loaded with riboflavin and monitored over time: time zero, 5 min, 2h and 24 h (in two different regions of the same sample). Scale bars: 50 μm.

In addition, fluorescence spectroscopy results indicate that riboflavin was retained in the fibres formed. When excited at 440 nm riboflavin shows emission with a maximum at 530 nm in water. Once incorporated into the hydrophobic core of the micelles, the emission intensity decreases and this is indeed confirmed by the evaluation of riboflavin behaviour in solvent with different polarities (Fig. 4.13).

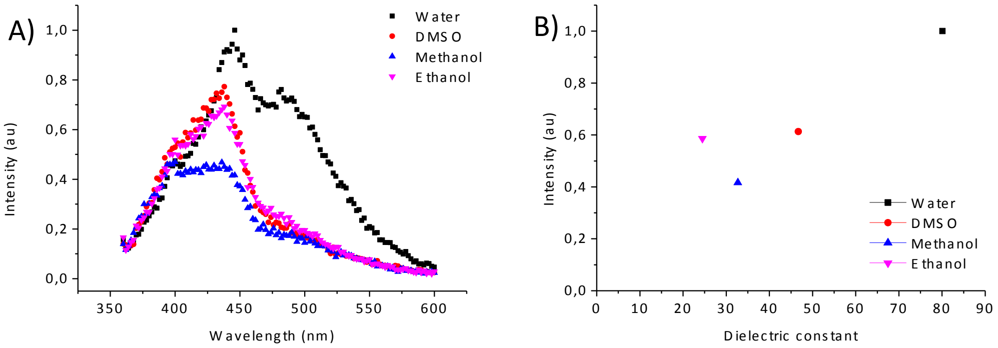

Figure 4.13. A) Fluorescent emission spectroscopy (normalized) of riboflavin in solvents with different polarities (i.e. dielectric constant): ethanol, methanol, DMSO and water. B) Maximum riboflavin emission intensity (446 nm) when excited at 350 nm, plotted against the dielectric constant of the examined solvents.

Furthermore, after treating the micelles with MMP-9 it is expected that riboflavin should be retained in the fibres, as shown for doxorubicin in Chapter 3 (see figures 3.20 A and 3.21 A). Unlike doxorubicin, riboflavin shows a decrease in fluorescence intensity with hydrophobicity (Fig. 4.13) therefore different results are expected than those shown for doxorubicin (Chapter 3, Fig. 3.33). Riboflavin entrapment in fibres would be expected to result in a decrease in fluorescence intensity, in contrast to the observations for doxorubicin (increase in fluorescence intensity observed- Chapter 3). To confirm this hypothesis, three sets of experiments were run monitoring the change in riboflavin fluorescence over 72 h individually and within the peptide system: riboflavin loaded micelles in presence and absence of the enzyme. We observed that the riboflavin emission remains constant for riboflavin in water over 72 h and is quenched in presence of micelles for both peptides **1a** and **2a**. In addition, a decrease in emission is observed when the micelles are treated with MMP-9, suggesting that the riboflavin transfers from the micellar to the newly created, more hydrophobic environment of the fibres formed (Fig. 4.14).

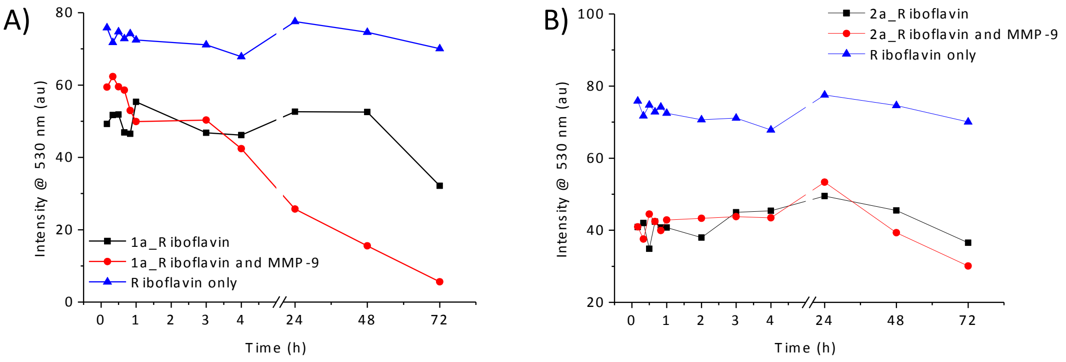

Figure 4.14. Fluorescence intensities of riboflavin monitored over time for riboflavin loaded into precursor peptide micelles A) **1a** and B) **2a** treated with MMP-9 (red) and untreated (black) compared to riboflavin on its own (blue).

In terms of fluorescence intensity, doxorubicin showed a different behaviour compared to riboflavin. Doxorubicin showed higher fluorescence intensity in a more hydrophobic environment (see doxorubicin emission intensities in solvents with different polarities, Chapter 3, Fig. 3.33). In contrast, riboflavin does not show a pronounced difference in emission in ethanol, methanol and DMSO. However, when the fluorescence intensity of riboflavin is measured in water, it is higher in the hydrophilic environment. Therefore the observed decrease in emission suggests that riboflavin is retained, not released. Even if doxorubicin and riboflavin show some structural similarity (figure 4.15), riboflavin is more hydrophilic, compared to doxorubicin. The electron density and the conjugation of these two molecules are different and therefore they are expected to have different emission properties and their behaviour cannot be directly compared.

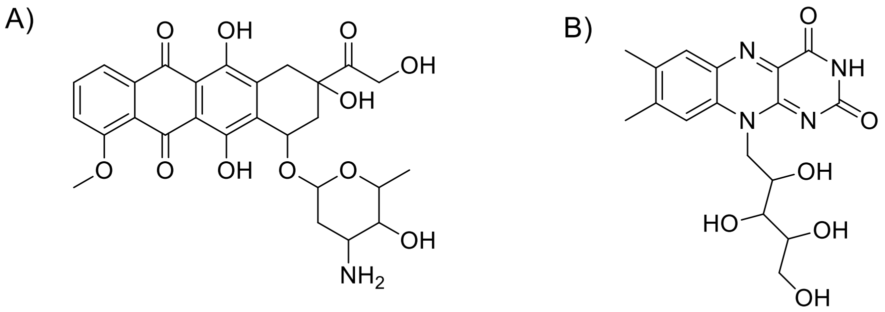

Doxorubicin

Riboflavin

Figure 4.15. Chemical structures of doxorubicin (A) and riboflavin (B).

Based on these initial results, the same experimental setup was used in the presence of MDA-MB-231-luc-D3H2LN cells. The cells were seeded in glass-bottom dishes and treated for 72 h with the riboflavin loaded micelles. Confocal microscopy imaging was performed on cells treated with riboflavin only (control) and on cells treated with riboflavin loaded micelles of **1a** and **2a**. The images show that riboflavin was internalised by cells in all three cases. This allows visualization of the cells. Since riboflavin is loaded in **1a** and **2a** it is possible that either the free riboflavin or peptide micelles are internalised by cells. In addition, release from micelles either outside or inside cells should be taken into account.

In the presence of riboflavin loaded **1a** micelles, higher signal intensity (when compared to figure 4.16 A showing cells and riboflavin without peptides) can be seen on the surface of cells suggesting that the **1a** loaded peptides mainly stay outside the cells. However, no clear fibrillar structures are observed suggesting that the resolution is limiting a better visualisation (of nanosized fibrillar structures) and that no bigger, micron-sized fibrillar aggregates are present (Fig. 4.16 B). In case of cells treated with **2a** loaded micelles, micron-sized fibrillar structures are observed between cells (Fig. 4.16 C). This could be due to self-assembly structures formed after enzyme treatment. However, due to resolution limitations of confocal microscopy this cannot be confirmed. Nevertheless, the sample containing cells treated with riboflavin loaded **2a** micelles were further analysed using the confocal setup- giving rise to individual layers being imaged separately, with each layer being 1 μm thick (Fig. 4.17).

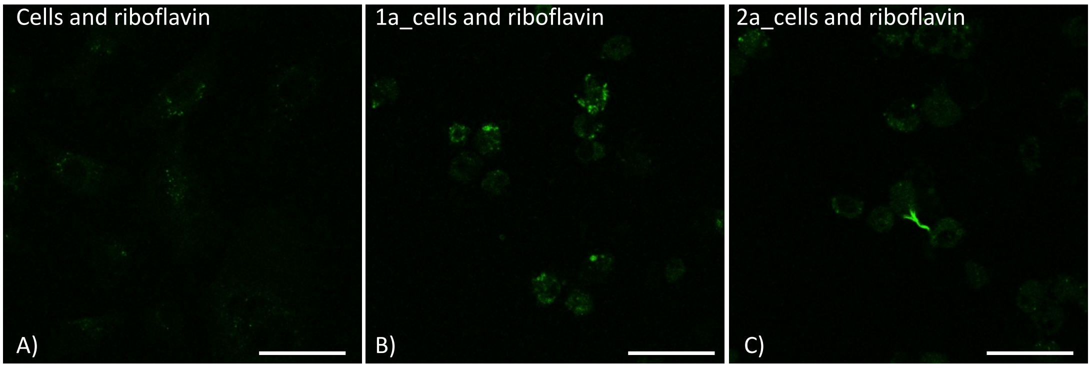

Figure 4.16. Confocal images of MDA-MB-231-luc-D3H2LN cells treated with A) riboflavin only; B) and C) with riboflavin loaded peptides **1a** and **2a** respectively. Scale bars: 50 μm.

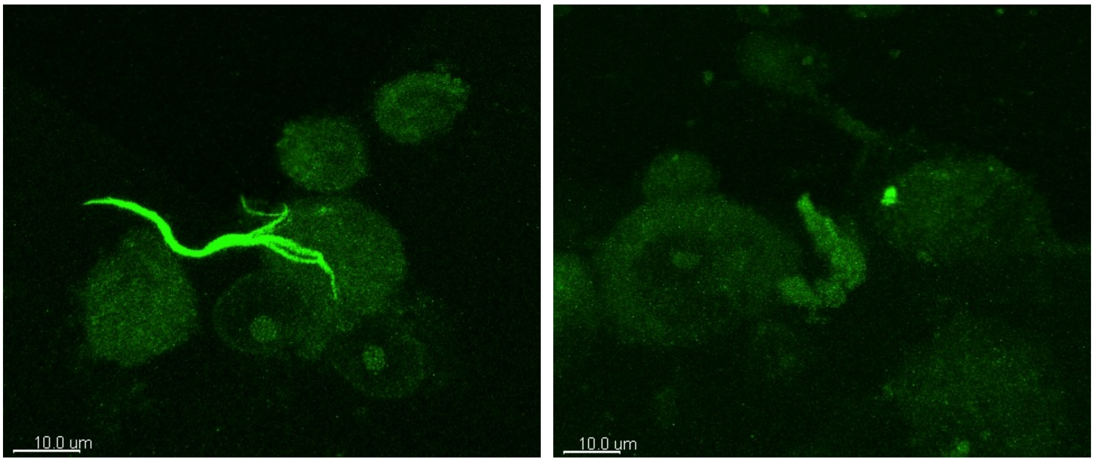

Figure 4.17. Confocal images- 3D rendered pictures of MDA-MB-231-luc-D3H2LN cells treated with riboflavin loaded **2a** (with number of scans being 14; z=14 μm; 1 μm steps).

Overall, confocal microscopy is useful for confirming riboflavin (doxorubicin; See Chapter 3) entrapment in the fibres. However, no conclusive information about morphological transition is obtained. The fibre-like structures observed in the presence of cells are most likely made of bundles of fibres, or they may represent a local gelation point. Also micron-size spots observed in the presence of riboflavin loaded peptides could be composed of fibres and require a higher resolution imaging technique. For comparison, Xu and co-workers found similar, micron-sized regions (figure 4.1 A)[3a] for enzyme triggered supramolecular assemblies (fibres) when examined with confocal microscopy. This is in agreement with what we see using confocal microscopy. The fact that these fluorescent spots in

Xu's work are made of fibres was confirmed only by TEM.[3a] In addition, in the presence of cells, Xu and co-workers study the ability of certain fluorescently labeled aromatic peptide amphiphiles to enter cells (their spatial distribution in cellular environment) based on their assembly state (dictated by the presence of the fluorophores that can disrupt/enhance fibre formation).[182] The peptide amphiphile spatial distribution in cellular environment studied using confocal microscopy is useful for visualisation purposes (i.e. demonstration of existence) of the self-assembly molecules in the presence of cells but it does not show the precise morphology of the assemblies (assessed by TEM, in absence of cells by Xu's team).[182] It is only by using CLEM that these two techniques (confocal and transmission electron microscopy) can be directly compared as the same sample region is imaged. However, TEM images (from CLEM, figure 4.3)[3b] in this example show low electron-dense pools that according to the authors should contain the hydrogelator but there is still no direct evidence of fibres in the presence of cells.

Resolution limitations of confocal microscopy make it difficult to be conclusive in the visualisation of physically trapped riboflavin molecules inside peptide nanostructures. Confirmation of fibre formation is needed and as such STORM should be a valid alternative to the confocal microscopy, to observe single fibres.

4.4.3 TEM and SEM on cells

Electron microscopy (TEM and SEM) was used to directly visualise the fibre formation around cancer cells and to study the effect of peptide administration on the overall integrity of the cells. These microscopy techniques, in addition to the confocal microscopy are challenging because of the two to three orders of magnitude size difference between cells (tens of µm) and fibres (tens of nm). In addition, as discussed above, the cancer cell surface is covered by different features such as membrane protrusions and/or secreted vesicles that make the clear visualisation of exogenous peptide nanofibres challenging.

Transmission electron microscopy

Prior to TEM imaging, HeLa cells were seeded on glass slides and incubated with 2.5 mM of each peptide for 72 h (alongside with the untreated cells). In order to image them, the cells were fixed with glutaraldehyde and underwent a complex processing including post fixation with osmium tetroxide, washing steps with different gradations of ethanol, followed by embedding in the resin that could have destroyed the fibres as recently suggested by Xu and co-workers.[3c] Representative TEM images for the **2a** treated cells are shown in figure 4.18.

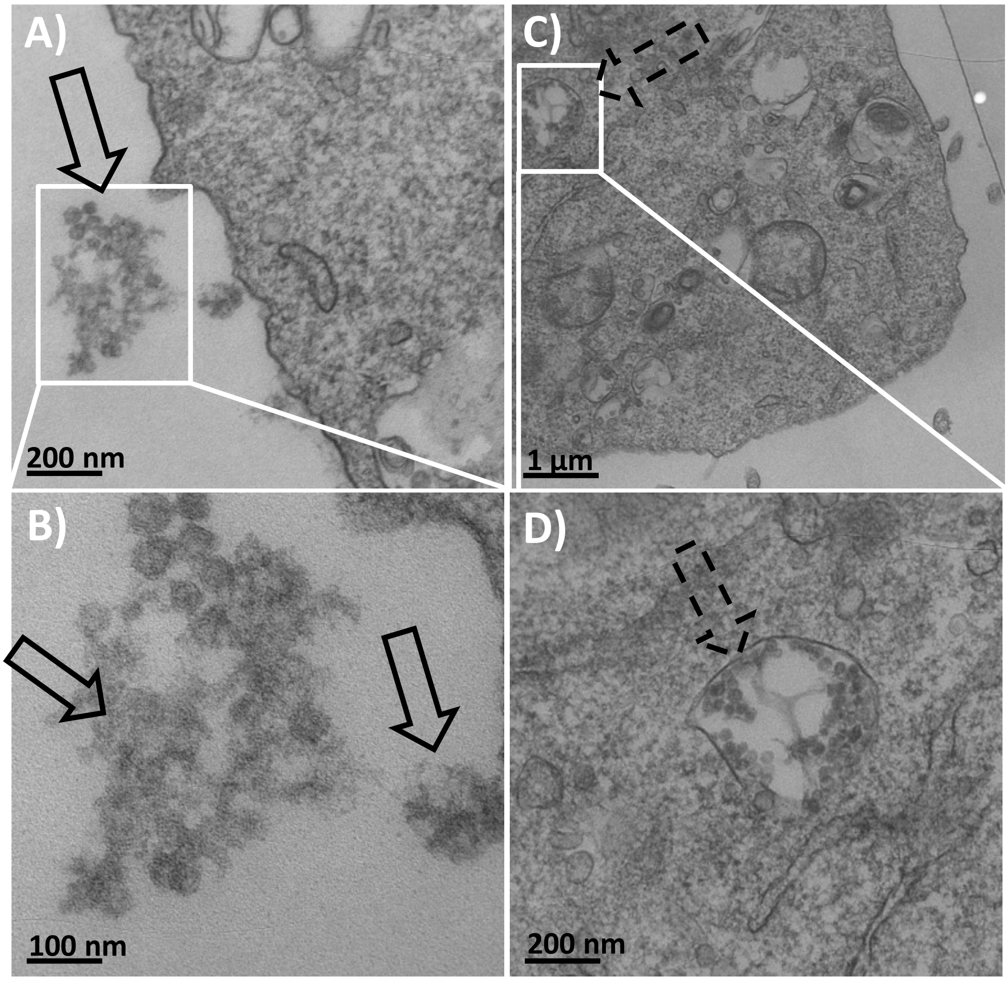

Figure 4.18. TEM images of HeLa cells treated with **2a** for 72 h: A) and B) exogenous peptide nanostructures (micellar aggregates) and the points of their digestion (left panels) are indicated with solid arrows; C) and D) internalised micellar aggregates (right panels) are indicated with dashed arrows.

TEM images of HeLa cells treated with **2a** show spherical aggregates close to the cell membrane being digested and broken, however no clear fibrillar structures are observed. The average size (diameter) of the spherical aggregates found outside the cell is 48 nm which corresponds to the size (42 nm) of the micellar aggregates found by AFM (Chapter 3). In addition, some of the micellar aggregates (38 nm) can be also seen inside the cell (Fig. 4.18 indicated by dashed arrows) suggesting some internalisation of the peptide in accordance with confocal microscopy imaging. TEM images of HeLa cells treated with **1a** are shown in figure 4.19. No clear fibrillar or micellar structures are visible in these images. It should be noted that the peptide nanostructures could be easily mistaken for sections of lamellipodia and filopodia-cytoskeleton actin projections on the edge of cells or invadopodia- actin rich protrusions in the cell membrane (usually found at the bottom of the cells; their presence requires a more precise characterisation). Invadopodia are an indication of high proteolysis and cell signaling and are found in metastatic cancer cells.[188] The presence of filopodia is confirmed by the SEM images (Fig. 4.20).

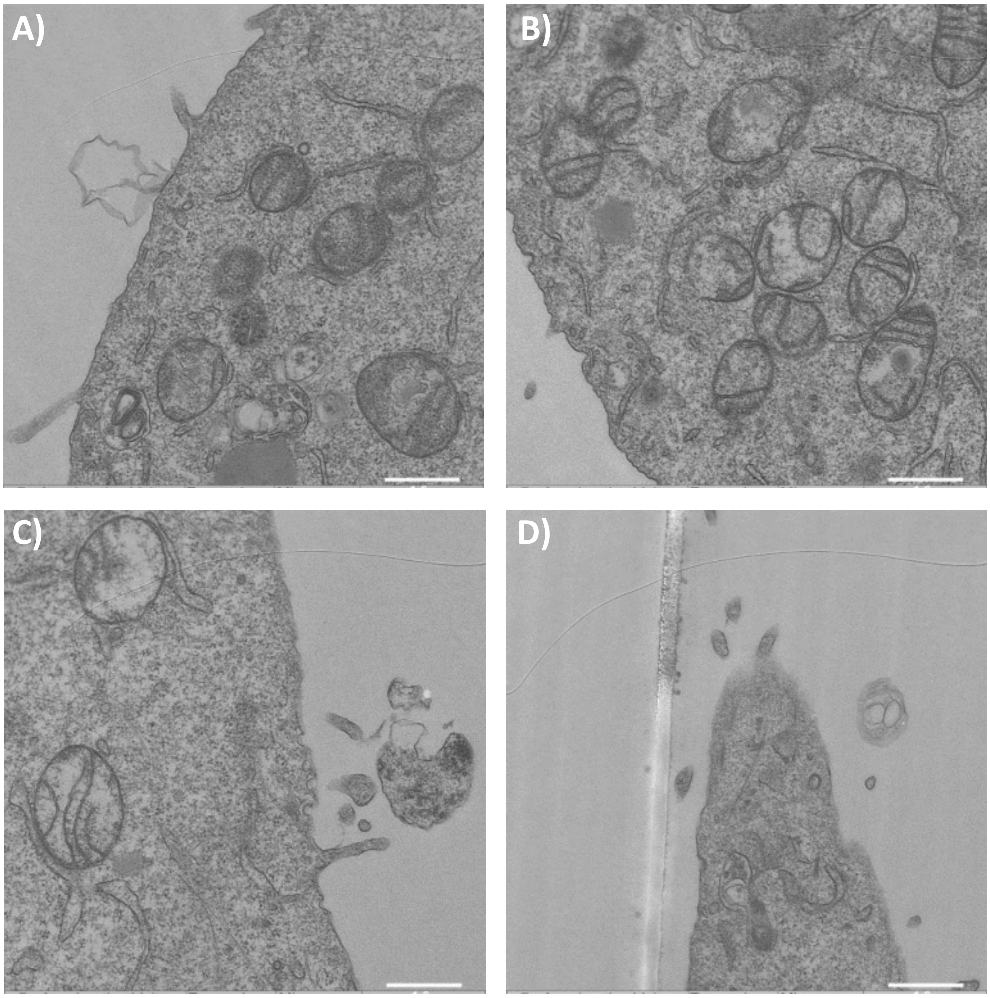

Figure 4.19. TEM images of HeLa cells treated with **1a** for 72 h showing the cell morphology including vesicles and sections of filopodia. No clear exogenous fibrillar or micellar structures are visible in these images. Scale bars: 1μm.

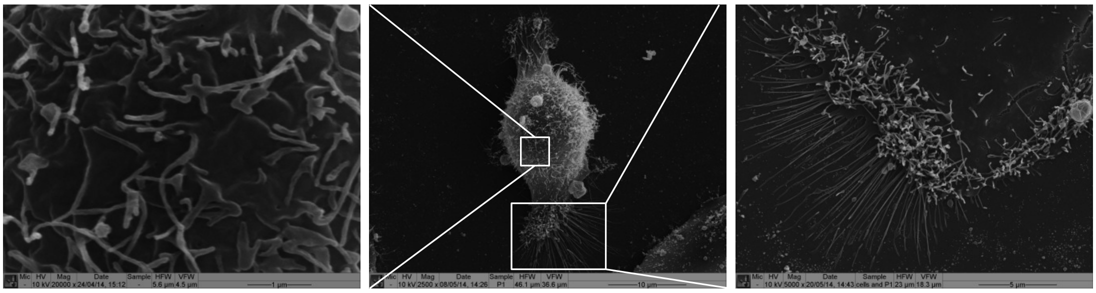

Figure 4.20. SEM images of MDA-MB-213 indicating cell protrusions- filopodia.

In conclusion, TEM imaging did not provide a useful technique to confirm fibre formation in presence of cancer cells. TEM is widely used to visualise nanostructures and serves as confirmation of their formation where issues with resolution limits arise i.e. TEM is often used in addition to confocal microscopy. However, in the presence of cells, where complex sample processing is required and the endogenous cell components (organelles, vesicles, cytoskeleton, protrusions) are visualised, it is not easy to demonstrate the presence of exogenous nanostructures based on peptide self-assembly. Therefore, TEM is not suggested as a first choice technique in this case, however, in combination with other techniques might provide useful information. Cryogenic-TEM could be a technique of interest, as it does not require staining and pre-treatment (fixation) steps allowing the analysis of the samples in their native environment, in the frozen-hydrated state (directly after freezing). In addition, the three-dimensional information about structures of interest (by three-dimensional reconstitution or cryo-electron tomography) can be obtained.[189]

Scanning electron microscopy

MDA-MB-231 cells were seeded on glass slides and incubated with 2.5 mM of each peptide for 72 h (alongside with the untreated cells) for SEM imaging. The cells were fixed with glutaraldehyde on the glass slides and freeze-dried. A gold coating was then applied using sputter coating and the samples imaged. No clear exogenous fibrillar structures were observed for the peptide treated samples. However, it is clear that the cell surface morphology is different compared to that of the untreated cells. When MDA-MB-231 cells are treated with **1a** or **2a** peptides show high secretion of vesicles. We speculate the increased secretion could be related to the cells secreting more MMP-9. Studies to confirm this hypothesis will be required to see whether the cells present higher MMP-9 activity/concentration. Representative SEM images for the cells on their own and cells incubated with **1a** and **2a** are shown in figure 4.21. This is shown for comparison of cell surface morphology in presence and absence of peptide amphiphiles. In addition, more SEM images for both **1a** and **2a** MDA-MB-231 treated cells and untreated ones are shown in figures 4.23, 4.24, 4.25 and 4.26. A control sample with **2a** in the presence of MMP-9 but without cells was examined showing fibre formation (Fig. 4.22).

Compared with the SEM images reported by Xu and co-workers showing porous network formation on cell surface, we do not observe this type of morphology. The difference in sample preparation consisted in pre-fixation step with glutaraldehyde in our case. In future experiments, we will consider the direct freeze-drying of cells after peptide treatment as an alternative way of sample preparation.

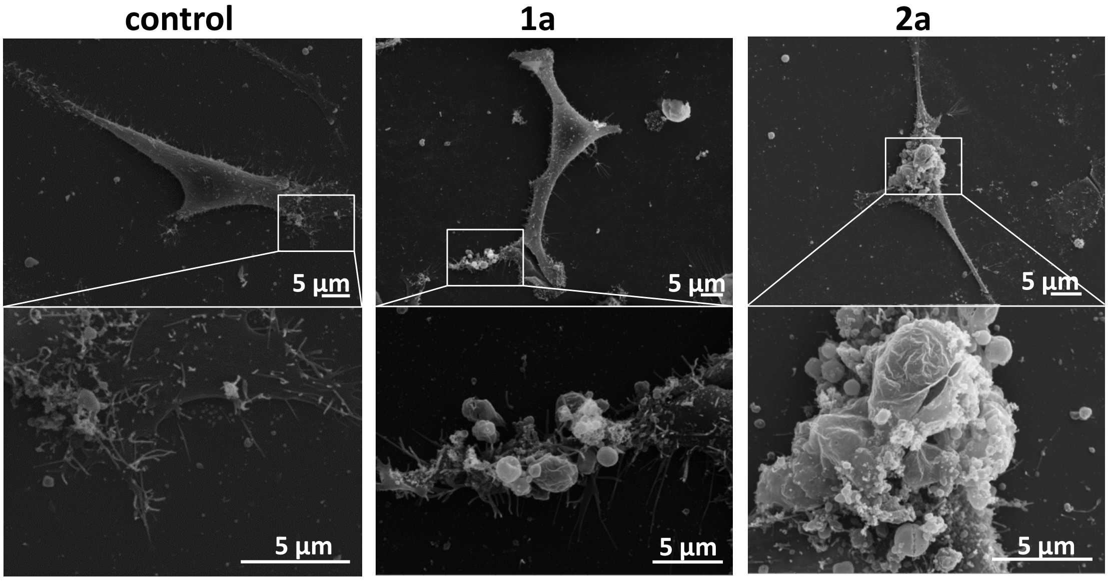

Figure 4.21. SEM images of MDA-MB-231 cells on their own and upon treatment with peptides **1a** and **2a** showing increased secretion of vesicles in peptide treated samples when compared to untreated cells. However, no clear evidence of networks of fibres can be found on cells or in their proximity.

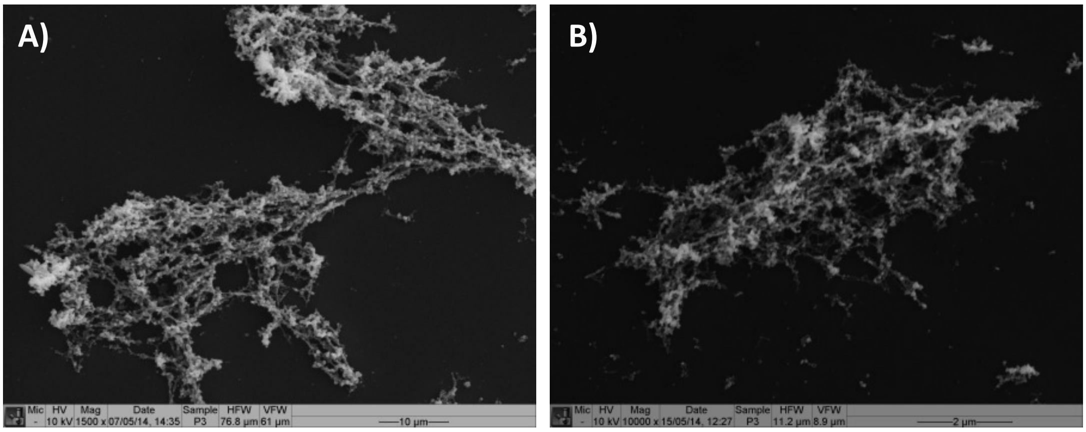

Figure 4.22. SEM images of **2a** (control sample) treated with MMP-9 for 72 h (in absence of cells) showing networks of fibres. These kinds of structures were expected to be found also in proximity of cancer cells.

Networks of fibres as shown in figure 4.22 for the peptide amphiphile **2a** treated with MMP-9, are expected to be seen on surface or in proximity of cancer cells. SEM images of peptide treated MDA-MB-231 cancer cells do not clearly show the presence of such a network. If we look closely there are some features that may be peptide nanostructures. For example, network like structures can be observed in figure 4.24 B and C for cells treated with **2a**. Porous, network like structures, similar to those shown by Xu and co-workers (Fig. 4.3) can be seen in figure 4.23 D for cells treated with **1a** and in figure 4.24 A for cells treated with **2a**. The main difference with Xu's work is that in our examples, these network like-structures are not covering the whole cell surface but are found on a smaller scale i.e. present only on vesicles or parts of cells. Cells show many features on their surface and in most cases vesicles are found to rupture as can be seen in 4.23 A and 4.24 B. In addition, small spherical features are often present on the surface of cells and also in cell proximity as can be seen in figures 4.23 B and C, and 4.25 B. These features could be the micelle forming peptide precursors. Their sizes are between 120-300 nm and are larger than expected when compared to the sizes obtained by AFM, shown in Chapter 3 (42-43 nm). When compared to the sizes obtained from DLS measurements in Chapter 3 (R_H between 165 and 240 nm) the spherical aggregates found with SEM are smaller. This is in agreement with the observation in Chapter 3, that in the solution state (R_H values) the aggregates are larger than the dry ones (sizes obtained from AFM and SEM). However, hydrodynamic radii cannot be directly compared to the dry samples visualised by SEM.

In figure 4.25 C, fibrous structures can be seen on the cell surface and near the cell. The most challenging part of analysing SEM results is the fact that is difficult to distinguish between intrinsic cell components and a possible exogenous peptide base nanostructure.

SEM images of untreated cells show similar morphology seen in the control samples reported by Schneider[62], Austin[185] and Kniss[186] and their co-workers described/presented in the introduction of this Chapter. However, vesicles (1-7 μm) and larger spherical features (13-18 μm) are not visible on the cell surface of untreated cells (control sample) which differentiates the peptide treated (Figs. 4.21, 4.23, 4.24, 4.25 and 4.26) from the untreated ones (Fig. 4.26).

Endocytosis/exocytiosis trafficking involved in the delivery of proteolytic enzymes- including matrix metalloproteinases (MMPs) has been associated with the delivery of MMPs to invadopodia. These specialized protrusions are utilized by cells for degradation of ECM. In addition, in cancer cell migration the recycling of focal adhesion proteins (i.e., integrin receptor recycling) also occurs through endocytosis/exocytosis processes.[186] Examples of specific peptides such as Neopetrosiamide A (NeoA, a tricyclic peptide 28 amino acid residues long, with no extended secondary structure reported) were found to induce the release of membrane bound vesicles, with integrin subunits and various receptors/proteins leading to inhibition of tumour cell adhesion. In addition, NeoA was found to trigger the formation of membrane projections. The biological activity of NeoA seems to be dependent on its disulfide bond pattern.[185] SEM and TEM images of MDA-MB-231 showing membrane projections are comparable to those presented in this thesis.[185] In our case we believe the vesicles could be secreting more MMP-9, however this hypothesis still needs to be confirmed.

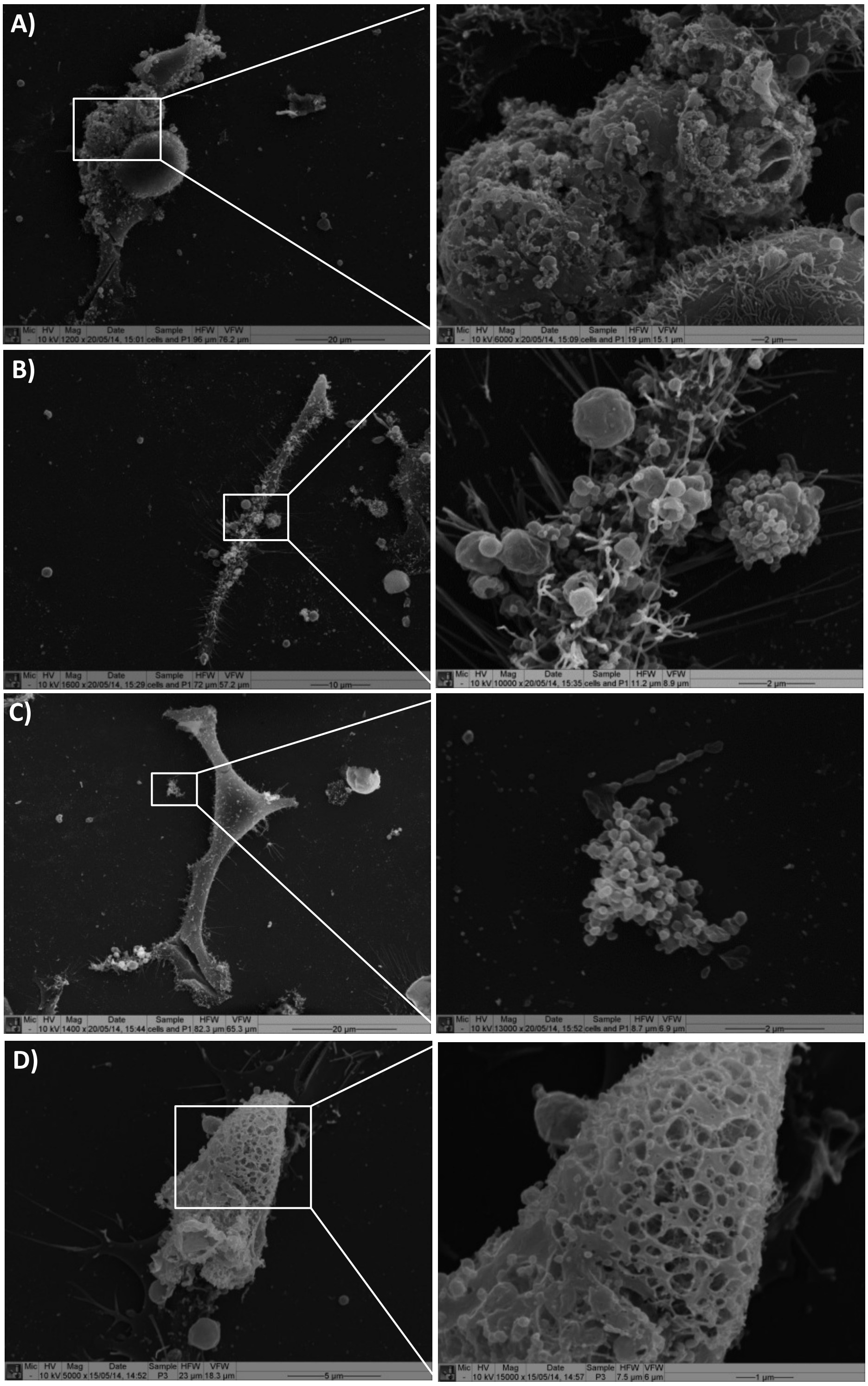

Figure 4.23. SEM images of MDA-MB-231 cells after incubation with **1a** for 72 h. A) An example of cell showing many features on the surface and is representative of the rupture of vesicles. B) and C) Examples of cells showing small spherical features on their surface and in their proximity (size between 120-300 nm). D) Example of cell showing porous, network like structures (maybe as result of the drying process).

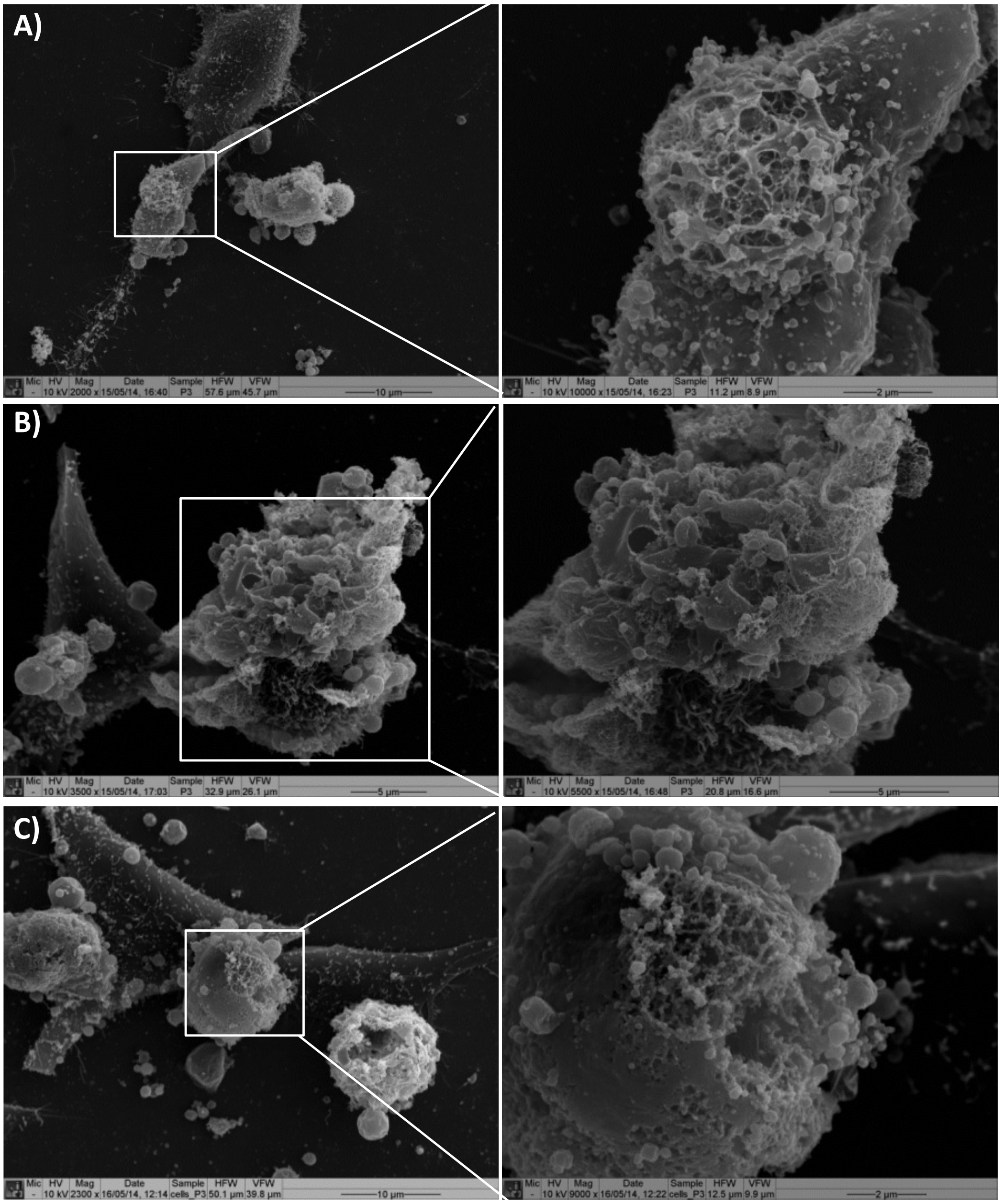

Figure 4.24. SEM images of MDA-MB-231 cells after incubation with **2a** for 72 h. A) Cell showing porous, network like structures maybe due to drying process. B) and C) Cells representative of vesicle rupture, where small and large (13-18 µm) spherical features can be found on the cell surface. Network like structures can be observed for both cells (at points of rupture).

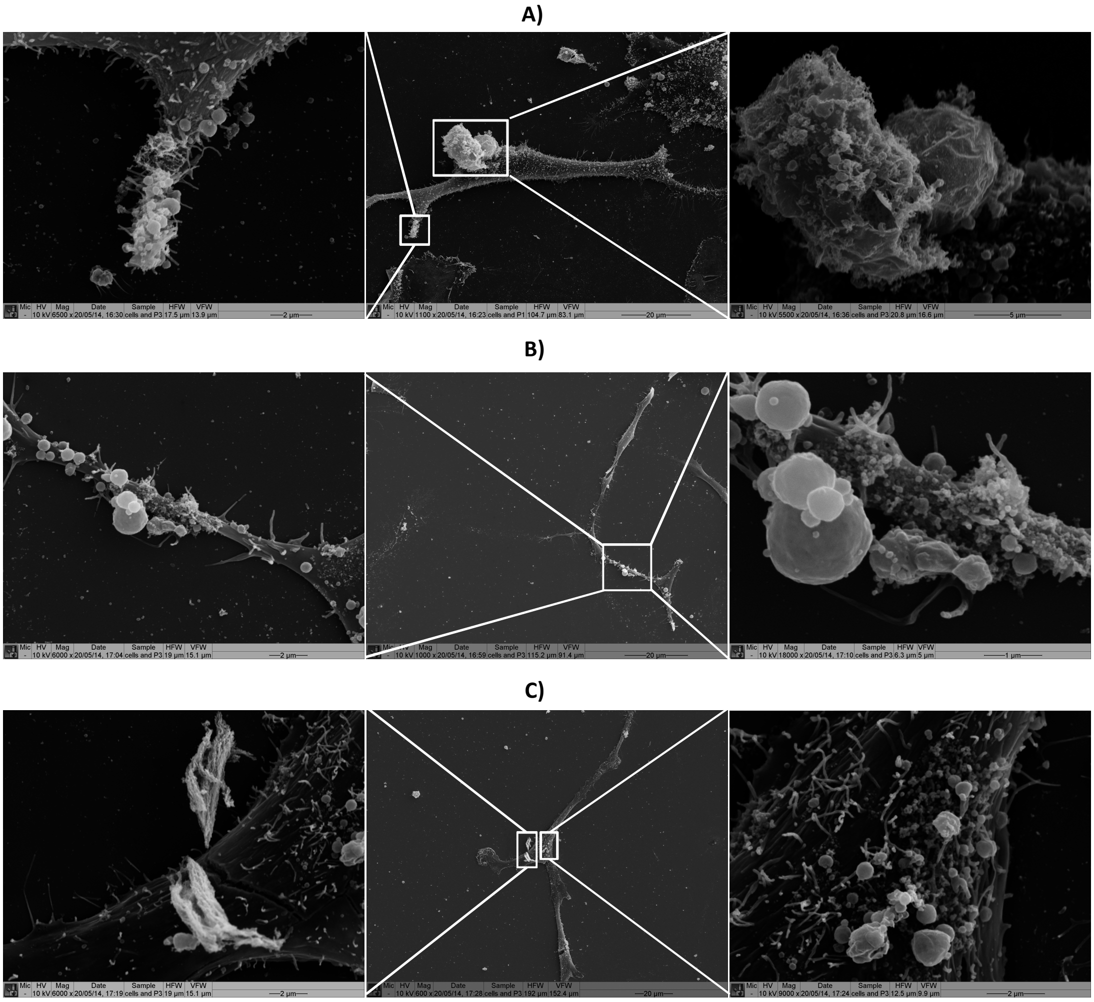

Figure 4.25. Additional SEM images of MDA-MB-231 cells after incubation with **2a** for 72 h. A) Left panel shows the enlargement of the cell surface pointing out the presence of small spherical features while the right panel is the enlargement showing the rupture of large features. B) Example of cells secreting vesicles and presenting small spherical features on the surface. C) Left panel shows the enlargement of fibrous structures found on the cell surface and in proximity of the cell (possibly indicating a dried ruptured feature) while the right panel indicates vesicles and the presence of filopodia on the cell surface.

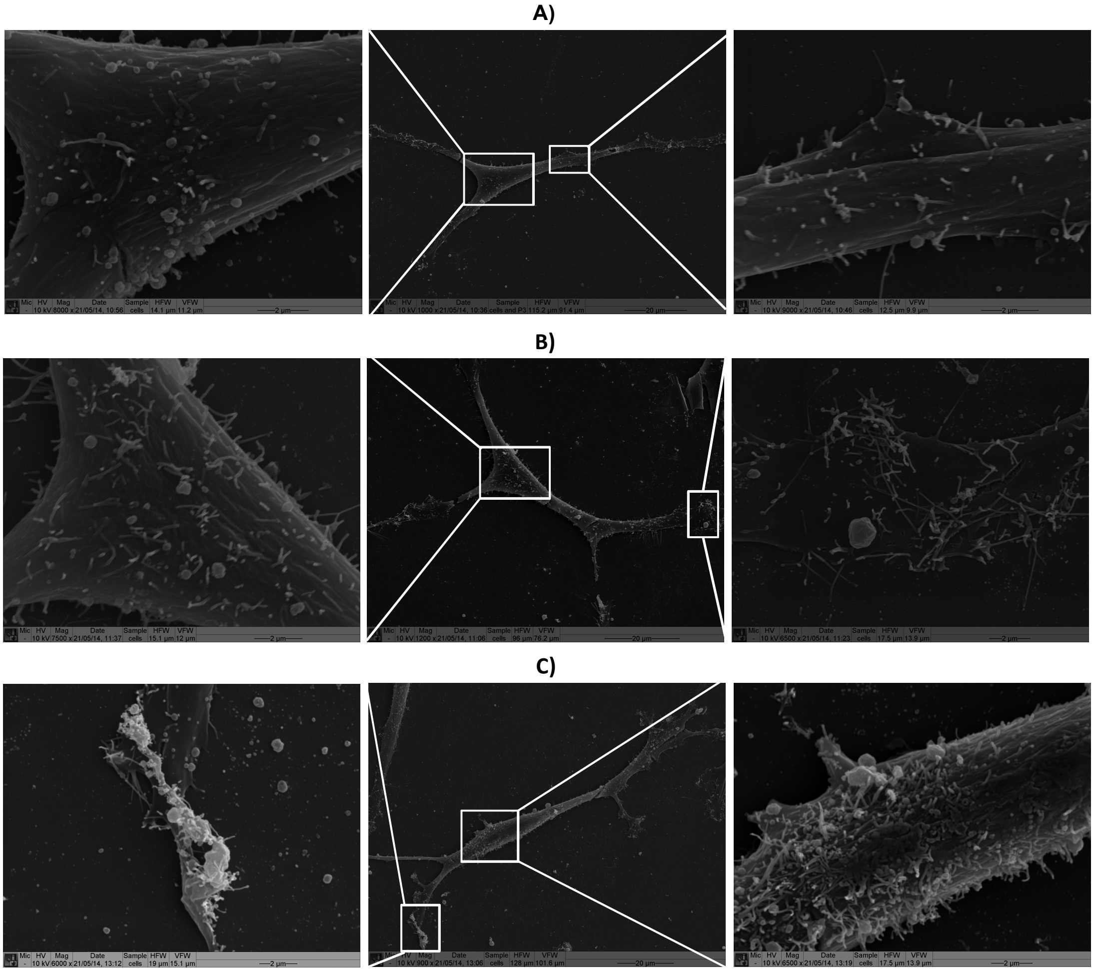

Figure 4.26. A), B) and C) show three examples of SEM images of MDA-MB-231 cells-control samples (not treated with peptide amphiphiles) indicating the presence of filopodia and vesicles on the cell surface. It can be noted that in these examples some spherical features can be observed but on a lower scale than that found on peptide treated cells.

Many different features were observed with SEM and an overall conclusion about the feasibility of SEM to image fibres around cancer cells is difficult to formulate. Some of the images point in the direction of expected fibrillar structures, however, it is difficult to be objective in this type of studies. The results presented here highlight the most common features observed over a wide number of cells imaged. Moreover with the methodology used, there is not enough evidence to support our hypothesis of fibre formation around cancer cells.

4.5 Conclusions and future work

In this study we analysed **1a** and **2a** enzyme responsive peptide amphiphiles that undergo micelle to fibre transition in the presence of MMP-9. We sought to establish a method for fibre visualisation in presence of cancer cells that secrete MMP-9. For this purpose we firstly quantified the MMP-9 secreted by human cancer cell lines (HeLa, MDA-MB-231 and MDA-MB-231-luc-D3H2LN) and found that the highest concentration of 32 ng/mL was secreted by the highly invasive MDA-MB-231-luc-D3H2LN cell line. As a consequence our future *in vivo* studies will be based on this cell line. In addition, this gave us an estimate of the average concentration of MMP-9 secreted by the examined cell lines to be in the range of 14-32 ng/mL and is in agreement with the enzyme concentrations used in Chapter 3 (50 ng/mL). *In vivo*, other MMP-s will be present, and especially the presence of MMP-2 (over-expressed in cancer) which may recognise and cleave the **1a** and **2a** sequences has to be taken into account.

While the results from fluorescence spectroscopy and confocal microscopy in the absence of cells look promising in terms of riboflavin entrapment in the fibres and fibrillar structure formation after enzyme treatment, the fibre visualisation in the presence of cancer cells still remains a challenge. After successful quantification of MMP-9 in different human cancer cells lines and attempts of fibre visualisation in their proximity using confocal microscopy seemed promising, resolution limits associated with this technique have to be overcome.

TEM and SEM imaging led to important insights about the feasibility of cell visualisation using EM and most importantly about the need to optimise (simplify) sample preparation conditions. Overall, microscopy techniques including confocal and electron microscopy were not successful in developing a straightforward method for fibre visualisation in proximity of cancer cells. Challenges include the resolution threshold of the confocal microscopy and the size difference of cells and exogenous peptide based fibrils for electron microscopy. In addition, cells analysed by electron microscopy present many fibrillar features on their surface (lamellipodia, filopodia, invadopodia) that makes a clear visualisation of peptide based fibres difficult. Overall, the results obtained are promising, but not yet conclusive.

A need of exploring the use of other techniques such as STORM for better resolution, cryo-TEM and cryo-SEM to avoid artefacts in drying, and CLEM to be able to use two different imaging techniques for the analysis of the same sample or localised part of sample, is required. Even though Xu and co-workers showed successful network formation, a more detailed study would be needed in order to prove that the porous structure observed is not formed due to drying or membrane degradation as shown by Schneider and co-workers. In addition, the smooth cell surface observed by Xu's team would need to be further examined as other examples of cancer cells show different cell surfaces.

Future work will involve use of a β-sheet specific stain such as Thioflavin T or Congo red (specific for β-sheet visualisation) to selectively stain only the fibres formed. D-peptides will be used as negative controls, as resistant to proteolysis by MMP-9. In addition, a FRET peptide containing the previously described substrate **2a** will be designed for confocal imaging.

4.6 Materials and methods

4.6.1 Materials

All reagents were purchased from Sigma Aldrich and used without further purification unless differently stated. The SensoLyte® Plus 520 MMP-9 assay kit and EDANS-glutamic acid were purchased from Anaspec. Fmoc-D-Phe-OH, Fmoc-D-Ala-OH and Fmoc-D-Leu-OH were purchased from Novabiochem (Merck).

4.6.2 SPPS

For the SPPS procedure See Chapter 3. D-peptides were synthesized following the same procedure using commercially available D-amino acids: Fmoc-D-Phe-OH, Fmoc-D-Ala-OH, Fmoc-D-Leu-OH (Appendix V). The SPPS of the **2a** FRET peptide included the commercially available EDANS-glutamic acid during a normal conjugation step while Dabcyl was conjugated to the N-terminus of the growing peptide chain (glycine) in the last step of SPPS prior to cleavage form the resin to obtain **Dabcyl-**GFFLGL**E(EDANS)**D-OH (See Appendix VI).

4.6.3 Confocal Microscopy

Samples were imaged in a liquid state using a Nikon A1 (Tokyo, Japan) or an Olympus FV1000 (Leica, Milton Keynes, UK) at the Beatson Cancer Research Institute (Glasgow). Identical exposure times and processing were used in all experiments. For riboflavin visualization images were acquired using a 405 nm laser, 8 % laser power over a field of view of 200 by 200 μm.

4.6.4 Fluorescence

Riboflavin was solubilized in 0.1 M NaOH by sonication to obtain a 1 mM stock solution. This was further diluted to obtain a 0.05 mM stock 2 solution. Fluorescence emission spectra of riboflavin (1.25 μM) were measured in the presence and absence of peptides on a Jasco FP-6500 spectrofluorometer. Riboflavin was excited at 440 nm and the data collected in the range between 480 and 750 nm. The excitation and emission bandwidths were both set to 5 nm. Fluorescence emission spectra for determination of riboflavin emission intensities in solvents with different polarities were measured on an X Fluor Safire 2 fluorescence plate reader (version: V 4.62n) at the Beatson Cancer Research Institute (Glasgow). Riboflavin was excited at 350 nm and the emission data were collected in the range between 360 to 600 nm. The emission wavelength step size was set to 2 nm and the excitation and emission bandwidths to 5 nm each.

4.6.5 Transmission electron microscopy (TEM)

TEM imaging was performed at the University of Glasgow Electron Microscopy facility. Cells were allowed to adhere on previously sterilized glass coverslips, serum starved overnight and treated with 100 nM PMA to induce MMP-9 production. Then, they were treated with 2.5 mM of peptide amphiphiles (**1a** and **2a**) for 72 h to allow the morphological transition to occur. Primary fixation (1.5% glutaraldehyde in 0.1 M sodium cacodylate buffer) was performed for 1 h at 4°C. After fixation the cells were rinsed (3 x 5 min) with sodium cacodylate to remove any residual glutaraldehyde. After this step, the samples where post-fixed with 1% osmium tetroxide for 1h at room temperature followed by washes with distilled water (3 x 10 min). Following this, 0.5% aqueous uranyl acetate was added and allowed to stain for 1 h in dark. The sample was then dehydrated with a graded series of ethanol (30%, 50%, 70%, 90%, absolute ethanol and dried absolute ethanol) to 100% ethyl alcohol, and treated with propylene oxide. Subsequently the sample was infiltrated with Epon-Araldite resin overnight at room temperature and cured at 60°C for 24 h in embedding moulds. Coverslips were removed from the blocks, which were then re-embedded at 60°C overnight. The sectioning (60-70 nm sections) was performed followed by a contrastaining step (2% methanolic uranyl acetate + Reynolds lead citrate). Images were acquired using a LEO G12 energy filtering transmission electron microscope operating at 120kV fitted with 14 bit/2 K Proscan CCD camera.

4.6.6 Scanning electron microscopy (SEM)

SEM imaging was performed at the University of Glasgow Electron Microscopy facility. Sample preparation was performed as described for TEM. After peptide treatment, the cells were fixed on glass coverslips as described above (primary fixation with glutaraldehyde in cacodylate buffer for 1 h). The cells were then freeze-dried in liquid nitrogen. Samples were subsequently sputter coated with gold (8 nm thick coating) under vacuum and imaged using a JEOL-JSM 6400 field emission scanning electron microscope operated at an acceleration voltage of 10 kV.

4.6.7 MMP-9 activity assay

The activity of the MMP-9 was assessed using the SensoLyte® Plus 520 MMP-9 assay kit (Anaspec). Briefly, a 96-well plate covered with MMP-9 antibodies was used to capture the MMP-9 from the sample supernatant. Once the pro-MMP-9 was captured by the antibodies the activation step with APMA (2h) was performed. After activation the assay substrate (5-FAM/QXL™ 520 FRET) was added and the fluorescence reading performed using an X Fluor Safire 2 fluorescence plate reader ($\lambda_{ex}/\lambda_{em}$ 490 nm/520 nm). The company protocol was followed to obtain the MMP-9 activity. The MMP-9 in the supernatant of HeLa, MDA-MB-231 and MDA-MB-231-luc-D3H2LN cells was quantified.

5 Post-polymerisation functionalization of amine rich microgels

5.1 Introduction

Microgels are crosslinked polymer particles that swell in a good solvent or when certain external stimuli are applied (Chapter 2, Section 2.6.1).[86,190] These particles are prepared by polymerizing monomers in the presence of crosslinking agents resulting in the formation of stable, covalently crosslinked networks.[136] The presence of chemical crosslinks within the structure prevents the dissolution of polymer chains. Because of their particular structure, chemically crosslinked polymers (compared to physically crosslinked gels such as those described in Chapter 3) don't dissolve, but tend to swell in compatible solvents.[191] As a result they form colloidal suspensions rather than solutions.[192] Depending on the monomer composition microgels can swell in different solvents. If the solvent is water they are called hydrogels. These three-dimensional polymer networks can contain large amounts of water making them potentially useful in medicinal applications.

The introduction of carboxylic acids or primary amine containing monomers within the microgel structure is advantageous because these functional groups introduce pH responsiveness but also provide reactive sites that allow for further functionalization.[193] Different functionalities, including e.g. sugars or peptides for biological recognition or to introduce enzyme-responsiveness (See Chapter 2) can be conjugated to microgels to obtain targeting systems for drug delivery. To attach peptides to polymers post-polymerization two main methods are used, either adding them step-wise on the surface (using solid phase peptide synthesis[194]) or grafting to pre-synthesized peptides in one-step.[195] An example of solid phase peptide synthesis directly onto polymeric particles (in this case micron sized) was previously reported on polyethyleneglycol acrylamide based particles.[148a] On smaller (nanoscale) particles, step wise solid phase peptide synthesis is challenging because some basic steps of SPPS such as washing and filtration are incompatible with small particles, resulting in loss of material and difficulty of recovery during each step.

Hydrogels that are functionalised with peptides may be of use in development of enzyme-responsive materials (See Chapter 2). Microgels have not been used in this context, but design principles for macroscopic gel structures or beads may inform the synthesis of enzyme-responsive microgels. One approach to develop enzyme responsive hydrogels is the introduction of enzyme cleavable linkers as crosslinks within the polymer particles (Chapter 2, Section 2.6.1). In these examples, the final physical structure of the polymer changes upon enzyme cleavage of crosslinking peptides, eventually leading to dissolution. An alternative approach in developing enzyme responsive microgels can be followed where the peptide sequences are not introduced as crosslinks but as pendant sequences that carry charged groups (in this case introduced by SPPS). In particular, by introducing zwitterionic peptide sequences which carry oppositely charged amino acids at either side of the cleavable linker on the particles and by cleaving this linker using enzymatic catalysis, their charge density changes which can induce swelling (Chapter 2, Section 2.6.1).[148a]

A variety of pH responsive colloidal microgels have been demonstrated (See Chapter 2, Section 2.6.1). The presence of ionisable groups within their structure makes them pH responsive. The majority of the research conducted on pH responsive microgels is based on anionic, carboxylic acid functionalised microgels. The first example of pH responsive microgels with high concentration of primary amines was recently presented by Saunders and co-workers.[144] These amine rich microgels may be suitable candidates for the development of enzyme responsive microgels. They could constitute a platform for development of vehicles for anticancer agents. Their size and enzyme responsiveness would be advantageous for targeted cancer therapy (See Chapter 2).

Therefore as part of introduction of this Chapter, a detailed description of the work performed by Saunders and co-workers focused on the preparation of amine rich microgel particles will be presented.

5.1.1 Synthesis and characterisation of amine rich microgel particles

Microgels used in this Chapter were synthesized and characterised following the optimized procedure developed by Saunders and co-workers.[144] A two-step synthetic method was used to prepare colloidal stable, pH sensitive microgels as can be seen in figure 5.1. Poly (N-vinylformamide-*co*-(N-vinylformamido) ethyl ether) - poly(NVF-NVEE) microgels were synthesised using non-aqueous dispersion (NAD) polymerisation. Subsequently, the microgels were hydrolysed to give amine rich, pH responsive microgel particles poly(vinylamine-*co*-bis (ethyl vinylamine) ether) - poly(VAM-BEVAME). The mechanism of poly(NVF-NVEE) formation involves dispersion polymerisation where both the monomers (NVF, NVEE) and the initiator (AIBN- azobisisobutyronitrile) are soluble in the polymerization medium (ethanol in this case) while the resulting polymer (poly(NVF-*co*-NVEE)) is not soluble. The initiation step takes place in homogeneous medium where the primary particles form during a nucleation step. This is due to the aggregation of growing polymer chains that become insoluble in ethanol. As the NVEE monomer is more hydrophobic than the NVF is, the proposed mechanism involves the primary particles with high NVEE content forming and precipitating from ethanol.[144] This results in a greater concentration of the crosslinker in the core of the particles. After nucleation, colloidal stabilization of the particles occurs due to the adsorption of the PVP-*co*-PVA (poly(1-vinylpyrrolidone-*co*-vynil acetate)) stabilizer. When the PVP-*co*-PVA concentration is sufficient to guarantee particle stability the aggregation stops. The particle growth then proceeds in individual particles as they absorb monomer from the continuous phase, at a constant particle concentration. The resultant microgels were relatively monodisperse and characterised by NMR, FTIR and optical microscopy.

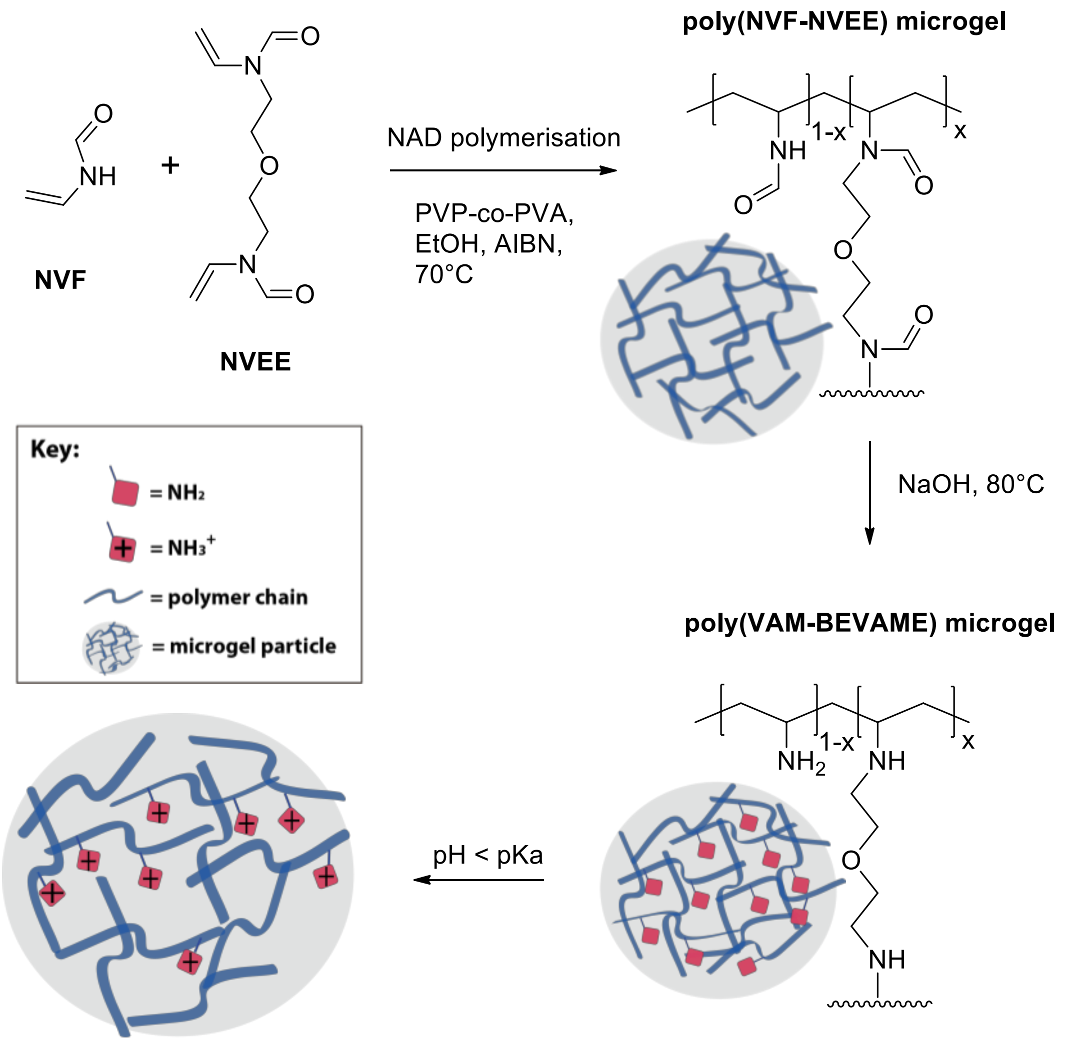

Figure 5.1. Schematic representation of poly(NVF-NVEE) microgel synthesis by non-aqueous dispersion (NAD) polymerisation followed by hydrolysis to poly(VAM-BEVAME) microgel. By setting the pH to values higher than the pK_a of the microgel, swelling due to amine protonation is achieved. [Adapted from reference 144- Saunders and co-workers].[144]

The crosslink density determines the behaviour of polymers, such as the extent of their swelling and can be controlled during the synthesis.[196,197] A set of microgels with varying crosslinking densities pVAM-xBEVAME (x being 4, 9 or 13 mol%) were examined previously by Saunders group and the best performing formulation was VAM-9BEVAME having better stability compared to 4 mol% and having better swelling properties compared to 13 mol%. These VAM-9BEVAME microgels have been show to be functionalizable with pyrene molecules.[144]

5.2 Objectives

In this Chapter, the objective is to develop enzyme responsive systems based on amine functionalised microgels by post-polymerisation introduction of pendant enzyme cleavable linkers. We set out to develop a method for microgel particles modification in order to make them enzyme responsive- undergo swelling/deswelling in response to disease related enzymes such as MMP-9 and phosphatase.

Firstly, we sought to reproduce Saunders's work with the focus on the synthesis of the microgels, as described in the introduction. Briefly, NVEE crosslinker needs to be synthesised and characterised. The obtained NVEE can then be co-polymerised by NAD polymerisation with the commercially available NVF monomer to obtain crosslinked particles, followed by hydrolysis to obtain primary amine rich microgels.

Next, to introduce pendant enzyme cleavable linkers on microgel particles the methodology of conjugation needs to be developed. Several strategies were explored resulting in the development of the most promising one, performed in DMF, following conventional solid phase peptide synthesis rules. Two different substrates, sensitive to two different cancer related enzymes (phosphatase and MMP-9) were chosen to be conjugated on the polymeric particles (Fig. 5.2). Throughout this chapter the main characterisation techniques used to assess functionalization are DLS and zeta potential to assess size and charge changes after each reaction step.

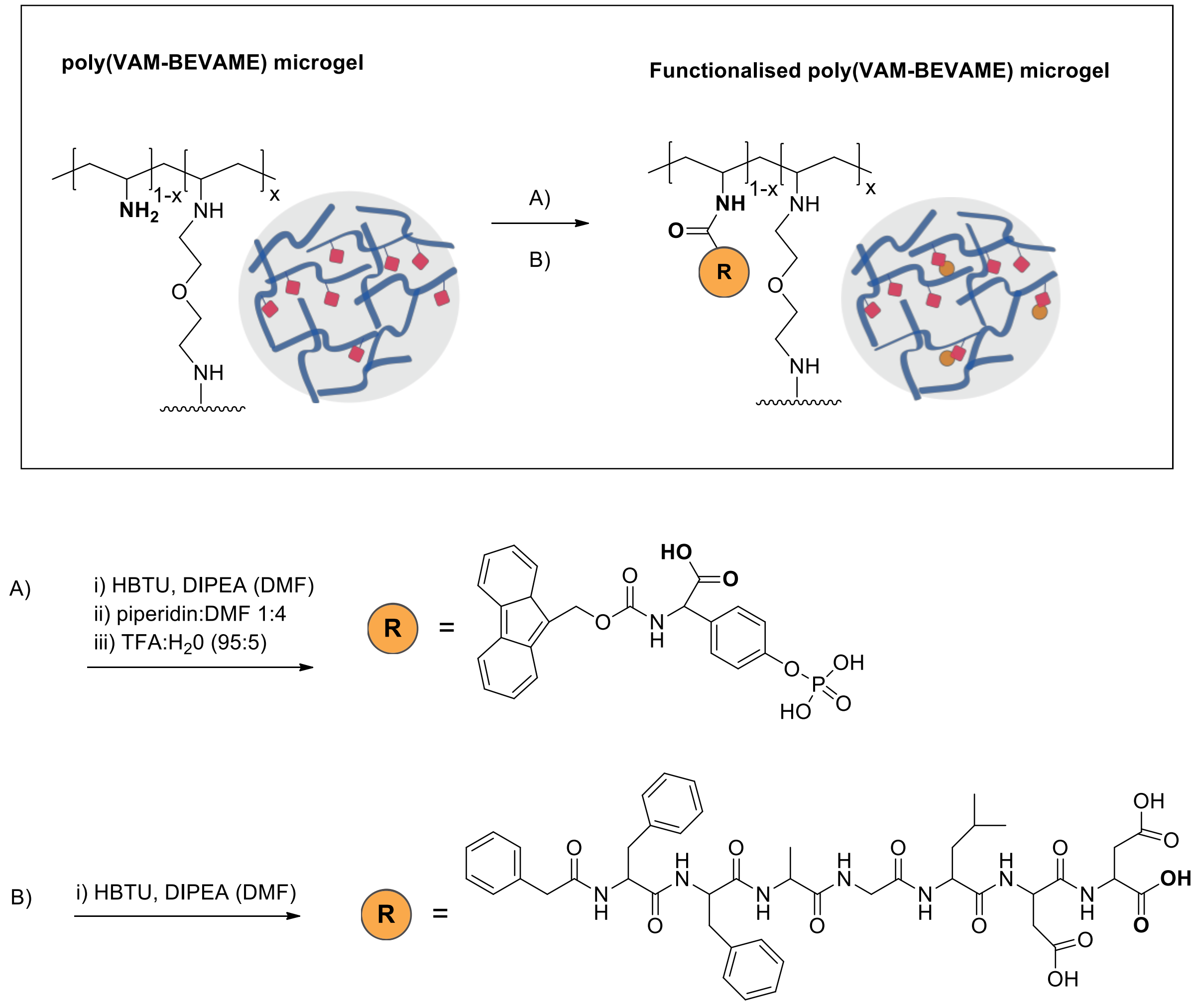

Figure 5.2. Schematic representation of the poly(VAM-BEVAME) microgel and functionalization conditions for two different systems: to obtain A) a phosphatase responsive and B) an MMP-9 responsive microgel. After functionalization i.e. reaction between the amine groups on the microgel and the carboxyl groups of A) Fmoc-Yp and B) PhAc-FFAGLDD amide bond formation is expected.

5.3 Results and discussion

The first objective was to reproduce production of poly(VAM-BEVAME) microgels developed by Saunders and co-workers.[144] In order to prepare the microgels, the acid stable crosslinker, NVEE was first synthesised by modifying the NVF monomer with an ether linker (Bis (2-bromoethyl) ether) and characterised by nuclear magnetic resonance (NMR), Fourier transform infrared spectroscopy (FTIR) and elemental analysis and the results compared to the previously reported data.[144] The FTIR spectrum for NVEE is shown in figure 5.3 A. The bands due to the vinyl groups (1632 cm^{-1}), the –NHC(=O)H stretch (1680 cm^{-1}) and that of the ether-type band (CH_2-O-CH_2) at 1090 cm^{-1} for NVEE are the same as those reported by Saunders and co-workers.[144] To confirm that the product did not have residual NVF the *absence* of the bands typical for starting material was assessed. The NVEE spectrum does not show: the amide II band (1510 cm^{-1}), the N-C-H bending mode at 1380 cm^{-1} and the N-H band at 3260 cm^{-1}. The ^{1}H-NMR spectrum of NVEE (figure 5.3 B) shows peak positions that match those reported by Saunders and co-workers.[144] Two environments have been observed for the hydrogen atoms attached to the amide (e_{cis} and e_{trans}) and the vinyl hydrogen closer to the nitrogen atom (c_{cis} and c_{trans}). ^{1}H NMR data show that the proportion of the integrated areas for $e_{\text{cis}}/e_{\text{trans}}$ and for $c_{\text{cis}}/c_{\text{trans}}$ is 2:1 for the NVEE crosslinker.[144] The elemental analysis data (figure 3 c) show the measured (and expected) %C, %H and %N values for NVEE to be 46.8 % (56.6 %), 6.5 % (7.6 %) and 8.7 % (13.2 %), respectively. These data show that NVEE is not compositionally pure as reported previously as the values are lower than the expected ones.[144]

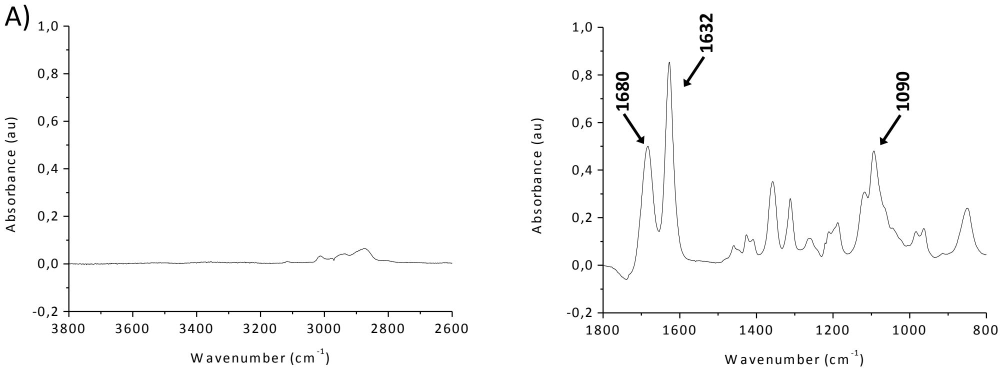

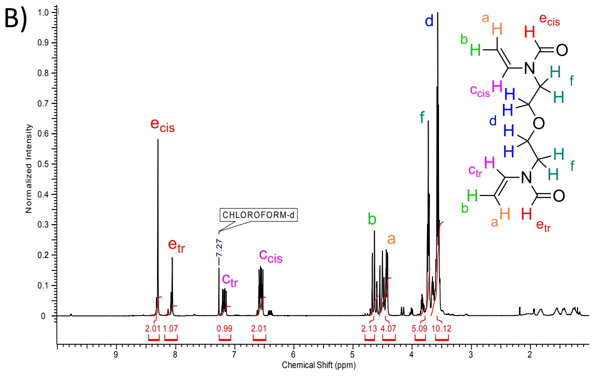

C)

Element	%C	%H	%N
Measured	46.8	6.5	8.7
Expected	56.6	7.6	13.2

Figure 5.3. A) FTIR spectra of NVEE; B) NMR spectra of NVEE and C) elemental analysis data for NVEE.

Due to difficulties in obtaining pure material after several attempts, the polymerisation was then completed at the University of Manchester, using pure material obtained together with the Saunders group. NAD polymerisation of NVF and NVEE in ethanol was performed to obtain poly(NVF-9NVEE) microgel particles. The polymerisation was followed by hydrolysis in NaOH to obtain amine rich poly(VAM-9BEVAME) particles. Microgel particles obtained after both steps, polymerisation and hydrolysis, were monitored using optical microscopy. Optical images (Fig. 5.4) show poly(NVF-NVEE) microgels in ethanol and water to be monodispersed particles. After hydrolysis some aggregation is observed as can be seen in figure 5.4 C and D. In figure 4 C, showing a larger scan area can be seen that there are monodispersed colloidal stable particles in addition to aggregates. Optical microscopy was used to confirm monodispersed particles as reported by Saunders and co-workers.[144]

In this study only the VAM-9BEVAME was synthesised and considered for further functionalization. These microgels have the highest primary amine proportion reported so far for colloidal stable microgels. In detail, after complete hydrolysis the 9 mol% crosslinking density microgels present 90 mol% of primary amines. However this is an estimated value as it is still a challenging to determine experimentally the exact amine content. Based on this approximation and on the molecular weight of the VAM monomer the number of moles of primary amine was determined as a starting point for further functionalization.

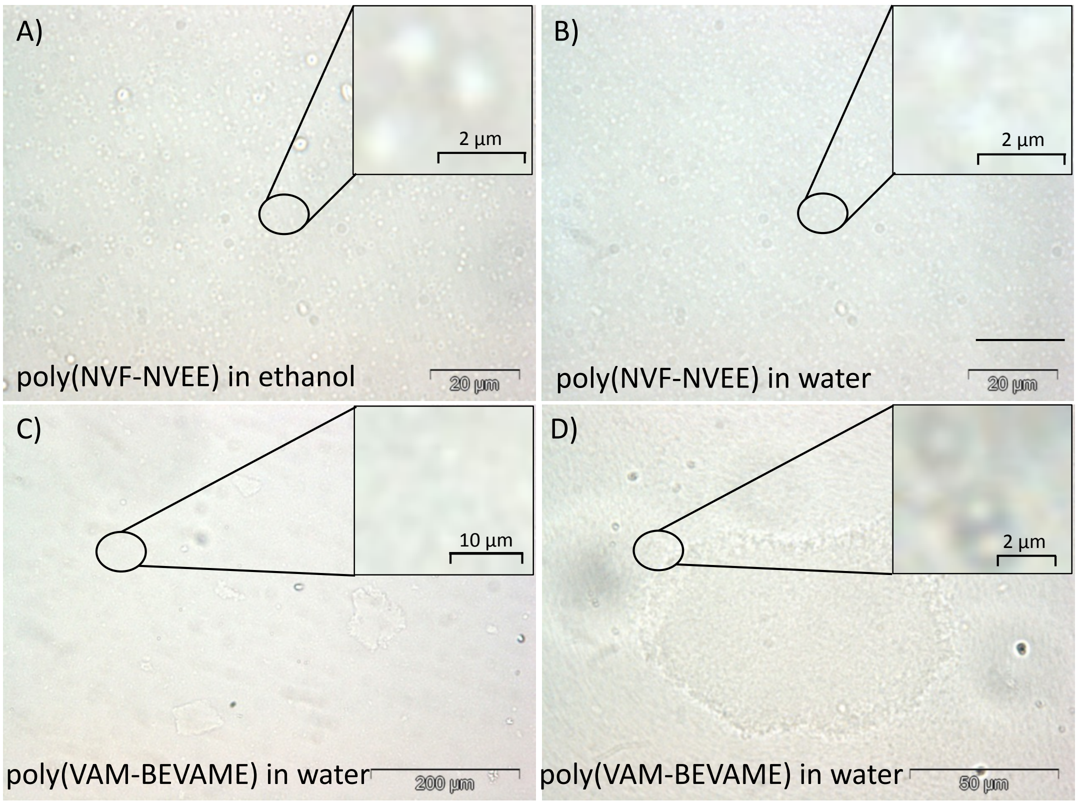

Figure 5.4. Optical microscopy images for poly(NVF-NVEE) in ethanol (A) and water (B); and for poly(VAM-BEVAME) in water (C and D).

5.3.1 Post-polymerisation modification

Post-polymerisation modification of poly(VAM-9BEVAME) microgels required method development and optimisation. For this purpose functionalization in two different solvents was performed: water and DMF (dimethylformamide) with the latter giving better results. Therefore we will focus on the microgel functionalization in DMF and those results will be presented in this Chapter of the thesis. The issues encountered in water state will be only briefly described (data not shown).

Post-polymerisation modification in water

Firstly, post-polymerisation modification of poly(VAM-BEVAME) was studied in water using a variety of conditions and reagents (data not shown) based on a previously reported functionalization with pyrene.[144] The reactions conditions were chosen with relatively low reagent concentrations in order to only functionalize a proportion of the amines present. Due to strong, irreversible aggregation in water after addition of reagents, visible by eye which, was also confirmed by optical microscopy (data not shown) these methods were abandoned. Problems with colloidal stability were due to electrostatic interaction between positively charged amines and negatively charged phosphate groups. Three ways to improve colloidal stability were assessed: (i) lowering the pH to values below the pK_a of FmocYp (pK_a of the carboxyl group is 2.2 while that of the phosphate group of the side chain are 2 and 5.8) in order to protonate carboxyl and the phosphate groups, (ii) increasing the ionic strength by addition of NaCl and (iii) using low concentrations of reagents (FmocYp-OH, NHS, EDC). None of the mentioned conditions significantly improved the colloidal stability and aggregation was observed for all of them. Therefore it was decided that water was not the optimal solvent for poly(VAM-BEVAME) functionalization and that FmocYp with protected phosphate group should be used.

Post-polymerisation modification in DMF

Subsequently, reaction conditions were chosen based on a conventional SPPS and performed in DMF followed by Fmoc removal and phosphate group deprotection (Fig. 5.7). Because of problems with solvent exchange such as freeze-drying and resuspension in a new solvent which resulted in irreversible aggregation (data not shown), and because of the strong electrostatic interaction between the microgel and the phosphorylated amino acid, DMF was chosen as solvent, because it is miscible with water. With a few cycles of centrifugation and resuspension solvent exchange can be performed without affecting the colloidal stability of microgel particles. The R_H of microgel particles (0.1 wt%) after solvent exchange was calculated to be 3.6×10^2 nm. Also in DMF the electrostatic interactions are expected to be minimised.

Firstly, a commercially available phosphotyrosine (FmocYp-$N(CH_3)_2$), a single amino acid containing the protected phosphate group was chosen for conjugation (in order to avoid cross-reactions and aggregation). This simple system requires a single coupling of the amino acid followed by deprotection steps and subsequent enzyme responsiveness assessment.

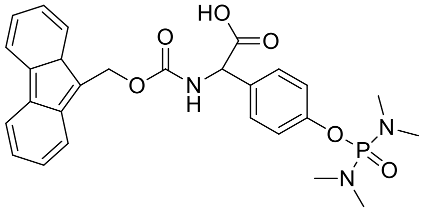

Figure 5.5. Chemical structure of (FmocYp-N(CH_3)$_2$).

In a later stage, an MMP-9 responsive sequence (PhAc-FFAGLDD – See Chapter 3) was chosen for coupling to the microgel. This sequence was used to explore the feasibility of one-step conjugation of a longer peptide to microgel particles. It is hoped that this optimised approach of conjugation described here could then be extendable to other peptide sequences (to obtain responsiveness to other enzymes).

a) *Phosphatase responsive microgels*

A three-step reaction was chosen for microgel functionalization involving conjugation and two orthogonal deprotections performed stepwise (figure 5.7). By coupling FmocYp-N(CH_3)$_2$ on microgels, changes in microgel behaviour are expected as can be seen in figure 5.6. In detail, after coupling a deswelling is expected due to a change in the overall charge of the microgel as amine groups are reacted with carboxyl groups of amino acids/peptides to form peptide bonds. This post-polymerisation modification results in introduction of highly negatively charged phosphate groups (after deprotection) on microgel particles. This is expected to result in the shrinkage of the particles due to electrostatic attraction between free amines and phosphate groups. After functionalization, microgel swelling can be assessed by addition of phosphatase and monitoring of changes in particle size. Enzymatic removal of the phosphate groups should trigger swelling due to an overall positive charge restored on the particles. The swelling would increase the mesh size and could result in the release of physically entrapped drugs. The prediction of microgel behaviour at different stages shown in figure 5.6 is based on the charge repulsions/attractions in water.

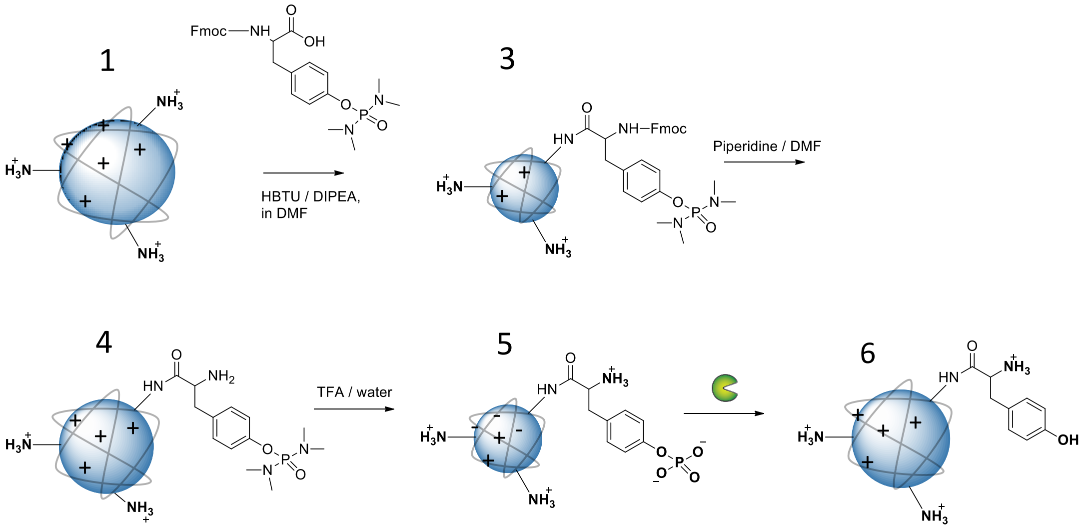

Figure 5.6. Schematic representation of the functionalization of microgel particles with FmocYp-N$(CH_3)_2$ followed by enzymatic removal of phosphate groups with graphic representation of expected size change of microgels at different stages (1-6).

In order to make easier data interpretation and to allow a more straightforward comparison of the DLS data with each stage of reaction, a number was attributed to each step, being: stage **1**- microgels only, stage **2**- control sample without coupling reagents (microgels and FmocYp-N$(CH_3)_2$), stage **3**- microgels and FmocYp-N$(CH_3)_2$ in presence of coupling reagents), stage **4**- Fmoc removal, stage **5**- phosphate group deprotection (TFA treatment), and stage **6**- addition of the enzyme (phospahatase). For simplicity only numbers **1-6** are indicated in the figures. When different conditions apply for measuring the samples at the same stage, the variations **a** and **b** are indicated i.e. **2a** and **2b** for control sample before and after resuspension, respectively; **3a** and **3b** for the coupled amino acid before and after resuspension, respectively and **5a** and **5b** for different sample handling after TFA treatment. This also helps to visualise how the results compare with the expectations. For discussion **2b**, **3b** and **5b** stages will be taken into account as representative of stages **2**, **3** and **5** respectively.

The coupling was performed overnight using HBTU and DIPEA as coupling reagents (stage **3**). A control sample without coupling reagents was also examined (stage **2**). The changes in behaviour of microgels after coupling were assessed by DLS and zeta potential. UV-vis was used to assess the complete removal of unreacted reagents (i.e. FmocYp-N(CH_3)$_2$).

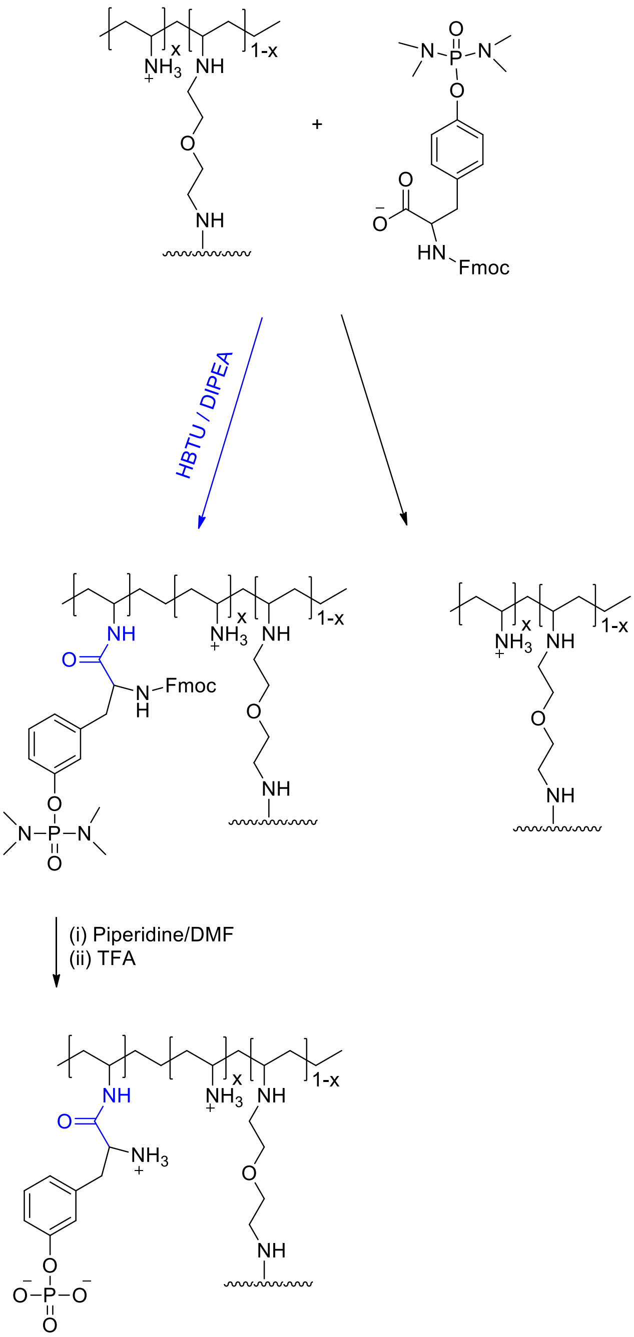

Figure 5.7. Schematic representation of the complete functionalization reaction consisting in three steps: (i) coupling in DMF, (ii) Fmoc removal using piperidine/DMF and (iii) phosphate protecting group deprotection in TFA.

Every reaction step was monitored by DLS and microgel particle size changes were measured (Figs. 5.8 and 5.9). DLS measurements were performed on the samples directly after 24 h treatment (stage **3a**) and also after a centrifugation and resuspension cycle with DMF (stage **3b**). The size of the functionalised microgels increased for the reaction (stage **3a**) sample (R_H = 7.1x10^2 nm) and slightly increased for the control (stage **2a**) sample (R_H = 3.8x10^2 nm). However, after removal of the supernatant and the re-dispersion in DMF the microgel size of the control (stage **2b**) sample (R_H = 2.4x10^2 nm) shows lower values than that of the starting material (stage **1**) (R_H = 3.6x10^2 nm). In contrast, the sample with coupling agents presents larger microgel particle size (R_H = 6.5x10^2 nm) compared to the starting material and similar size to the R_H recorded before the wash. This indicated that the coupling of the amino acid to the microgel was successful only in the presence of coupling reagents.

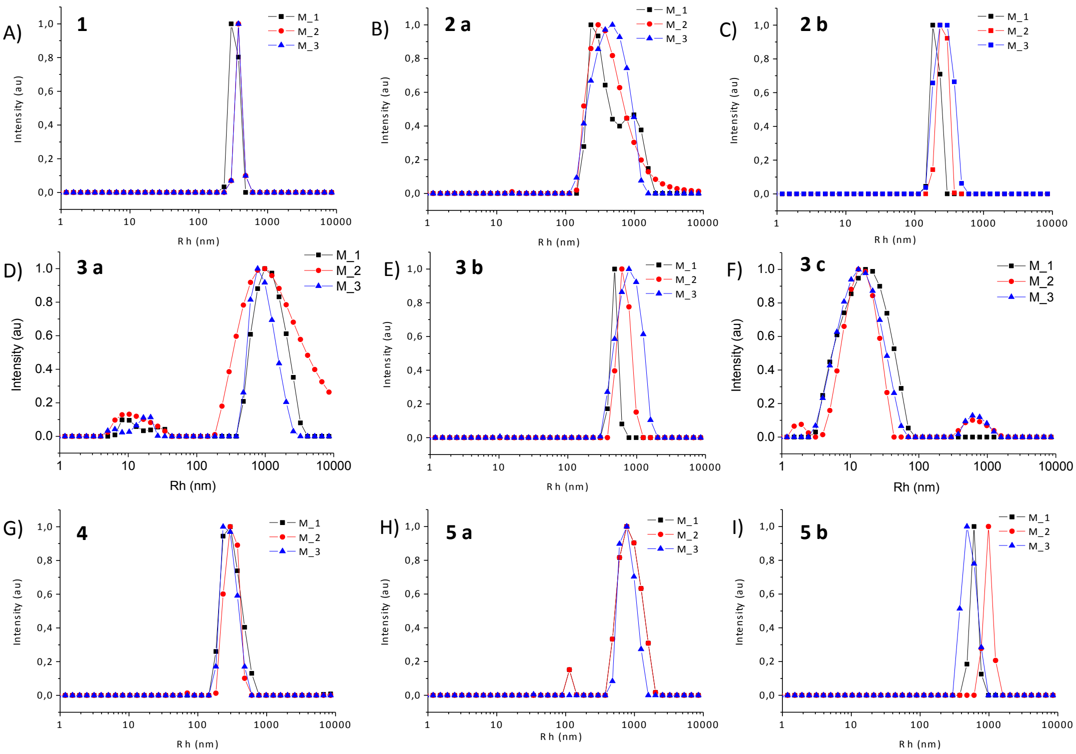

Figure 5.8. DLS measurements conducted in triplicate in each stage (indicated by a number): A) microgels only (stage **1**); B) control sample measured directly after 24 h (stage **2a**) and C) after resuspension in DMF (stage **2b**); D) reaction sample measured directly after 24 h (stage **3a**) and E) after resuspension in DMF (stage **3b**), F) supernatant of the reaction

sample (stage **3c**); G) after Fmoc removal (stage **4**); after phosphate group deprotection (stage **5**): H) centrifuged and washed 3 times with water (stage **5a**) or I) TFA evaporated and resuspended in water (stage **5b**). (M 1,2 and 3 in each graph indicate measurements 1,2 and 3).

As DLS measurements were performed in DMF the expected changes of particle size described for water do not apply. After coupling, microgels showed bigger size compared to starting material probably due to different surface properties of the particles. An amino acid containing an Fmoc group and a phosphate group were introduced and the size change to bigger values could be the confirmation of the introduction of the amino acid on the microgel. Following the same concept, the decrease in size after Fmoc removal could represent the smaller size of particles due to the removal of a big hydrophobic group. To more easily visualise size changes after each step a histogram summarizing the DLS data (from figure 5.8) is shown in figure 5.9. Once the sample was treated with TFA for phosphate group deprotection an increase of size is observed due to irreversible aggregation in highly acidic conditions. These stages (**5a** and **5b**) are not to be compared with the previous stages (**1-4**) as the solvent is different. The results presented in figures 5.8 and 5.9 point in the direction that the coupling of the amino acid to the microgel was successful. However, these are not conclusive and would require more controlled conditions i.e. absence of aggregation and possibility of resuspension in order to compare all the changes observed.

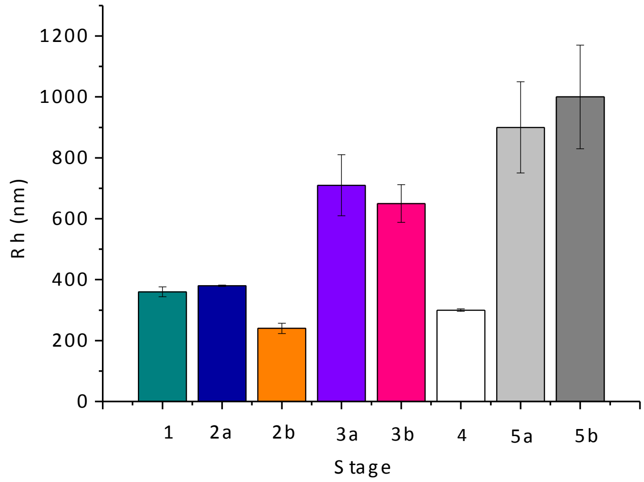

Figure 5.9. Histogram showing the average values of R_H for all the stages (**1-5b**) of microgel modification.

In figure 5.10 the comparison between the two conditions (before and after re-dispersion) is shown for each sample: reaction sample (figure 5.10 B) and control (figure 5.10 A), to better visualise the main changes i.e. coupling or physical attachment respectively. In Fig 5.10 A can be observed that after the washes and resuspension in DMF (stage **2a**) a decrease of particle size with respect to starting material occurs. This might be due to the physical interaction between the amino acid and the microgel that possibly results in the shrinkage of the particles. It is speculated that some amino acids could enter the core of microgel particles.

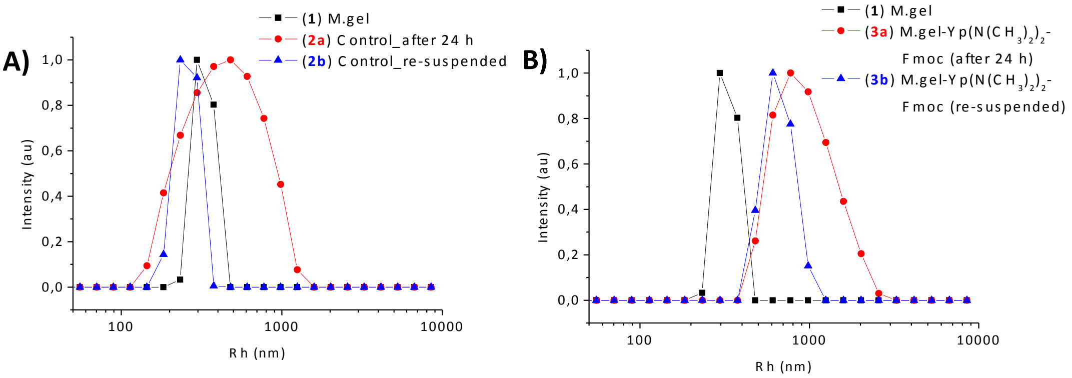

Figure 5.10. Size distributions of functionalised microgel centrifuged and re-suspended in DMF for A) control and B) sample: microgel (starting material- **1**)- black, after 24 h functionalization (**2a**/**3a**)- red, after re-suspension (**2b**/**3b**)- blue.

In addition to DLS data, also the observation of samples by eye indicates changes in sample appearance in presence or absence of coupling reagents. After addition of the reagents, both vials looked the same (i.e. vial 2). In figure 5.11 A the difference in sample appearance after 24 h can be seen. Vial 1 (reaction vial) containing microgel, HBTU, DIPEA and FmocYp-$N(CH_3)_2$ is where covalent attachment (amide bond formation) was performed. Vial 2 (control) is where no coupling agents were added and only physical interaction occurred. The appearance of the microgel suspension in vial 2 suggests that the microgels are in the collapsed state due to electrostatic interactions the amine groups of the microgels and the carboxyl groups of the amino acid (FmocYp-$N(CH_3)_2$), while the microgel in vial 1 is more swollen.

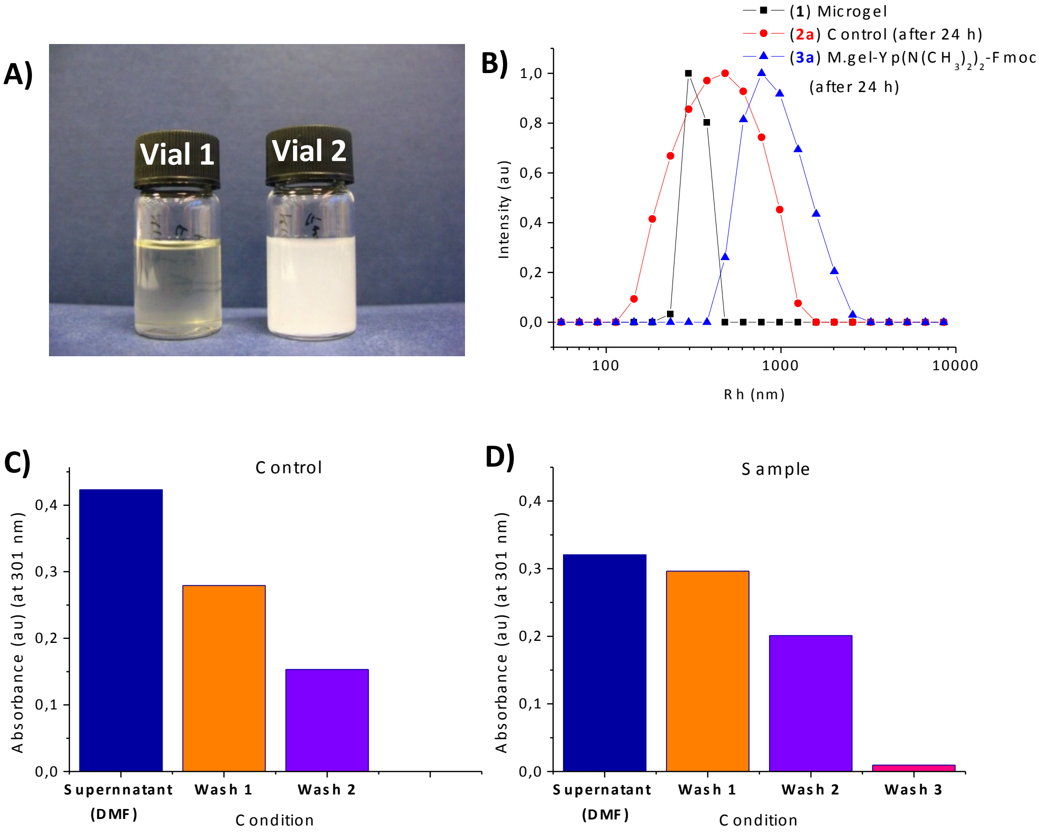

Figure 5.11. A) Photo of vial 1: microgel, FmocYp-N$(CH_3)_2$, HBTU and DIPEA in DMF after 24 h (sample) and vial 2: microgel and FmocYp-N$(CH_3)_2$ in DMF after 24 h (control). B) DLS size distributions of the reaction sample and control measured directly after 24 h. C) and D) UV-vis measurements showing Fmoc absorbance intensity at 301 nm after coupling, followed by 3 washes with DMF to remove the unreacted Fmoc-Yp- N$(CH_3)_2$.

UV-vis measurements were performed at this stage to assess the presence in solution of the unreacted FmocYp-N$(CH_3)_2$ on the supernatant of both control and reaction sample followed by 3 DMF washes (figure 5.11 C and D). Based on previous experiments on microgel functionalization for optimisation of the process (data not shown) 3 washes with DMF are sufficient to completely remove the unreacted FmocYp-N$(CH_3)_2$. In figure 5.11 D this hypothesis is confirmed being zero the absorbance intensity at λ=301 nm (absorbance maximum of Fmoc). The complete removal of unreacted FmocYp-N$(CH_3)_2$ is important for the next step which consists of Fmoc removal from chemically coupled amino acid using piperidine and DMF. In order to be able to observe an indicative increase in UV intensity due to increase of free Fmoc in solution (due to its removal from the particles) all unreacted Fmoc from the previous step should be removed, as observed (Fig. 5.11 D).

In addition, DLS measurements were performed on the supernatant of the reaction sample collected after centrifugation (Fig. 5.12). The main peak shows a R_H value of 12 nm and it corresponds to self-aggregation of $FmocYp\text{-}N(CH_3)_2$, while a peak at a R_H value of $7.0x10^2$ nm are some of the particles that did not settle during precipitation (when the particles are swollen is more difficult to spin them down).

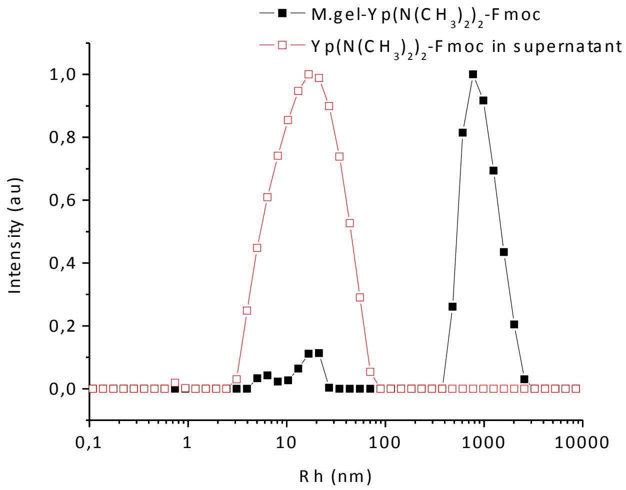

Figure 5.12. Size distributions of the supernatant of the reaction (red) compared to the resuspended sample (black).

The next step consisted of the Fmoc removal (stage **4**) using piperidine/DMF (4 ml) for 30 min. After 2 washes (5 ml DMF each) DLS measurements were performed on the resuspended microgel particles. The DLS data show the decrease in particle size to $R_H = 3.0x10^2$ nm compared to the previous stage ($R_H = 6.5x10^2$ nm). The UV-vis data confirm the removal of Fmoc through the increase from zero absorbance (figure 5.10 D) to 0.82 arbitrary units (figure 5.13 C) after treatment with piperidine/DMF. From the data shown in figure 5.13 C we can also conclude that after 2 washes with DMF most of the Fmoc present in solution was removed, as its' absorbance values stay constant after 2 washes.

The removal of the phosphate protecting group from microgel-$Yp\text{-}N(CH_3)_2$ was performed in TFA for 24 h (stage **5**). A strong aggregation was visible, by eye, after exposure of the microgels to TFA. The samples were treated in two different ways before DLS:

a) centrifuged, washed 2 times with DI water (however very little sample was present)- stage **5a**.
b) TFA removed (evaporated), microgels resuspended in water and DLS measurement repeated- stage **5b**.

The particles were left to settle prior to DLS measurement. In both cases the aggregation to bigger particles is observed: in the first case R_H=9.0x10^2 nm, while in the second R_H=1.0x10^3 nm were measured. A repeat measurement was performed on the latter example and R_H=7.0x10^2 nm, and after 10 min R_H=2.6x10^3 nm, were measured. It can be concluded that the particles are highly unstable after TFA treatment and tend to form irreversible aggregates unable to be resuspended in water. This can be explained by the fact that the particles aggregate in highly acidic (pH=2) environment (data not shown). A possible explanation can also be that in water after phosphate group deprotection there is a strong electrostatic attraction that results in microgel aggregation.

Enzyme responsiveness of these systems was studied by treating the microgels for 4 h with phosphatase (stage **6**). The expected swelling of the microgels did not occur after 4 h. No re-dispersion was observed and the aggregates observed at the starting point (before enzyme addition) remained in the sample. The irreversible aggregation was confirmed even in the presence of phosphatase. These experiments could be potentially repeated for longer times (e.g. 24 h) as the aggregation might have made the enzyme action slower (substrate availability to enzyme is reduced).

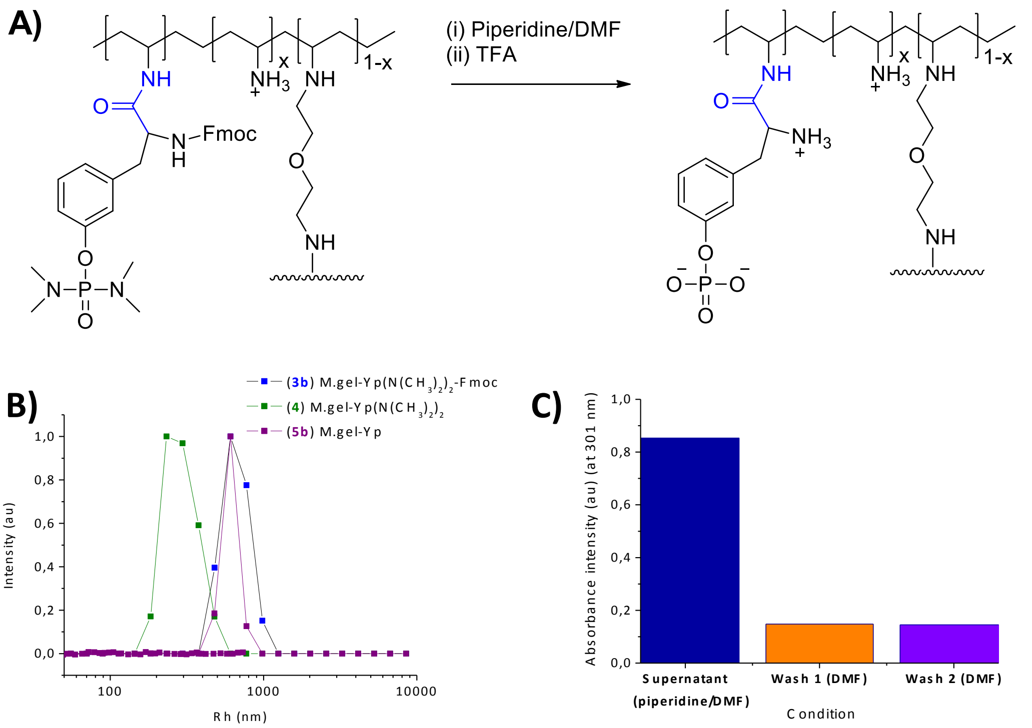

Figure 5.13. A) Schematic representation of the Fmoc removal and phosphate group deprotection; B) DLS measurements after Fmoc deprotection (**4**; green) and phosphate group deprotection (**5b**; purple) compared to microgel conjugated with FmocYp-N$(CH_3)_2$ reaction sample (blue); C) UV-vis after Fmoc deprotection showing Fmoc absorbance intensity at 301 nm of supernatant (blue), wash 1 (orange) and wash 2 (purple) with DMF.

Zeta potential results are summarized in table 5.1 and can be compared to the expected behaviour of microgels shown in figure 5.6. All the measurements were performed after 3 washes in water followed by resuspension in water. In this way, pH values for zeta potential measurements were maintained in the range of 7.5-8.1. The microgels (starting material) at pH=7 (below their pK_a value) are showing $\zeta=+47 \pm 4$ mV (stage **1**). After coupling of FmocYp-N$(CH_3)_2$ the zeta potential values dropped to $\zeta=22 \pm 4$ mV (stage **3**) showing the decrease of the positive charge correlated to the lower availability of free amines on the particles. Also the control sample (with no coupling agents added) showed a drop in zeta potential values to $\zeta=27 \pm 3$ mV (stage **2**) probably due to the electrostatic interaction. After Fmoc removal (stage **4**) and thus deprotection of amine groups of the amino acid the zeta potential was expected to increase. However, the measured value was $\zeta=18 \pm 3$ mV most likely indicating the incomplete Fmoc removal. Also the DLS data showed an unexpected decrease in particle size. After TFA treatment (stage **5**) and deprotection of the phosphate group the zeta potential drops to ζ=5 ± 6 mV indicating the introduction of negatively charged groups on the surface of the particles. The pH for this measurement was low (pH=2.3) as it was difficult to remove TFA after 3 washes with water.

Table 5.1. Summary of zeta potential and DLS measurements.

Entry (Stage)	**Structure**	**Zeta potential ζ (mV)**	**pH**	**R_H (nm) DMF**	**R_H (nm) Water**
1	Microgel	47 ± 4	8.0	$3.6\text{x}10^2 \pm 16$	630[¥] [144]
2 b	Control (no HBTU, DIPEA)	27 ± 3	7.6	$2.4\text{x}10^2 \pm 17$	
3 b	Microgel-$Yp(N(CH_3)_2)_2$-Fmoc	22 ± 4	7.7	$6.5\text{x}10^2 \pm 62$	
4	Microgel-$Yp(N(CH_3)_2)_2$	18 ± 3	8.1	$3.0\text{x}10^2 \pm 4$	
5 b	Microgel-Yp	5 ± 6	2.3		$7.0\text{x}10^2 \pm 240$[¥¥]
6	Microgel-Y[¥¥¥]	/	/	/	Massive aggregation

[¥] Value taken from reference 144 (Saunders and co-workers).[144]

[¥¥] Instable behaviour observed with massive aggregation, the presented result is not representative of the sample variation in time.

[¥¥¥] Microgel-Y results are not reported as after enzyme treatment the sample was not resuspended as expected but remained in the aggregated state.

In order to compare the behaviour of microgels in terms of zeta potential and R_H values plots are presented (Fig. 5.14) where each stage of functionalization corresponds to a number (taken from table 5.1). However, as R_H values were obtained from DLS measurements in DMF they are not directly comparable to the expected behaviour in water due to different swelling properties of the microgels in these two solvents (seen from the $R_{H\ DMF} = 3.6x10^2$ nm and $R_{H\ water} = 6.3x10^2$ nm for the starting material- microgel only) and a more pronounced charge based behaviour (attraction/repulsion of charged residues) in water.

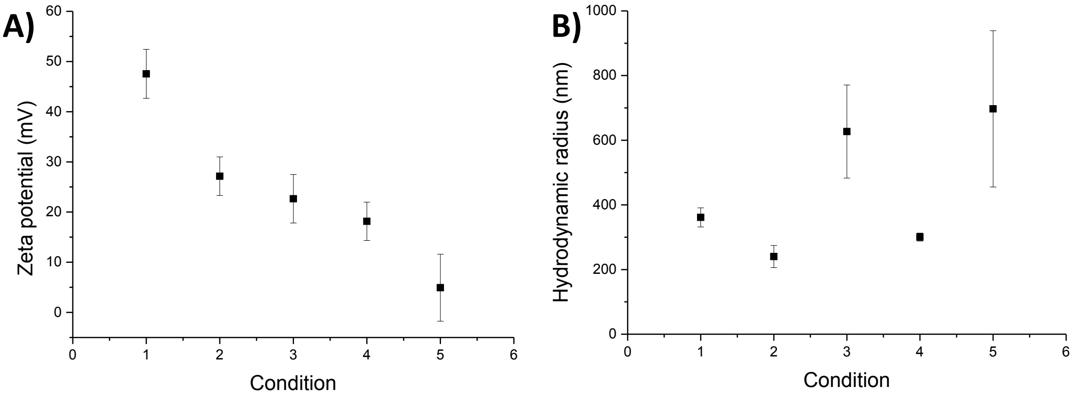

Figure 5.14. Plots of a) zeta potential and b) R_H values vs. condition indicated by number **1-5** (taken form table 1). The variation of zeta potential and R_H can be visualised regarding the stage of functionalization.

In addition, FTIR analysis was carried out but the results (data not shown) are inconclusive. The focus was put on the analysis of the amide region of the spectra as FTIR was expected to be useful for confirmation of amide bond formation in case of FmocYp-$N(CH_3)_2$ conjugation. In comparison with the published data[144] the FTIR spectra are complex and show different peaks (regions) than those expected and they would require better interpretation and comparison with other techniques. Therefore, FTIR analysis would require more work and these results are not included in this thesis.

b) *MMP-9 responsive microgels*

To obtain MMP-9 responsive poly(VAM-BEVAME) microgels a peptide sequence (PhAc-FFAGLDD) was conjugated to the microgels. The advantages of using PhAc-FFAGLDD (**1a**) as peptide sequence are that is MMP-9 responsive (proved in Chapter 3) and protected at the N-terminus with the acetyl group to avoid cross-reactions during coupling. Three different concentrations of peptide (**1a**) were used to determine whether the functionalization is concentration dependent. 12.5% (0.015 mmol), 25% (0.03 mmol) and 50% (0.06 mmol) of peptide related to the total free amines present on the microgel particles, taken as 100% (0.12 mmol), were used. **1a**_1 (stages **2**- DMF and **3**- water), **1a**_2 (stages **4**- DMF and **5**- water) and **1a**_3 (stages **6**- DMF and **7**- water) are indicating the 50%, 25% and 12.5% peptide concentrations, respectively. The same procedure was followed as for the phosphatase responsive microgels. A 24h coupling in DMF, with HBTU and DIPEA was performed. In this case, a one step synthesis was performed consisting in the coupling of the pre-made, N-protected peptide sequence. Similarly as described for the phosphatase responsive system, shrinkage of the particles is expected after conjugation due to the change in the overall charge. In this case, in addition to peptide bond formation, each peptide sequence carries two additional negative charges (from the aspartic acid side chains) (Fig. 5.16). Therefore the introduction of increasing concentrations of peptide on the particles is expected to result in higher extent of their shrinkage (Figs. 5.15 and 5.17).

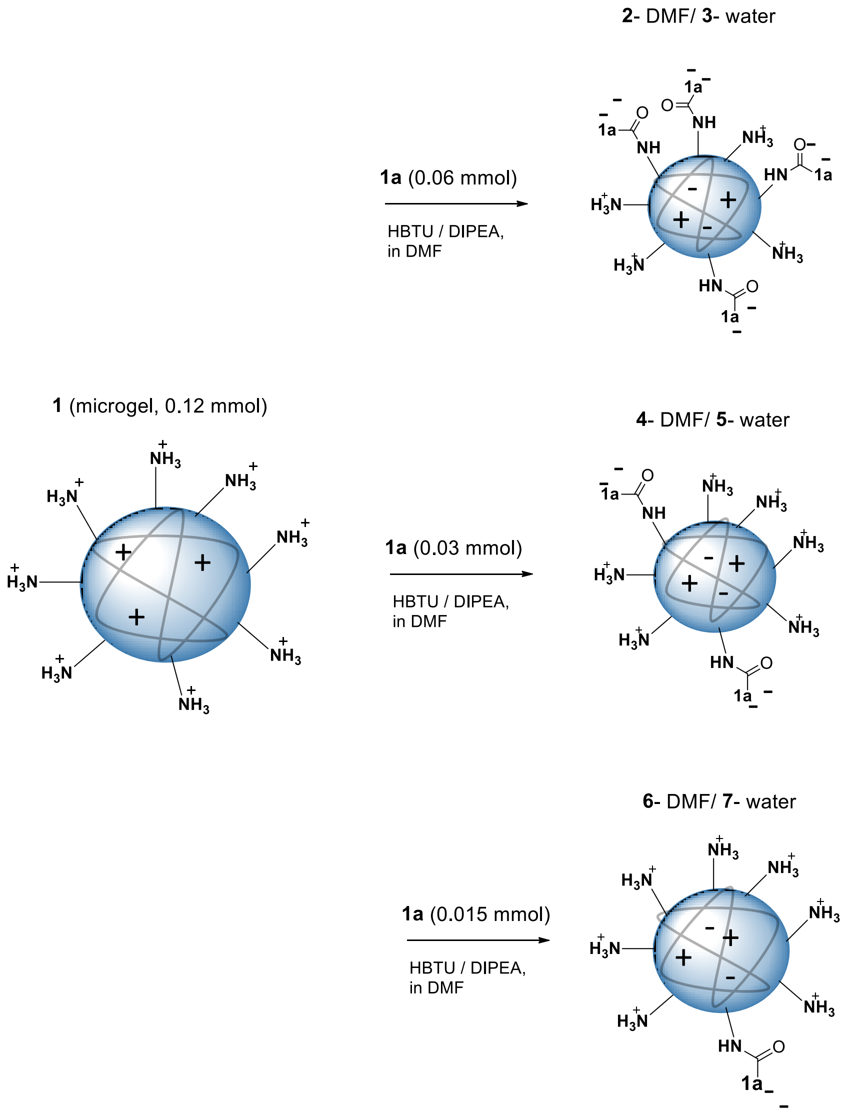

Figure 5.15. Schematic representation of the functionalization of microgel particles with PhAc-FFAGLDD (**1a**) with graphic representation of expected size change of microgels after coupling. Different numbers (**2** to **7**)- corresponding to different concentration of **1a** used for coupling are indicated for DMF (even numbers) and water (odd numbers).

The chemistry of the proposed coupling reaction is shown in figure 5.16. The peptide is activated with HBTU and DIPEA for 15 min before addition to the amine rich microgel. The reaction is allowed to proceed for 24 h (based on previous experiments). Subsequently DLS and zeta potential were performed.

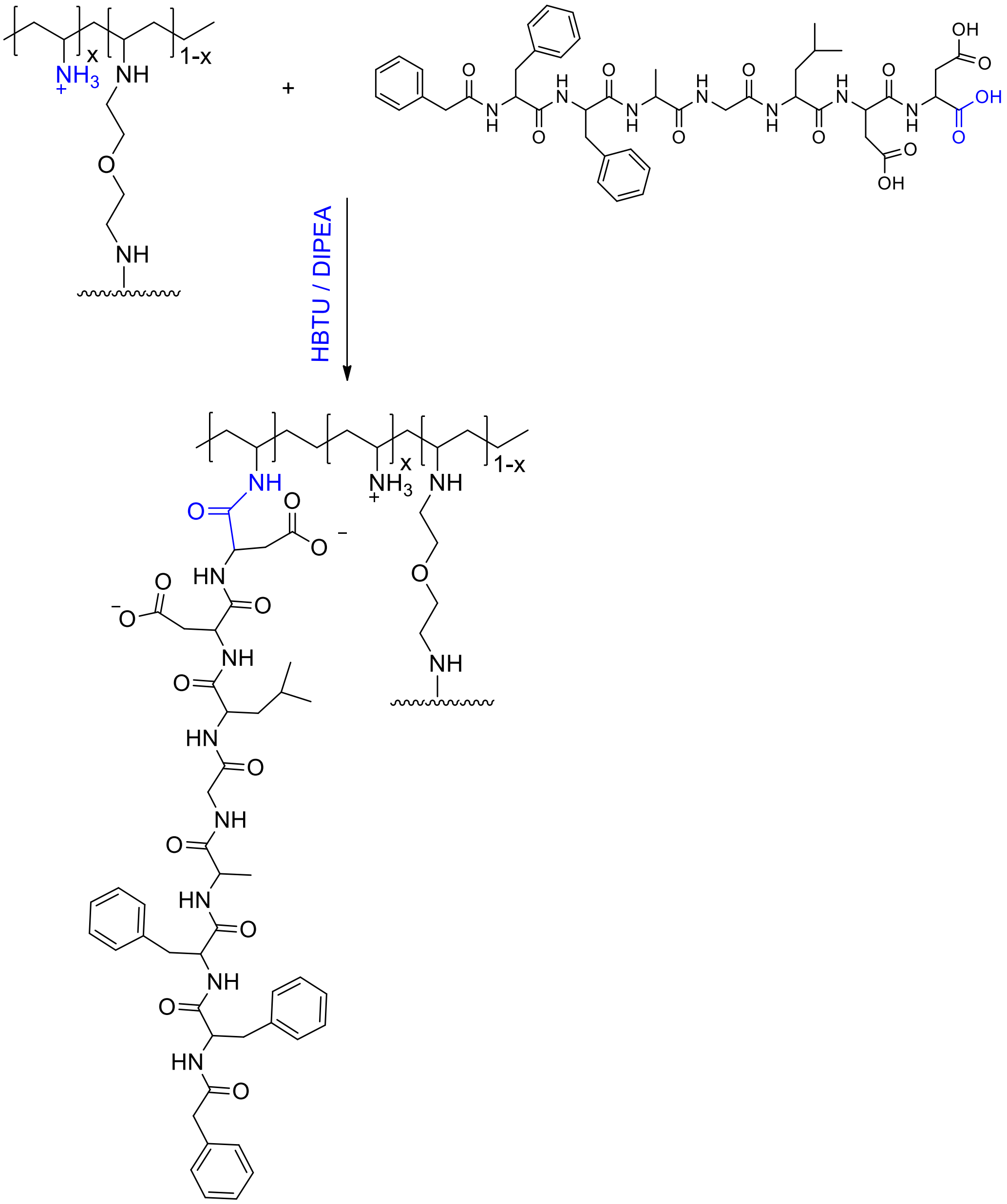

Figure 5.16. Schematic representation of the chemical reaction of microgel funcionalisation with PhAc-FFAGLDD (**1a**).

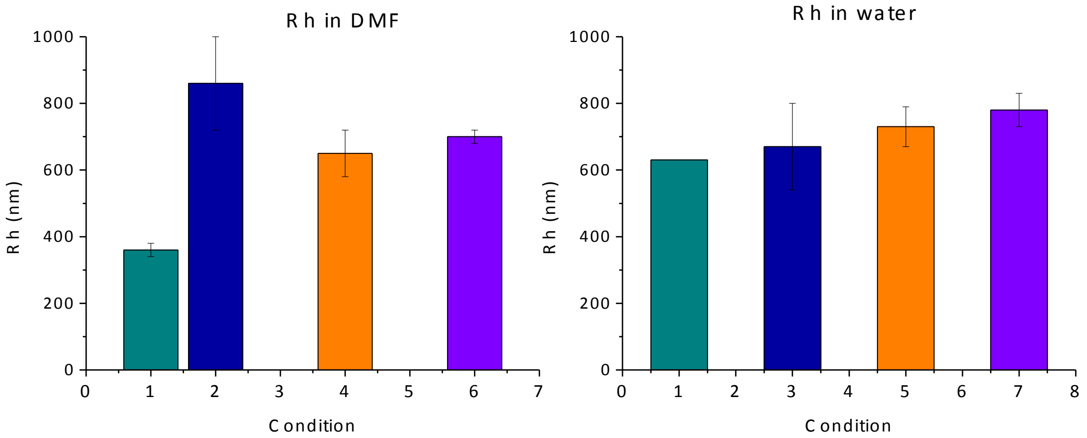

Figure 5.17. Histograms showing the average values of R_H for all the stages (**1-7**) of microgel modification measured in DMF (graph on the left, stages presented by even numbers) and water (graph on the right, stages presented by odd numbers).

From the histograms reported in figure 5.17 can be seen that the R_H recorded in water show a concentration dependent size change from the starting material (R_H=6.3x10^2 nm for microgels only- **1**) to R_H=6.7x10^2 nm (**3**), R_H=7.3x10^2 nm (**5**) and R_H=7.8x10^2 nm (**7**). This is in accordance with what is expected (Fig. 5.15) in terms of introduction of negative charges on the microgel particles. By increasing the concentration of **1a** introduced on microgels a higher conjugation extent is expected i.e. more amine group should be converted to amide bonds. In addition, a higher quantity of negative charges would be introduced (each molecule of **1a** conjugated has two aspartic acid side chains). The higher the extent of coupling the lower the size of particles is expected. On the contrary, in DMF no trend was observed between R_H and concentration of **1a** (R_H=8.6x10^2 nm (**2**), R_H=6.5x10^2 nm (**4**) and R_H=7.0x10^2 nm (**6**)) used suggesting that the conjugation is not concentration dependent and/or that the electrostatic repulsion is not the main driving force for microgel swelling behaviour.

DLS measurements were performed to determine size changes at different stages: after 10 min, after 24 h and after 3 washing/redispersion cycles in DMF for each concentration of peptide. DLS measurements showed R_H values summarised in table 5.2.

Table 5.2. R_H (nm) values of microgels during different stages of coupling and after 3 washes in DMF.

Entry	Step	Microgel-1a_1	Microgel-1a_2	Microgel-1a_3
1	Time zero[¥]	$3.6x10^2 \pm 16$		
2	10 min	$1.3x10^3 \pm 50$	$9.6x10^2 \pm 50$	$1.0x10^3 \pm 20$
3	24 h	$1.4x10^3 \pm 70$	$9.7x10^2 \pm 50$	$1.0x10^3 \pm 40$
4	After 3 washes with DMF	$8.6x10^2 \pm 140$	$6.5x10^2 \pm 70$	$7.0x10^2 \pm 20$

[¥] Microgel particles only, before addition of reagents

Subsequently, the particles were resuspended in water and the zeta potential measurement was performed. For all three examples the zeta potential values decreased compared to the starting material (ζ=47 ± 4 mV). The zeta potential for 1a_1 (**3**), 1a_2 (**5**) and 1a_3 (**7**) were ζ=35 ± 5 mV, ζ=36 ± 3 and ζ=28 ± 4 mV, respectively. The R_H values for 1a_1, 1a_2 and 1a_3 when resuspended in water are R_H=6.7x10^2 nm, R_H=7.3x10^2 and R_H=7.8x10^2, respectively. It can be noted that the concentration dependent size change previously stated for DLS in water (Fig. 5.15) for different concentrations of **1a** was not confirmed by zeta potential. A decrease of zeta potential with decrease of **1a** concentration used for coupling was observed while the opposite behaviour (decrease of zeta potential with increasing concentration of **1a**) would be expected.

Table 5.3. Zeta potential values and R_H in DMF and in water for all the concentrations of peptide examined.

Entry	Structure	Condition (microgel : 1a)	Zeta potential ζ (mV)	R_H (nm) DMF redispersed	R_H (nm) Water
1	Microgel	/	47 ± 4	$3.6 \times 10^2 \pm 16$	630.0*
2	Microgel-1a_1 (DMF)	1 : 0.5¥	/	$8.6 \times 10^2 \pm 140$	/
3	Microgel-1a_1 (water)	1 : 0.5	35 ± 5	/	$6.7 \times 10^2 \pm 130$
4	Microgel-1a_2 (DMF)	1 : 0.25¥¥	/	$6.5 \times 10^2 \pm 70$	/
5	Microgel-1a_2 (water)	1 : 0.25	36 ± 3		$7.3 \times 10^2 \pm 60$
6	Microgel-1a_3 (DMF)	1 : 0.125¥¥¥	/	$7.0 \times 10^2 \pm 20$	/
7	Microgel-1a_3 (water)	1 : 0.125	28 ± 4	/	$7.8 \times 10^2 \pm 50$

¥ Microgel : 1a = 1 : 0.5 (50% peptide related to the total number of NH_2 groups on microgel particles)

¥¥ Microgel : 1a = 1 : 0.25 (25% peptide related to the total number of NH_2 groups on microgel particles)

¥¥¥ Microgel : 1a = 1 : 0.125 (12.5% peptide related to the total number of NH_2 groups on microgel particles)

The coupling of MMP-9 responsive sequence, PhAc-FFAGLDD, to the microgel particles performed at three different concentrations of peptide resulted in coupling confirmed by changes in size and in zeta potential. Even though it is not possible to determine the dependence of peptide concentration on the efficiency of coupling, no irreversible aggregation was observed compared to the phosphatase responsive system (described in the previous section) as no highly acidic conditions were employed. The advantage is presented by the ease of the procedure requiring only one coupling step compared to the three steps used to introduce FmocYp on the microgel. Therefore, this system seems to be more promising for future enzyme responsiveness studies.

In addition, FTIR does not seem useful in case of **1a** conjugation to microgels because **1a** contains several peptide bonds within the structure and little difference in the amine region is expected. The FTIR spectra are complex and they would require better interpretation and comparison with other techniques. Therefore, these results are not included in this thesis as inconclusive.

5.4 Conclusions

In conclusion, the microgel synthesis was carried out following the procedure optimised by Saunders group at the University of Manchester (collaboration project between the University of Manchester and University of Strathclyde). The NVEE crosslinker, poly(NVF-NVEE) and poly(VAM-BEVAME) microgels were synthesized. Only the basic characterisation on the particles was performed to confirm the successful synthesis of the particles showing results comparable to the ones published by Saunders and co-workers. However, the NVEE synthesis resulted challenging as the conditions had to be further optimised due to the different experimental setup used at Strathclyde. Microgel aggregation following the hydrolysis was also an issue.

Following the synthetic step, the post-polymerisation functionalization of microgels using two different residues was performed. In the first case the phosphatase responsive, FmocYp-N$(CH_3)_2$ was coupled to the microgels. Even though the attachment was successful, confirmed by size changes (DLS) and zeta potential measurement the endpoint was hit after TFA treatment causing irreversible aggregation. Enzyme responsiveness could not be further tested because of this aggregation.

A further development of the system was achieved by coupling of MMP-9 responsive sequences on the microgel particles. The PhAc-FFAGLDD sequence previously characterised (see Chapter 3) was used at three different concentrations. All result in coupling that is concentration independent according the zeta potential (water) and DLS measurements in DMF. This system has not been examined for enzyme responsiveness even if it holds better promise than the phosphatase responsive one. No irreversible aggregation was observed and the ease of the procedure requiring only one coupling step is advantageous. However, we decided not to proceed with this system as to develop a drug delivery application would need more time for optimisation and further analysis. The other system, we developed (presented in Chapter 3) holds better promise to achieve applications *in vivo* as the biocompatibility issues are absent and was therefore the focus of the thesis.

5.5 Materials and methods

5.5.1 Materials

NVF, potassium tert-butoxide, dicyclohexano-18-crown-6, bis (2-bromoethyl) ether, azobisisobutyronitrile (AIBN) and poly(1-vinylpyrrolidone-*co*-vynil acetate) (PVP-*co*-PVA) were purchased by Sigma Aldrich and used as received. The PVP-*co*-PVA had a weight-average molecular weight of 50 000 $gmol^{-1}$ and a VA content of 43 mol%. FmocYp-$N(CH_3)_2$ was purchased by Novabiochem (Merck). Phosphatase (alkaline bovine), (EC 3.1.3.1.) was purchased from Sigma Aldrich, and was diluted with 4.5 mL of pH=9 phosphate buffer prior to use (1µl = 1 unit).

5.5.2 ^{1}H nuclear magnetic resonance (NMR)

NMR spectra were recorded on Bruker AV300 spectrometer (^{1}H: 500 MHz) in the deuterated solvent stated (chloroform). All chemical shifts (δ) are quoted in ppm and coupling constants (J) given in Hz. Residual signals from the solvents were used as an internal reference.

5.5.3 Dynamic Light Scattering (DLS)

DLS measurements were carried out by using a ALV (ALV, GMBH, Germany) spectrophotometers using vertically polarized He-Ne laser light (25 mW with wavelength of 632.8 nm) with an avalanche photodiode detector. The DLS measurements were carried out at angle of 90° at 25 °C. Intensity autocorrelation functions were recorded and analysed by means of the cumulative method in order to determine the intensity weighted diffusion coefficients D and the average hydrodynamic radius R_H by using the Stokes-Einstein equation, $R_H = kBT/6\pi\eta D$, where kB is the Boltzmann constant, T is the absolute temperature and η is the solvent viscosity at the given temperature. All DLS measurements were conducted in triplicate.

5.5.4 Zeta potential analysis

Zeta potential measurements were performed using Malvern Zetasizer Nano instrument that uses Laser Doppler Velocimetry (LDV) technique combined with Phase Analysis Light Scattering (PALS) to measure zeta potential. The zeta potential distribution was measured using water as dispersant and the value of *f (Ka)* of 1.5 known as Smoluchowski approximation of the Henry's function *f(Ka)*. Smoluchowski approximation is valid for measurements in aqueous media and moderate electrolyte concentration. For each sample 3 measurements were performed at a temperature of 25°C using a clear disposable flow cell.

5.5.5 UV visible spectroscopy

UV-vis spectroscopy was used to monitor the unreacted reagents from the reaction and to confirm Fmoc removal after cleavage with piperidine/DMF. The absorbance spectra were recorded using UV Jasco V-660-spectrofotometer.

5.5.6 Optical microscopy

Optical microscopy was conducted with an Olympus BX41 microscope at the School of Materials, University of Manchester.

5.5.7 Crosslinking monomer synthesis

2-(N-vinylformamido) ethyl ether (NVEE) was synthesized following a method reported before.[144,198] 7.1 g of NVF and 0.99 g of dicyclohexyl -18-crown-6 were dissolved in 100 ml of anhydrous THF and 11.97 g of potassium t-butoxide (last added) were stirred vigorously at room temperature for 45 min (figure 11 a). After cooling in ice bath for 20 min 9.28 g of Bis (2-bromoethyl) ether was added dropwise. The reaction mixture was then stirred at room temperature for 72 h. Potassium bromide was removed by filtration and the reaction mixture concentrated under vacuum and diluted with 100 ml of DI water. NVEE was then extracted with chloroform. The extracts were combined, washed with brine and dried over anhydrous sodium sulphate. The chloroform was removed completely using the rotavapor. The compound was characterized by elemental analysis, ^{1}H NMR and FTIR.

Figure 5.18. Photos taken during the synthesis of NVEE: a) and b) experimental setup and synthesis; c) filtration to remove KBr; d) extraction with chloroform; e) drying over anhydrous sodium sulphate; and e) freeze dried NVEE, ready for further characterization (FTIR).

5.5.8 Microgel synthesis

Poly(NVF-co-NVEE) microgel particles were prepared by non-aqueous dispersion (NAD) polymerization as described before.[144] Ethanol (68 g), NVF monomer (6 g), PVP-*co*-PVA (1.8 g), AIBN 0.2416 g and NVEE crosslinker (0.845 g) were mixed together in a 4-neck round bottom flask equipped with an overhead stirrer, nitrogen supply and a reflux condenser (figure 12 a). Nitrogen was purged for 10 minutes while the solution was stirred vigorously, and heated to 70°C while stirring (500 rpm) for 60 minutes to allow polymerisation. The obtained dispersion was then purified by cycles of centrifugation/ re-dispersion in ethanol. Finally, the hydrolysis (figure 12 b) was performed using 1 g of poly(NVF-co-NVEE) in 100 ml of 1 M NaOH, under N_2, at 80°C for 16 h in order to hydrolise primary amides (NVF) and secondary amides (NVEE) to primary amines (VAM) and secondary amines (BEVAME), respectively. The final product poly(VAM-*co*-BEVAME) was washed using cycles of centrifugation/re-dispersion in DI water.

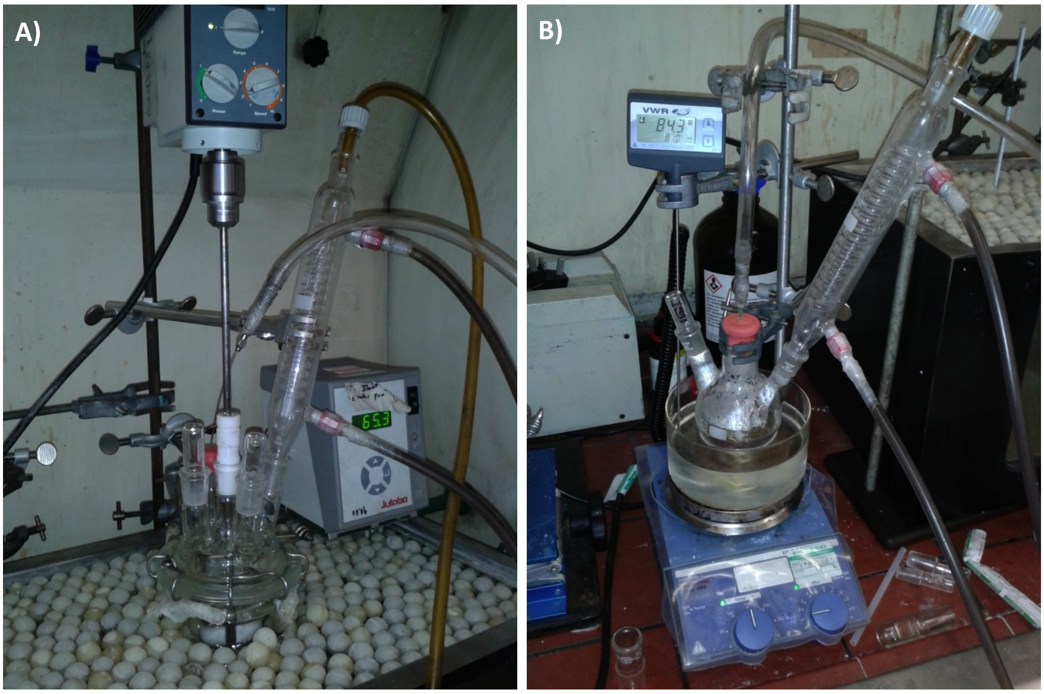

Figure 5.19. Photos showing the experiment setup, taken during: (a) polymerisation and (b) hydrolysis of microgels.

SPPS of PhAc-FFAGLDD

See Chapter 3.

Functionalization with FmocYp-N(CH_3)$_2$ via HBTU/DIPEA coupling

The functionalization of microgel particles with FmocYp-N(CH_3)$_2$ was performed in DMF, using HBTU and DIPEA as coupling agents. FmocYp-N(CH_3)$_2$ (0.06 mmol) was dissolved in DMF and HBTU (0.06 mmol) and DIPEA (0.12 mmol) were added mixed (vortexed and sonicated), and let to activate for 15 min. This was then added to a suspension of microgels and left to react on a shaker for 24 h (overnight) at room temperature. The ratio of reagents based on microgel (1 eq = 0.12 mmol) was:

a) microgel : amino acid : HBTU : DIPEA = 1 : 0.5 : 0.49 : 1.

After FmocYp-N(CH_3)$_2$ coupling to microgels, Fmoc deprotection was performed for 1 h (on shaker) in 5 mL piperidine:DMF (1:4). Phosphate group deprotection was performed in 5 mL TFA:water (95:5) for 1 h, followed by the addition of 10% of volume of water (500 µL) and left for further 18 h (on shaker) to allow complete deprotection. After each step characterization was performed (before and after washing and re-suspension in DMF for the first two steps and before and after washing and re-suspension in water after TFA cleavage).

Functionalization with PhAc-FFAGLDD via HBTU/DIPEA coupling

The functionalization of microgel particles was performed at 3 different concentrations of peptide **1a** (0.06 mmol, 0.03 mmol and 0.015 mmol). An excess of microgel was used (0.12 mmol- 0.1 wt%). The peptide was dissolved in DMF and HBTU (0.06 mmol, 0.03 mmol and 0.015 mmol) and DIPEA (0.12 mmol, 0.06 mmol and 0.03 mmol) were added, mixed and let to activate for 15 min. This mixture was then added to a suspension of microgels and left to react on a shaker for 24 h (overnight) at room temperature. After 24 h characterization was performed (before and after washing and re-suspension in DMF).

The ratios of reagents based on microgel (1 eq = 0.12 mmol) were:

a) Microgel : peptide : HBTU : DIPEA = 1 : 0.5 : 0.49 : 1

b) Microgel : peptide : HBTU : DIPEA = 1 : 0.25 : 0.24 : 0.5

c) Microgel : peptide : HBTU : DIPEA = 1 : 0.125 : 0.124 : 0.25

6 Conclusions and future work

6.1 Conclusions

Two different MMP-9 responsive peptide amphiphiles able to self-assemble into spherical aggregates that undergo enzyme triggered micelle to fibre transition and are capable of encapsulation and controlled release of doxorubicin are presented in this thesis. These mobile carriers of anticancer drugs are designed to selectively deliver the payload to tumour tissues where they assemble to form localised fibrous depots by exploiting local MMP-9 overexpression. Furthermore, the assembled fibres provide a scaffold for prolonged drug delivery due to the partial entrapment of the drug and the intrinsic biodegradable nature of peptide carriers themselves. Creating localised depots of anticancer drugs around cancer cells is beneficial for the development of anticancer therapy.

Different techniques were used to characterize the peptides and to fully understand the mechanism of the peptide amphiphiles as drug delivery systems. HPLC and LCMS were used to assess the purity of products and to confirm their formation. In a few examples, MALDI was used in addition to the previously mentioned techniques for individuation of the products after enzyme cleavage. In LCMS, extensive fragmentation of peptides occurred and as the samples were not desalted positive ion adducts of fragments were often seen in addition to the expected products making data interpretation difficult. This was later confirmed by MALDI indicating the presence of di and tri-sodium adducts. Therefore, for future work would be recommendable to desalt the samples before LCMS is performed. Attention has to be paid during data interpretation as many product adducts are possible to find as well as potential interference or contaminant ions (found in electrospray ionisation and MALDI).[199]

AFM and TEM, were both successful in assessing the micelle to fibre morphology change. However, both techniques require sample drying which could lead to artefacts, including fibrillar structures present in the starting materials as the effect of dying. Cryogenic-TEM would be a better choice in terms of morphology transition visualisation. Fluorescence spectroscopy was a useful method for the characterisation of the aggregation behaviour of peptide amphiphiles. In addition, it provided the main technique in the analysis of the behaviour/suitability of the peptide amphiphiles as drug delivery systems. Confocal microscopy in combination with fluorescent spectroscopy is a powerful way to analyse peptide amphiphiles loaded with doxorubicin/riboflavin. However, due to resolution limits it would need to be used together with a technique at higher resolution (e.g. STORM) which would also have the advantage of (potential) real-time visualization of enzymatic transitions. An analysis technique based on the combination of confocal microscopy and electron microscopy (i.e. CLEM) could be of interest for fibre visualisation in proximity of cells as it would allow the visualisation of the same sample at different scales. In addition, by analysing the same sample region better comparison of results obtained with two different techniques could be achieved and a more straightforward interpretation of results would be guaranteed.

DLS experiments were useful for size comparisons of micelle and fibre forming peptides. However, R_H calculations obtained with DLS are based on the Stokes-Einstein approximation for spheres. Therefore, diffusion coefficients were presented in addition to R_H values to better compare the obtained results. In literature, examples of R_H values reported for non-sherical structures can often be found. A better way to distinguish between micellar and fibrillar structures would have been the SLS (static light scattering) measurement which would analyse the sample at different angles (compared to the DLS, measured at a fixed angle). In our case, SLS was not crucial as many techniques used in this thesis provide sufficient proof of the micelle to fibre transition. Nevertheless it could provide additional evidence of fibre formation/presence.

Peptide amphiphiles were treated with MMP-9 at a concentration corresponding to that secreted by human cancer cell lines. These conditions gave response times of 48 to 96 h. Response times can be changed (to faster) by choosing better enzyme substrates. This can be achieved by changing and/or lengthening the peptide sequences which would accelerate the response times/digestion of peptide amphiphiles. As these systems were developed for biomedical applications, the experiments were designed based on mimicking the *in vivo* environment.

Many challenges were encountered in proving these systems capable of performing as drug delivery vehicles. In terms of MMP-9 specificity, the substrate has to contain the right structural information to behave as a smart system able to undergo a morphological transition. Regarding MMP-9 cleavage efficiency, the cleavage of the substrate at the expected cleavage site G↓L being well known for longer substrates and/or proteins is often difficult to achieve using short peptide amphiphiles. Difference in size of two-three orders of magnitude between cells and fibres formed due to enzyme activity makes it challenging to image the desired effect around/in the presence of cancer cells. In addition, harsh fixing conditions and sample processing normally used for TEM and partly for SEM might result in fibre damage and/or washing. Therefore sample preparation might request milder conditions such as freeze-drying with no fixing in order to successfully image fibres.

In order to prove the feasibility of the system to treat cancer states and its ability to function *in vitro* and *in vivo* further examination and mechanism clarification is needed. However, the ability to reorganize from a micellar to fibrillar supramolecular structures and its application is drug delivery is a new concept not demonstrated before. When used *in vivo* these systems may also respond to other MMPs and specifically to MMP-2 due to some overlapping in specificity profiles. This could be potentially overcome by studying in detail the specificity of MMP-2 and MMP-9 (in terms of catalytic activity) on a library of substrates and by picking the ones that undergo faster degradation by MMP-9 compared to MMP-2. However, changing the peptide sequence to better, more specific substrates for MMP-9 might result in the loss of the possibility of the peptide amphiphiles to undergo self-assembly and therefore the desired micelle to fibre transition.

In Chapter 5, an alternative approach to enzyme responsive delivery systems was presented based on the polymeric particles- microgels. A method for post-polymerisation functionalization of a newly developed (by collaborators in Brian Saunders' group) amine rich microgel was presented. The functionalization was achieved but handling of these particles was proven to be challenging due to aggregation. Being polymers based on new design, there may be biocompatibility issues and potential long routes to FDA approval. Therefore, their development for real life applications is far and not achievable in this thesis.

Overall, the work in this thesis has presented two different enzyme responsive systems, one based on self-assembly of small peptidic molecules and the other on swelling properties of more complex chemically crosslinked polymer particles. We demonstrated that in response to a cancer associated enzyme a morphology transition from micelles to fibres is achieved that can be exploited in the treatment of cancer cells by releasing doxorubicin in the site of interest.

6.2 Future work

Following the main experimental section of this thesis, based on enzyme responsive morphologic transition of two peptide amphiphiles and their possible application as drug delivery systems (for cancer treatment) in addition to the development of the methodology for visualisation of the fibres formed in proximity of cancer cells some questions remain unanswered and a few aspects could be further examined. It would be interesting to measure the specificity of MMP-9 for the examined peptide amphiphiles. It was confirmed that they are MMP-9 substrates but the rate of their cleavage has not been determined yet.

As MMP-2 and MMP-9 are closely related enzymes they have some overlapping specificity profiles. Eventually our substrates are expected to be cleaved by MMP-2 but also potentially by other members of the MMP family. It would be interesting to assess this potential cross reactivity. We believe that in this case generality would not necessarily be a disadvantage as MMP-2 is also overexpressed by cancer cells.

Physical incorporation of hydrophobic heavy metal containing complexes, following the same procedure developed for doxorubicin would be useful for imaging purposes. *In situ* TEM would be the technique of interest to assess the micelle to fibre morphology transition in liquid/gel state. Furthermore, techniques with higher resolution such as STORM need to be considered for better visualisation of fibres in proximity of cancer cells and the real time reconfiguration from micelles to fibres in the presence of cells. In addition, CLEM would be beneficial as it combines fluorescent with electron microscopy.

Regarding to the imaging methodology it would be interesting to assess the **2a** FRET peptide in the presence of MMP-9 using confocal microscopy. First, it should be tested if the expected cleavage product is able to self-assemble into fibres as the presence of fluorescent groups (dabcyl and EDANS) could disrupt the self-assembly. The co-assembly method where low, μM-range concentrations of **2a** FRET could be used in addition to higher, mM-range concentrations of **2a** would be interesting to explore to guarantee better visualisation of the morphology transition.

Following Chapter 5, focused on enzyme responsive microgels it could be of interest to assess whether the peptide (**1a**) functionalised microgels are able to undergo swelling/deswelling in the presence of MMP-9. In general, testing enzyme responsiveness for drug delivery would be of interest. Using the optimized conditions employed for the functionalization of microgels with **1a**, other peptide sequences could be tested having different charge dispositions.

A way forward with these systems would need to consider working with more biocompatible materials. In addition, testing their toxicity *in vitro* could be beneficial as a starting point towards a possible biomedical application. Moreover, the influence of amine rich microgels on membrane integrity of cancer cells could be assessed, as cationic molecules are known to be toxic to cancer cells (negatively charged on the outer leaflet of the membrane).

An alternative approach could be to make microgels by directly polymerizing modified amino acids to obtain biocompatible polymers. This would be based on introducing vinyl groups on amino acids of interest (e.g. phosphorylated tyrosine) giving rise to polymerisable biocompatible monomers. Co-polymerisation of negatively (phosphorylated tyrosine) and positively (lysine) charged amino acids would be interesting to explore. After phosphatase addition and removal of the phosphate group form the microgel an overall positive charge would result in swelling. However, for this study to be performed a method development would be needed first. In addition, the ability to swell (behave as microgels) and size of such new systems should be studied in detail.

The most straightforward direction to follow in the design of further experiments is related to the *in vivo* application of the developed MMP-9 responsive systems. Testing the ability of self-assembling peptides (**1a** and **2a**) to perform as anticancer drug carriers in mice is of interest. For this purpose peptide cytotoxicity has to be assessed and *in vivo* results on animal models (mice) collected in order to show the potential for further development of the proposed carriers. As peptide nanostructures are relatively new materials in terms of cancer applications elucidation of the mechanisms governing the tumour inhibition are essential.

While not discussed in this thesis, a start has been made with *in vivo* evaluation of the doxorubicin loaded peptide systems for cancer management. Preliminary data are included in Appendix I for completeness. The results are promising, showing a substantial reduction in tumour growth and are the subject of further, ongoing studies.

7 References

(1) Peer, D.; Karp, J. M.; Hong, S.; Farokhzad, O. C.; Margalit, R.; Langer, R. *Nature nanotechnology* **2007**, *2*, 751.

(2) Schroeder, A.; Heller, D. A.; Winslow, M. M.; Dahlman, J. E.; Pratt, G. W.; Langer, R.; Jacks, T.; Anderson, D. G. *Nature Reviews Cancer* **2012**, *12*, 39.

(3) (a) Gao, Y.; Shi, J. F.; Yuan, D.; Xu, B. *Nat. Commun.* **2012**, *3*(b) Gao, Y.; Berciu, C.; Kuang, Y.; Shi, J.; Nicastro, D.; Xu, B. *ACS nano* **2013**, *7*, 9055(c) Kuang, Y.; Shi, J.; Li, J.; Yuan, D.; Alberti, K. A.; Xu, Q.; Xu, B. *Angewandte Chemie International Edition* **2014**.

(4) Patel, J. D.; Krilov, L.; Adams, S.; Aghajanian, C.; Basch, E.; Brose, M. S.; Carroll, W. L.; de Lima, M.; Gilbert, M. R.; Kris, M. G. *Journal of Clinical Oncology* **2014**, *32*, 129.

(5) Wang, X.; Yang, L.; Chen, Z. G.; Shin, D. M. *CA: a cancer journal for clinicians* **2008**, *58*, 97.

(6) Safra, T.; Muggia, F.; Jeffers, S.; Tsao-Wei, D.; Groshen, S.; Lyass, O.; Henderson, R.; Berry, G.; Gabizon, A. *Annals of Oncology* **2000**, *11*, 1029.

(7) Miele, E.; Spinelli, G. P.; Miele, E.; Tomao, F.; Tomao, S. *International journal of nanomedicine* **2009**, *4*, 99.

(8) Duncan, R.; Gaspar, R. *Molecular pharmaceutics* **2011**, *8*, 2101.

(9) Torchilin, V. P. *Nature Reviews Drug Discovery* **2005**, *4*, 145.

(10) (a) Nasongkla, N.; Bey, E.; Ren, J.; Ai, H.; Khemtong, C.; Guthi, J. S.; Chin, S.-F.; Sherry, A. D.; Boothman, D. A.; Gao, J. *Nano letters* **2006**, *6*, 2427(b) Oerlemans, C.; Bult, W.; Bos, M.; Storm, G.; Nijsen, J. F. W.; Hennink, W. E. *Pharmaceutical research* **2010**, *27*, 2569.

(11) Slowing, I. I.; Trewyn, B. G.; Lin, V. S.-Y. *J. Am. Chem. Soc.* **2007**, *129*, 8845.

(12) (a) Sykes, E. A.; Chen, J.; Zheng, G.; Chan, W. C. *ACS nano* **2014**(b) Brown, S. D.; Nativo, P.; Smith, J.-A.; Stirling, D.; Edwards, P. R.; Venugopal, B.; Flint, D. J.; Plumb, J. A.; Graham, D.; Wheate, N. J. *J. Am. Chem. Soc.* **2010**, *132*, 4678.

(13) (a) Jordan, A.; Scholz, R.; Wust, P.; Fähling, H.; Felix, R. *Journal of Magnetism and Magnetic Materials* **1999**, *201*, 413(b) Harisinghani, M. G.; Saksena, M.; Ross, R. W.; Tabatabaei, S.; Dahl, D.; McDougal, S.; Weissleder, R. *Urology* **2005**, *66*, 1066.

(14) (a) Gao, X.; Cui, Y.; Levenson, R. M.; Chung, L. W.; Nie, S. *Nature biotechnology* **2004**, *22*, 969(b) Luo, G.; Long, J.; Zhang, B.; Liu, C.; Ji, S.; Xu, J.; Yu, X.; Ni, Q. *Expert opinion on drug delivery* **2012**, *9*, 47.

(15) Sohdi, A. A.; Campbell, D.; Topham, P. D. *Chiang Mai J. Sci.* **2012**, *39*, 351.

(16) Kratz, F.; Müller, I. A.; Ryppa, C.; Warnecke, A. *ChemMedChem* **2008**, *3*, 20.

(17) (a) Cho, K.; Wang, X.; Nie, S.; Shin, D. M. *Clinical Cancer Research* **2008**, *14*, 1310(b) Wolinsky, J. B.; Colson, Y. L.; Grinstaff, M. W. *Journal of Controlled Release* **2012**, *159*, 14(c) de las Heras Alarcón, C.; Pennadam, S.; Alexander, C. *Chem. Soc. Rev.* **2005**, *34*, 276.

(18) (a) Ruggiero, A.; Villa, C. H.; Bander, E.; Rey, D. A.; Bergkvist, M.; Batt, C. A.; Manova-Todorova, K.; Deen, W. M.; Scheinberg, D. A.; McDevitt, M. R. *Proceedings of the National Academy of Sciences* **2010**, *107*, 12369(b) Robinson, J. T.; Welsher, K.; Tabakman, S. M.; Sherlock, S. P.; Wang, H.; Luong, R.; Dai, H. *Nano research* **2010**, *3*, 779.

(19) Chow, E. K.; Zhang, X.-Q.; Chen, M.; Lam, R.; Robinson, E.; Huang, H.; Schaffer, D.; Osawa, E.; Goga, A.; Ho, D. *Science translational medicine* **2011**, *3*, 73ra21.

(20) (a) Andersen, E. S.; Dong, M.; Nielsen, M. M.; Jahn, K.; Subramani, R.; Mamdouh, W.; Golas, M. M.; Sander, B.; Stark, H.; Oliveira, C. L. *Nature* **2009**, *459*, 73(b) Tørring, T.; Voigt, N. V.; Nangreave, J.; Yan, H.; Gothelf, K. V. *Chem. Soc. Rev.* **2011**, *40*, 5636.

(21) Petros, R. A.; DeSimone, J. M. *Nature Reviews Drug Discovery* **2010**, *9*, 615.

(22) Duncan, R. *Nature Reviews Cancer* **2006**, *6*, 688.

(23) Danhier, F.; Feron, O.; Préat, V. *Journal of Controlled Release* **2010**, *148*, 135.

(24) Lehn, J.-M.; Sanders, J. *Supramolecular chemistry: concepts and perspectives*; Vch Weinheim, 1995.

(25) (a) Zhang, S. *Nature biotechnology* **2003**, *21*, 1171(b) Woolfson, D. N.; Mahmoud, Z. N. *Chem. Soc. Rev.* **2010**, *39*, 3464(c) Collier, J. H.; Rudra, J. S.; Gasiorowski, J. Z.; Jung, J. P. *Chem. Soc. Rev.* **2010**, *39*, 3413(d) Samad, A.; Sultana, Y.; Aqil, M. *Current drug delivery* **2007**, *4*, 297(e) Allen, T. M.; Cullis, P. R. *Advanced drug delivery reviews* **2013**, *65*, 36(f) Patil, S. D.; Rhodes, D. G.; Burgess, D. J. *The AAPS journal* **2005**, *7*, E61.

(26) Silva, G. A.; Czeisler, C.; Niece, K. L.; Beniash, E.; Harrington, D. A.; Kessler, J. A.; Stupp, S. I. *Science* **2004**, *303*, 1352.

(27) Ghadiri, M. R.; Granja, J. R.; Milligan, R. A.; McRee, D. E.; Khazanovich, N. *Nature* **1993**, *366*, 324.

(28) Zhang, S.; Holmes, T.; Lockshin, C.; Rich, A. *Proceedings of the National Academy of Sciences* **1993**, *90*, 3334.

(29) (a) Naskar, J.; Palui, G.; Banerjee, A. *The Journal of Physical Chemistry B* **2009**, *113*, 11787(b) Fichman, G.; Gazit, E. *Acta Biomater.* **2013**(c) de la Rica, R.; Matsui, H. *Chem. Soc. Rev.* **2010**, *39*, 3499.

(30) Winkler, S.; Wilson, D.; Kaplan, D. *Biochemistry* **2000**, *39*, 12739.

(31) Yang, Z.; Gu, H.; Fu, D.; Gao, P.; Lam, J. K.; Xu, B. *Advanced Materials* **2004**, *16*, 1440.

(32) Pauling, L.; Corey, R. B. *Proc Natl Acad Sci USA* **1951**, *37*, 251.

(33) (a) Crick, F. H. *Acta crystallographica* **1953**, *6*, 689(b) Pauling, L.; Corey, R. B. **1953**.

(34) (a) Cui, H.; Webber, M. J.; Stupp, S. I. *Peptide Science* **2010**, *94*, 1(b) Hamley, I. *Soft Matter* **2011**, *7*, 4122(c) Hughes, M.; Birchall, L. S.; Zuberi, K.; Aitken, L. A.; Debnath, S.; Javid, N.; Ulijn, R. V. *Soft Matter* **2012**, *8*, 11565.

(35) Raeburn, J.; Cardoso, A. Z.; Adams, D. J. *Chem. Soc. Rev.* **2013**, *42*, 5143.

(36) Sadownik, J. W.; Leckie, J.; Ulijn, R. V. *Chem. Commun.* **2011**, *47*, 728.

(37) Banwell, E. F.; Abelardo, E. S.; Adams, D. J.; Birchall, M. A.; Corrigan, A.; Donald, A. M.; Kirkland, M.; Serpell, L. C.; Butler, M. F.; Woolfson, D. N. *Nature materials* **2009**, *8*, 596.

(38) Papo, N.; Shai, Y. *Biochemistry* **2003**, *42*, 9346.

(39) (a) Pandya, M. J.; Spooner, G. M.; Sunde, M.; Thorpe, J. R.; Rodger, A.; Woolfson, D. N. *Biochemistry* **2000**, *39*, 8728(b) Potekhin, S.; Melnik, T.; Popov, V.; Lanina, N.; Vazina, A.; Rigler, P.; Verdini, A.; Corradin, G.; Kajava, A. *Chemistry & biology* **2001**, *8*, 1025.

(40) Zhang, S.; Gelain, F.; Zhao, X. Seminars in cancer biology, 2005; p 413.

(41) (a) Hartgerink, J. D.; Beniash, E.; Stupp, S. I. *Science* **2001**, *294*, 1684(b) Beniash, E.; Hartgerink, J. D.; Storrie, H.; Stendahl, J. C.; Stupp, S. I. *Acta Biomater.* **2005**, *1*, 387.

(42) Standley, S. M.; Toft, D. J.; Cheng, H.; Soukasene, S.; Chen, J.; Raja, S. M.; Band, V.; Band, H.; Cryns, V. L.; Stupp, S. I. *Cancer research* **2010**, *70*, 3020.

(43) (a) Zha, R. H.; Sur, S.; Stupp, S. I. *Advanced healthcare materials* **2013**, *2*, 126(b) Soukasene, S.; Toft, D. J.; Moyer, T. J.; Lu, H.; Lee, H.-K.; Standley, S. M.; Cryns, V. L.; Stupp, S. I. *ACS nano* **2011**, *5*, 9113.

(44) Adams, D. J. *Macromol. Biosci.* **2011**, *11*, 160.

(45) Reches, M.; Gazit, E. *Science* **2003**, *300*, 625.

(46) (a) Jayawarna, V.; Ali, M.; Jowitt, T. A.; Miller, A. F.; Saiani, A.; Gough, J. E.; Ulijn, R. V. *Advanced Materials* **2006**, *18*, 611(b) Kuang, Y.; Xu, B. *Angewandte Chemie International Edition* **2013**, *52*, 6944.

(47) Yang, Z.; Xu, K.; Guo, Z.; Guo, Z.; Xu, B. *Advanced Materials* **2007**, *19*, 3152.

(48) Strebhardt, K.; Ullrich, A. *Nature Reviews Cancer* **2008**, *8*, 473.

(49) Chen, J.-X.; Xu, X.-D.; Chen, W.-H.; Zhang, X.-Z. *ACS applied materials & interfaces* **2013**, *6*, 593.

(50) Zelzer, M.; Todd, S. J.; Hirst, A. R.; McDonald, T. O.; Ulijn, R. V. *Biomaterials Science* **2013**, *1*, 11.

(51) Ku, T. H.; Chien, M. P.; Thompson, M. P.; Sinkovits, R. S.; Olson, N. H.; Baker, T. S.; Gianneschi, N. C. *J. Am. Chem. Soc.* **2011**, *133*, 8392.

(52) Chien, M. P.; Thompson, M. P.; Barback, C. V.; Ku, T. H.; Hall, D. J.; Gianneschi, N. C. *Advanced Materials* **2013**.

(53) Wang, Q.; Yang, Z.; Gao, Y.; Ge, W.; Wang, L.; Xu, B. *Soft Matter* **2008**, *4*, 550.

(54) Webber, M. J.; Newcomb, C. J.; Bitton, R.; Stupp, S. I. *Soft Matter* **2011**, *7*, 9665.

(55) Zhao, Y.; Ji, T.; Wang, H.; Li, S.; Zhao, Y.; Nie, G. *Journal of Controlled Release* **2014**.

(56) Zhao, Z.; Meng, H.; Wang, N.; Donovan, M. J.; Fu, T.; You, M.; Chen, Z.; Zhang, X.; Tan, W. *Angewandte Chemie International Edition* **2013**, *52*, 7487.

(57) Moitra, P.; Kumar, K.; Kondaiah, P.; Bhattacharya, S. *Angewandte Chemie International Edition* **2014**, *53*, 1113.

(58) Kono, K.; Yoshino, K.; Takagishi, T. *Journal of Controlled Release* **2002**, *80*, 321.

(59) Wilson, M. W.; Kerlan Jr, R. K.; Fidelman, N. A.; Venook, A. P.; LaBerge, J. M.; Koda, J.; Gordon, R. L. *Radiology* **2004**, *230*, 287.

(60) McBain, S.; Griesenbach, U.; Xenariou, S.; Keramane, A.; Batich, C.; Alton, E.; Dobson, J. *Nanotechnology* **2008**, *19*, 405102.

(61) Koppenol, W. H.; Bounds, P. L.; Dang, C. V. *Nature Reviews Cancer* **2011**, *11*, 325.

(62) Sinthuvanich, C.; Veiga, A. S.; Gupta, K.; Gaspar, D.; Blumenthal, R.; Schneider, J. P. *J. Am. Chem. Soc.* **2012**, *134*, 6210.

(63) Maeda, H.; Wu, J.; Sawa, T.; Matsumura, Y.; Hori, K. *Journal of Controlled Release* **2000**, *65*, 271.

(64) Wong, C.; Stylianopoulos, T.; Cui, J.; Martin, J.; Chauhan, V. P.; Jiang, W.; Popović, Z.; Jain, R. K.; Bawendi, M. G.; Fukumura, D. *Proceedings of the National Academy of Sciences* **2011**, *108*, 2426.

(65) Akhtar, M. J.; Ahamed, M.; Alhadlaq, H. A.; Alrokayan, S. A.; Kumar, S. *Clinica Chimica Acta* **2014**, *436*, 78.

(66) Desgrosellier, J. S.; Cheresh, D. A. *Nature Reviews Cancer* **2010**, *10*, 9.

(67) Hartmann, L. C.; Keeney, G. L.; Lingle, W. L.; Christianson, T. J.; Varghese, B.; Hillman, D.; Oberg, A. L.; Low, P. S. *Int. J. Cancer* **2007**, *121*, 938.

(68) (a) Liang, J.; Wu, W.-L.; Xu, X.-D.; Zhuo, R.-X.; Zhang, X.-Z. *Colloids and Surfaces B: Biointerfaces* **2014**, *114*, 398(b) Guler, M. O.; Hsu, L.; Soukasene, S.; Harrington, D. A.; Hulvat, J. F.; Stupp, S. I. *Biomacromolecules* **2006**, *7*, 1855.

(69) Nel, A. E.; Mädler, L.; Velegol, D.; Xia, T.; Hoek, E. M.; Somasundaran, P.; Klaessig, F.; Castranova, V.; Thompson, M. *Nature materials* **2009**, *8*, 543.

(70) Hendrickson, G. R.; Smith, M. H.; South, A. B.; Lyon, L. A. *Adv. Funct. Mater.* **2010**, *20*, 1697.

(71) Bala, V.; Rao, S.; Boyd, B. J.; Prestidge, C. A. *Journal of Controlled Release* **2013**, *172*, 48.

(72) Zachowski, A. *BIOCHEMICAL JOURNAL-LONDON-* **1993**, *294*, 1.

(73) (a) Chaurio, R. A.; Janko, C.; Muñoz, L. E.; Frey, B.; Herrmann, M.; Gaipl, U. S. *Molecules* **2009**, *14*, 4892(b) Zwaal, R.; Comfurius, P.; Bevers, E. *Cellular and Molecular Life Sciences CMLS* **2005**, *62*, 971.

(74) Reis, C. A.; Osorio, H.; Silva, L.; Gomes, C.; David, L. *Journal of Clinical Pathology* **2010**, *63*, 322.

(75) (a) Papo, N.; Seger, D.; Makovitzki, A.; Kalchenko, V.; Eshhar, Z.; Degani, H.; Shai, Y. *Cancer research* **2006**, *66*, 5371(b) Schweizer, F. *European journal of pharmacology* **2009**, *625*, 190.

(76) Newcomb, C. J.; Sur, S.; Ortony, J. H.; Lee, O.-S.; Matson, J. B.; Boekhoven, J.; Yu, J. M.; Schatz, G. C.; Stupp, S. I. *Nat. Commun.* **2014**, *5*.

(77) Kato, Y.; Ozawa, S.; Miyamoto, C.; Maehata, Y.; Suzuki, A.; Maeda, T.; Baba, Y. *Cancer Cell Int* **2013**, *13*, 89.

(78) Le, A.; Cooper, C. R.; Gouw, A. M.; Dinavahi, R.; Maitra, A.; Deck, L. M.; Royer, R. E.; Vander Jagt, D. L.; Semenza, G. L.; Dang, C. V. *Proceedings of the National Academy of Sciences* **2010**, *107*, 2037.

(79) Tennant, D. A.; Durán, R. V.; Gottlieb, E. *Nature Reviews Cancer* **2010**, *10*, 267.

(80) Schmaljohann, D. *Advanced drug delivery reviews* **2006**, *58*, 1655.

(81) Gialeli, C.; Theocharis, A. D.; Karamanos, N. K. *Febs J.* **2011**, *278*, 16.

(82) (a) Basel, M. T.; Balivada, S.; Shrestha, T. B.; Seo, G. M.; Pyle, M. M.; Tamura, M.; Bossmann, S. H.; Troyer, D. L. *Small* **2012**, *8*, 913(b) Troyer, D. *J Cancer Sci Ther* **2013**, *5*, 142.

(83) Magennis, E. P.; Fernandez-Trillo, F.; Sui, C.; Spain, S. G.; Bradshaw, D. J.; Churchley, D.; Mantovani, G.; Winzer, K.; Alexander, C. *Nature materials* **2014**.

(84) Kantarjian, H.; Shah, N. P.; Hochhaus, A.; Cortes, J.; Shah, S.; Ayala, M.; Moiraghi, B.; Shen, Z.; Mayer, J.; Pasquini, R. *New England Journal of Medicine* **2010**, *362*, 2260.

(85) McDonald, T. O.; Qu, H. L.; Saunders, B. R.; Ulijn, R. V. *Soft Matter* **2009**, *5*, 1728.

(86) Saunders, B. R.; Laajam, N.; Daly, E.; Teow, S.; Hu, X. H.; Stepto, R. *Adv. Colloid Interface Sci.* **2009**, *147-48*, 251.

(87) (a) Bosslet, K.; Straub, R.; Blumrich, M.; Czech, J.; Gerken, M.; Sperker, B.; Kroemer, H. K.; Gesson, J.-P.; Koch, M.; Monneret, C. *Cancer research* **1998**, *58*, 1195(b) Tranoy-Opalinski, I.; Legigan, T.; Barat, R.; Clarhaut, J.; Thomas, M.; Renoux, B.; Papot, S. *European Journal of Medicinal Chemistry* **2014**.

(88) Buckley, C. D.; Pilling, D.; Henriquez, N. V.; Parsonage, G.; Threlfall, K.; Scheel-Toellner, D.; Simmons, D. L.; Akbar, A. N.; Lord, J. M.; Salmon, M. *Nature* **1999**, *397*, 534.

(89) Philchenkov, A.; Zavelevich, M.; Kroczak, T. J.; Los, M. J. *Experimental oncology* **2004**, *26*, 82.

(90) Devarajan, E.; Sahin, A. A.; Chen, J. S.; Krishnamurthy, R. R.; Aggarwal, N.; Brun, A.-M.; Sapino, A.; Zhang, F.; Sharma, D.; Yang, X.-H. *Oncogene* **2002**, *21*, 8843.

(91) Minko, T.; Kopečková, P.; Kopeček, J. *Int. J. Cancer* **2000**, *86*, 108.

(92) Glangchai, L. C.; Caldorera-Moore, M.; Shi, L.; Roy, K. *Journal of Controlled Release* **2008**, *125*, 263.

(93) Dos Santos, S.; Chandravarkar, A.; Mandal, B.; Mimna, R.; Murat, K.; Saucède, L.; Tella, P.; Tuchscherer, G.; Mutter, M. *J. Am. Chem. Soc.* **2005**, *127*, 11888.

(94) Pro, B.; Dang, N. **2004**.

(95) Thomas, G. *Nature Reviews Molecular Cell Biology* **2002**, *3*, 753.

(96) Biswas, A.; Joo, K.-I.; Liu, J.; Zhao, M.; Fan, G.; Wang, P.; Gu, Z.; Tang, Y. *ACS nano* **2011**, *5*, 1385.

(97) Stern, R. Seminars in cancer biology, 2008; p 275.

(98) Yang, Z.; Liang, G.; Wang, L.; Xu, B. *J. Am. Chem. Soc.* **2006**, *128*, 3038.

(99) Bacinello, D.; Garanger, E.; Taton, D.; Tam, K. C.; Lecommandoux, S. *Biomacromolecules* **2014**.

(100) Kratz, F.; Drevs, J.; Bing, G.; Stockmar, C.; Scheuermann, K.; Lazar, P.; Unger, C. *Bioorganic & medicinal chemistry letters* **2001**, *11*.

(101) Rodriguez, A. R.; Kramer, J. R.; Deming, T. J. *Biomacromolecules* **2013**, *14*, 3610.

(102) Yang, Z.; Xu, B. *Chem. Commun.* **2004**, 2424.

(103) van Dijk, M.; van Nostrum, C. F.; Hennink, W. E.; Rijkers, D. T.; Liskamp, R. M. *Biomacromolecules* **2010**, *11*, 1608.

(104) West, J. L.; Hubbell, J. A. *Macromolecules* **1999**, *32*, 241.

(105) Bremmer, S. C.; McNeil, A. J.; Soellner, M. B. *Chem. Commun.* **2014**, *50*, 1691.

(106) Laromaine, A.; Koh, L.; Murugesan, M.; Ulijn, R. V.; Stevens, M. M. *J. Am. Chem. Soc.* **2007**, *129*, 4156.

(107) Denmeade, S. R.; Nagy, A.; Gao, J.; Lilja, H.; Schally, A. V.; Isaacs, J. T. *Cancer research* **1998**, *58*, 2537.

(108) Denmeade, S. R.; Lou, W.; Lövgren, J.; Malm, J.; Lilja, H.; Isaacs, J. T. *Cancer research* **1997**, *57*, 4924.

(109) Mazhar, D.; Ngan, S.; Waxman, J. *BJU international* **2006**, *98*, 725.

(110) Koga, T.; Kitamura, K.-i.; Higashi, N. *Chem. Commun.* **2006**, 4897.

(111) Bremmer, S. C.; Chen, J.; McNeil, A. J.; Soellner, M. B. *Chem. Commun.* **2012**, *48*, 5482.

(112) Guarise, C.; Pasquato, L.; De Filippis, V.; Scrimin, P. *Proceedings of the National Academy of Sciences of the United States of America* **2006**, *103*, 3978.

(113) Gao, J.; Zheng, W.; Kong, D.; Yang, Z. *Soft Matter* **2011**, *7*, 10443.

(114) Law, B.; Weissleder, R.; Tung, C.-H. *Biomacromolecules* **2006**, *7*, 1261.

(115) Lowe, S. B.; Dick, J. A.; Cohen, B. E.; Stevens, M. M. *ACS nano* **2011**, *6*, 851.

(116) Andreasen, P. A.; Kjøller, L.; Christensen, L.; Duffy, M. J. *Int. J. Cancer* **1997**, *72*, 1.

(117) Woessner, J. F. *The FASEB Journal* **1991**, *5*, 2145.

(118) Nagase, H. In *Matrix Metalloproteinase Inhibitors in Cancer Therapy*; Springer, 2001.

(119) Schechte.I; Berger, A. *Biochem. Biophys. Res. Commun.* **1967**, *27*, 157.

(120) Huang, Y.; Shi, J.; Yuan, D.; Zhou, N.; Xu, B. *Biopolymers* **2013**, *100*, 790.

(121) de Graaf, A. J.; Mastrobattista, E.; Vermonden, T.; van Nostrum, C. F.; Rijkers, D. T.; Liskamp, R. M.; Hennink, W. E. *Macromolecules* **2012**, *45*, 842.

(122) Garripelli, V. K.; Kim, J. K.; Son, S.; Kim, W. J.; Repka, M. A.; Jo, S. *Acta Biomater.* **2011**, *7*, 1984.

(123) Jun, H. W.; Yuwono, V.; Paramonov, S. E.; Hartgerink, J. D. *Advanced Materials* **2005**, *17*, 2612.

(124) Koda, D.; Maruyama, T.; Minakuchi, N.; Nakashima, K.; Goto, M. *Chem. Commun.* **2010**, *46*, 979.

(125) Chau, Y.; Luo, Y.; Cheung, A. C. Y.; Nagai, Y.; Zhang, S. G.; Kobler, J. B.; Zeitels, S. M.; Langer, R. *Biomaterials* **2008**, *29*, 1713.

(126) Giano, M. C.; Pochan, D. J.; Schneider, J. P. *Biomaterials* **2011**, *32*, 6471.

(127) Yang, Z. M.; Ma, M. L.; Xu, B. *Soft Matter* **2009**, *5*, 2546.

(128) Swintosk.Jv; Adams, H. J.; Caldwell, H. C.; Dittert, L. W.; Ellison, T.; Rivard, D. E. *J. Pharm. Sci.* **1966**, *55*, 992.

(129) Albert, A. *Nature* **1958**, *182*, 421.

(130) Stella, V. *Abstr. Pap. Am. Chem. Soc.* **1974**, 19.

(131) Seymour, L. W.; Ferry, D. R.; Kerr, D. J.; Rea, D.; Whitlock, M.; Poyner, R.; Boivin, C.; Hesslewood, S.; Twelves, C.; Blackie, R.; Schatzlein, A.; Jodrell, D.; Bissett, D.; Calvert, H.; Lind, M.; Robbins, A.; Burtles, S.; Duncan, R.; Cassidy, J. *Int. J. Oncol.* **2009**, *34*, 1629.

(132) Chau, Y.; Tan, F. E.; Langer, R. *Bioconjugate Chem.* **2004**, *15*, 931.

(133) Woodward, N. C.; Chowdhry, B. Z.; Snowden, M. J.; Leharne, S. A.; Griffiths, P. C.; Winnington, A. L. *Langmuir* **2003**, *19*, 3202.

(134) Staudinger, H.; Husemann, E. *Berichte Der Deutschen Chemischen Gesellschaft* **1935**, *68*, 1618.

(135) Baker, W. O. *Industrial and Engineering Chemistry* **1949**, *41*, 511.

(136) Nayak, S.; Lyon, L. A. *Angew. Chem.-Int. Edit.* **2005**, *44*, 7686.

(137) Murray, M.; Snowden, M. *Adv. Colloid Interface Sci.* **1995**, *54*, 73.

(138) Alemán, J.; Chadwick, A. V.; He, J.; Hess, M.; Horie, K.; Jones, R. G.; Kratochvíl, P.; Meisel, I.; Mita, I.; Moad, G. *Pure and Applied Chemistry* **2007**, *79*, 1801.

(139) Gupta, P.; Vermani, K.; Garg, S. *Drug Discov. Today* **2002**, *7*, 569.

(140) Eichenbaum, G. M.; Kiser, P. F.; Simon, S. A.; Needham, D. *Macromolecules* **1998**, *31*, 5084.

(141) Dai, S.; Ravi, P.; Tam, K. C. *Soft Matter* **2008**, *4*, 435.

(142) Raemdonck, K.; Demeester, J.; De Smedt, S. *Soft Matter* **2009**, *5*, 707.

(143) Pelton, R. *Adv. Colloid Interface Sci.* **2000**, *85*, 1.

(144) Thaiboonrod, S.; Berkland, C.; Milani, A. H.; Ulijn, R.; Saunders, B. R. *Soft Matter* **2013**, *9*, 3920.

(145) Plunkett, K. N.; Berkowski, K. L.; Moore, J. S. *Biomacromolecules* **2005**, *6*, 632.

(146) Lutolf, M. P.; Raeber, G. P.; Zisch, A. H.; Tirelli, N.; Hubbell, J. A. *Advanced Materials* **2003**, *15*, 888.

(147) (a) Kim, S.; Healy, K. E. *Biomacromolecules* **2003**, *4*, 1214(b) Kim, S.; Chung, E. H.; Gilbert, M.; Healy, K. E. *Journal of Biomedical Materials Research Part A* **2005**, *75A*, 73.

(148) (a) Thornton, P. D.; Mart, R. J.; Ulijn, R. V. *Advanced Materials* **2007**, *19*, 1252(b) Thornton, P. D.; Mart, R. J.; Webb, S. J.; Ulijn, R. V. *Soft Matter* **2008**, *4*, 821.

(149) Williams, R. J.; Mart, R. J.; Ulijn, R. V. *Biopolymers*, *94*, 107.

(150) Yang, Z.; Liang, G.; Xu, B. *Accounts Chem. Res.* **2008**, *41*, 315.

(151) (a) Toledano, S.; Williams, R. J.; Jayawarna, V.; Ulijn, R. V. *J. Am. Chem. Soc.* **2006**, *128*, 1070(b) Das, A. K.; Collins, R.; Ulijn, R. V. *Small* **2008**, *4*, 279.

(152) Roy, S.; Ulijn, R. V. In *Enzymatic Polymerisation*; Palmans, A. R. A., Heise, A., Eds.; Springer-Verlag Berlin: Berlin, 2010; Vol. 237.

(153) Mutter, M.; Chandravarkar, A.; Boyat, C.; Lopez, J.; Dos Santos, S.; Mandal, B.; Mimna, R.; Murat, K.; Patiny, L.; Saucède, L. *Angewandte Chemie International Edition* **2004**, *43*, 4172.

(154) Kühnle, H.; Börner, H. G. *Angewandte Chemie International Edition* **2009**, *48*, 6431.

(155) Amir, R. J.; Zhong, S.; Pochan, D. J.; Hawker, C. J. *J. Am. Chem. Soc.* **2009**, *131*, 13949.

(156) Akers, W. J.; Xu, B. G.; Lee, H.; Sudlow, G. P.; Fields, G. B.; Achilefu, S.; Edwards, W. B. *Bioconjugate Chem.* **2012**, *23*, 656.

(157) Yamamoto, N.; Bryce, N. S.; Metzler-Nolte, N.; Hambley, T. W. *Bioconjugate Chem.* **2012**, *23*, 1110.

(158) Lin, Y.-A.; Ou, Y.-C.; Cheetham, A. G.; Cui, H. *Biomacromolecules* **2014**.

(159) Kim, K.; Bae, B.; Kang, Y. J.; Nam, J.-M.; Kang, S.; Ryu, J.-H. *Biomacromolecules* **2013**, *14*, 3515.

(160) Kulkarni, P. S.; Haldar, M. K.; Nahire, R. R.; Katti, P.; Ambre, A. H.; Muhonen, W. W.; Shabb, J. B.; Padi, S. K.; Singh, R. K.; Borowicz, P. P. *Molecular pharmaceutics* **2014**.

(161) Lee, S.; Kang, S.-W.; Ryu, J. H.; Na, J. H.; Lee, D.-E.; Han, S. J.; Kang, C. M.; Choe, Y. S.; Lee, K. C.; Leary, J. F. *Bioconjugate Chem.* **2014**, *25*, 601.

(162) Caponi, P.-F.; Qiu, X.-P.; Vilela, F.; Winnik, F. M.; Ulijn, R. V. *Polymer Chemistry* **2011**, *2*, 306.

(163) Chien, M.-P.; Carlini, A. S.; Hu, D.; Barback, C. V.; Rush, A. M.; Hall, D. J.; Orr, G.; Gianneschi, N. C. *J. Am. Chem. Soc.* **2013**, *135*, 18710.

(164) (a) Williams, R. J.; Mart, R. J.; Ulijn, R. V. *Biopolymers* **2010**, *94*, 107(b) Hahn, M. E.; Gianneschi, N. C. *Chem. Commun.* **2011**, *47*, 11814.

(165) (a) Gao, Y.; Yang, Z. M.; Kuang, Y.; Ma, M. L.; Li, J. Y.; Zhao, F.; Xu, B. *Biopolymers* **2010**, *94*, 19(b) Gao, Y.; Shi, J.; Yuan, D.; Xu, B. *Nat. Commun.* **2012**, *3*, 1033.

(166) Itoh, Y.; Nagase, H. *Essays Biochem* **2002**, *38*, 21.

(167) (a) Brinckerhoff, C. E.; Rutter, J. L.; Benbow, U. *Clinical Cancer Research* **2000**, *6*, 4823(b) Egeblad, M.; Werb, Z. *Nature Reviews Cancer* **2002**, *2*, 161(c) Roomi, M. W.; Monterrey, J. C.; Kalinovsky, T.; Rath, M.; Niedzwiecki, A. *Oncol. Rep.* **2009**, *21*, 1323.

(168) Lutolf, M.; Lauer-Fields, J.; Schmoekel, H.; Metters, A.; Weber, F.; Fields, G.; Hubbell, J. *Proceedings of the National Academy of Sciences* **2003**, *100*, 5413.

(169) Koda, D.; Maruyama, T.; Minakuchi, N.; Nakashima, K.; Goto, M. *Chem. Commun.* **2010**, *46*, 979.

(170) Rawlings, N. D.; Morton, F. R.; Kok, C. Y.; Kong, J.; Barrett, A. J. *Nucleic Acids Res.* **2008**, *36*, D320.

(171) (a) Seltzer, J. L.; Weingarten, H.; Akers, K. T.; Eschbach, M. L.; Grant, G. A.; Eisen, A. Z. *J. Biol. Chem.* **1989**, *264*, 19583(b) Seltzer, J. L.; Akers, K. T.; Weingarten, H.; Grant, G. A.; McCourt, D. W.; Eisen, A. Z. *J. Biol. Chem.* **1990**, *265*, 20409(c) Netzelarnett, S.; Sang, Q. X.; Moore, W. G. I.; Navre, M.; Birkedalhansen, H.; Vanwart, H. E. *Biochemistry* **1993**, *32*, 6427.

(172) Hahn, M. E.; Randolph, L. M.; Adamiak, L.; Thompson, M. P.; Gianneschi, N. C. *Chem. Commun.* **2013**, *49*, 2873.

(173) Fleming, S.; Frederix, P. W.; Ramos Sasselli, I. n.; Hunt, N. T.; Ulijn, R. V.; Tuttle, T. *Langmuir* **2013**, *29*, 9510.

(174) Barth, A.; Zscherp, C. *Quarterly reviews of biophysics* **2002**, *35*, 369.

(175) Welsh, D. J.; Posocco, P.; Pricl, S.; Smith, D. K. *Org. Biomol. Chem.* **2013**, *11*, 3177.

(176) Dilly, A. k.; Ekambaram, P.; Guo, Y.; Cai, Y.; Tucker, S. C.; Fridman, R.; Kandouz, M.; Honn, K. V. *Int. J. Cancer* **2013**, *133*, 1784.

(177) Thornton, K.; Abul-Haija, Y. M.; Hodson, N.; Ulijn, R. V. *Soft Matter* **2013**, *9*, 9430.

(178) Albertazzi, L.; van der Zwaag, D.; Leenders, C. M.; Fitzner, R.; van der Hofstad, R. W.; Meijer, E. *Science* **2014**, *344*, 491.

(179) Roy, S.; Dasgupta, A.; Das, P. K. *Langmuir* **2007**, *23*, 11769.

(180) Birchall, L. S.; Roy, S.; Jayawarna, V.; Hughes, M.; Irvine, E.; Okorogheye, G. T.; Saudi, N.; De Santis, E.; Tuttle, T.; Edwards, A. A. *Chemical Science* **2011**, *2*, 1349.

(181) Azhdarinia, A.; Ghosh, P.; Ghosh, S.; Wilganowski, N.; Sevick-Muraca, E. M. *Molecular imaging and biology* **2012**, *14*, 261.

(182) Gao, Y.; Kuang, Y.; Du, X.; Zhou, J.; Chandran, P.; Horkay, F.; Xu, B. *Langmuir* **2013**, *29*, 15191.

(183) Hule, R. A.; Nagarkar, R. P.; Altunbas, A.; Ramay, H. R.; Branco, M. C.; Schneider, J. P.; Pochan, D. J. *Faraday discussions* **2008**, *139*, 251.

(184) Rughani, R. V.; Schneider, J. P. *MRS bulletin* **2008**, *33*, 530.

(185) Austin, P.; Heller, M.; Williams, D. E.; McIntosh, L. P.; Vogl, A. W.; Foster, L. J.; Andersen, R. J.; Roberge, M.; Roskelley, C. D. *PloS one* **2010**, *5*, e10836.

(186) Li, R.; Ackerman IV, W. E.; Mihai, C.; Volakis, L. I.; Ghadiali, S.; Kniss, D. A. *PloS one* **2012**, *7*, e39766.

(187) Tacar, O.; Sriamornsak, P.; Dass, C. R. *Journal of Pharmacy and Pharmacology* **2013**, *65*, 157.

(188) Weaver, A. M. *Clinical & experimental metastasis* **2006**, *23*, 97.

(189) Kuntsche, J.; Horst, J. C.; Bunjes, H. *International journal of pharmaceutics* **2011**, *417*, 120.

(190) Saunders, B. R.; Vincent, B. *Adv. Colloid Interface Sci.* **1999**, *80*, 1.

(191) Young, R. J.; Lovell, P. A. *Introduction to polymers*; second ed., 1991.

(192) Murray, M. J.; Snowden, M. J. *Advances in Colloid and Interface Science* **1995**, *54*, 73.

(193) Bradley, M. *Soft Matter* **2012**, *8*, 1268.

(194) Merrifield, R. B. *J. Am. Chem. Soc.* **1963**, *85*, 2149.

(195) Birchall, L. S.; Qu, H.; Ulijn, R. V. In *Surface modification of biomaterials Methods, analysis and applications*; Williams, R., Ed.; Woodhead Publishing Limited, 2011.

(196) Vinogradov, S. V. *Current Pharmaceutical Design* **2006**, *12*, 4703.

(197) Richter, A.; Paschew, G.; Klatt, S.; Lienig, J.; Arndt, K. F.; Adler, H. J. P. *Sensors* **2008**, *8*, 561.

(198) Mohammadi, Z.; Cole, A.; Berkland, C. J. *The Journal of Physical Chemistry C* **2009**, *113*, 7652.

(199) Keller, B. O.; Sui, J.; Young, A. B.; Whittal, R. M. *analytica chimica acta* **2008**, *627*, 71.

APPENDIX I

In vivo evaluation of doxorubicin loaded peptides for anticancer applications[†]

Preliminary results that were carried out by collaborators at the Beatson institute consist in cell cytotoxicity studies performed on micelle forming **1a** and **2a** peptides and their proteolysis resistant (**1a (D)** and **2a (D)**) versions. In addition, the cytotoxicity was assessed for the expected cleavage products **1b** and **2b**.

Possible toxic effects of micellar aggregates (L- and D- **1a** and **2a** peptides) assessed in there types of cells (HeLa, MDA-MB-231 and MDA-MB-231-luc-D3H2LN) using MTT assay showed low, concentration dependent cytotoxicity (Fig. I.1). HeLa cells seem to be more vulnerable to the presence of **1a** and **2a** peptides when compared to the other two cell lines assessed. Cell viability is concentration dependent. For peptide concentrations of 2.5 mM and lower cells show 100% or higher viability. When the viability is higher than 100% some internalisation and metabolism of the peptides seem to occur.

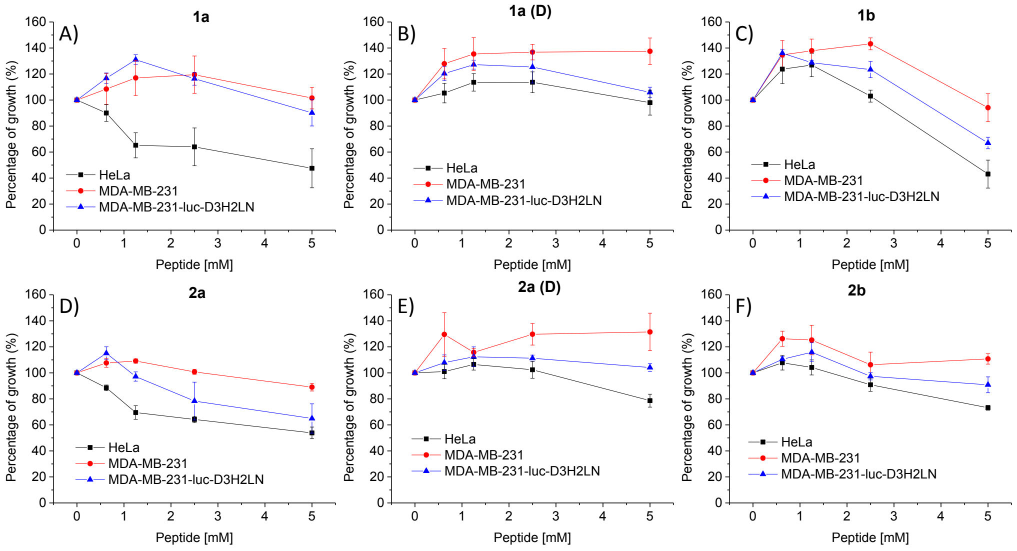

Figure I.1. MMT assays of HeLa, MDA-MB-231 and MDA-MB-231-luc-D3H2LN cells

---

[†] Cell work (MTT assays) and *in vivo* studies performed by Max Nobis, Beatson Cancer Research Institute.

treated for 3 days with increasing concentrations of peptides **1a** and **2a** as well as their counterparts **1a (D)** and **2a (D)** which are not cleavable by MMP-9 as well as the expected cleavage products **1b** and **2b**.

Based on MMP-9 quantification *in vitro* (Chapter 4) and MTT assays performed on three different cell lines, the invasive MDA-MB-231-L3H2LN cell line was chosen to induce tumours in mice. After the tumour reached the target size, mice were treated (subcutaneous injection) with doxorubicin loaded **2a** peptide micelles and the effect on tumour growth studied. Control experiments, to report the effect of doxorubicin, vehicle (PBS) and **2a** peptide micelles individually were performed for each of the mentioned categories. The first results show stasis of tumour growth only when doxorubicin loaded peptide (**2a**) micelles are used (Fig. I.2). In addition, when proteolysis resistant peptide (**2a (D)**) micelles are used as doxorubicin nanocarriers tumour growth can be seen.

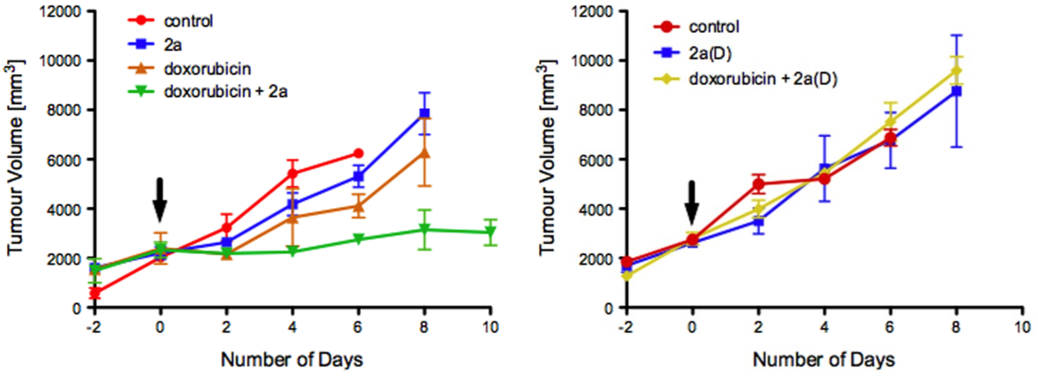

Figure I.2. *In vivo* tumour progression of MDA-MB-231-luc-D3H2LN subcutaneous tumours treated with **L-** (graph on the left) and **D-** (graph on the right) **2a** peptide (36 mg/kg), doxorubicin (1 mg/kg) or in combination of the two showing stasis of tumour growth in the combination treatment when **2a (L)** is used. In contrast, tumour growth is observed when **2a (D)** is used as nanocarrier for doxorubicin.

APPENDIX II

List of amino acid and their 3 and 1 letter code abbreviations

Entry	**Amino Acid**	**3 Letter Code**	**1 Letter Code**
1	Alanine	Ala	A
2	Arginine	Arg	R
3	Asparagine	Asn	N
4	Aspartic acid	Asp	D
5	Cysteine	Cys	C
6	Glutamic acid	Glu	E
7	Glutamine	Gln	Q
8	Glycine	Gly	G
9	Histidine	His	H
10	Isoleucine	Ile	I
11	Leucine	Leu	L
12	Lysine	Lys	K
13	Methionine	Met	M
14	Phenylalanine	Phe	F
15	Proline	Pro	P
16	Serine	Ser	S
17	Threonine	Thr	T
18	Tryptophan	Trp	W
19	Tyrosine	Tyr	Y
20	Valine	Val	V

APPENDIX III

Peptide characterisation

The complete LCMS spectra for **1a**, **1b**, **2a** and **2b** not shown in the main text to avoid redundancy are presented in this appendix. Complete MS spectra are shown here (only fragments of MS spectra were shown in the main text).

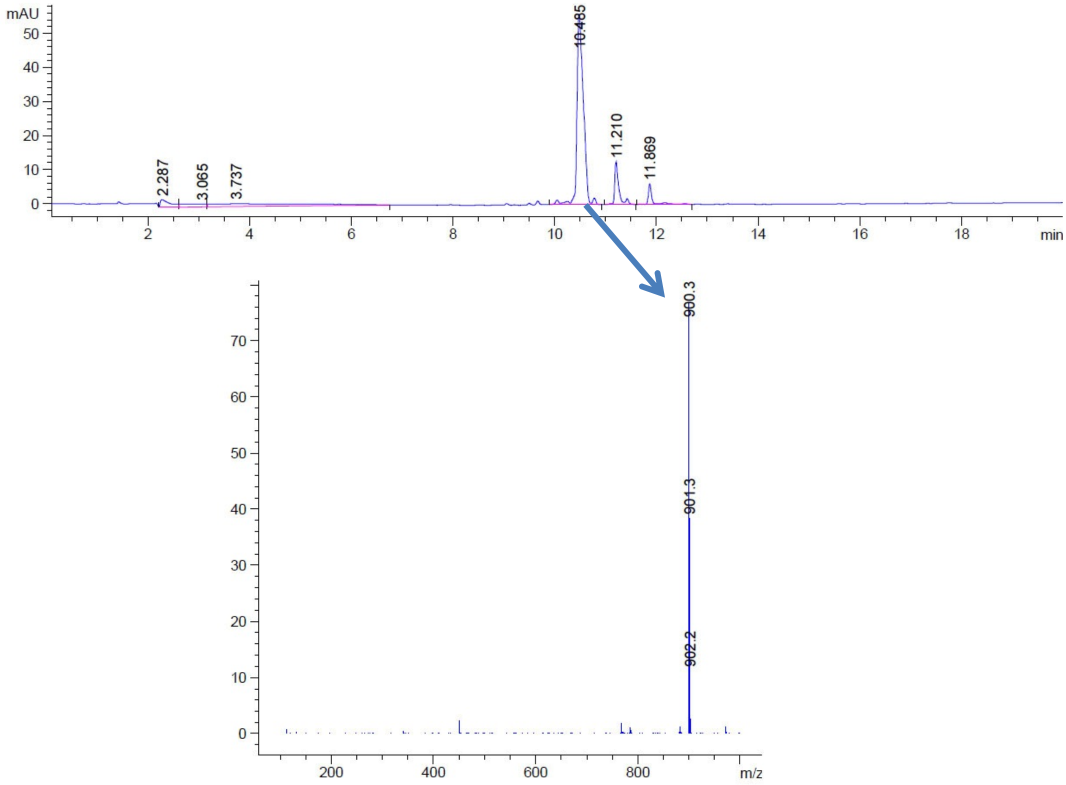

Figure III.1. LCMS data showing the LC chromatogram and the MS trace of PhAc-FFAGLDD (**1a**).

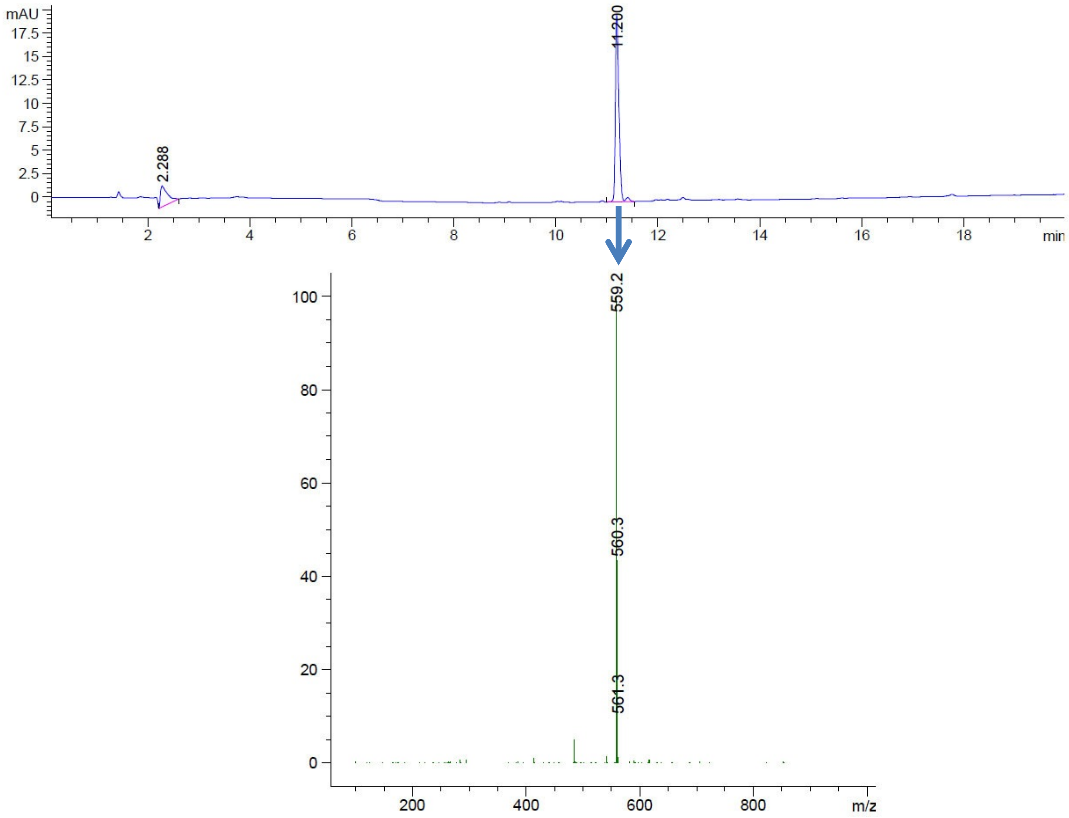

Figure III.2. LCMS data showing the LC chromatogram and the MS trace of PhAc-FFAG (**1b**).

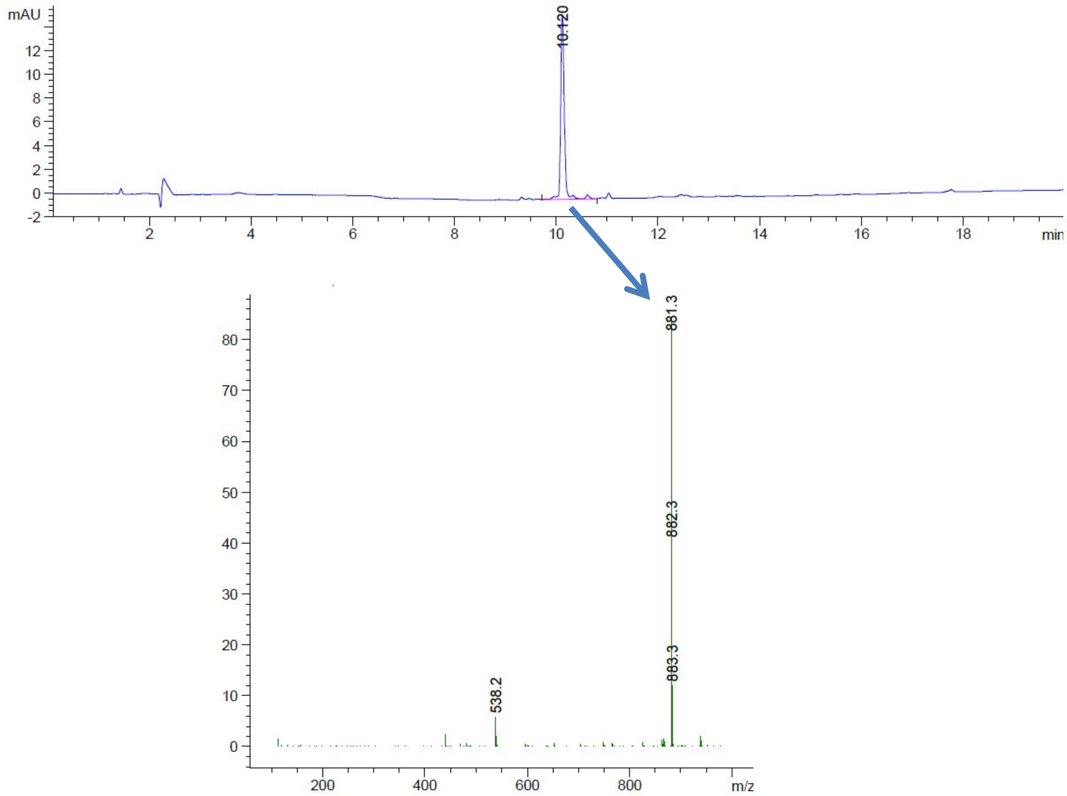

Figure III.3. LCMS data showing the LC chromatogram and the MS trace of GFFLGLDD (**2a**).

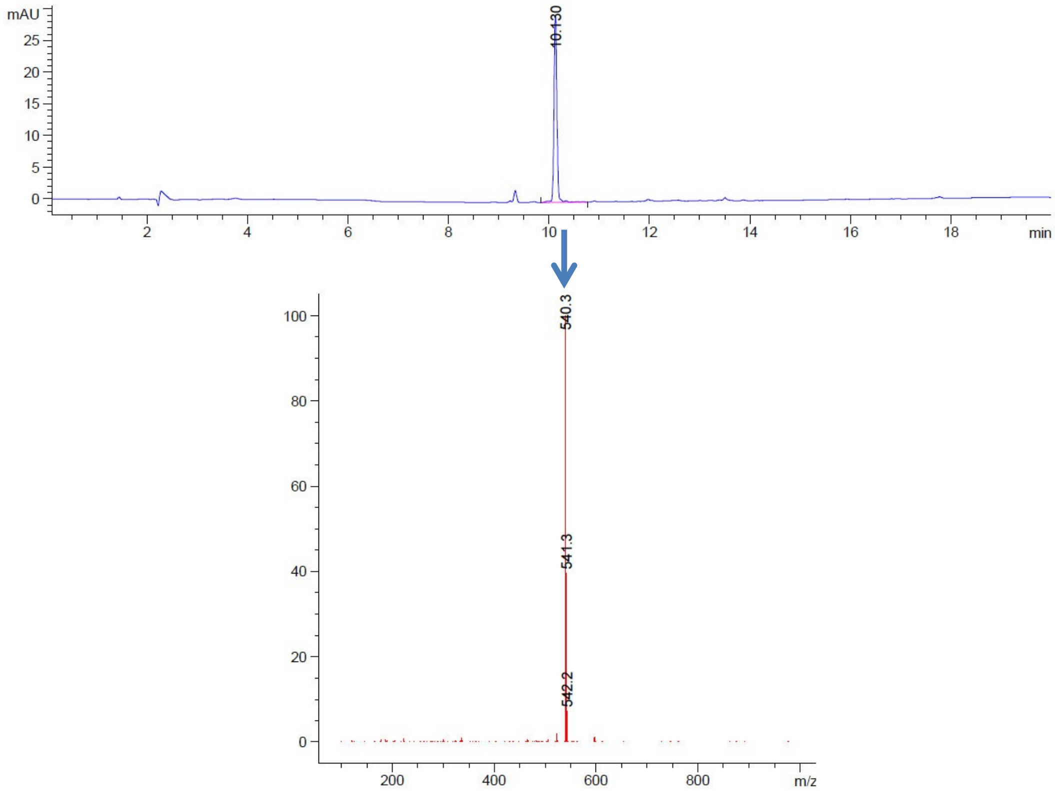

Figure III.4. LCMS data showing the LC chromatogram and the MS trace of GFFLG (**2b**).

APPENDIX IV

Enzyme hydrolysis product characterisation

Complete MS spectra showing the products of MMP-9 cleavage on 2a are presented (only fragments shown in the main text).

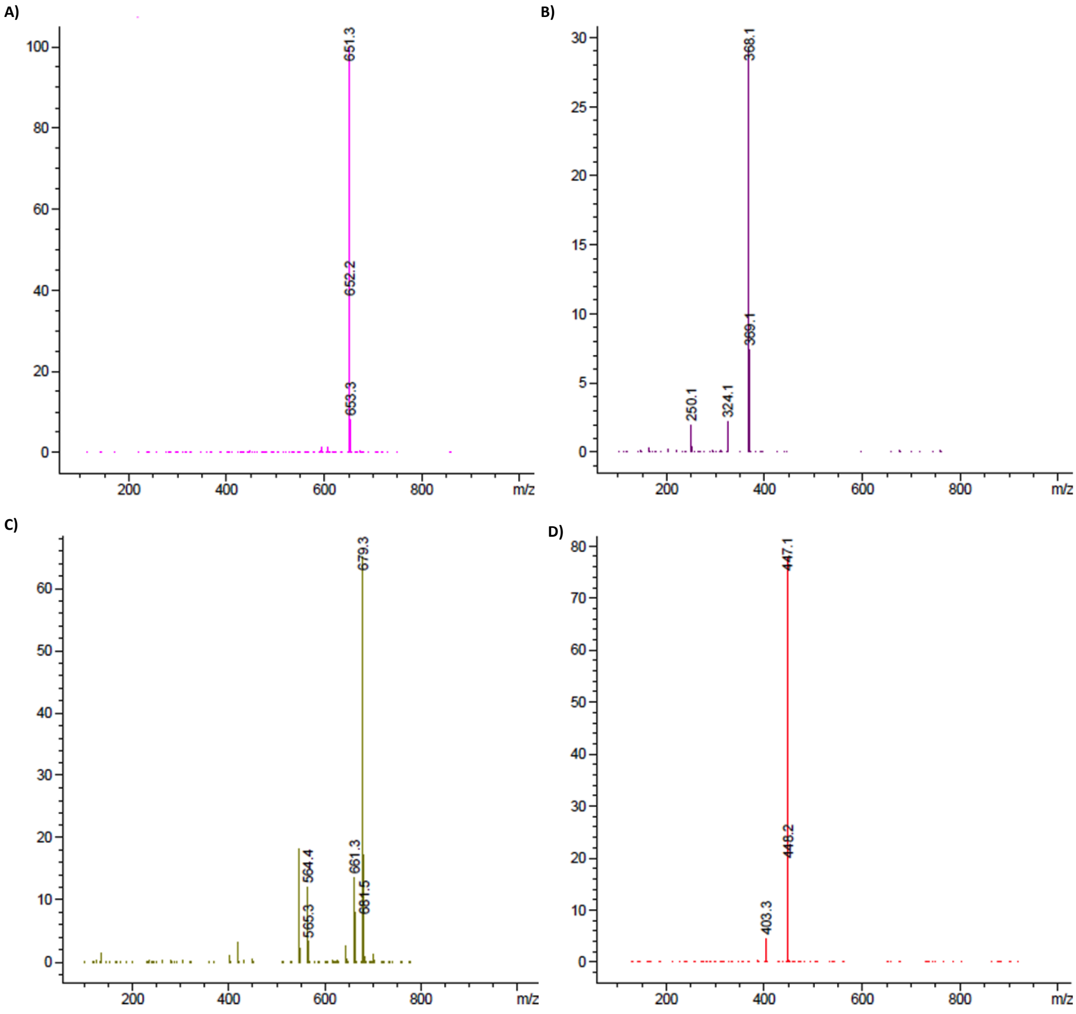

Figure IV.1. MS spectra of MMP-9 induced hydrolysis of GFFLGLDD (**2a**) into: A) **2c**; B) **2d**; C) **2e** and D) **2f.**

APPENDIX V

D-peptides characterisation

Proteolysis resistant, D- versions of **1a** and **2a** were synthesized for *in vitro* and *in vivo* studies and used as controls (not expected to show the same behaviour *in vivo* as their L- counterparts- See Appendix I).

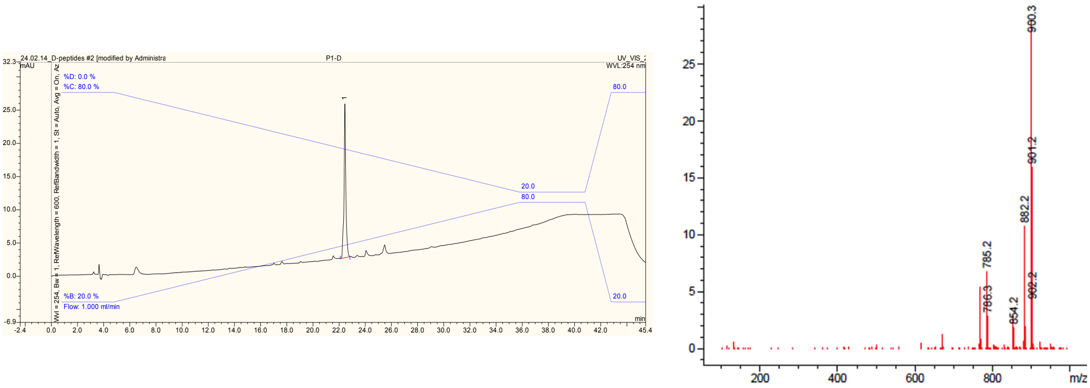

Figure V.1. HPLC chromatogram at 254 nm and MS spectra of PhAc-^{D}F^{D}F^{D}AG^{D}LDD (**1a (D)**) showing retention time of 22.4 min and [M-H]$^-$ = 900.3 (mass calculated: [M-H]$^-$ = 900.4).

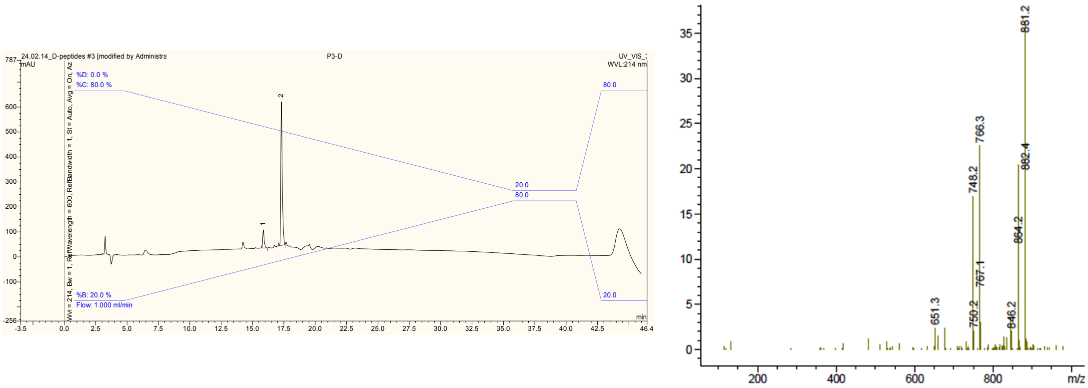

Figure V.2. HPLC chromatogram at 214 nm and MS spectra of G^{D}F^{D}F^{D}LG^{D}LDD (2a (D)) showing retention time of 17.3 min and [M-H]$^-$ = 881.2 (mass calculated: [M-H]$^-$ = 881.4).

APPENDIX VI

FRET peptide characterisation

Preliminary results include the synthesis of **2a** FRET peptide (Dabcyl-GFFLGLE(Edans)D-OH) and its characterisation (HPLC, MS). FRET peptide consists in Dabcyl (acceptor) – EDANS (donor) FRET pair separated by MMP-9 cleavable linker (GFFLGLED) as shown in figure VI.3.

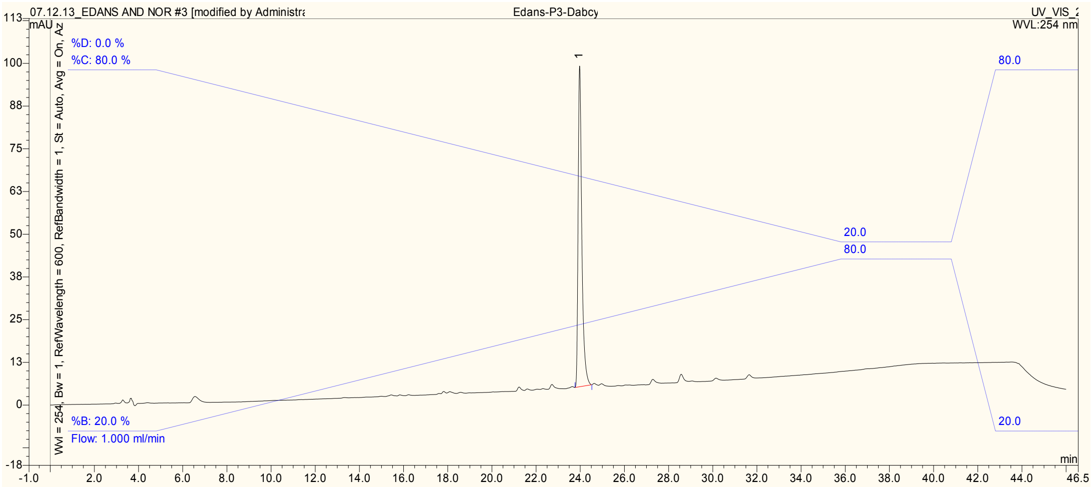

Figure VI.1. HPLC chromatogram of **2a** FRET (at 254 nm) showing a retention time of 24 min.

Figure VI.2. Mass spectrum of **2a** FRET showing $[M+H]^+$=1396.5 (mass calculated: $[M+H]^+$=1395.6)

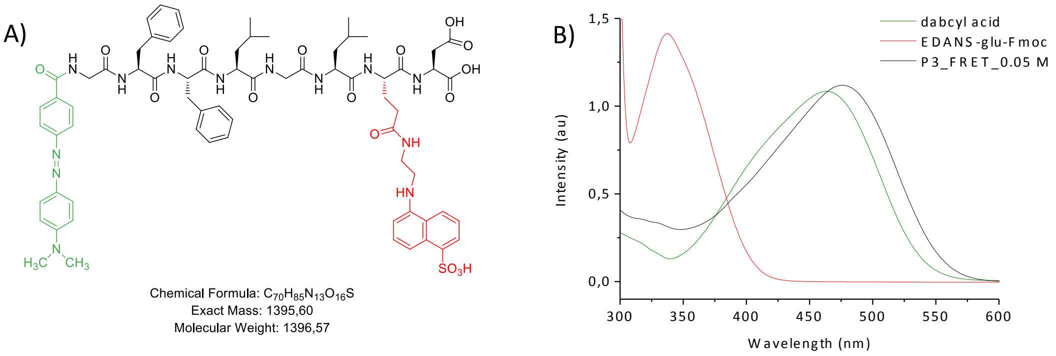

Figure VI.3. A) Chemical structure of the FRET peptide; B) UV-vis absorbance of dabcyl acid (green), EDANS-glu-Fmoc (red) and the FRET peptide (black).